January 2015

Impacts of Land-Atmosphere Interactions on Regional Convection and Rainfall

Yue Zheng
Purdue University

Recommended Citation

Zheng, Yue, "Impacts of Land-Atmosphere Interactions on Regional Convection and Rainfall" (2015). *Open Access Dissertations*. 1491.
https://docs.lib.purdue.edu/open_access_dissertations/1491

Graduate School Form 30
Updated 1/15/2015

PURDUE UNIVERSITY
GRADUATE SCHOOL
Thesis/Dissertation Acceptance

This is to certify that the thesis/dissertation prepared

By Yue Zheng

Entitled
Impacts of Land-Atmosphere Interactions on Regional Convection and Rainfall

For the degree of Doctor of Philosophy

Is approved by the final examining committee:

Jon Harbor Chair	Kiran Alapaty
Nathanial Brunsell	
Qianlai Zhuang	
Dev Niyogi	

To the best of my knowledge and as understood by the student in the Thesis/Dissertation Agreement, Publication Delay, and Certification Disclaimer (Graduate School Form 32), this thesis/dissertation adheres to the provisions of Purdue University's "Policy of Integrity in Research" and the use of copyright material.

Approved by Major Professor(s): Dev Niyogi

Approved by: Indrajeet Chaubey 11/5/2015
Head of the Departmental Graduate Program Date

IMPACTS OF LAND-ATMOSPHERE INTERACTIONS ON REGIONAL CONVECTION AND RAINFALL

A Dissertation
Submitted to the Faculty
of
Purdue University
by
Yue Zheng

In Partial Fulfillment of the
Requirements for the Degree
of
Doctor of Philosophy

December 2015
Purdue University
West Lafayette, Indiana

To my beloved daughters Yuyi Sophia Han and Xiaoniuniu Liliya Han, my husband Tianhe Han, my mother Zhi Wang, my father Linkui Zheng, and my grandparents, for their endless inspiration, support, and love.

ACKNOWLEDGEMENTS

This study benefitted in part through support of National Science Foundation (NSF) CAREER (AGS-0847472), NSF Hydrology Community-based Data Interoperability Networks (INTEROP), NSF CISE 1250232 Strong City Program, USDA National Institute of Food and Agriculture (NIFA) Drought Trigger projects through Texas A&M at Purdue (2011-67019-20042), USDA NIFA Hatch project 1007699, US EPA's Air, Climate, and Energy (ACE) Program, Department of Energy's Atmospheric Radiation Measurement Program (DOE-ARM), U.S. Department of Energy Atmospheric System Research Program. Additional support for the KON Ameriflux site was provided through a subcontract to the NSF Long Term Ecological Research Program at the Konza Prairie Biological Station (DEB-0823341; subcontract: SS1093) and subcontract number 7114774 from the Lawrence Berkeley National Laboratory under DOE contract DE-AC02-05CH11231. Financial support given by the Earth System Science Organization, Ministry of Earth Sciences, Government of India (Grant/Project no. MM/SERP/CNRS/2013/INT-10/002) to conduct this research under Monsoon Mission, and computational resources by Purdue Rosen Center for Advanced Computing and US EPA/ORD supercomputing are also gratefully acknowledged.

The graduate committee comprising of Drs. Jon Harbor, Kiran Alapaty, Nathanial Brunsell, Qianlai Zhuang, and Dev Niyogi is also gratefully acknowledged for their role as true mentors.

Special thanks to Drs. Anil Kumar, Joseph Alfieri at USDA/ARS, Anthony Del Genio at NASA Goddard Institute for Space Studies, John Kain of NOAA, Megan Mallard of UNC, and Mr. Russell Bullock, Drs. Jerold Herwehe and Christopher Nolte, and Ms. Tanya Spero at US EPA, for their help in many ways facilitating the research. My appreciation also goes to Mr. John Halley Gotway at NCAR/RAL for the help on MET, and Mrs. Dan Dietz and Lev Gorenstein at ITaP Research Computing (RCAC) for their help on the WRF runs. Thanks to Ms. Dallas Staley for her usual outstanding editing.

The land surface lab and Indiana State Climate Office consist of the major part of my Purdue research life and will continue to have positive influence on my life ahead. Thanks to all the group members!

Most importantly, I am deeply thankful to my family. Thanks to my parents for their endless love, support, and sacrifices. Thanks to my daughter Sophia and my upcoming baby daughter Liliya, your love makes it worth it all. Finally, thanks to my loving and dearest husband, Tianhe Han, for always being my side, loving, encouraging, supporting, and believing me.

Yue Zheng

West Lafayette, Indiana, 2015

TABLE OF CONTENTS

LIST OF TABLES

LIST OF FIGURES

Figure Page

Figure Page

ABSTRACT

Zheng, Yue. Ph.D., Purdue University, December 2015. Impacts of Land-Atmosphere Interactions on Regional Convection and Rainfall. Major Professor: Dev Niyogi.

High resolution (1-10 km) numerical weather prediction (NWP) models face major challenges trying to improve representation of moist processes. In particular, simulating the interaction between the land surface and regional convection and rainfall is a source of uncertainties and presents three main barriers: (i) NWP models generally have simple land surface schemes, (ii) land-atmosphere coupling is not properly represented in models, and (iii) many assumptions made in deriving the theory of convective parameterizations are no longer valid at “gray scales” (e.g., 1-10 km). In this dissertation, interactions between land-surface heterogeneities, land-atmosphere coupling, and moist convection and related mesoscale circulations were investigated in four major studies to improve and advance the understanding of high-resolution model simulations of regional convection and precipitation. A number of short-term (i.e., 24-48 hours) retrospective numerical experiments were conducted over a variety of land-atmosphere coupling hotspot regions across the globe.

First, impacts of heterogeneous land surface on turbulent flow and mesoscale simulations were assessed. Experiments were conducted using the Weather Research and Forecasting

(WRF) model coupled with a simple (slab) land surface model (LSM), a modestly complex Noah LSM, and a land data assimilation system (LDAS) with detailed surface fields. Three heterogeneity length scales: 1, 3, and 9 km, were employed to alter land cover and land use. The response of high-resolution model simulations' to spatial scales changes of land-surface heterogeneity by modification of land-surface properties and changes in land-surface representation were investigated. Results indicate that both land-surface parameterizations and surface heterogeneity affect model simulations, and the impact of land-surface parameterizations is found to be more important, particularly for low frequency ($f < 10^{-4}$ hz) eddies and mesoscale circulations. Replacing a simple slab land model with more detailed land surface models (LSMs) (e.g., Noah or High-Resolution Land Data Assimilation System) can help reduce uncertainties in the simulation of surface fluxes which may be greatly affected by land-surface heterogeneity via improved turbulent characteristics over heterogeneous landscapes. An important result that emerges from the analysis is that the impact of land-surface heterogeneity on atmospheric feedbacks can be detected in mesoscale circulations that are roughly four times the heterogeneity spatial scale. It follows that the heterogeneity length scale that can influence mesoscale circulations would be a function of grid spacing in the model.

Second, the role of land-atmosphere coupling over regions with relatively strong coupling between land-surface conditions and moist convection were assessed. The need for adopting a dynamic coupling strength within the land surface model was assessed by analyzing rainfall events and impacts of land-atmosphere coupling using the Noah land model and WRF model simulations over the U.S. southern Great Plains (SGP), Europe, northern India, and West Africa. Land-atmosphere coupling strength impacts on model parameterizations (i.e., land surface processes, PBL dynamics, and moist convection) were quantified and the range of regional variation in the coupling coefficient for model simulations was documented. Results indicate that the adoption of a dynamic land-atmosphere coupling formulation helps improve the simulation of surface fluxes and the resulting atmospheric state, thus dynamic coupling shows promise in modulating model results and improving convective system simulation and precipitation forecasts. For the four regions, the surface coupling coefficient does not affect the general location but could improve the intensity of simulated precipitation. Results highlight that there is high uncertainty in land-atmosphere coupling and the results from this and prior studies need to be considered with caution. In particular, zones identified as coupling hotspots in climate studies and their coupling strength would likely change depending on the model formulations and coupling coefficient assigned.

Third, impacts of an updated convection scheme on high-resolution precipitation forecasts were assessed. At high resolution spatial scales, precipitation biases and errors can occur due to uncertainties in initial meteorological conditions, grid-scale cloud microphysics schemes, and/or subgrid-scale convection schemes. To reduce precipitation biases and uncertainties, scale-aware parameterized cloud dynamics were introduced to high-resolution forecasts by making several changes to the Kain-Fritsch (KF) convection parameterization scheme (CPS) in the WRF model. These changes include subgrid-scale cloud radiation interactions, a convective adjustment timescale, the cloud updraft mass flux impacting grid-scale vertical velocity, and a LCL-based methodology for parameterizing entrainment. This updated KF (UKF) CPS allows the convection scheme to facilitate a smooth transition from parameterized cloud physics to resolved grid-scale cloud physics across different grid resolutions. Results indicate that (1) high-resolution precipitation forecasting is more sensitive to the source of initial conditions than to grid-scale microphysics or convective parameterizations, and (2) the UKF CPS greatly alleviates excessive precipitation at 9 km grid spacing and improves results at 3 km grid spacing as well.

In the last part of this dissertation, impacts of land-atmosphere-convection interactions on regional precipitation intensity and variation in the WRF model were assessed. Sensitivity experiments including effects of LSM, land-atmosphere coupling strength, and CPS on the fields of precipitation, surface scalars, and convection reveal that including a more detailed land surface parameterization, a dynamical surface coupling strength coefficient, and UKF CPS together, improves mesoscale simulations of several meteorological and convection parameters in the short-term high-resolution WRF model, increasing accuracy about 40% for precipitation intensity forecasts.

Overall, results highlight the persistent role of land-surface heterogeneity for turbulent flow and mesoscale circulation, the essential role of land-atmosphere coupling for regional convection and precipitation formation over hotspot regions, and in particular, the important role of a scale-dependent subgrid-scale convection scheme on convective precipitation at intermediate scales. Together the improvements in land-surface representation, land atmosphere coupling, and convection parameterization can yield positive impacts on the model performance for short-term regional rainfall predictions, and therefore land-atmosphere-convection feedbacks can be well represented.

Key words: Convection parameterization, High-resolution, Land-atmosphere interaction, Land-atmosphere coupling, Land-surface heterogeneity, LSM, Mesoscale convection, PBL, Precipitation, Subgrid-scale, Surface coupling strength, Surface fluxes, WRF-ARW

CHAPTER 1. INTRODUCTION

1.1 Background

Many of the central problems in meteorology and climate science involve moist (atmospheric) convection. The deep, precipitating moist convection contributes to severe weather, such as excessive rainfall and flash floods, straight-line winds, hail, lightning, and tornadoes (Stevens 2005). There is growing evidence that changes in land-surface properties can significantly influence convective rainfall on regional and global scales through dynamic processes (Pielke et al. 2001).

The land surface consists of different features; the heterogeneous land surfaces behave as sources and sinks of heat and moisture, and the spatial structure of the surface characteristics are shown to influence heat and moisture fluxes within the planetary boundary layer (PBL) (e.g., Zhong and Doran 1995; Baldi et al. 2005; Holt et al. 2006; Niyogi et al. 2006; Zhang et al. 2010; Niu et al. 2011). Additionally, the different scales of land surface heterogeneity, ranging from meters to kilometers, could generate different sizes and strengths of turbulent eddies, which in turn influence the atmospheric convection resulting in enhanced cloud formation and associated precipitation due to higher surface evapotranspiration (e.g., Hadfield et al. 1992; Pielke and Uliasz 1993; Avissar and Liu 1996; Avissar et al. 1998; Weaver and Avissar 2001; Koster et al. 2003;

Weaver 2004a, b; Kang 2007; LeMone et al. 2007a; Huang and Margulis 2009; Niyogi et al. 2009a; Alfieri and Blanken 2012). Avissar and Chen (1993) pointed out that correctly representing turbulent fluxes over heterogeneous surfaces is important to improve parameterizations in atmospheric models. Most current land surface models (LSMs) characterize land surface properties, such as surface exchange coefficients of heat and moisture, roughness length, and albedo, by effective parameters, and the mechanism of coupled different LSMs in representing impacts of land-surface heterogeneity is therefore also necessary for improved simulations of land-atmospheric interactions. Thus, it is necessary to understand both the statistical properties of turbulent flow and mesoscale predictions by different land surface parameterizations coupled to mesoscale weather forecasting models over a heterogeneous land surface.

Literature suggests that the overlying air properties are influenced to some extent by the underlying land surface heterogeneity through land-atmosphere feedback which may be linked to the land-atmosphere coupling strength through exchange coefficients of heat and momentum (e.g., Niyogi et al. 1999; Pielke 2001; Trier et al. 2004; Holt et al. 2006; Koster et al. 2003, 2004, 2006; LeMone et al. 2008, 2010; Seneviratne et al. 2010; Hirsch et al. 2014). The surface heating strongly depends on the land-atmosphere coupling, as lesser (or more) precipitation results in dryer (or wetter) soil, which contributes to a decrease (or increase) in the cooling effects from latent heat flux and thus amplifies (or reduces) summertime temperatures (Koster et al. 2004; Fischer et al. 2007). These kinds of global regions were identified as "hot spot" areas of strong coupling between summer rainfall and land-surface conditions (Koster et al. 2004). A number of atmospheric models [(e.g., 12 participating atmospheric general circulation models (AGCM) in the Global Land-Atmosphere Coupling Experiment (GLACE)] have been studied to see if the land-atmospheric coupling effect can be well represented. However, the hot spots land-atmosphere coupling effect could be incorrectly captured due to a lack of knowledge of the model-prescribed coupling strength (Koster et al. 2003; Ruiz-Barradas and Nigam 2005; Dirmeyer et al. 2006; Hirsch et al. 2014; Lorenz and Pitman 2014).

Recently the role of the coefficient C in the Zilitinkevich (1995) equation (C_{zil}) for the coupling strength between land and atmosphere has been examined (e.g., LeMone et al. 2008, 2010; Chen and Zhang, 2009; Trier et al. 2011). The parameter of C_{zil} describes the influence of surface turbulence on surface heat transfer and has been identified as the only parameter that could bring the Noah land surface model-based HRLDAS and observations into agreement (LeMone et al. 2008). Most importantly, the parameter of C_{zil} has a significant impact on model response to surface and boundary layer feedback which can affect predictions of weather/climate and more specifically convection and associated cloud-radiation-precipitation. Thus, it is necessary to explore model sensitivity to C_{zil} and its coupling capabilities over the hotspot regions.

Atmospheric moist convection is a result of parcel-environment instability, and the moist processes play an important role in accurately predicting severe weather, air pollution, climate, and the hydrological cycle. Convectively active clouds play a central role in the interaction of radiative, dynamical, and hydrological processes in the atmosphere.

Cloud microphysics schemes have been widely used in Numerical Weather Prediction (NWP) forecast models (e.g., Done et al. 2004; Deng and Stauffer 2006; Wulfmeyer et al. 2006; Case et al. 2008; Niyogi et al. 2011). However, at finer spatial and temporal scales, cloud microphysics schemes have limitations in representing moist convection due to two primary facts: 1) cloud grid-scale dynamics are separated from cloud physics; and 2) the subgrid-scale cloud effects need to be accounted for in high spatial resolution forecasts (e.g., ~1 to 10 km grid spacing; Arakawa and Jung 2011; Gustafson Jr. et al. 2013; Molinari and Dudek 1992).

The convective parameterization (CP) has always been a key factor to improve numerical modeling of the atmosphere (Arakawa and Jung 2011). Particularly, the subgrid-scale cumulus cloudiness in many high-resolution NWP models can influence simulations of atmospheric radiation and the resulting precipitation. However, the subgrid-scale convective parametrization scheme (CPS) has been greatly neglected outside of global climate models. Therefore many CPSs could not work properly at intermediate-scales (e.g., ~1 to 10 km grid spacing) due to the many assumptions tied to scales around 25 km. To improve the representation of subgrid-scale clouds for higher resolutions, there is a need to relax some of the assumptions towards achieving scale independence in the CPSs [e.g., the Kain-Fritsch (KF) CPS].

Along with increasing resolution, the impact of parameterized convection is expected to become less and less significant. However, the tendencies produced by parameterized convection would dominate over resolved convection at higher resolutions, resulting in improper simulation of moist convection and precipitation. To address these issues, the scale-aware parameterized cloud dynamics will be introduced to the KF scheme for high-resolution forecasts by making several changes.

One of the many key parameters to modify in the CPS is the convective adjustment timescale. It is the time over which the convective available potential energy (CAPE) is “removed” to stabilize the atmosphere. It determines the duration of convective heating, drying, precipitation, and radiative fluxes, and is set as a constant value in many regional and global models. Another key parameter is the entrainment rate which is often specified in many global models. For high-resolution simulations, the assumptions made in the formulations for adjustment timescale and entrainment of the KF scheme should be reconsidered to make CPSs seamless across the spatial scales. Additionally, the importance of including subgrid-scale convective momentum transport on grid-scale vertical motions deserves attention. One potential benefit is that adding the subgrid-scale vertical velocity could help reduce model spin-up time.

Based on the above considerations, a few changes have been made to the KF CPS in this dissertation. These changes include subgrid-scale cloud-radiation interactions, a dynamic adjustment timescale, impacts of cloud updraft mass fluxes on grid-scale vertical velocity, and lifting condensation level-based entrainment methodology that includes scale dependency.

Thus, the premise of this Ph.D. dissertation research is that accurate representations of the heterogeneous land surface, land-atmosphere coupling, and cloud convection at high resolutions are of vital importance for regional and global numerical models to accurately simulate mesoscale convection and forecast precipitation. This study will assess the land-atmosphere interactions associated with regional convection and precipitation over the U.S. southern Great Plains (SGP), and in particular, assess the land-atmosphere coupling impacts over four hotspot regions (U.S. SGP, Europe, northern India, and West Africa) across the globe.

The Weather Research and Forecasting (WRF) model (Skamarock and Klemp 2008) is the main modeling tool used in this research. The WRF model has been commonly used around the world for a wide range of meteorological studies and operational purposes across spatial scales ranging from meters to thousands of kilometers and timescales from days to decades. It is a fully compressible non-hydrostatic, primitive-equation model with multiple-nesting capabilities to enhance resolution over the areas of interest.

Therefore, this dissertation research is specifically guided by the following four questions: i) how does land-surface heterogeneity affect LSM/WRF simulations and the differences arising from different LSMs impact the turbulent flow and mesoscale predictions? ii) How do current meteorological models represent land-atmosphere surface coupling strength and what is the impact of surface-atmosphere coupling strength on regional (and though not considered here, global) model performance? iii) To what extent can a subgrid-scale convection scheme be modified to bring in scale-awareness for improving high-resolution short-term precipitation forecasts in the WRF model? And iv) How could the land-atmosphere-cloud connection linkage be improved in a coupled model framework?

1.2 Study Objectives

The main objective of this dissertation is to improve the understanding and model forecast ability for regional convection and precipitation. The main hypothesis is that accurate representation of fine-scale heterogeneous land surfaces and land-atmosphere coupling strength in conjunction with an improved CPS within the high-resolution (1-10 km) WRF model, can significantly improve mesoscale convection and precipitation forecasts. The unique focus of this research is to investigate NWP model performance at multi-scale processes involving turbulent processes, mesoscale circulations, subgrid-scale convective clouds, and the interactions between them.

A variety of techniques including numerical modeling, field and satellite observations, and data assimilation were used in this study. Sensitivity analysis and statistical-dynamical approaches for improving high-resolution weather forecasts were also employed to assess the simulations of regional convection and rainfall.

A four-pronged strategy was undertaken as shown below.

i. Examined the role of land use and land cover variability on boundary layer dynamics and assessed the importance of the turbulent processes for mass and energy transfer between the heterogeneous land surface and boundary layer in the NWP model.

- Coupled model simulations were conducted utilizing observations (e.g., eddy covariance data and surface fluxes from AmeriFlux and ARM, and radiosonde data).
- Spectral characteristics of landscape heterogeneity and observed turbulent data were analyzed.
- Reduced uncertainty of surface flux simulations over heterogeneous landscapes.
- Improved boundary layer and mesoscale process simulations via turbulent processes by using detailed land surface models coupled to the WRF model.

ii. Investigated the impact of land-atmosphere coupling on different hotspot regions across the globe and assessed the impacts on mesoscale convection and rainfall.

- Analyzed rainfall events over four land-atmosphere coupling hotspot regions (U.S. SGP, Europe, northern India, and West Africa) by conducting offline model and coupled Noah-WRF modeling experiments.
- Improved simulations of surface fluxes, atmospheric state, and precipitation intensity by using a dynamic land-atmosphere coupling coefficient.
- Processed and utilized precipitation observations (e.g., MPE and TRMM data).

iii. Improved the prediction accuracy of fine scale (1-10 km) short-term precipitation by incorporating a subgrid-scale cloud convection effect in the WRF model.

- Implemented improved methodologies to update the KF CPS in the WRF model by introducing scale-aware parameterized cloud dynamics for high-resolution forecasts.
- Evaluated the impact of physics, dynamics, and initial conditions on high-resolution short-term precipitation forecasts based on the updated KF (UKF) scheme.

iv. Explored the impact of interaction between land-surface and cloud on mesoscale convection and precipitation intensity and distribution.

- Improved model forecast capabilities for convection and precipitation at mesoscale and convection permitting scales.
- Explored the impact of land-atmosphere-cloud interactions on precipitation for heavy rainfall events.
- Examined the performance of PBL schemes, land surface schemes, and CPSs for severe thunderstorm events.

A flowchart of the research experimental design is shown in Fig. 1.1.

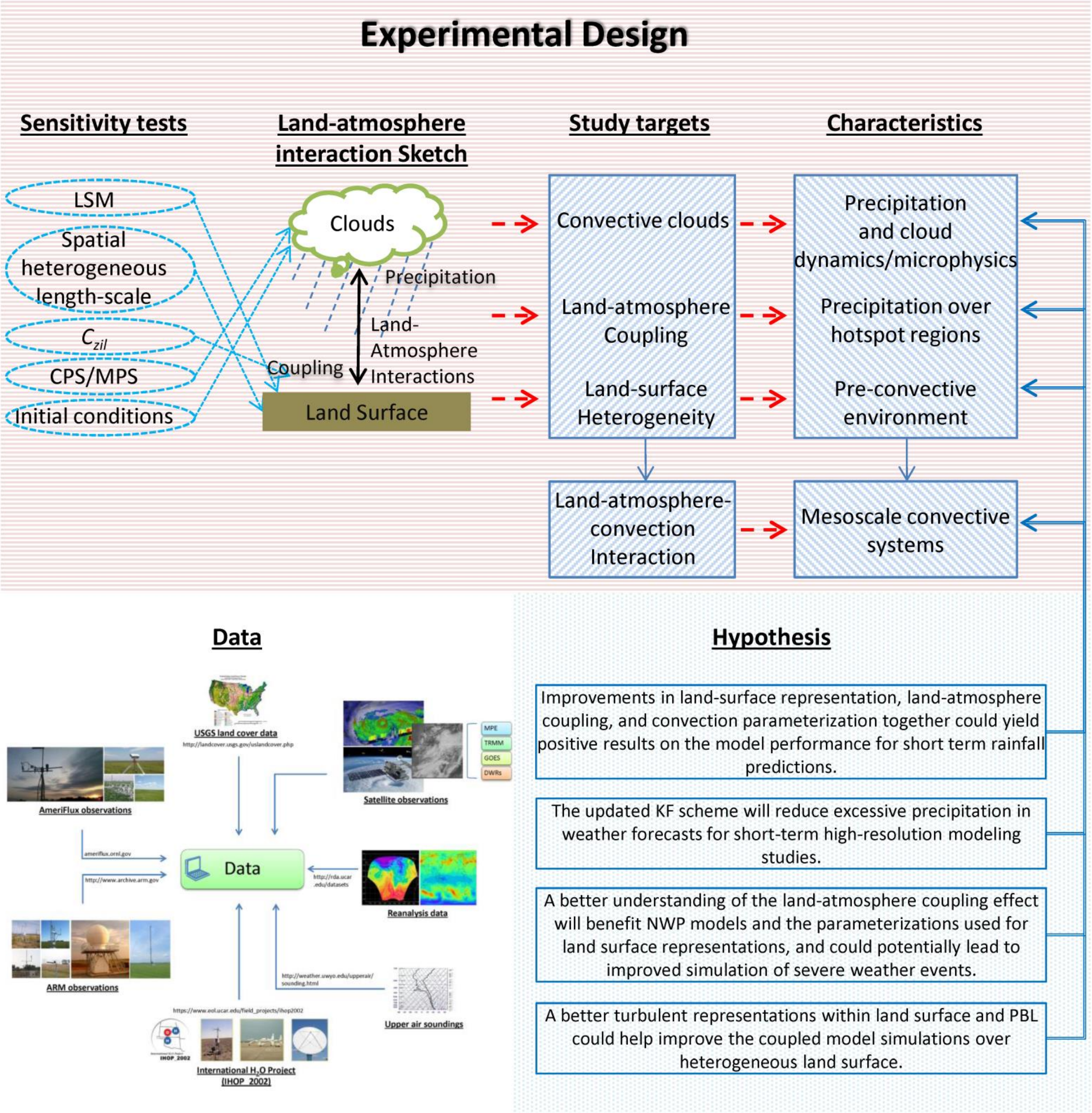

Improvements in land-surface representation, land-atmosphere coupling, and convection parameterization together could yield positive results on the model performance for short term rainfall predictions.

The updated KF scheme will reduce excessive precipitation in weather forecasts for short-term high-resolution modeling studies.

A better understanding of the land-atmosphere coupling effect will benefit NWP models and the parameterizations used for land surface representations, and could potentially lead to improved simulation of severe weather events.

A better turbulent representations within land surface and PBL could help improve the coupled model simulations over heterogeneous land surface.

Fig. 1.1 The experimental design flowchart

1.3 Case Studies and Observational Data

A number of short-term (24- or 48-hour) retrospective numerical experiments over four different land-atmosphere coupling hotspot regions across the globe (U.S. SGP, Europe, northern India, and West Africa) were chosen for study. The main study domain is centered on the U.S. SGP due to its importance as a land-atmosphere coupling hotspot and the availability of various high quality observations. The four different sets of mesoscale events designed and studied are:

1) Pre-convective environment: A wet “few clouds” day without precipitation over the U.S. SGP in summer 2007 was selected so that the cloud influence bias could be avoided. The wet land-surface has a larger latent heat flux which leads to relatively high atmospheric water vapor content in the PBL enhancing surface net radiation. Heterogeneous landscape under wet conditions is important to improve the understanding of land-atmosphere coupling processes and mesoscale convection.
2) Precipitation over regions with strong coupling between land-surface conditions and moist convection: The four regions, U.S. SGP, Europe, India, and West Africa, were selected since each region was identified as a land-atmosphere coupling hotspot in different global studies.   These hotpots are also diverse in landscape with intense mesoscale convection and heavy precipitation events. As stated previously, the U.S. SGP has been a popular domain of many land-atmosphere coupling studies with high quality observational data. Europe is a region with large amounts of orographic precipitation due to its various mountainous terrains. Northern India is selected because of its monsoon region where heavy rainfall events and mesoscale convection are primarily associated with monsoon rainfall. The concentrated rainfall in West Africa has revealed the critical importance of studying the interactions between land surface and atmosphere.
3) Precipitation, cloud dynamics, and microphysics: four representative regional rainfall cases with different patterns and time periods over the U.S. SGP were selected and four sets of (thirty-six runs as total) 48-hour WRF experiments were conducted. Case

1: 0000 UTC 4 June – 0000 UTC 6 June 2002; Case 2: 0000 UTC 28 July – 0000 UTC 30 July 2010; Case 3: 0000 UTC 5 July – 0000 UTC 7 July 2010; and Case 4: 0600 UTC 14 June – 0600 UTC 16 June 2002. The purpose is to assess the high-resolution model's ability with the UKF scheme to forecast regional precipitation intensity and distribution.

4) Mesoscale convective system: A convective event was selected where there was a squall line with extended trailing stratiform over the U.S. SGP from the MC3E field campaign in May 2011.

1.4 Model Configurations

The WRF model (Skamarock and Klemp 2008) is a useful tool to understand earth system processes across spatial scales ranging from meters to thousands of kilometers and timescales from days to decades. It is the main modeling tool used in this dissertation. Numerical model simulations were designed and conducted with multiple nested domains according to the research tasks. The model configurations were based on previous studies (e.g., Krishnan et al. 2003; Venkata Ratnam and Cox 2006; Bukovsky and Karoly 2009; Flaounas et al. 2011). The lateral boundary and initial conditions were provided by NCEP Global Final Analysis (FNL) data derived from the Global Forecast System (GFS) and Climate Forecast System Reanalysis (CFSR) data.

A number of short-term retrospective numerical experiments were performed over a variety of land-atmosphere coupling hotspot regions across the globe to study the improvements in heterogeneous land surface representation, land-atmosphere surface coupling effect, and CPSs. It is hypothesized that together, these improvements can provide a positive impact on predictions of high-resolution regional convection and rainfall.

One of the key aspects for simulating regional convection and rainfall is the representation of fine-scale heterogeneity land surface. To address the roles of land-surface heterogeneity in affecting land-surface processes and the corresponding PBL responses, the WRF model was coupled to a simple LSM (slab), a detailed LSM (Noah), and a fine-scale heterogeneous field analyses as provided by the High-Resolution land data assimilation system (HRLDAS).

Slab model calculates ground temperature from a five-layer soil thermal diffusion option without explicit representation of vegetation effects (Blackadar 1976, 1979). In the slab model, the ground wetness (as soil moisture availability) is set at a constant value during the WRF-ARW simulations, and this constant soil moisture value may result in difficulty in modeling latent heat flux due to the vegetation-process interactive complexity.

In addition to the slab scheme, the other LSM used was the Noah model originated by Pan and Mahrt (1987), has and was significantly modified later (see Koren et al. 1999; Ek et al. 2003; Chen and Dudhia 2001). The Noah model has explicit representation of vegetation effects and time-varying soil moisture/temperature, and has been used in the WRF model for a variety of mesoscale applications (e.g., Leung et al. 2003; Trier et al.

2004; Niyogi et al. 2006; Weisman et al. 2008; Chen et al. 2011; Otte et al. 2012; Bullock et al. 2015).

HRLDAS runs in an uncoupled, offline mode at 1 km resolution with 30 months of spin-up initialization using a variety of atmospheric forcings and surface conditions (Chen et al. 2007) and was also used in this study. HRLDAS integrates static fields of land use and soil texture and prognostic vegetation and meteorology based on Noah LSM. In addition to running offline, HRLDAS is then run in a coupled mode with WRF using the Noah LSM on the same WRF nested grids. It is capable of providing a more realistic mesoscale environment and captures fine-scale land-surface heterogeneity (Holt et al. 2006; Case et al. 2008; Charusombat et al. 2012).

In addition to land-surface parameterization changes, WRF runs were also conducted for sensitivity analysis of the C_{zil} values by using the same physical options over the four selected hot spot regions to constrain the confounding variables. Along with studies involving land-atmosphere coupling, high-resolution experiments to determine the role of convection schemes were also performed. Three convective treatments were designed with a combination of two cloud microphysics schemes [the Goddard microphysics scheme and the WRF double-moment 6-class scheme (WDM6)] and two types of initial conditions (as discussed above): (1) no CPS; (2) the latest KF scheme; and (3) the UKF scheme.

WRF is a state-of-the-art atmospheric modeling system and has been largely developed and maintained over the past years. This dissertation is based on research that has spanned several years during which a few of the model versions were released. In each of the model simulations, the latest available WRF version at the time of the study (WRF 3.4.1) was used. More details about the current and previous WRF releases can be found at http://www2.mmm.ucar.edu/wrf/users/download/get_source.html.

1.5 Dissertation Layout

This dissertation is organized as follows. The following four chapters deal with the four research strategies undertaken in this dissertation. Chapter 2 discusses the role of landscape heterogeneity on atmospheric mesoscale predictions and turbulent flow. Chapter 3 assesses the role of land-atmosphere coupling strength over regions with strong coupling between land-surface conditions and moist convection. Chapter 4 improves the prediction of precipitation distribution and variability by introducing scale-aware parameterized cloud dynamics for high-resolution forecasts. Chapter 5 summarizes and assesses the impact of the improvements in land-surface representation, land atmosphere coupling strength, and CP on high-resolution precipitation forecasts. The overall conclusions from the dissertation are summarized in Chapter 6.

CHAPTER 2. IMPACTS OF HETEROGENEOUS LAND COVER AND LAND SURFACE PARAMETERIZATIONS ON TURBULENT FLOW AND MESOSCALE SIMULATIONS IN THE WRF MODEL[1]

2.1 Introduction

Land surface models (LSMs) parameterize energy and water exchanges and their coupling between the terrestrial biosphere and atmosphere (Henderson-Sellers et al. 1995, 1996; Niyogi et al. 1999; Pitman 2003). Recent progress in LSMs in NWP models has demonstrated their utility in providing accurate and high-resolution representations of surface properties (e.g., LeMone et al. 2008; Niyogi et al. 2009a; Niu et al. 2011; Wei et al. 2013; Cai et al. 2014). Many studies have employed different LSMs to represent land heat and water storage and their relationships with fluxes (Dirmeyer et al. 2006), and the overall mesoscale model forecasts are influenced by the representation of land-surface heterogeneity (Avissar and Pielke 1989).

Land-surface heterogeneity has been primarily represented in LSMs as horizontal changes in surface properties, such as land use/land cover (LULC), topography, and soil moisture (e.g., Chen and Avissar 1994; Eastman et al. 1998; Trier et al. 2004; Holt et al 2006). The land-surface heterogeneity also results in a mosaic of spatial gradients in surface energy and water budgets (e.g., Pielke and Uliasz 1993; LeMone et al. 2007;

---

[1] Zheng, Y., N. A. Brunsell, J. G. Alfieri, D. Niyogi, 2015: Impacts of land surface coupling on Boundary Layer simulation over heterogeneous landscapes. *Earth Interact., Land Use Land Cover Change Special Issue.*

Niyogi et al. 2009a; Alfieri and Blanken 2012). The differential heating of the atmosphere caused by land-surface heterogeneity can lead to mesoscale atmospheric circulations and convective weather processes in the PBL over a broad range of spatial and temporal scales (Hadfield et al. 1992; Avissar and Liu 1996; Avissar et al. 1998; Koster et al. 2003; Niyogi et al. 2006; Kang et al. 2007; Weaver 2004a, b).

The coupled simulated mesoscale features can be influenced by the scale of the heterogeneity. For example, Wang et al. (1996) showed that in the lower atmosphere, fine scale thermal variability of the landscape influenced convection initiation in a three-dimensional stochastic linear model of the mesoscale circulation. Baidya Roy and Avissar (2000) found notable turbulent thermals were developed when the length scale of the surface heterogeneity exceeded 5-10 km, highlighting that subgrid-scale parameterization needs to include mesoscale processes instead of only accounting for turbulence. Yates et al. (2003) showed that the effect of scale changes of land-surface heterogeneity is evident in modeled estimates of the domain mean flux. While for larger length scales of land-surface heterogeneity, which could be regarded as relatively homogeneous conditions, the modeled latent heat flux became increasingly important (Brunsell et al. 2011). As a result, the increasing heterogeneity scale may change the subgrid heterogeneity effects, and lead to significant changes in modeled surface energy partitioning which in turn affects the vertical fluxes of heat and moisture in the planetary boundary layer (PBL) and the simulation of mesoscale circulations (Zhong and Doran 1995; Baldi et al. 2005; Zhang et al. 2010).

Understanding the mechanisms of coupled LSMs/WRF in representing impacts of land-surface heterogeneity is necessary for improving simulation of land-atmospheric interactions. While a number of LSMs coupled to atmospheric models have been used to investigate the impacts of heterogeneous surface forcings on the PBL and the resulting mesoscale circulations, there has been limited attempt to quantify how changes in length scales of land-surface heterogeneity affect the development of mesoscale circulations and turbulent flow in high-resolution (1~10 km) mesoscale models (Holt et al. 2006; Niyogi et al. 2006; Trier et al. 2008; Niu et al. 2011). Therefore, in this study we conduct a number of numerical experiments to address the roles of land-surface heterogeneity in affecting land-surface processes and the corresponding mesoscale responses. Our objectives include two primary aspects: 1) to understand to what extent land-surface heterogeneity impacts high-resolution (1~10 km) coupled LSMs/WRF simulations; and 2) to investigate how the differences arising from different land-surface parameterizations impact turbulent flow and mesoscale circulations.

2.2 Numerical experiments

A series of numerical experiments were conducted using the WRF model (version 3.4.1; Skamarock et al. 2008) coupled to a simple LSM (slab), a relatively detailed LSM (Noah), and a fine-scale heterogeneous field analyses as provided by a High-Resolution land data assimilation system (HRLDAS).

2.2.1 A brief description of the land-surface parameterizations

The slab model is a simple but effective land model which prognostically calculates ground temperature from a five-layer soil thermal diffusion option (with layer thickness from top to bottom of 0.01, 0.02, 0.04, 0.08, and 0.16 m) without explicit representation of vegetation effects (Blackadar 1976, 1979). The soil moisture availability in the slab model is a spatially varying but temporally constant parameter which is defined as a function of land use type in the WRF-ARW simulation. The constant soil moisture availability values can introduce difficulty in modeling latent heat flux due to the complex interactions among vegetation and evapotranspiration process (Chen and Dudhia 2001).

The other LSM model used is the Noah model, which was developed with the consideration of the sensitivity of boundary layer development to surface moisture and vegetation (Chen and Dudhia 2001). The Noah LSM has explicit representation of vegetation effects and time-varying soil moisture. It has been used in WRF by including simplified approaches of canopy resistance, surface evaporation, vegetation transpiration, surface and sub-surface runoff scheme, and treatment of soil thermal and hydraulic properties. One canopy layer and four soil layers with thickness of 0.1, 0.3, 0.6, and 1.0 m from the ground surface to the bottom of the soil depth are used in the Noah LSM.

In addition, HRLDAS which runs in an uncoupled, offline mode at higher resolution with 30 months of spinup initialization using a variety of atmospheric forcings and surface conditions (Chen et al. 2007), is employed to provide a more realistic mesoscale environment (Holt et al. 2006). In addition to running offline, HRLDAS is then employed in a coupled analysis with WRF using the Noah LSM on the same WRF nested grids. HRLDAS integrates static fields of land use and soil texture with four soil layers as well as time-varying fields of vegetation and meteorology based on Noah LSM. It is capable of capturing land-surface heterogeneity at a spatial scale ranging from 1 to 10 km, which is a typical magnitude for mesoscale applications (Holt et al. 2006; Charusombat et al. 2012). Details of the spinup period and model configuration of HRLDAS will be provided in the next section.

Thus, this study employed the slab model which has constant soil moisture but prognostic soil temperature; the Noah model which has time-varying soil moisture and soil temperature with explicit representation of vegetation effects; and, the HRLDAS which provides more detailed land surface conditions, coupled to the WRF model separately. The purpose of using these different LSMs is to confine the land-surface heterogeneity as much as realistically possible to (i) only soil temperature varying (i.e., slab LSM), (ii) both soil temperature and moisture varying (i.e., Noah LSM), and (iii) finer length scale of heterogeneity (i.e., HRLDAS).

2.2.2 Numerical model configuration

The study domain is centered on the U.S. SGP due to its importance as a land-atmosphere coupling “hotspot” (Koster et al. 2004; Zheng et al. 2015) and the availability of various observations. The WRF model is configured with 2 two-way nests of 3 km (490 × 470 grid points) and 1 km (607 × 574 grid points) horizontal grid spacing. The main land-cover types which include grassland, cropland, forests, and savannas and a mixture of crop and natural vegetation with considerable LULC heterogeneity are shown in Fig. 2.1a. The topography exhibits a higher western side elevation and a lower eastern side elevation (Fig. 2.1b). The emphasis is on the higher-resolution 1 km grid spacing domain, so all the following figures and discussion will pertain to the 1 km nest. The model was run with 42 vertical levels applied from the surface to the level of 100 hPa, with 20 vertical levels below the height of 3 km to resolve the PBL processes.

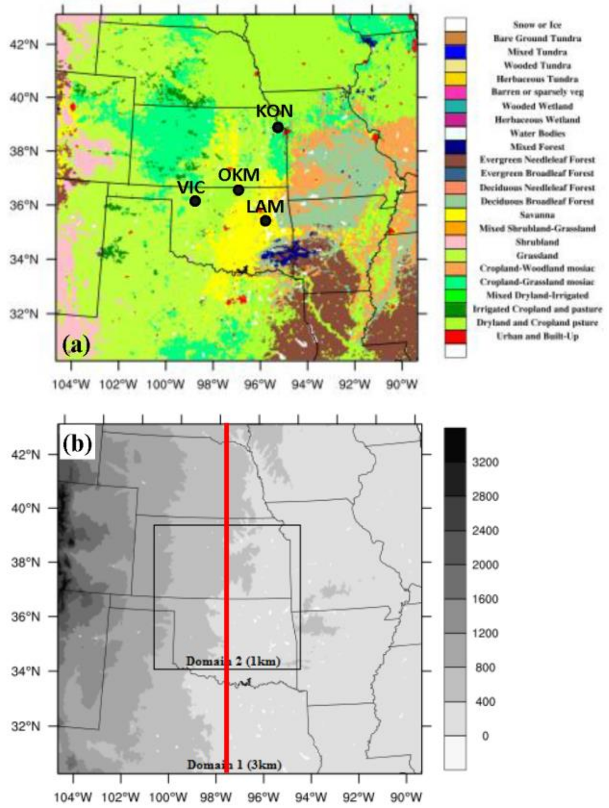

FIG. 2.1 Model domains for (a) the land-use category (the black dots represent specific site locations in Table 3); (b) topography (the red bold line is the selected position for the vertical cross section in Fig. 2.6).

A one degree, 6-hourly National Centers for Environmental Prediction (NCEP) Global Final Analysis (FNL) dataset derived from the Global Forecast System (GFS) was used to set the boundary and initial conditions for the large-scale atmospheric fields, soil parameters (i.e., soil moisture and temperature), and sea surface temperature (SST). Additionally, a long-term (30-months) offline high-resolution spinup and a variety of atmospheric forcing and surface conditions, including NCEP Stage-IV Rainfall Analysis at 4 km grid spacing, 50 km Geostationary Operational Environmental Satellite (GOES) solar downward radiation, other atmospheric forcing conditions from model-based analysis, and the United States Geological Survey (USGS) land-use and land-cover map with 24 vegetation types, were used in HRLDAS to initialize surface and soil fields.

The major physical options used for this study included the Kain-Fritsch CPS (Janjic 1994, 2000), the Morrison double-moment microphysics scheme (Hong and Pan 1996), the Mellor-Yamada-Janjic (MYJ) PBL scheme (Janjic 2001), and the Rapid Radiative Transfer Model (RRTM) for longwave and shortwave radiation (Mlawer et al. 1997). For model comparisons, data from the AmeriFlux network and the Atmospheric Radiation Measurement (ARM) (Stokes and Schwartz 1994) observations over U.S. SGP were used. The data includes surface fluxes averaged every 30 minutes, air temperature at 1.5 m, specific humidity at 1.5 m, and wind speed at 1.5 m measured every 5 seconds. To study the model performance over the study region, the operational observed vertical sounding profiles from the NOAA/National Weather Service as archived at the University of Wyoming (http://weather.uwyo.edu/upperair/sounding.html) were also employed.

2.2.3 Model experiments

A number of short-term numerical experiments using the WRF model coupled with three different land-surface parameterizations were conducted and compared. A relatively calm day with few scattered clouds and no precipitation [from 1200 UTC on 7 July (i.e., 0600 CST on 7 July) to 1200 UTC on 8 July (i.e., 0600 CST on 8 July)] was selected to capture the PBL processes. The study region exhibits a relatively wet condition in which the surface net radiation would tend to be enhanced along with a larger latent heat flux and relatively high atmospheric water vapor content in the PBL. The coupling between the land-surface processes and the PBL is expected to be important under such conditions (Eltahir 1998; Findell et al. 2011; Santanello 2013a,b).

The WRF Preprocessing System (WPS) was used to initialize USGS soil texture map, terrain height, land-water mask, and land use/land cover. To represent the continuous land-surface heterogeneity in this study for simulations of the coupled models, three different surface heterogeneity length scales (1, 3, and 9 km) of LULC are generated (or upscaled) from the 30 s resolution USGS 24-class LULC datasets using 4-point interpolation. Note that the length scales are only used to filter LULC but not change the actual grid spacing of the model runs. The land surface becomes more homogenous as the length scale increases, resulting in substantially altered LULC type information for the coupled modeling.

A total of nine coupled mesoscale numerical experiments have been conducted and the summary of these experiments is shown in Table 2.1. Each set of numerical simulations has been assigned an experiment name and these are referred to as WS (slab/WRF), WN (Noah/WRF), and WH (HRLDAS/WRF). Each of the LSM/WRF run includes three sets of experiments corresponding to the heterogeneity length scale. For example, the WS case has three numerical simulations including WS01, WS03, and WS09, as identified under Case name in Table 2.1, referring to the 1, 3, and 9 km length scales respectively.

Table 2.1 Summary of the numerical experiments

Case name	Land-surface initialization	Land-surface grid spacing (km)
WS01	slab	1
WS03		3
WS09		9
WN01	Noah	1
WN03		3
WN09		9
WH01	HRLDAS	1
WH03		3
WH09		9

2.3 Results and discussion

The analyses of the simulation results are undertaken to understand to what extent the change in surface heterogeneity due to increased LULC length scales affects the mesoscale model fields. The assessments are primarily centered on the impact of LSMs and the land-surface heterogeneity on WRF simulated surface heat fluxes, surface parameters, turbulent characteristics and vertical turbulent fluxes, and mesoscale circulations.

2.3.1 Impacts of LSMs affected by land-surface heterogeneity on surface heat fluxes

To investigate the impacts of the scale issue caused by land-surface heterogeneity on LSMs, we compared the surface latent and sensible heat fluxes over the domain (Figs. 2.2 and 2.3). As the length scale of LULC type increases, the spatial variations of surface heat fluxes for WS and WN become more homogenous while WH results show insignificant changes. This is because the decreased resolution of the LULC in WS and WN affect the simulations of surface albedo, soil moisture, and surface skin temperature, thereby changing the surface radiation components resulting in the spatial changes of surface fluxes. However, since the land-surface initialization of WH is based on a high-resolution (1 km) uncoupled land-surface modeling system, the grid cells in WH retain the land-surface details of different surface types in the following coupled runs with 1, 3, and 9 km length scales. As a result, the surface heat fluxes for WH do not show any notable differences. The surface heat fluxes for WS show similar spatial patterns to those for WH. However, the *LE* fluxes for WS for the different length scales at 2100 UTC (1500 CST), 7 July 2007 are significantly higher than WH with a maximum difference of about 300 W m^{-2} on the west side of Kansas where the main land-surface type is mixed dry-land-irrigated. In such wet conditions, the constant soil moisture values prescribed in the slab model becomes the important cause of such differences. Although HRLDAS is built upon the Noah LSM, WN has a larger range of surface heat fluxes and different heat flux patterns compared to WH. More interestingly, it is found that over the domain in WN, *LE* on the east side is much lower than that on the west side, and this may be related to the precipitation gradient across the region and the soil wetness. Thus, both fine-scale gradients and model physics affect the model outputs.

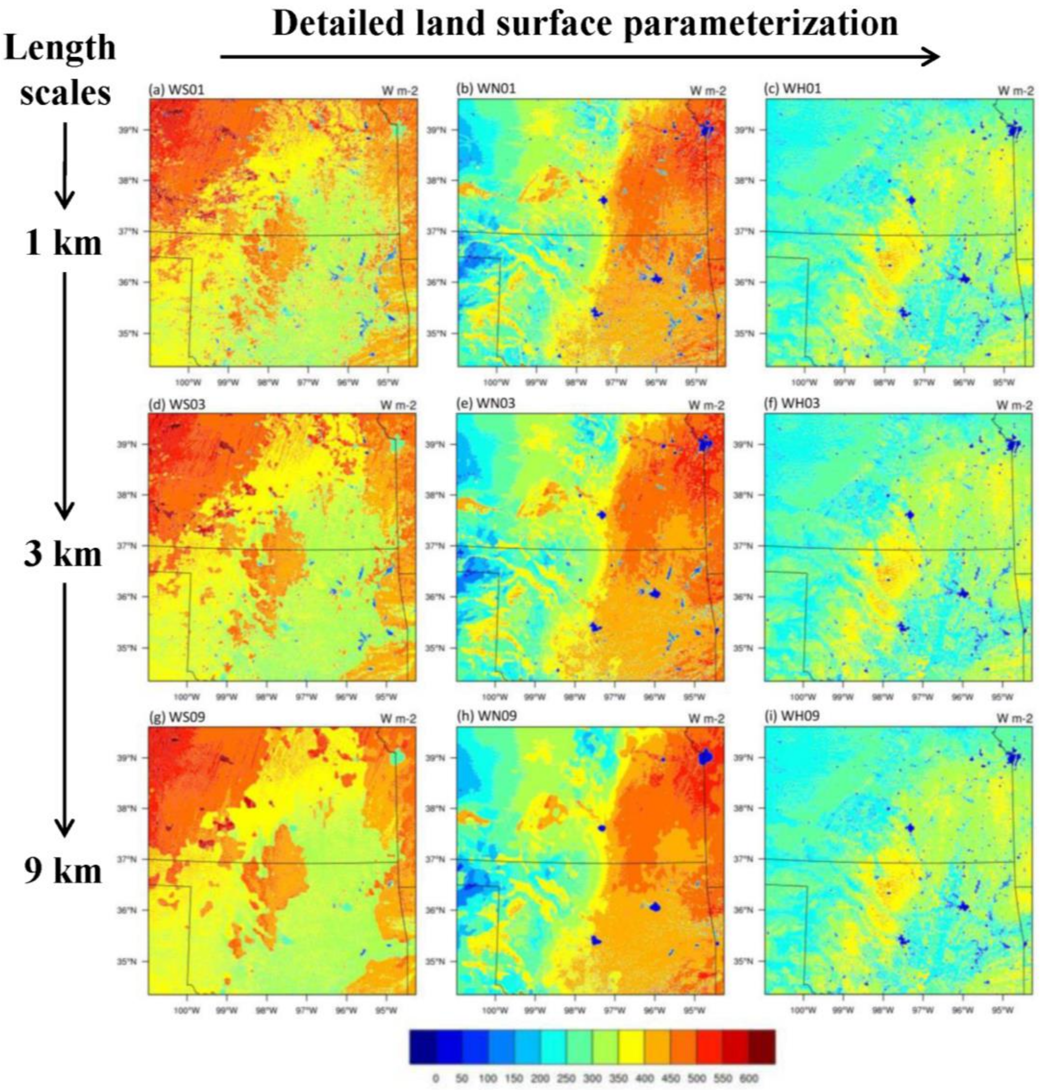

FIG. 2.2 Spatial variations in surface latent heat flux (W m^{-2}) at 2100 UTC (1500 CST) 7 July 2007 in (a-c) WS01, WN01, WH01, (d-f) WS03, WN03, WH03, and (g-i) WS09, WN09, WH09.

To further analyze the influence of land-surface heterogeneity on land-surface fluxes, mean values of diurnal variations [from 1200 UTC on 7 July (i.e., 1200 CST on 7 July) to 1200 UTC on 8 July (i.e., 0600 CST on 8 July)] of surface heat fluxes were area-averaged over the domain and shown in Table 2.2. The WS shows the largest area-averaged *LE* (the smallest area-averaged *H*), whereas the WN results in the smallest area-averaged *LE* which is about 30 W m^{-2} less than that for WS. Results show that *LE* decreases with increasing length scales for the three coupled cases where the impact of smoothing land-surface heterogeneity from 1 to 9 km on *LE* for WS is the largest (2.3 W

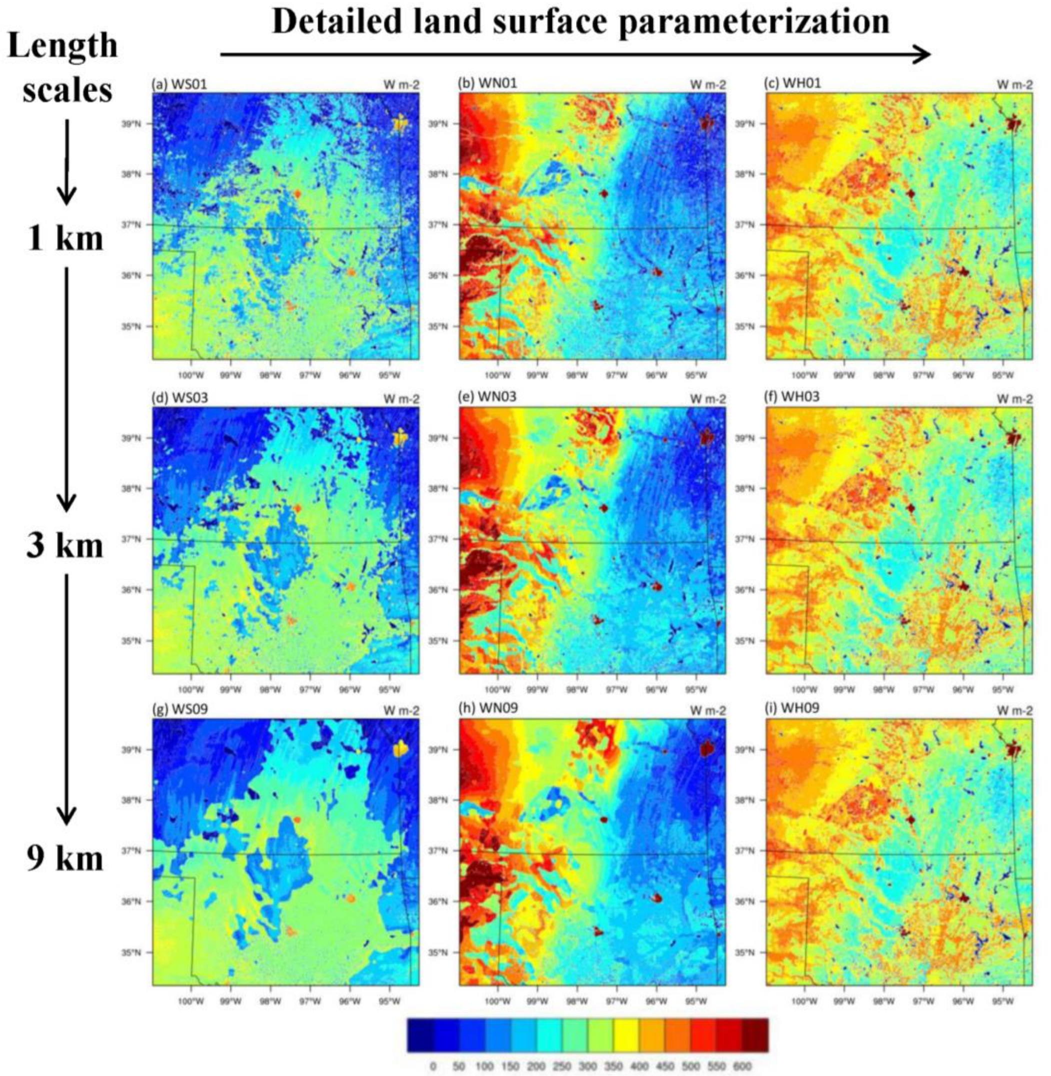

FIG. 2.3 Spatial variations in surface sensible heat flux (W m^{-2}) at 2100 UTC (1500 CST) 7 July 2007 in (a-c) WS01, WN01, WH01, (d-f) WS03, WN03, WH03, and (g-i) WS09, WN09, WH09.

m^{-2}). This shows that the slab model is more sensitive to land-surface heterogeneity impacts. The area-averaged *H* for WS increases when the land-surface becomes more homogeneous. The changing length scale modifies the amount of surface energy, and for WS the impact of the length scale changing from 1 to 9 km on *H* (6.8%) is more significant than on *LE* (1.6%). Thus, the increased length scales weaken the heterogeneity effects in the slab/WRF simulations, and this can result in significant changes of surface energy partitioning simulated in the slab model. This in turn affects the simulated heat and moisture within the PBL. The Noah and HRLDAS runs show less sensitivity to the land-surface heterogeneity length scale changes, indicating that a more detailed land-surface parameterization can help reduce the uncertainty in surface representation.

Table 2.2 Mean values of diurnal averaged of area-averaged surface heat fluxes

Case name	H (W m^{-2})	LE (W m^{-2})
WS01	32.12	144.78
WS03	33.64	143.10
WS09	34.30	142.48
WN01	45.09	138.43
WN03	45.64	138.29
WN09	44.02	138.02
WH01	56.87	113.63
WH03	56.87	113.63
WH09	57.15	112.92

Four typical land-surface types (grassland, forest, wet cropland, and dry cropland) in the domain were selected to study the responses of LSMs in the high-resolution coupled model (Table 2.3). Comparisons of diurnal variations of surface heat fluxes between the model runs over the domain and the measurements over four specific locations with different land cover types are shown in Figs. 2.4 (latent heat flux) and 2.5 (sensible heat flux). In the high-resolution coupled models, the different land-surface parameterizations greatly influence surface heat fluxes over grassland, forest, and wet cropland which have higher evaporation during wet conditions. The impacts of the different land-surface parameterizations on surface heat fluxes over dry cropland are relatively small. It is also found that Noah LSM performs better over all four land-surface types in all simulations.

Table 2.3 Summary of the land-cover type selection[*]

Site name	Vegetation type	Lat/Lon	Data source
KON	C_4 tallgrass prairie	39.08°N, 96.56°W	AmeriFlux
LAM	Croplands (wet)	36.61°N, 97.49°W	ARM
OKM	Forest	35.62°N, 96.07°W	ARM
VIC	Croplands (dry)	36.06°N, 99.13°W	ARM

[*] Specific site locations are shown as black dots in Fig. 2.1a.

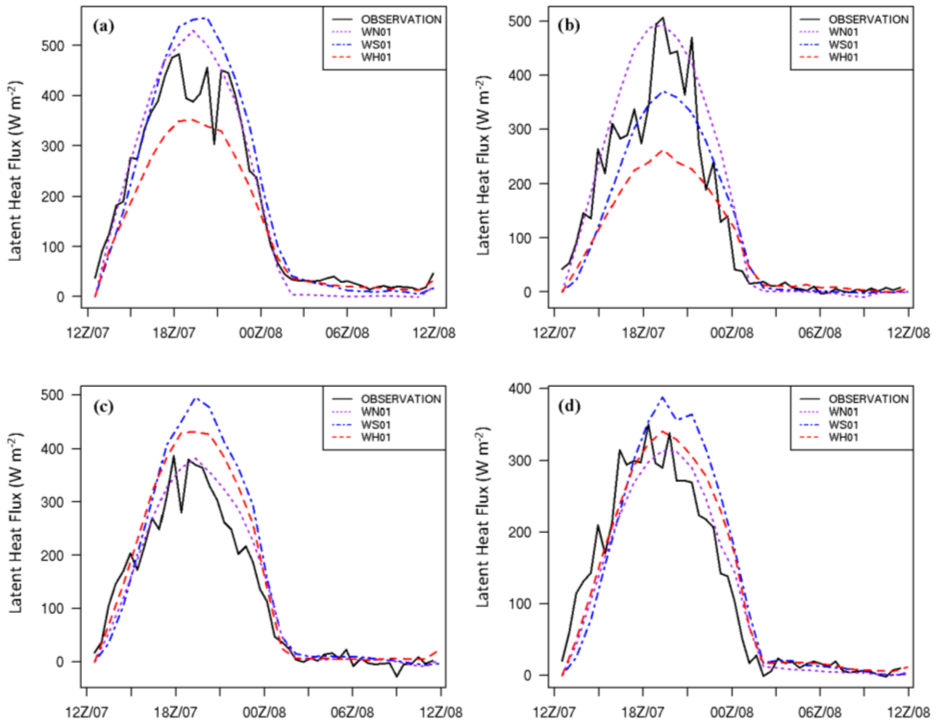

FIG. 2.4 Comparisons of diurnal variations in surface latent heat flux (W m^{-2}) between the model runs at 1 km length scale initiated at 1200 UTC (0600 CST) 7 July 2007, and the observations over (a) grassland (KON), (b) forest (OKM), (c) wet cropland (LAM), and (d) dry cropland (VIC). Details of the land-cover types are in Table 2.3.

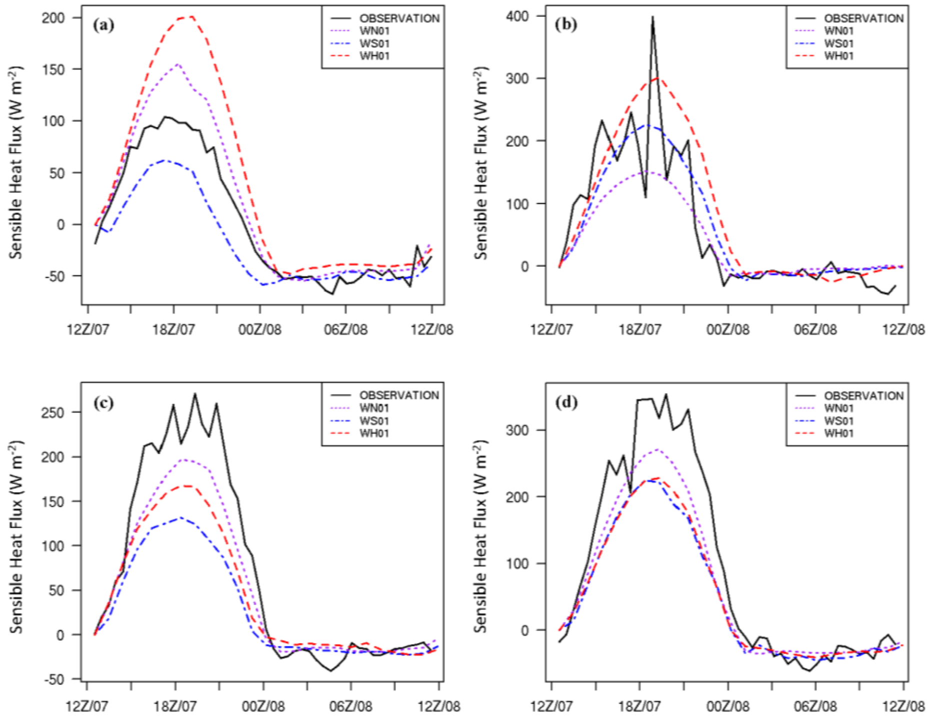

FIG. 2.5 Comparisons of diurnal variations of surface sensible heat flux (W m^{-2}) between the model runs at 1 km length scale initiated at 1200 UTC (0600 CST) 7 July 2007, and the observations over (a) grassland (KON), (b) forest (OKM), (c) wet cropland (LAM), and (d) dry cropland (VIC). Details of the land-cover types are in Table 2.3.

2.3.2 Impact of land-surface heterogeneity on modeling bias

A vertical cross section in the north-south direction through the middle of the domain was analyzed for temperature and relative humidity at 2100 UTC (1500 CST) 7 July 2007 (Fig. 2.6). Similar patterns are noted for the three schemes in the 1-km length scale simulations. As the heterogeneity length scale increases the cross sections of relative humidity show differences compared to those at the 1 km length scale. The PBL depth for WS and WN runs at the 9 km length scale are much lower compared to that at the 1 km length scale. This may be related to the eddies growing faster in the simulations with 1 km length scale than those with 9 km length scale, and that the MYJ PBL scheme in the 1-km-heterogeneity simulation aids the vertical transport of energy flux (Ching et al. 2014; LeMone et al. 2013; Zhou et al. 2014). The cross section for WH at the 9 km length scale shows very different patterns for temperature and relative humidity when compared to those for WS and WN. Consistent to the results noted for surface fluxes, the land-surface heterogeneity has less impact on the HRLDAS/WRF runs. Thus, the land-surface parameterization impacts the high-resolution coupled LSMs/WRF simulations more significantly than land-surface heterogeneity. This is not surprising considering that to some extent the land-surface heterogeneity is dictated by the land-surface model. Additionally, the PBL depth for WH is less dependent on the spatial heterogeneity scale, and stays similarly high for increasing heterogeneous length scale. This may be caused by the larger surface sensible heat flux in the WH simulations which leads to stronger resolved eddy motions and a deeper boundary layer.

Surface heat fluxes would eventually account for the difference in PBL processes and affect mesoscale simulations, modeling biases and the model's ability to simulate mass and energy exchanges at the microscale (e.g., Bukovsky and Karoly 2009; Weaver et al. 2002; LeMone et al. 2013, 2014; Reen et al. 2013). To assess the impacts of land-surface heterogeneity on coupled model biases, the simulated atmospheric variables were analyzed further.

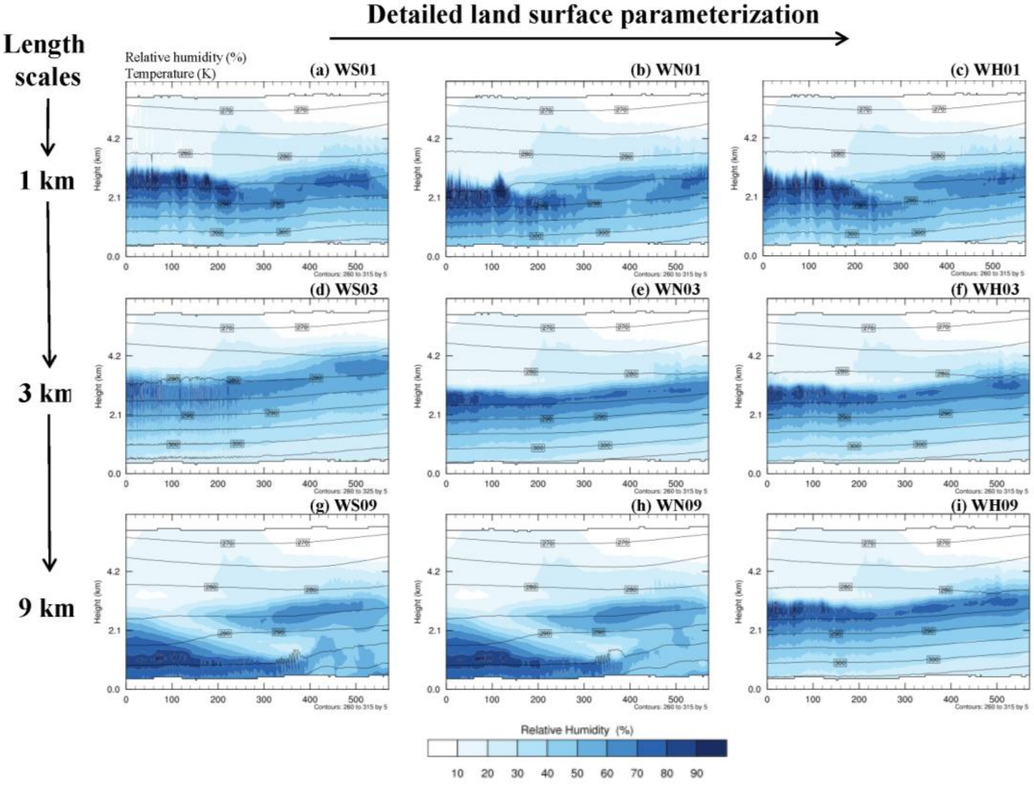

FIG. 2.6 Vertical cross section in the north-south direction through the middle of the domain (as seen in Fig 1b) for temperature (K) and relative humidity (%) at 2100 UTC (1500 CST) 7 July 2007 in (a-c) WS01, WN01, WH01, (d-f) WS03, WN03, WH03, and (g-i) WS09, WN09, WH09. The red bold marker "cross" in Fig 1a is the selected position for the cross section.

Results of diurnal-averaged RMSE of air temperature at 2 m (T_{2m}), specific humidity at 2 m (q_{2m}), and wind speed at 10 m (U_{10m}) over the domain are shown in Table 2.4. It is found that for the atmospheric variables of T_{2m} and q_{2m}, WS has the largest RMSE while WN shows the smallest RMSE. However for U_{10m}, the RMSE of WS is smaller than those of the other two coupled models. In addition, the RMSEs of T_{2m} for WS and WN is higher with an increase in the length scale of surface heterogeneity while the RMSEs of WH01 and WH03 are the same. These differences again indicate that the simulations of atmospheric variables are affected by both surface heterogeneity and land-surface parameterizations, and the impacts of land-surface parameterizations are more important.

Table 2.4 Diurnal averaged RMSE of 2 m temperature (T_{2m}) and moisture (q_{2m}), and 10 m wind speed (U_{10m}) for model forecasts over the domain

Case name	**RMSE**		
	T_{2m} (K)	**q_{2m} (g kg^{-1})**	**U_{10m} (m s^{-1})**
WS01	2.656	2.920	1.692
WS03	2.662	2.924	1.691
WS09	2.668	2.922	1.708
WN01	2.118	1.758	1.768
WN03	2.129	1.762	1.733
WN09	2.158	1.762	1.781
WH01	2.203	2.540	1.890
WH03	2.203	2.540	1.890
WH09	2.220	2.562	2.162

2.3.3 Impacts on turbulent characteristics

Previous studies have shown that correctly representing turbulent fluxes can yield better predictions of the effects of surface variability in the PBL (Alapaty et al. 1997) and improve parameterizations in NWP models over heterogeneous land surfaces (Avissar and Pielke 1989; Avissar and Chen 1993; Weaver 2004a, b; Alfieri et al. 2009; Case 2011). Additionally, a model's ability to reproduce observed energy spectra can help indicate whether the model has correct energy transfer and if it can reliably reproduce multiscale forecasts within the atmosphere (Skamarock 2004). The improved representation of small-scale phenomena therefore may contribute to improving mesoscale forecasts. We hypothesize that the land-surface heterogeneity affects turbulent flow and mesoscale circulations which can be represented by LSMs coupled to WRF model; and the turbulent representations are important for improving the coupled model simulations when replacing a simple slab model to a more detailed LSM. This hypothesis builds off prior results of Skamarock and Dempsey (2005) that showed that WRF-ARW forecasts produced kinetic energy spectra that bear close resemblance to climatologically observed spectra.

The maps of the vertical velocity and wind fields at the middle of the PBL height (~ 1 km) have shown the convective structure of the PBL at 2100 UTC 7 July 2007 (Fig. 2.7). The domain averaged turbulent vertical velocities are as expected close to zero and are negative (downward) for all the simulations. The vertical velocity fields show pockets of updrafts or downdrafts notably in the northwestern part of the domain (Fig. 2.7A), and these patterns are more apparent in the HRLDAS runs [Figs. 2.7A (c,f,i)]. A reason for this might be related to the land-surface heterogeneity induced in the high-resolution HRLDAS/WRF experiment. Since the convective eddies have positively correlated to the vertical velocity, these eddies provide a source of turbulent kinetic energy and positive heat flux. For the runs with 9-km land-use heterogeneity length scale, slab/WRF and Noah/WRF runs show stronger downward vertical velocity over the domain. This might indicate there are some eddies in these two runs that are tightly coupled to the landscape. However, the HRLDAS/WRF runs have insignificant changes in the vertical velocities and wind speeds due to the high-resolution (1 km) uncoupled land-surface modeling system initialization. The averaged wind speed at the mid-PBL level height is about 5 m s^{-1}, and show stronger gradients. Thus, the spatial averaged energy spectra could be reasonably representing the impacts of spatial heterogeneity and different land-surface parameterizations.

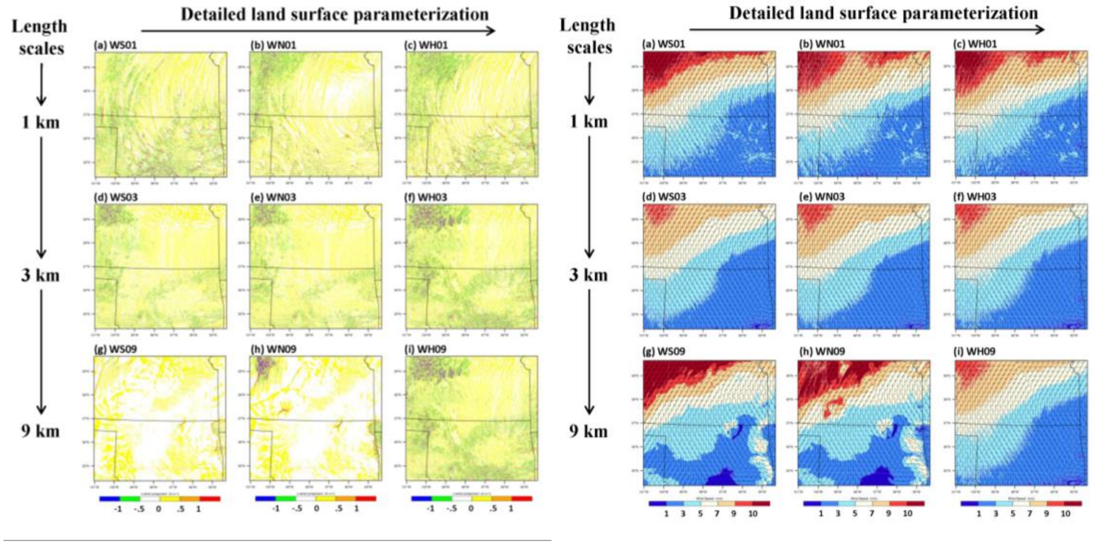

FIG. 2.7 Maps of (A) mid-PBL vertical velocity and (B) the wind fields at 2100 UTC 7 July 2007 with 1-km grid spacing.

Fast Fourier Transform (FFT) analysis was conducted and the WRF model kinetic energy spectra were developed to understand how the characteristics of the mesoscale energy spectra simulated by different LSMs/WRF are influenced by land-surface heterogeneity.

For short periods and the condition that the advection velocity of the turbulence is much greater than the turbulent vertical scale, Taylor's hypothesis of frozen turbulence can be invoked so that the spectrum of the time series data can be assumed to be representative of the spatial turbulent structure (Stull 1988). To satisfy Taylor's hypothesis, the simulated data over the domain were processed according to the condition that the standard deviation of wind speed is smaller than half of the mean wind speed (Willis and Deardorff 1976). A total of 558 × 591 data points were produced in the domain. To minimize the effects of the lateral boundary conditions, the energy densities were spatially averaged from grids beginning 15 points away from all the boundaries (Skamarock 2004). The energy densities were horizontally averaged using a one-dimensional spectral decomposition of the related scalars along the west-east direction. The kinetic energy spectra for the three different coupled models over the heterogeneous land surface were then computed at the height of each model's surface layer using data from these selected points.

The energy densities were calculated correspondingly to intense turbulent activity at 2100 UTC (1500 CST) 7 July 2007. The model results were compared against turbulence observations obtained using the eddy covariance (EC) technique which employed a Campbell Scientific CR1000 datalogger to sample velocities and virtual temperatures at 20 Hz. The EC tower in our research is from the AmeriFlux network and located at KON (39.08°N, 96.56°W; Fig. 2.1a).

The direct forcing from the flow interaction with topography and convection, the downscale cascade from lower frequencies, and upscale cascade from higher frequencies, are three substantial processes in the build-up of energy in the mesoscale portion of the spectrum (Skamarock 2004). Fig. 2.8 shows the energy spectra with standard deviation log-log plots of simulated T_{2m}, q_{2m} (Figs. 2.8 a and b), and the log-log plots of horizontal wind velocities at 10 m (U_{10m}, V_{10m}), and vertical velocity (W) [Figs. 2.8 (c-e)] at the model's lowest layer for the three different coupled models at the 1 km length scale. Note that since variations in variables such as temperature and humidity can persist as "footprints" of former turbulent flow, the resulting spectra of these variables cannot be associated with eddy motions (Stull 1988; Schmid 2002). It is noted that the energy spectra show similar trends of curves. This is likely because the initial and lateral boundary conditions for all the models are derived from the same 1 degree FNL analysis data. However, the spectra can be sensitive to the different land-surface features. The spectra of simulated T_{2m} and q_{2m} for WS depart from those for WN and WH and are much stronger (Fig. 2.8a), while the spectra for WN are the smallest but very close to the observations (Figs. 2.8 a and b). A large portion of the turbulent observations are found when the frequency is larger than 10^{-4} hz, indicating that the large eddies that are resolved in WRF model contribute essentially to the turbulence state. Additionally, the surface turbulence is a mix of some low-level frequencies related directly to the surface wind and some related to the PBL wind. By analyzing the spectra for temperature and humidity, we concluded that the LSMs/WRF can capture most of the turbulent eddies that contribute to turbulence variances.

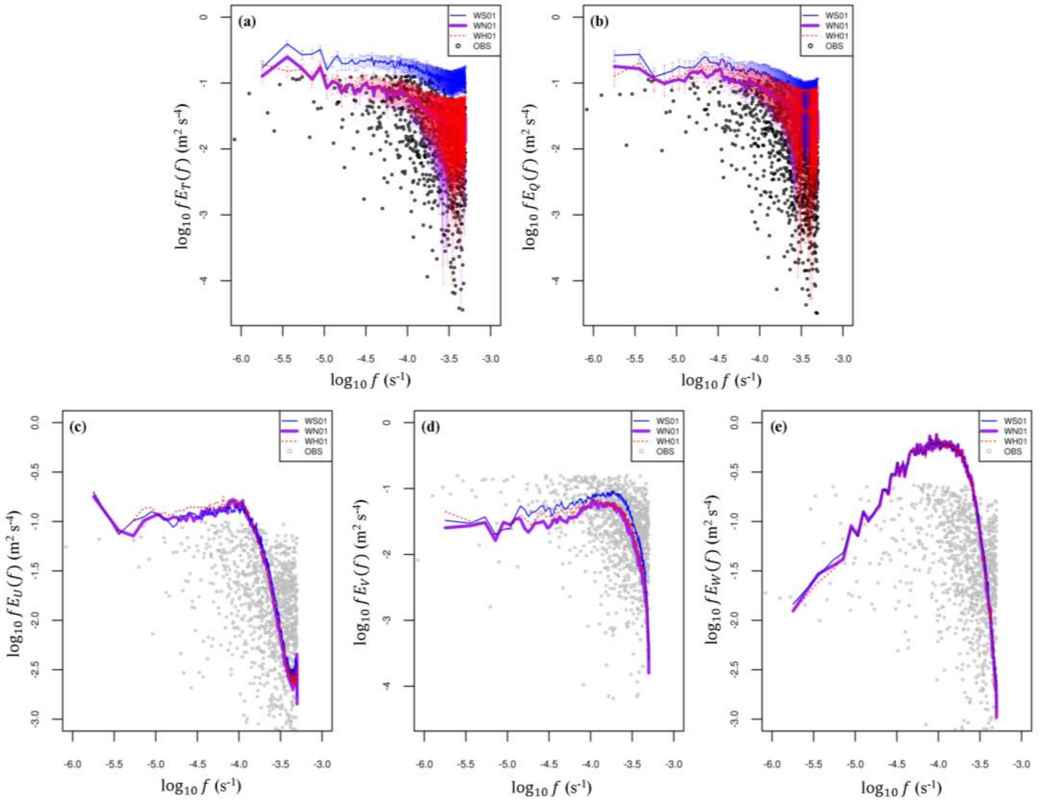

FIG. 2.8 Energy spectra (m^2 s^{-4}) multiplied by frequency (s^{-1}) computed from coupled WRF simulations compared to observations at 2100 UTC (1500 CST) on 7 July 2007 for (a) temperature at 2 m, (b) specific humidity at 2 m, (c) U-wind at 10 m, (d) V-wind at 10 m, and (e) vertical velocity.

By decomposing a series of measurements into frequency, the contributions from eddies of different time and space scales to the overall turbulence can be quantified. Impacts of LSMs on the spectra of U_{10m} and V_{10m} are noted to be more significant at lower frequencies ($f < 10^{-4}$ hz) where the mesoscale circulations may be created as a result of land-surface heterogeneity (Fig. 2.9c and d). The spectral amplitude of U_{10m} for WH is larger than those of WN and WS (Fig. 2.9c). WS shows stronger spectral amplitude for V_{10m} (Fig. 2.8d), but all the simulated energy spectra of V_{10m} are much smaller than the observations, indicating that although the energy from large size eddies for V_{10m} of WS is stronger than those for WN and WH, the coupled models still underestimate the energy spectra of V_{10m} that are contributed to by large eddies. All spectra of vertical velocity collapse to a series of close curves in the middle and higher frequencies (Fig. 2.8e).

The spectra have also been analyzed to estimate heterogeneity influences. Fig. 2.9 shows log-log plots of energy spectra (m^2 s^{-3}) multiplied by frequency (s^{-1}) at 2100 UTC (1500 CST) over the domain at 1, 3, and 9 km length scales for T_{2m}, q_{2m}, and vertical velocity in WS, WN, and WH. It is noted that the spectral amplitude of T_{2m} for all the experiments decreases as the length scale increases [Figs. 2.9 (a-c)]. At higher frequencies with 3 km length scale, an upturn occurs at the end of tail from the energy spectra of T_{2m}. The slopes of WS01 and WS03 for T_{2m} and q_{2m} are larger than the corresponding slopes of the observations, indicating that slab/WRF cannot well represent the energy spectra of T_{2m} and q_{2m} and underestimates the energy cascade. The spectra of q_{2m} for WN03 are smaller than those for WN01 and WN09, and in the inertial subrange and higher frequencies, WS01 and WN01 show the largest spectral magnitudes while at lower frequencies, the spectra of q_{2m} for WS09 and WN09 are the strongest (Figs. 2.9 d and e). For HRLDAS/WRF runs, non-linear changes in the log value of the energy spectra with the increase of the heterogeneous length scale have been noticed. The T_{2m} and q_{2m} show the largest energy over the 9 km heterogeneity spatial scale, whereas the energy spectra for the 3 km length scale experiments are the smallest (Fig. 2.9e and f). Thus under abundant soil moisture availability conditions, the impacts of surface heterogeneity on the spectra of simulated surface temperature and moisture can be noted at all frequencies. The more detailed LSM/WRF at the 1 km length scale simulates a better energy spectrum.

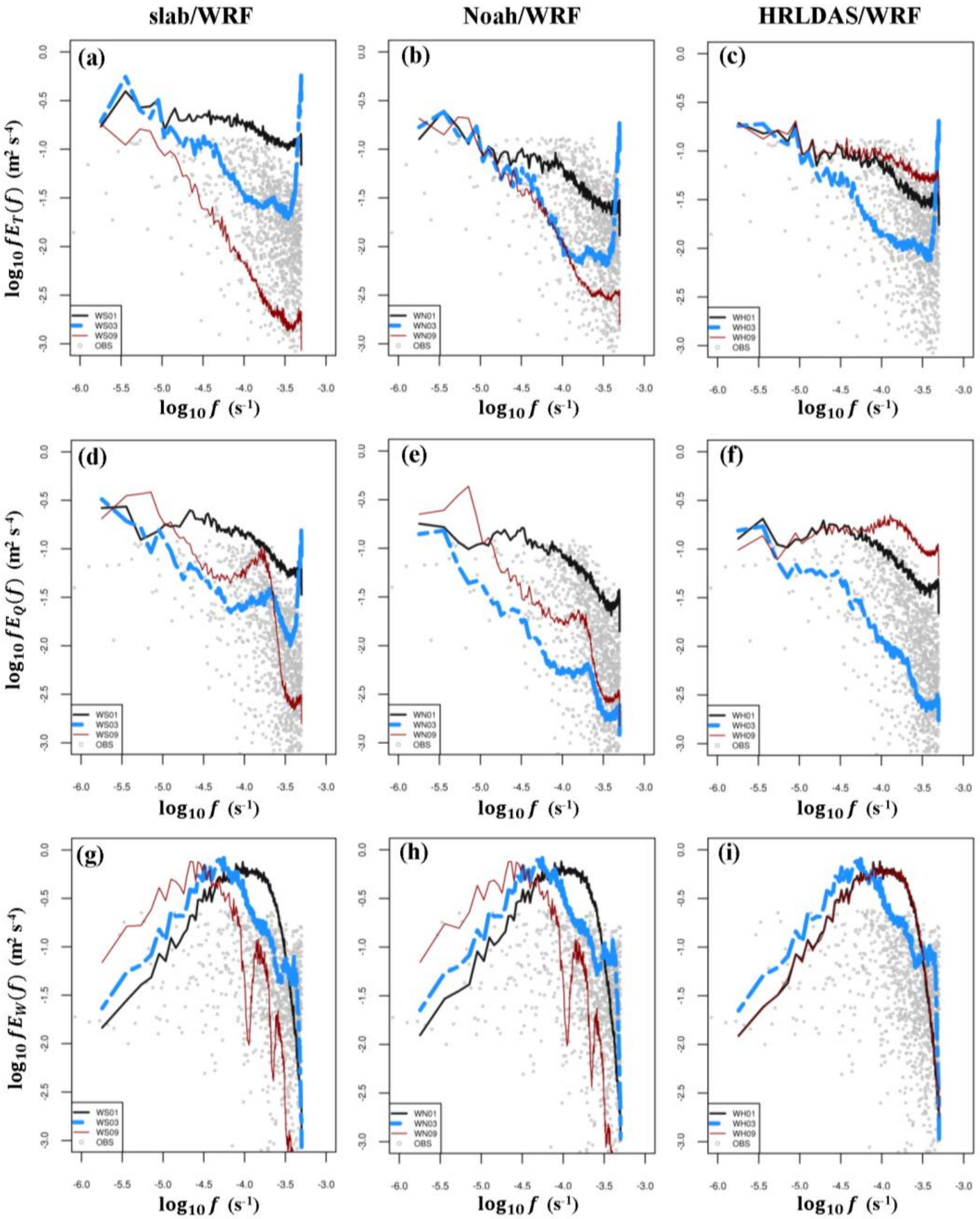

FIG. 2.9 Energy spectra (m^2 s^{-3}) multiplied by frequency (s^{-1}) computed from coupled WRF forecasts at 1, 3, and 9 km length scales at 2100 UTC (1500 CST) compared to observations on 7 July 2007 for temperature at 2 m (top), specific humidity at 2 m (middle), and vertical velocity (bottom) in WS (a, d, g), WN (b, e, h), and WH (c, f, i).

For *W* simulated by WS and WN at lower frequencies, the spectral energy amplitude increases as the length scale increases (Figs. 2.9 g and h), indicating the large size of eddies over the land surface with a 9 km length scale contain more energy than those with a 1 and 3 km length scale. In the inertial subrange, the energy spectra amplitudes are largest at the 1 km length scale, thus all the coupled models are able to represent land-surface heterogeneity impacts on the vertical velocity which is much stronger over a more heterogeneous land surface. WH01 and WH09 show close curves for the energy spectra of the vertical velocity. Additionally, as seen in Figs. 2.9(g-i) *W* is less sensitive to the different land-surface parameterizations, especially at the 1 km length scale.

Thus, in response to land-surface heterogeneity and LSMs, the impact of horizontal spatial scale of land-surface heterogeneity on mesoscale coupled model's energy spectra can be better captured at the 1 km length scale by a more detailed land-surface parameterization.

2.3.4 Impacts on surface-atmosphere interactions

Sounding profiles (Fig. 2.10) at 0000 UTC (1800 CST) 8 July 2007 for specific humidity, potential temperature, and wind speed at Norman, OK (OUN, 35.18°N, 97.44°W) and Topeka, KS (TOP, 39.07°N, 95.62°W) were simulated and compared to observations. We only show sounding profiles simulated at the 1 km length scale as an example of the responses of sounding profiles to changes in the land-surface parameterizations. The profiles of temperature, moisture, and wind speed in the WS model soundings are well simulated for the TOP site. Simulated potential temperature, wind speed, and surface and upper-level specific humidity by WS are also in good agreement with observations from the OUN site. From the surface to the 900 hPa level, WH shows cold biases for surface potential temperature while WN over-predicts temperature for both sites. Surprisingly, the slab model simulates the profiles of temperature, moisture, and wind speed better at the 1 km length scale.

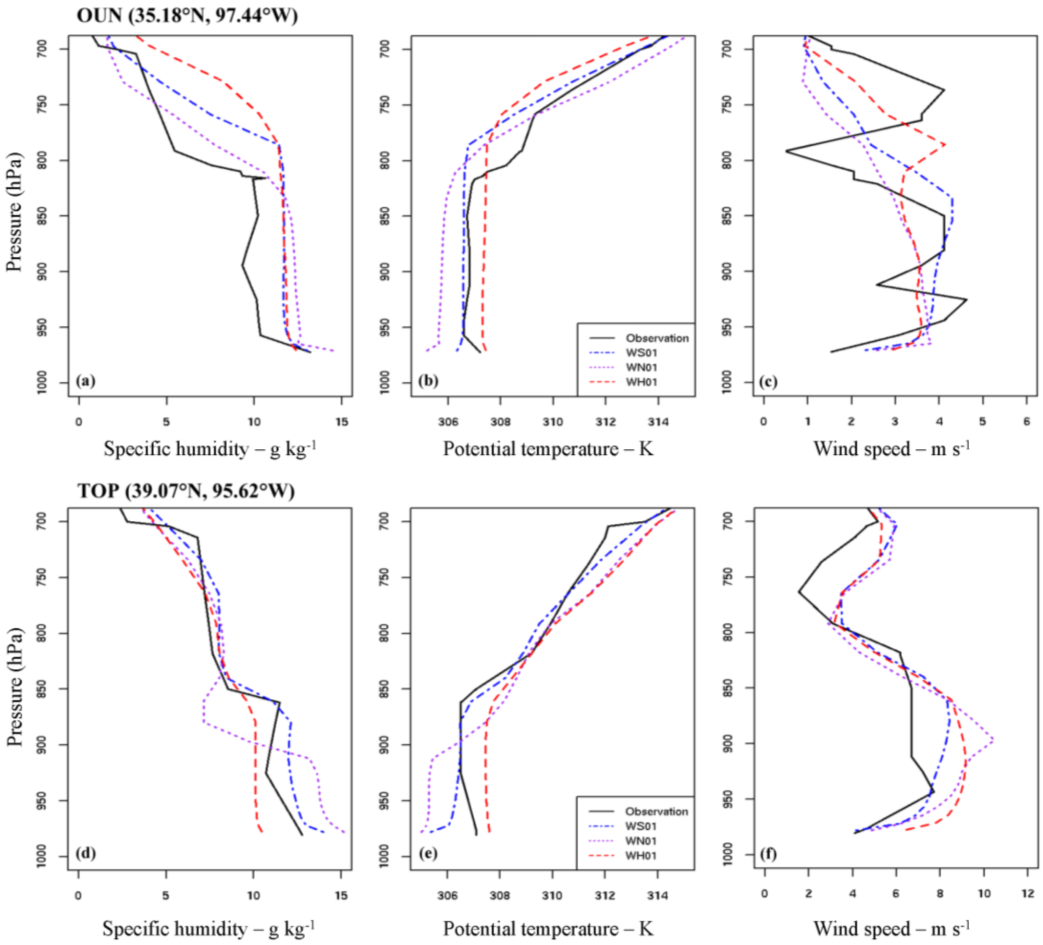

FIG. 2.10 Sounding profile at 0000 UTC (1800 CST) 8 July 2007 of specific humidity (g kg^{-1}) (a, d), potential temperature (K) (b, e), and wind speed (m s^{-1}) (c, f), valid at Norman, OK (OUN, 35.18°N, 97.44°W) (top) and Topeka, KS (TOP, 39.07°N, 95.62°W) (bottom).

The dimensionless vertical profiles of the turbulent moisture flux, turbulent thermal flux, buoyancy flux, turbulent kinetic energy (TKE), and wind velocities were averaged from 2100 UTC (1500 CST) to 2130 UTC (1530 CST) 7 July 2007 at specific site locations (Table 2.3) for each experiment and scaled using boundary layer heights. Since the modeled PBL top is very irregular and not a good parameter to compare with PBL depth, we used actual sounding profiles to estimate the PBL heights (Cheng et al. 2002). Fig. 2.11 shows the impacts of different land-surface schemes on turbulent processes in the PBL over wet/dry croplands. Results confirm that the turbulent characteristics vary over different land-surface properties, and the turbulence is stronger above the higher surface heat flux which agrees to the findings of Hadfield et al. (1992). As seen in Figs. 2.11 a and e, the difference among the vertical profiles of normalized turbulent thermal flux between WS01 and WH01 is positive toward the entrainment zone. This is because the stronger spectrum of T_{2m} for WS (Fig. 2.8a) leads to larger eddies and more energy vertically transported into the PBL. WN shows the largest normalized turbulent thermal flux over the wet cropland (Fig. 2.11a), however, the spectrum of T_{2m} for WN did not show the largest amplitude (Fig. 2.8a). Additionally, the higher surface sensible heat flux (e.g., Fig. 2.5) does not necessarily provide a higher averaged vertical turbulent thermal flux. In Fig. 2.11b and f, stronger gradients at the surface where water vapor is evaporated into the boundary layer and the entrainment zone where a cap on the mixed layer exists, are noted for all the land-surface parameterizations over wet cropland. This result further supports the findings of previous surface heterogeneity impact studies (Avissar and Schmidt 1998; Huang and Margulis 2009). However WN fails to simulate this phenomenon over dry cropland. WH shows the largest moisture flux in the near-surface layer. The mixed layer is dried due to entrained air, but the drying magnitudes of moisture flux are different due to the influence of the different LSMs (Figs. 2.11 b and f).

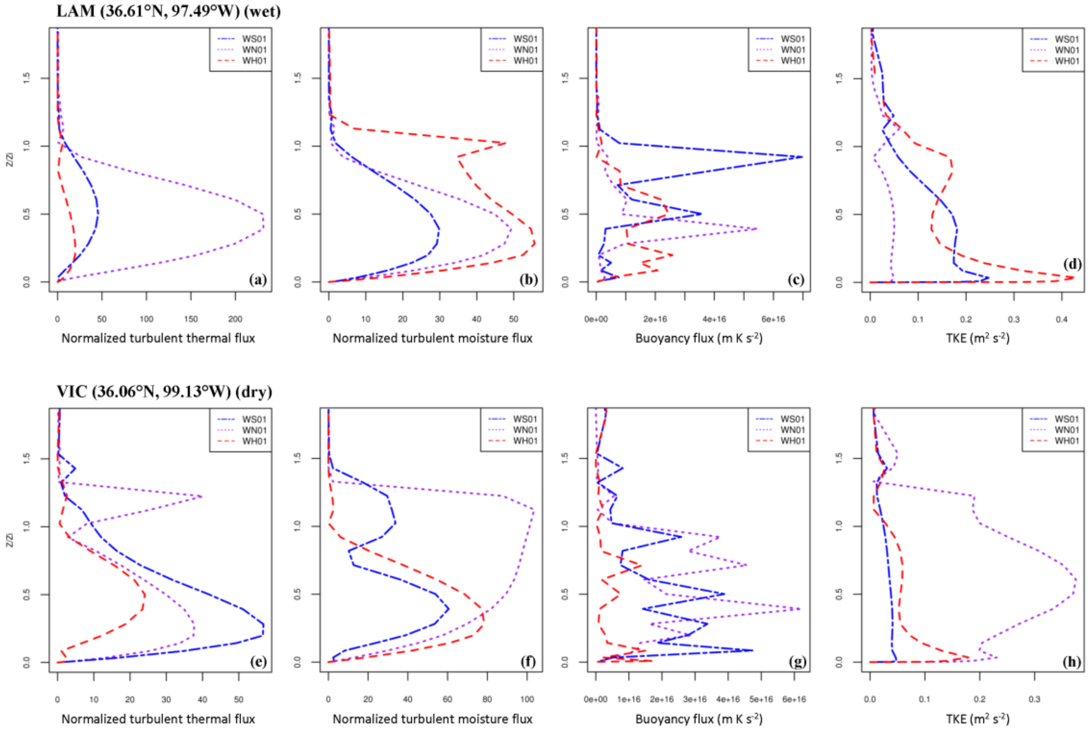

FIG. 2.11 Vertical profiles of normalized (a) turbulent thermal flux (W m^{-2}), (b) turbulent moisture flux (W m^{-2}), (c) buoyancy flux (m K s^{-2}), and (d) TKE (m^{2} s^{-2}) averaged from 2100 UTC (1500 CST) to 2130 UTC (1530 CST) 7 July 2007 for wet cropland (LAM) and dry cropland (VIC).

The production of TKE is directly related to the transport of momentum and scalars. For the case being simulated under relatively low wind and scattered cloud scenario, the TKE production is expected surface buoyancy dominated. It is further expected that larger buoyancy flux leads to higher total TKE and this feature is well represented by all the three different land-surface parameterizations coupled to WRF over wet cropland. The simulated total TKE profiles for all land-surface parameterizations approach the maximum values at the surface and by definition decrease along with the height below the boundary layer height (Fig. 2.11d). However, over dry cropland the total TKE for WN increases with height from the land surface to half of the boundary layer height and decreases when the normalized height is larger than 0.5 (Fig. 2.11h). Among all the three simulations over dry cropland, the buoyancy flux in the PBL for WH is smaller than that for WS (Fig. 2.11g), and the total TKE simulated by WS is the smallest (Fig. 2.11h). For WN, the vertical turbulent moisture flux and total TKE are not well simulated.

Fig. 2.12 shows vertical profiles of normalized vertical velocity (taken as the ratio of vertical velocity and convective velocity; Deardorff and Willis 1982) averaged from 2100 UTC (1500 CST) to 2130 UTC (1530 CST) 7 July 2007 over different land surfaces (Table 2.3). The vertical velocity is a key parameter which is associated with turbulent parameters. In general, the simulations differ with different land-surface parameterizations. The profiles of normalized vertical velocity are simulated differently by different land-surface parameterizations, but are identical in shape (Fig. 2.12). As shown in Fig. 2.12, over tall grass prairie, the magnitude of normalized vertical velocity for WS is much larger than those for WN and WH. The vertical velocity profiles for WN and WH show close curves over the tall grass prairie, but WS and WH show similar velocities below 500 m height above the land surface. The simulated vertical velocity show larger difference over the cropland, and is impacted significantly over dry cropland. The vertical profiles of horizontal velocity variance were also been studied. Results show over tall grass prairie and cropland, larger horizontal velocities occur near the land surface due to association with stronger wind shears during the daytime. Over forest, the near-surface horizontal velocity is small because of the larger surface roughness. Near the boundary layer height, all simulated horizontal velocities show a large gradient over tall grass prairie, but the magnitudes of the variations are different. Note that while these results reveal that there are differences in the turbulent structure simulated by the different land-surface parameterizations coupled to WRF model in response to the surface heterogeneity, they cannot be used to evaluate whether one land-surface scheme surpasses the other in representing turbulent characteristics.

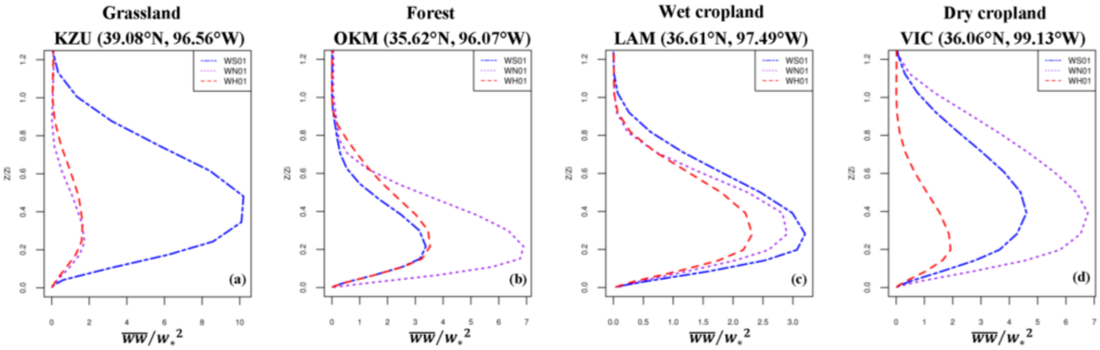

FIG. 2.12 Vertical profiles of vertical velocity averaged from 2100 UTC (1500 CST) to 2130 UTC (1530 CST) 7 July 2007 for grassland (KON) (a), forest (OKM) (b), wet cropland (LAM) (c), and dry cropland (VIC) (d). Details of the land-cover types are in Table 2.3.

The vertical profiles of normalized TKE with 1, 3, and 9 km length scales in WS, WN, and WH are shown in Fig. 2.13. TKE is a measure of turbulent intensity that can also be influenced by the heterogeneity induced atmospheric motions. The variation of TKE profile for WS is found to be the most significant at the 3 km length scale (Figs. 2.13 a and d). Large gradients of TKE for WN are noted near the boundary layer height over the wet cropland, indicating vigorous turbulence occurs in Noah/WRF simulations over wet cropland (Fig. 2.13b). For WH the TKE profiles have close curves for the 3 km and 9 km length scales, but the boundary layer is much more turbulent at the 1 km length scale (Figs. 2.13 c and f). However, the simulated boundary layers are much more turbulent for WS03 and WN01 over dry cropland, indicating that the different land-surface parameterization can result in significant difference in boundary layer simulations, particularly over the heterogeneous dry cropland.

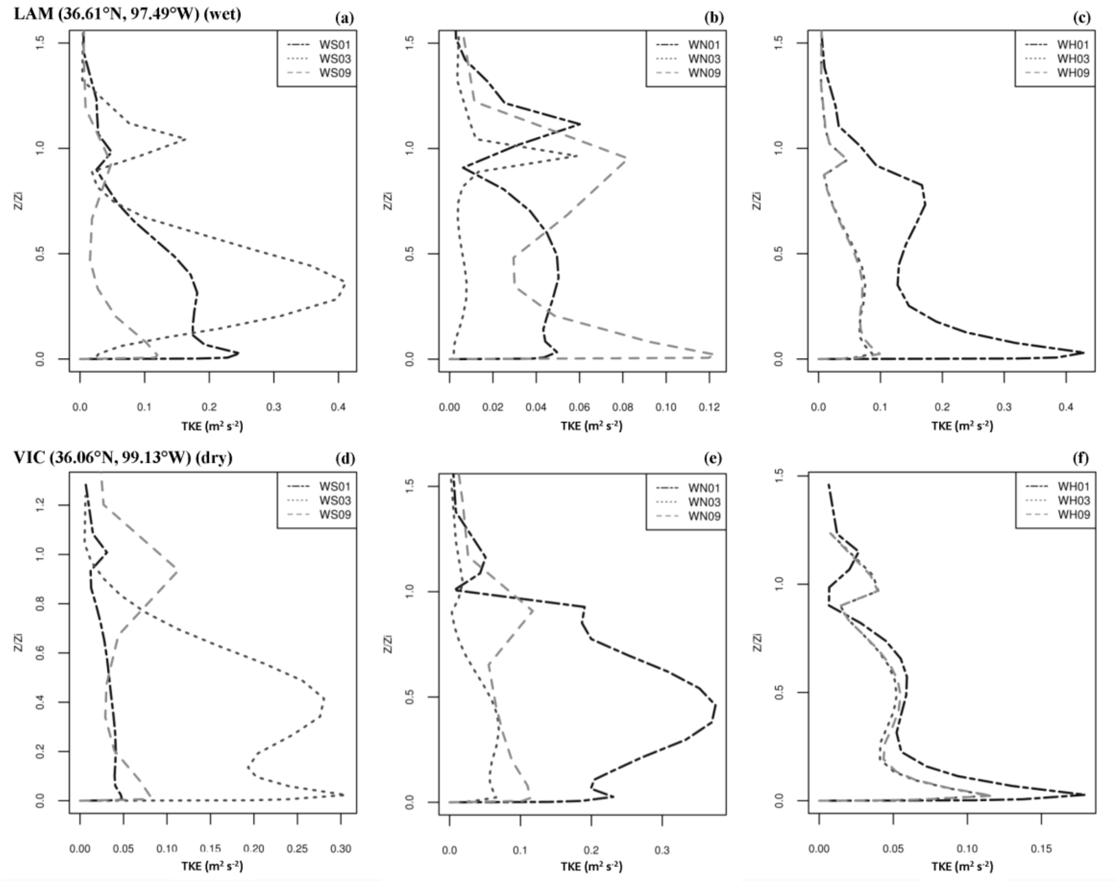

FIG. 2.13 Vertical profiles of normalized TKE (m^2 s^{-2}) averaged from 2100 UTC (1500 CST) to 2130 UTC (1530 CST) 7 July 2007 with 1, 3, and 9 km length scales in WN (a, d), WS (b, e), and WH (c, f) over wet cropland (LAM) and dry cropland (VIC).

2.4 Summary and conclusions

We conducted a series of numerical experiments (slab/WRF, Noah/WRF, and HRLDAS/WRF) to study the role of land-surface heterogeneity on the turbulent flow and mesoscale processes in the WRF model coupled within different land-surface parameterizations. Results show that the more detailed land-surface parameterizations over heterogeneous land surface typically help improve turbulent processes, leading to improved simulations of land-atmosphere interactions over heterogeneous land surface.

Changes of length scales of land-surface heterogeneity affect high-resolution model simulations through modification of land-surface properties. Typically the spatial variation of surface heat flux decreases as the length scale of land-surface heterogeneity increases. The slab model is found to be more sensitive to land-surface heterogeneity impacts, whereas the Noah and HRLDAS runs show less sensitivity to the land-surface heterogeneity length scale changes, indicating that the more detailed land-surface parameterizations (e.g., Noah LSM and HRLDAS) can help reduce the uncertainty of surface flux simulations over heterogeneous landscapes.

Land-surface heterogeneity and changes in land-surface initialization also result in impacts on modeling biases, and the impacts of changes in land-surface parameterizations are more significant. Nonlinear impacts are found in simulated surface temperature, moisture, and wind speeds due to landscape heterogeneity. Larger biases have been noted in the slab/WRF run.

The responses of turbulent spectra to land-surface heterogeneity indicate that the more detailed LSMs/WRF simulate more correct turbulent spectra over the heterogeneous land surface. The energy spectra response nonlinearly to changes in the heterogeneous length scales. The impacts of LSMs on turbulent energy spectra are more significant at lower frequencies of the spectra with 1 km heterogeneity length scale. *Results of the spectral analysis provide an important finding that the atmospheric feedbacks that are roughly four times of the land heterogeneity spatial scale can be adequately resolved in the coupled mesoscale model.* For example, for the 1 km heterogeneity length scale, the circulation larger than 4 km would be resolved; it would be larger than 12 km to be resolved for the 3 km length scale, and larger than 36 km for the 9 km length scale. This highlights the question such as “what is the minimum land heterogeneity required to trigger atmospheric circulation?”. The effect would be a function of the degree of spatial heterogeneity represented in the land surface model, which is often a function of the grid spacing. This emergent feature needs to be studied further.

Results also identify substantial variations in turbulent spectra and provide one piece of evidence showing the nonlinear influence of spatial length scales and the use of different land-surface parameterizations on turbulent energy spectra. However, the turbulent characteristics obtained at the surface may not be in equilibrium with the flow at height over a heterogeneous land surface (Schmid 1994), and it is possible to examine the change in the spatial energy spectra in relation to the length scale of heterogeneity. Results indicate that there are differences in the heterogeneity length scales represented by the model runs with different land-surface parameterizations.

The spatial heterogeneity represented by different land-surface parameterizations would resolve the atmospheric circulation which is at least four times of the spatial heterogeneity length scale. The vertical profiles of the turbulent fluxes and TKE can also be used to represent LSM influences and land-surface heterogeneity impacts. Our results agree with prior studies (e.g., Holt et al. 2006; Niyogi et al. 2006; Niyogi et al. 2009b; Niu et al. 2011) that showed a positive impact of the improved land-surface parameterization on model responses in terms of surface fluxes and mesoscale dynamical features. Additionally, this study has addressed the issue of how the detailed land surface representation affects the boundary layer and mesoscale processes via turbulent processes.

CHAPTER 3. IMPACTS OF LAND-ATMOPSHERE COUPLING ON REGIONAL RAINFALL AND CONVECTION[2]

3.1 Introduction

The coupling between the atmosphere and the land surface can play an important role in regional convection and precipitation (i.e., Trier et al. 2004; Holt et al. 2006; LeMone et al. 2010) and is one of the important components of any given weather and climate model (Pielke et al. 2011). The importance of land-atmosphere coupling has been emphasized in many observational and modeling studies (e.g., Dirmeyer 2000; Koster et al. 2003, 2004, 2006; Seneviratne et al. 2010). Wetter soils can cause higher evaporation, and higher latent heat flux, which in turn enhances the moisture availability within the planetary boundary layer (PBL), affects the atmospheric heating rates and cloud formation, and can impact local and regional precipitation (Niyogi et al. 1999; Pielke 2001; Kang et al. 2007; LeMone et al. 2008). The impacts of land-atmosphere coupling on regional temperature through a negative correlation between soil moisture and surface temperature also have been noted (Fischer et al. 2007; Hirsch et al. 2014).

It is expected that land-surface feedbacks can have a more dominant impact on regional precipitation in some regions of the globe as compared to others. Koster et al. (2004) identified global "hot spot" regions as areas of strong coupling between summer rainfall

---

[2] Zheng, Y., A. Kumar, and D. Niyogi, 2015: Impacts of land-atmosphere coupling on regional rainfall and convection. *Clim. Dyn.*, **44**, 2383–2409, doi: 10.1007/s00382-014-2442-8.

and land-surface conditions, and concluded that there was a significant impact on cloud formation, which was sensitive to the land-surface forcings such as soil moisture, land use, and topography (Koster et al. 2003; LeMone et al. 2008; Houze 2012). It has been noted that the coupling hot spots identified in the Global Land-Atmosphere Coupling Experiment (GLACE) study could be incorrectly capturing land-atmosphere coupling (Dirmeyer et al. 2006). In particular, the land surface models (LSM) may represent incorrect coupling in climate models, leading to too much evaporation and incorrect soil moisture-precipitation feedback (Ruiz-Barradas and Nigam 2005). As a result, models can overestimate moisture in summer due to a lack of knowledge in reference to the model-prescribed land-atmosphere coupling strength (Koster et al. 2003; Hirsch et al. 2014; Lorenz and Pitman 2014). Similarly, Zhang et al. (2008) for example, concluded that the U.S. SGP does not show up as a strong land-atmosphere coupling region in their regional model runs. This raises broad questions such as how do the current meteorological models represent land-atmosphere surface coupling strength? What would be the impact of surface-atmosphere coupling strength on regional (and though not considered here, global) model performance?

One way of representing the coupling strength between land and atmosphere is through the surface exchange coefficient. Recent studies such as LeMone et al. (2008) and Chen and Zhang (2009) concluded that the surface exchange coefficient is responsible for transferring surface energy into the lower atmosphere and that the land-atmosphere coupling strength depends on this coefficient for different land-cover types and climate regimes. Trier et al. (2011) explored the impacts of the coupling coefficient “*C*” based on the Zilitinkevich (1995) equation (thereafter C_{zil}) on the mesoscale warm rain processes over the U.S. SGP locale. Their results indicated that the representation of C_{zil} significantly affected precipitation and convection via a stronger surface exchange simulation, but the implication and possible advantages of dynamically changing C_{zil} in regional scenarios over different regions are not yet clear. Therefore, we investigated the coupling impact using an offline Noah land model and a coupled WRF model over U.S. SGP, Europe, India, and West African regions. These four regions were selected because of the diversity in landscape, and the preponderance of intense mesoscale convection and heavy precipitation cases. Further, each of these regions was identified as a land-atmosphere coupling hotspot in different global studies (Koster et al. 2004 and 2006; Xue et al. 2004; Seneviratne et al. 2006).

Thus, the objective of this study is to assess the role of coupling strength over regions with strong coupling between land-surface conditions and moist convection. We hypothesize that a better understanding of the coupling effect will benefit numerical weather prediction (NWP) and the parameterizations used for land surface representations, and could potentially lead to improved simulation of severe weather events. The main tasks undertaken are 1) to quantify the land-atmosphere coupling strength impacts on model parameterizations (i.e., land surface processes, PBL dynamics, and moist convection), 2) to document the range of the regional variations in C_{zil} for model simulations, and, 3) to identify if the dynamically changing C_{zil} could help improve the NWP model’s summer convection simulations over the different coupling hotspot regions.

This paper is organized as follows. Section 2 summarizes the experimental setup using the uncoupled Noah LSM and the coupled WRF mesoscale model as well as the study domain. Section 3 discusses the methodology adopted to assess the effects of the land-atmosphere coupling strength. Section 4 evaluates the different case studies and simulations. The study conclusions and discussions are provided in Section 5.

3.2 Numerical modeling framework and study domain

This section describes the model setup and the experimental study domain. The methodology first tests the impacts of the coupling coefficients within an offline model in order to study the impacts of surface coupling strength on energy partitioning and surface heat exchanges. This analysis is conducted over the U.S. SGP. Following the uncoupled diagnostics, the remainder of the experiments uses a coupled Noah-WRF modeling framework for regional coupling analysis across the four different regions.

3.2.1 Offline modeling system

The coupling strength needs to be studied in association with the land cover characteristics (Hirsch et al. 2014). As a result, a number of numerical experiments over three different land surfaces (grassland, cropland, and forest) are undertaken using a 1-D offline (uncoupled) Noah LSM within the High Resolution Land Data Assimilation System (HRLDAS; Chen et al 2007). The land model is forced by analysis fields or meteorological observations rather than coupled to an atmospheric model. HRLDAS integrates static fields of land use and soil texture as well as time-varying fields of vegetation and meteorology. The primary reason for using HRLDAS is that this framework is capable of capturing the land-surface heterogeneity at multiple scales that are important for resolving microscale to regional features (Holt et al. 2006; Charusombat et al. 2012).

As stated, the U.S. SGP domain has been a subject of recent land-atmosphere coupling studies (e.g., Koster et al. 2006; Zhang et al. 2008; Trier et al. 2011) and has a number of high quality observations. A 188 × 170 × 31 grid domain was set up with 4 km horizontal grid spacing (Fig. 3.1). An eighteen month spinup initialization was run from December 2000 to June 2002 following Chen et al. (2007). The atmospheric forcing and surface conditions used in HRLDAS were: i) National Centers for Environmental Prediction (NCEP) Stage-IV Rainfall Analysis at 4 km horizontal grid spacing; ii) 50 km GOES solar downward radiation; iii) other atmospheric forcing conditions from model-based analysis; and iv) the USGS land-use and land-cover map with 24 vegetation types. The domain was initialized using the USGS soil texture map, terrain height, land-water mask and land use through the WRF Pre-processing System (WPS). These data were interpolated to a regular 0.01 degree geographic projection according to the respective WRF grids. The offline (uncoupled) HRLDAS model is grid-based, and uses 1-D column version of Noah to execute single-site land-surface simulations. The soil conditions at four soil depth layers and the vegetation were initialized as model input parameters, and the physical processes were identical to that of the Noah LSM described by Chen et al. (1997, 2007). Surface heat flux observations were used to evaluate the model results.

3.2.2 WRF Model and domain configurations

WRF 3.4.1 (Skamarock et al. 2008) was used to conduct coupled simulations with Noah LSM. One degree 6-hourly NCEP Global Final Analysis (FNL) dataset, which was derived from the Global Forecast System (GFS), was used to set the boundary and initial conditions for the large-scale atmospheric fields, soil parameters (i.e., soil moisture and temperature), and sea surface temperature (SST). The WRF model was run with 28 vertical levels applied from the surface to 50 hPa level. The model was setup over four different regions, the U.S. SGP, Europe, northern India, and West Africa. Each region has unique land-surface characteristics, and the cases being simulated are typical for the regions and employed to study the coupling impacts on atmospheric convection simulations. A summary of the four regions is shown in Table 3.1 and discussed next.

Table 3.1 The characteristics of study regions

	Model grid points			
	9-km grid spacing	**3-km grid spacing**	**Land-cover type**	**Geographic feature**
U.S. SGP	290 × 280	307 × 274	Grassland, cropland, savannas and a mixture of crop and natural vegetation	Modestly higher elevation on the western side, synoptic and mesoscale weather events
Europe	250 × 240	307 × 274	Forest, arable land with permanent crops, and pastures and mixed mosaics	Mountainous terrain; Dominant orographic precipitation
India	250 × 240	307 × 274	Forest and agricultural land	A typical monsoon region with trough and associated weather patterns
West Africa	433 × 433	631 × 631	Forest, cropland, woodland and shrub land, grassland, and bare soil	Large flat area

3.2.2.1 U.S. SGP

The first study domain is over the U.S. configured with a two-way nesting. The parent (outer) domain has a coarser mesh with 290 × 280 grid points in the horizontal directions and a grid spacing of 9 km, while the nest (inner) domain has 307 × 274 grid points at 3 km grid spacing (Fig. 3.1a). The main land-cover types include grassland, cropland, savannas and a mixture of crop and natural vegetation. The topographic features are shown in Fig. 3.1a and indicate that the domain has a relatively higher elevation on the western side.

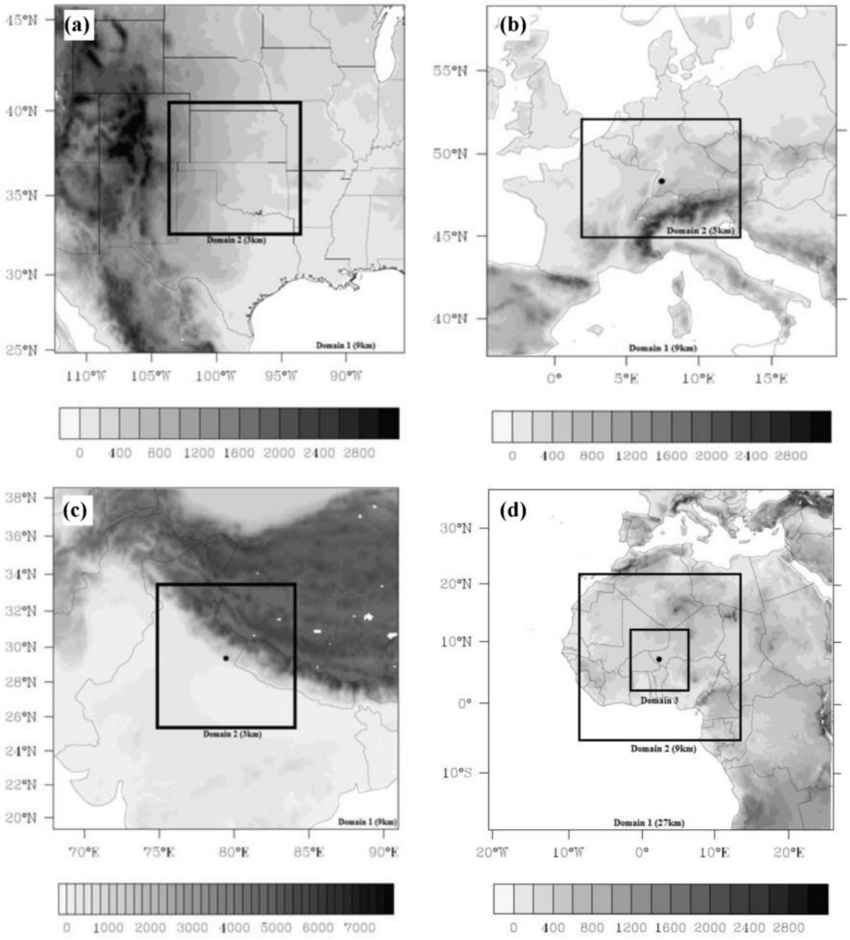

Fig. 3.1 Topography maps of the nested model domains over the (a) U.S. southern Great Plains (SGP), (b) Europe, (c) India, and (d) West Africa.

3.2.2.2 Europe

The second study region is over Europe and also has two-way nested domains of 9 km (250 × 240 grid points) and 3 km (307 × 274 grid points) grid spacing that cover most of Germany (Fig. 3.1b). The three dominant land types in the European domain are forest, arable land and permanent crops, and pastures and mixed mosaics. This region is complex with various mountainous terrains that affect regional circulation patterns and result in large amounts of orographic precipitation, particularly in the summertime. Because of the complex link between convective processes and orography, this domain is relatively difficult to simulate (Wulfmeyer et al. 2008).

3.2.2.3 Northern India

The third domain is set up over India using the two-way nesting with 250 × 240 grid points at 9 km horizontal grid spacing for the outer domain and 307 × 274 grid points with 3 km horizontal grid spacing for the inner domain (Fig. 3.1c). India is a typical monsoon region where heavy rain events and mesoscale convection are predominantly associated with monsoon rainfall. The major land-cover types over the Northern India domain are forest and agricultural land.

3.2.2.4 West Africa

The fourth domain covers West Africa (Fig. 3.1d). As this region is much larger than the previous three regions, we configure the model with two nested domains: a coarse mesh of 300 × 300 grid points with 27 km horizontal grid spacing, and 2, two-way nested domains of 433 × 433 grid points with 9 km, and 631 × 631 grid points with 3 km, respectively. The primary land-cover types are forest, cropland, woodland and shrubland, grassland, and bare soil.

3.2.2.5 Model configuration

We recognize that different model schemes and physical options may perform differently over different regions. For example, Bukovsky and Karoly (2009) found that the Kain-Fritsch (KF) scheme performed better over the U.S. in terms of mean precipitation, while Flaounas et al. (2011) pointed out that the combination of the KF scheme and the Mellor-Yamada-Janjic (MYJ) PBL scheme provided the best simulation of the West Africa monsoon. Similarly Venkata Ratnam and Cox (2006) reported that the KF scheme simulated more realistic moisture profile and rainfall distribution over India. To constrain the confounding variables in understanding the model response to study the regional sensitivity of the C_{zil} values, we use the same physical options to conduct model simulations over the four selected regions. The predominant physical options in the 9 and 3 km nests included: (a) The Goddard microphysics scheme which includes ice, snow and graupel processes and is suitable for high-resolution simulations (Tao, Simpson and McCumber 1989). (b) The KF scheme, which is a deep and shallow convection sub-grid scheme using a mass flux approach with downdrafts and CAPE removal time scale (Janjic 1994, 2000). (c) The MYJ PBL scheme (Janjic 2002), which is used together with the Eta similarity theory surface layer. The ability to represent moisture entrainment into the lower atmosphere within this local-closure PBL scheme provides more realistic convection triggering with the KF scheme. (d) The Noah LSM (Chen and Dudhia 2001), which has a single vegetation canopy layer and simulates soil moisture and temperature for four soil layers with the depth of 0.1, 0.3, 0.6, and 1.0 m respectively. Longwave radiation is based on the Rapid Radiative Transfer Model (Mlawer et al. 1997), while the shortwave radiation only considers a downward beam (Dudhia 1989). The surface layer scheme is used to determine the exchange coefficient which links surface heat and moisture fluxes to the LSM and the PBL.

3.2.3 Data for model case studies

We employed AmeriFlux data and the International H_2O Project 2002 (IHOP_2002) field campaign data as verification datasets. The AmeriFlux sites produce a full suite of relatively long-term measurements of the meteorological variables and exchange rates of surface heat fluxes, with the knowledge of ecosystem and the history of land use and land cover changes. The IHOP_2002 field campaign was conducted with an objective of improving convective initiation predictions and quantitative precipitation forecasts in NWP models. The field data provide continuous complete measurement of surface fluxes, near-surface meteorological variables, and soil conditions during the late spring and early summer of 2002 (Weckwerth and Parsons 2006; LeMone et al. 2008).

The experiments over Europe were carried out with data gathered during the Convective and Orographically-induced Precipitation Study (COPS) field campaign for the time period from 21 to 23 July 2007. The locations of the COPS field experiment are between southern Germany and eastern France. The Atmospheric Radiation Measurement (ARM) Mobile Facility (AMF) was deployed in the Black Forest region of Germany to capture the convection and orographic rainfall processes in the complex mountainous terrain. More details about the COPS field campaign can be found in Wulfmeyer et al. (2008).

Unlike the U.S. and European domains, the Indian domain has limited publicly available observations and conspicuously lacks flux measurements. There are only 15 observations within the inner domain. Therefore, we resort to using the radar reflectivity, atmospheric soundings, and the area-averaged bias of temperature, moisture, and wind speed to evaluate the model results. Similarly, there are limited surface sites, instrumentation, or spatial and temporal sampling as part of *in situ* field experiments over the region of West Africa. However, because of the ARM Mobile Facility (AMF) deployment in Niamey, Niger, West Africa as part of the African Monsoon Multidisciplinary Analysis (AMMA) field phases and observing periods (Redelsperger et al. 2006), there is an accessible meteorological dataset. Data from the Tropical Rainfall Measuring Mission (TRMM) precipitation [3B42 and *TRMM* Multi-satellite Precipitation Analysis (TMPA)] are also used for both the Indian and African model studies. All observed atmospheric soundings from selected weather stations over these four study regions are obtained from the University of Wyoming (http://weather.uwyo.edu/upperair/sounding.html).

3.3 Land-atmosphere coupling method and C_{zil} experiments

Detailed land-surface representation is essential for realistic model forecasts (Holt et al. 2006; Niyogi et al. 2006). The key parameters associated with a LSM include sensible and latent heat fluxes which control the diurnal evolution and development of the PBL (Trier et al. 2011). In the Noah LSM (Chen and Dudhia, 2001; Ek et al. 2003) the surface sensible (H) and latent (LE) heat fluxes are determined through the bulk aerodynamic method as:

$$H = \rho C_p C_h |U| (\theta_s - \theta_a) \tag{3.1}$$

$$LE = \rho C_q |U| (q_s - q_a) \tag{3.2}$$

where ρ is the air density, C_p is the specific heat of air at constant pressure, $|U|$ is the wind speed, θ_a and q_a are the air potential temperature and the air specific humidity at the lowest model level or at a specific measurement height above the ground (i.e., 2 m), and θ_s and q_s are the surface potential temperature and the surface specific humidity. The parameters C_h and C_q are the surface exchange coefficients of sensible heat and latent heat fluxes, and in the surface layer parameterization C_q is assumed to equal to C_h which controls the total heat flux inputs into the models' lower atmospheric layer.

Within the Noah LSM, the roughness length for moisture and heat, z_{ot}, is calculated according to Zilitinkevich (1995) and expressed as

$$z_{ot} = z_{om} \exp(-kC\sqrt{R_e}) \tag{3.3}$$

$$R_e = \frac{u_0^* z_{om}}{\upsilon}$$

where z_{om} is the roughness length for momentum, R_e is the roughness Reynolds number, k = 0.4 is the von kármán constant, υ is the kinematic molecular viscosity, u_0^* is the surface friction velocity, and C (thereafter C_{zil}) is an empirical constant, which is set to 0.1 by default in the existing Noah LSM.

The C_{zil} term controls the ratio of z_{ot}/z_{om} , and the roughness lengths for momentum and heat are used to compute C_h based on Monin-Obukhov similarity theory in surface layer parameterization as:

$$C_h = \frac{k^2/R}{\left[ln\left(\frac{z_a}{z_{om}}\right)-\psi_m\left(\frac{z_a}{L}\right)+\psi_m\left(\frac{z_{om}}{L}\right)\right]\left[ln\left(\frac{z_a}{z_{ot}}\right)-\psi_h\left(\frac{z_a}{L}\right)+\psi_h\left(\frac{z_{ot}}{L}\right)\right]} \qquad (3.4)$$

where L is the Obukhov length, z is the height above the ground, R is the Prandtl number, and $\psi_m$and ψ_h are stability functions (Stull 1988). In the Monin-Obukhov equation, z_{om} is the height at which the average wind goes to zero and scalars at $z_a < z_{om}$ are assumed to be transported by molecular processes, z_{ot} is the height at which the air temperature equals to the soil surface temperature. In convective conditions, the z_{ot}/z_{om} ratio has been demonstrated to impact surface fluxes more effectively than the treatment to Monin-Obukhov based stability functions (Chen et al. 1997).

The surface coupling strength C_{zil} relies on the surface exchange coefficient C_h. Smaller values of C_{zil} generate larger z_{ot} which indicates a rougher surface for heat and moisture, resulting in stronger turbulence and larger C_h. Therefore, smaller C_{zil} is indicative of stronger surface coupling. The values of C_{zil} are assumed to vary from 0.01 (strong coupling) to 1.0 (weak coupling) (Chen et al. 1997). It has been shown that the adjustment of C_{zil} can contribute towards the improvement of model estimates of improved surface fluxes at least for the U.S. SGP during the summer (Moncrieff et al. 2004; Gutmann and Small 2007; LeMone et al. 2008). Chen and Zhang (2009) reevaluated the surface exchange coefficients using multi-year AmeriFlux data and obtained C_{zil} values that are vegetation type dependent. They dynamically linked C_{zil} as a function of canopy height h (m) and represented it as:

$$C_{zil} = 10^{(-0.4h)} \tag{3.5}$$

These results motivate the need for investigating the impacts of C_{zil} on mesoscale land-atmospheric convection simulations over typical vegetation types and different regions. Experimental details of all experiments and related C_{zil} values are shown in Table 3.2.

Table 3.2 Summary of the coupling experiments

Case name	**Coupling coefficient (C_{zil})**	**Experimental focus**	**Regions**
UN	0.1, 0.5, 0.8	Uncoupled Noah LSM based simulated surface heat fluxes	U.S. SGP
BG BC BF	0.1, 0.3, 0.5, 0.8, 1.0	Bulk aerodynamic coefficient of heat (C_h) over U.S. SGP	Grassland Cropland Forest
CS CE CI CA	0.01, 0.05, 0.1, 0.3, 0.5, 0.8, *var*	Surface fluxes, 2 m temperature and moisture, vertical profiles of temperature, moisture, and wind speed, etc.	U.S. SGP Europe India West Africa

UN refers to uncoupled runs; B refers to uncoupled experiments for bulk C_h for grass (BG), cropland (BC), and Forest (BF). C refers to coupled runs over U.S. SGP (CS), Europe (CE), India (CI), and West Africa (CA).

3.4 Model verification and comparisons

3.4.1 Impact of the "C_{zil}" on the offline Noah LSM

We first analyze impacts of the surface coupling strength coefficient on surface heat fluxes within the offline or uncoupled experiments (UN). To obtain better surface fluxes and equilibrium soil conditions at small scales, 18-month-long HRLDAS runs with three different C_{zil} values (0.1, 0.5, and 0.8) were conducted as spinup for offline Noah land model experiments.

Fig. 3.2 shows a snapshot of the model output for the three different C_{zil} values (referred to as runs UN0.1, UN0.5, and UN0.8) and the impact on surface heat fluxes at the very end day of the HRLDAS 18-month-long simulations (1800 UTC on 2 June 2002). The area-averaged value of H decreases from 334 W m^{-2} to 205 W m^{-2} when the surface coupling strength changes from 0.1 to 0.8. However, the area-averaged LE has small variations, which are 2 W m^{-2} differences between UN0.1 and UN0.5 and 25 W m^{-2} differences between UN0.5 and UN0.8. It is noted that the influence of C_{zil} on LE is small compared to that on H. This is possibly due to the manner in which LE is computed as the residual of the energy balance, suggesting that the offsets between decreased net radiation and increased ground heat flux due to increasing C_{zil} and the decrease in H are small. Results also indicate that with increasing C_{zil}, the coupling strength becomes weak, resulting in less rough surface for heat/moisture, and the simulated surface fluxes are less spatially heterogeneous.

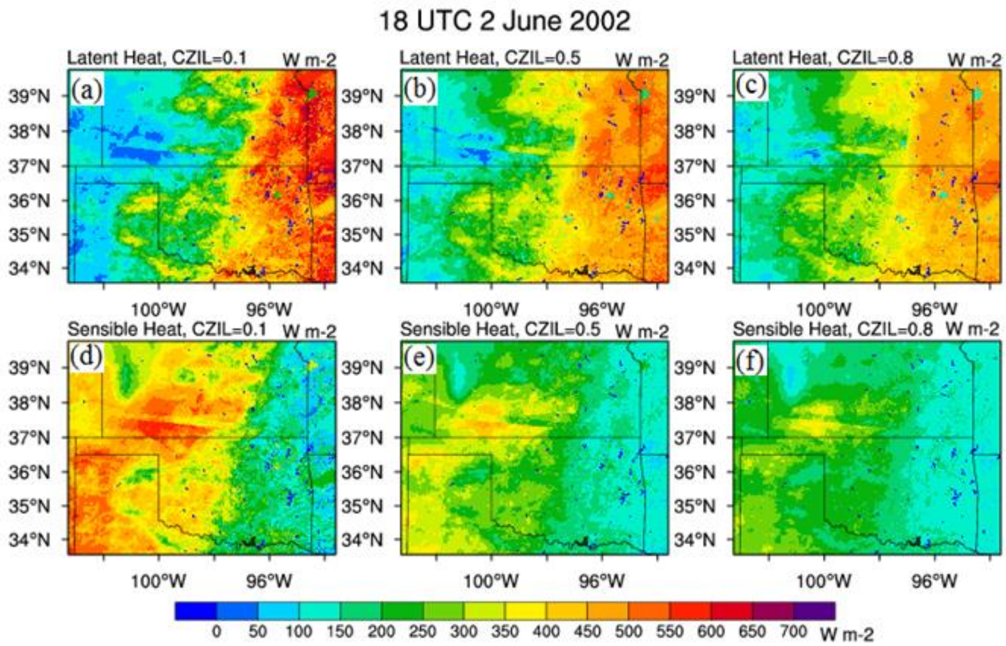

Fig. 3.2 A snapshot of cases (UN0.1, UN0.5, and UN0.8) with three different C_{zil} values and resulting impacts on latent heat flux (W m^{-2}) (upper row) and sensible heat flux (W m^{-2}) (bottom row) at 1800 UTC for 2 June 2002.

The diurnal surface heat fluxes are averaged from 1 to 25 June 2002 over three different land covers (grassland, cropland, and forest) in the U.S. SGP. As seen in Fig. 3.3, there are small differences between the observed and modeled temporal-averaged *LE* over grassland and cropland, but large impacts have been found on *H*. This may be caused by drier soils in these locations which allow greater *H* changes in the simulations (Trier et al. 2011). The observed *H* lies between the model experiments of UN0.1 and UN0.5 over grassland and cropland. The surface coupling strength has a notable effect on estimating heat fluxes over the forest land cover, where the maximum difference between the averaged observed and modeled surface fluxes is about 96.9 W m^{-2} for *LE* and 66.5W m^{-2}

for *H*. In spite of these relatively large impacts on heat fluxes over forest, the observed and modeled *LE* of UN0.1 are comparable, while *H* from UN0.8 is in better agreement with the observed data, indicating that only over a forest land cover the surface coupling strength of *LE* is stronger than that of *H*.

To further analyze the land-atmosphere coupling strength over the three different land-cover types, experiments were conducted with a broader range of C_{zil} values. These experiments are labeled as BG, BC, and BF. As seen in Fig. 3.4, C_{zil} values lead to different soil temperature and soil moisture fields. Higher soil moisture and warmer surface leads to higher *LE* due to more surface evaporation and transpiration. The impacts of soil moisture on surface heat fluxes are more significant on grassland and cropland when the soils are drier and not saturated. Smaller differences caused by coupling strength can be seen in soil moisture in the forest region, but the soil temperature differences are significant and affect *LE*. For example, the higher soil temperature leads to smaller *LE* and less surface evaporation into atmosphere.

Table 3.3 Comparisons of surface exchange coefficient of heat (C_h) between observation and model runs with different C_{zil} values over three vegetation types in U.S. SGP. The results are temporally averaged for June 2002.

Veg Types/ Observational Site	Observation	C_{zil}=0.1	C_{zil}=0.3	C_{zil}=0.5	C_{zil}=0.8	C_{zil}=1.0
Grassland (h < 1m)	0.0025	0.058	0.030	0.020	0.013	0.011
Cropland (h = 3m)	0.019	0.040	0.022	0.017	0.011	0.009
Forest (h = 25m)	0.037	0.042	0.016	0.010	0.003	0.001

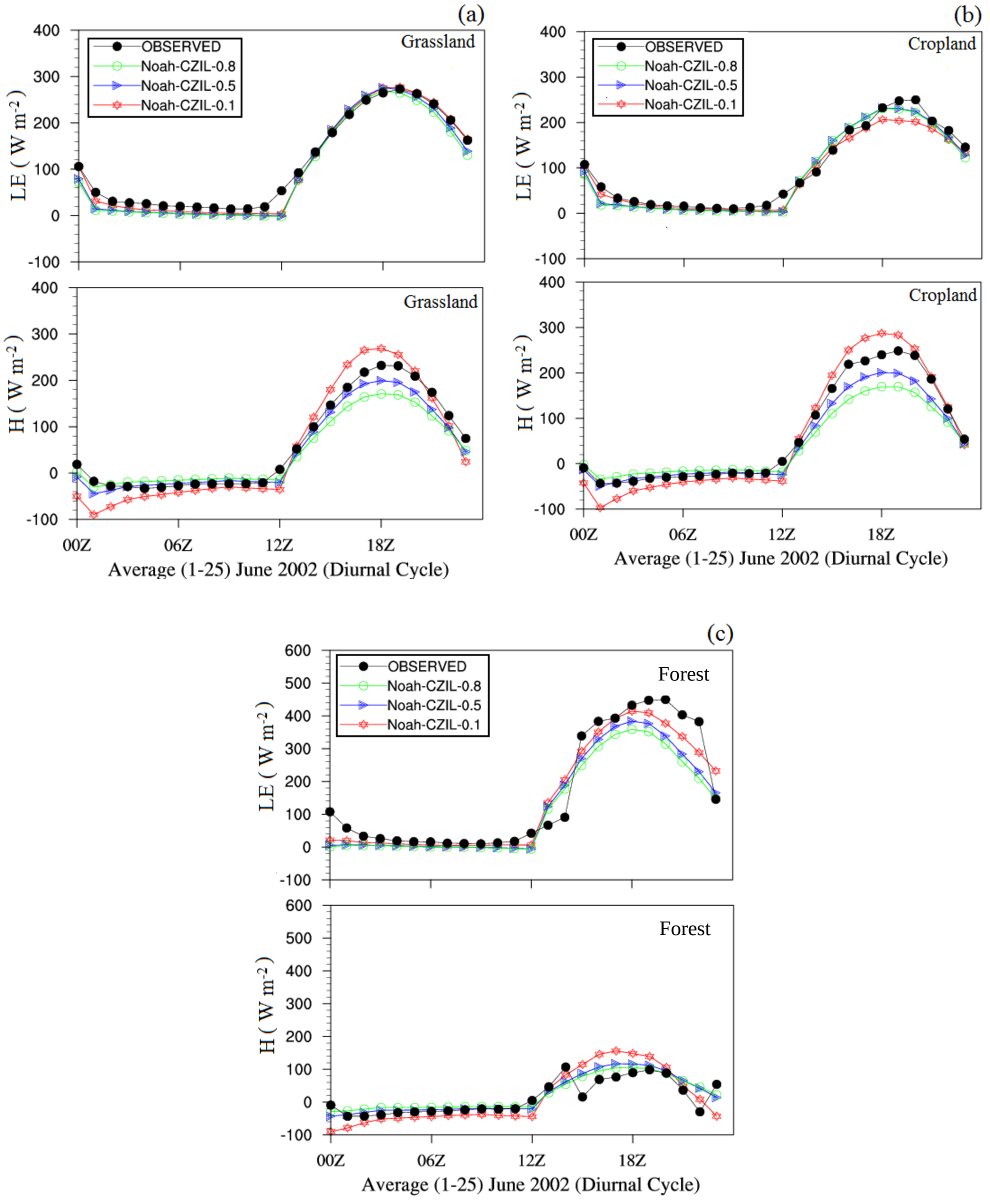

Fig. 3.3 Comparisons of 25 day-averaged surface latent heat flux (W m^{-2}) and sensible heat flux (W m^{-2}) between observation and offline experiments over (a) grassland, (b) cropland, and (c) forest in U.S. SGP.

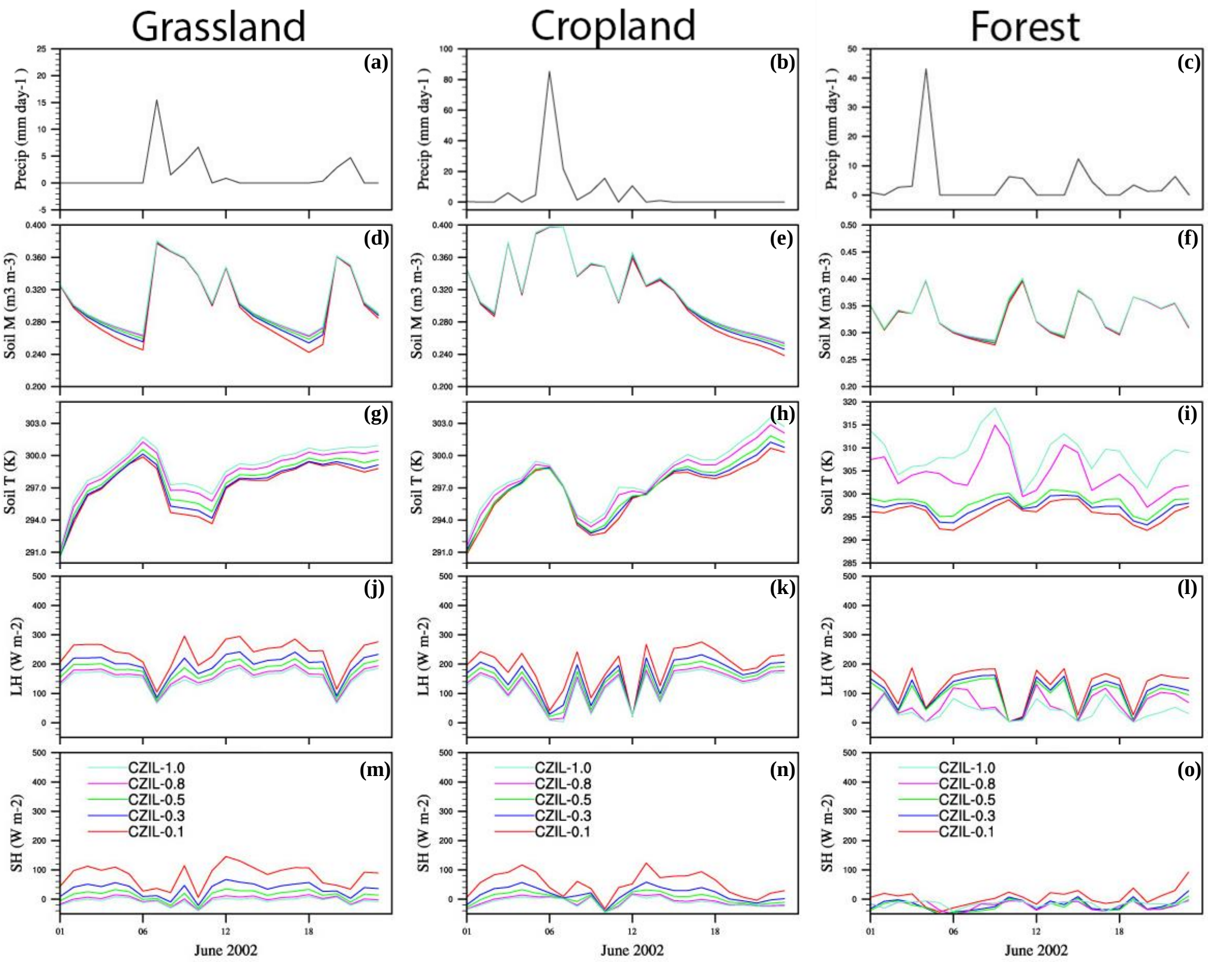

Fig. 3.4 Variations of averaged-daily simulated surface variables: (a-c) precipitation forcing (mm day^{-1}), (d-f) surface soil moisture (m^3 m^{-3}), (g-i) surface soil temperature (K), (j-l) latent heat flux (W m^{-2}), and (m-o) sensible heat flux (W m^{-2}) from offline Noah experiments over grassland (left column), cropland (middle column), and forest (right column).

The C_h, which is directly related to the coupling strength and controls the total energy flux, is evaluated to explore the land-atmosphere coupling strength. Using Eq. 3.1, the surface exchange coefficient, C_h, can be written as

$$C_h = H / \rho C_p |U| (\theta_s - \theta_a) \tag{3.6}$$

The IHOP_2002 experiment provided 30-minute observed surface data, including sensible heat flux, wind speed at 10 m, surface temperature, air temperature, downward solar radiation, and outgoing longwave radiation. Using observed air temperature and outgoing longwave radiation, θ_a and θ_s are calculated. These 30-minute data are then used to compute C_h which is referred to as observed C_h. The observed and offline Noah modeled C_h are then averaged from 1700 UTC to 2100 UTC in June 2002 to obtain midday values, the results of which are shown in Table 3.3 and Fig. 3.5. It can be seen that BG0.1, BC0.1, and BF0.1 have large averaged-daily variations of C_h. The modeled C_h of BG1.0 over the grass site located at Elmwood, OK (36.62°N, 100.62°W) is in better agreement with the observations. Over the Bondville, IL, a cropland site (40.00°N, 88.29°W, Table 3.3), the averaged value of C_h for BC0.5 is the closest to the observed C_h. The primary vegetation type in the Ozark, MO site (38.74°N, 92.20°W) is deciduous broadleaf forest land cover with typical plant height at 25 m. Tall vegetation sites, such as forest, have rougher surfaces and results in stronger turbulence and the observed C_h has large variability over the forest. The differences between air and surface temperatures which have effects on limiting the flux of net radiative heat transfer from the atmosphere to the soil are larger. Since the calculation of observed C_h is affected by the differences between potential surface and air temperatures, the observed C_h has large variability over the forest. The larger roughness also leads to larger C_h, indicating that the surface coupling effects in forest area are stronger. The result shown in Fig. 3.5c suggests a relatively good agreement between the modeled C_h of BF0.1 and the observation corresponds well. Thus, consistent with prior results, it is concluded that a constant value of C_{zil} cannot provide good agreement across different land-cover types in the version of the Noah LSM being used in WRF.

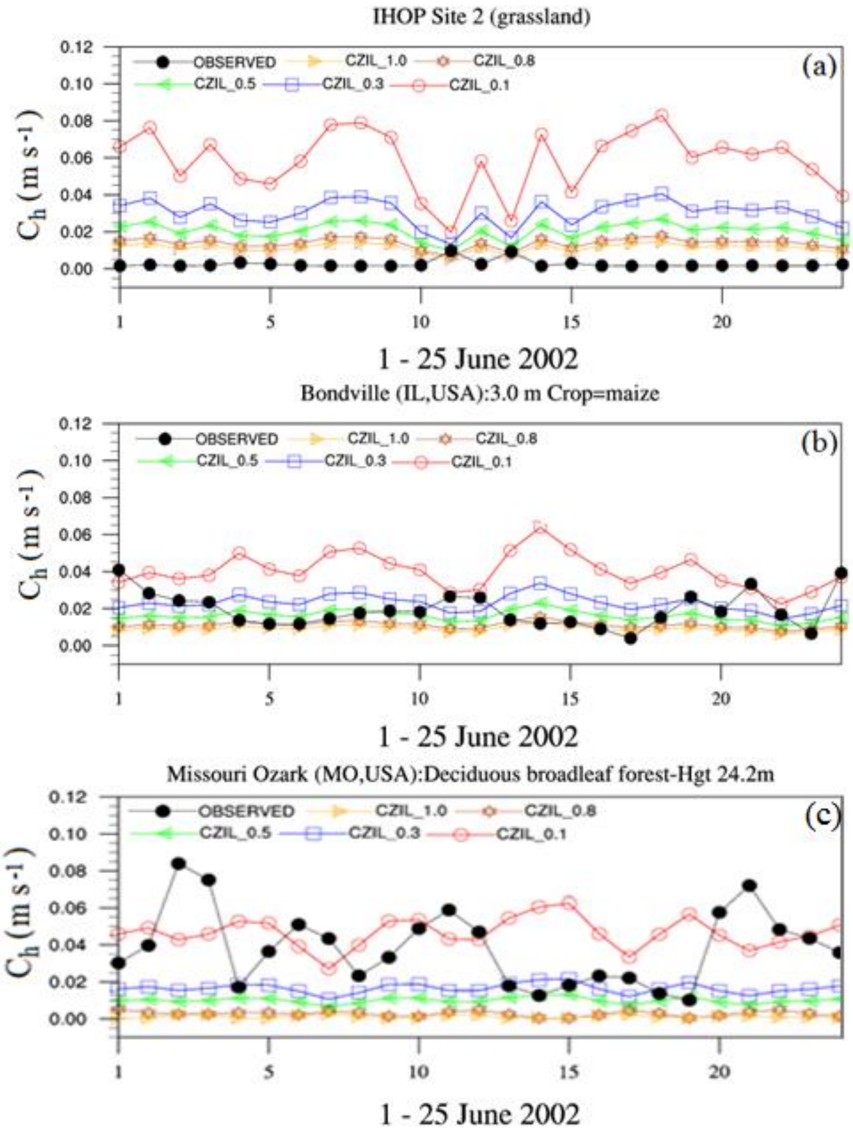

Fig. 3.5 Comparisons of midday values of C_h (m s^{-1}) averaged from 1700 UTC to 2100 UTC in June 2002 between observation and offline experiments: (a) BG, (b) BC, and (c) BF.

3.4.2 The impacts of the C_{zil} coupling parameter on the WRF-Noah model

The impacts of the coupling strength, especially the dynamic vegetation type-dependent coupling strength ($C_{zil\text{-}var}$) (Table 3.2), on convective WRF-Noah model simulations are investigated next. The experiments are over different hotspot regions (U.S. SGP, Europe, northern India, and West Africa) with different surface coupling strength. Impacts of surface coupling strength on surface and boundary layer variables such as surface heat fluxes, 2 m temperature and moisture, 10 m wind speed, precipitation, PBL soundings, are then analyzed and discussed.

3.4.2.1 U.S. SGP

(a) Surface flux analysis

Model simulations covering a 48-hr period were conducted with a variety of C_{zil} values initialized at 1200 UTC 12 June 2002. To study atmospheric feedback to surface coupling strength following spinup, the results in Fig. 3.6 show the second day runs over grassland and cropland simulated 24 hrs after the initial condition. The experiments with the weak coupling strength (CS0.8) have better match with the observations (Fig. 3.6), but the coupling strength once again modestly affects *LE* values over cropland. The runs CS0.8 over both grassland and cropland match the observed *H*. Rainfall modifies soil moisture and leads to higher *LE*. The increased *LE* is accompanied with a decreased *H* from the surface, indicating a smaller C_h, and hence weaker coupling strength of *H*. In response to the weak coupling strength the surface air temperature is increased as less *H* is transported from the surface, resulting in an increase in ground heat flux. As a result, the weak coupling strength runs overestimate the soil surface temperature and the maximum difference is about 5 K between runs with CS0.01 and CS0.8 at 0000 UTC. It is noted that the surface coupling strength can also directly affect soil surface temperature, and the stronger coupling strength reduces the modeled skin temperature.

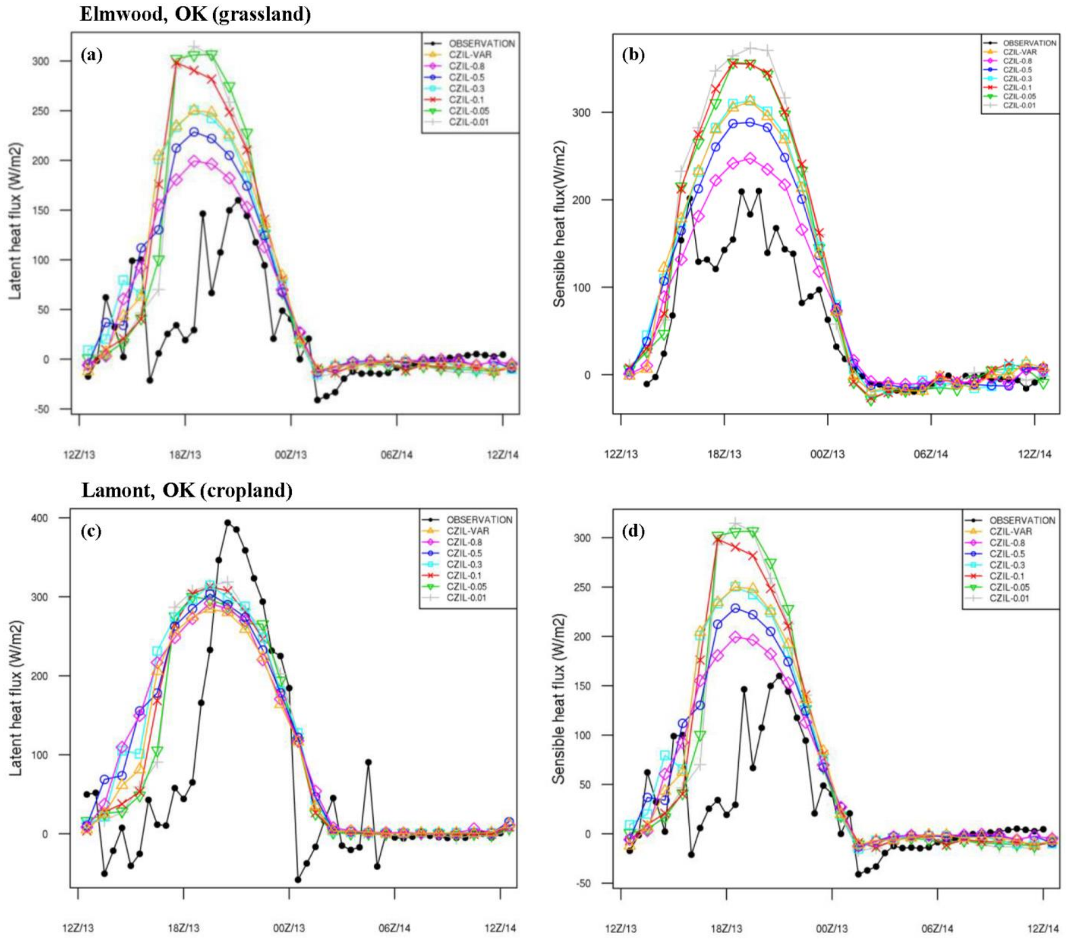

Fig. 3.6 Comparisons of surface heat fluxes (W m^{-2}) between the 24-48 hr CS experiments initialized at 1200 UTC 12 June 2002 and the observation over (a-b) grassland (Elmwood, OK, 36.62°N, 100.62°W) and (c-d) cropland (Lamont, OK, 36.61°N, 97.49°W).

(b) 2 m temperature and humidity and 10 m wind speed analysis

Area-averaged analysis is used to evaluate the bias and RMSE errors for 2 m temperature and moisture. In the 3 km grid spacing domain there are about 200 observation points. A majority of the observed data is from NCEP Automated Data Processing (ADP) Global Upper Air and Surface Weather Observations and obtained from meteorological sites with 6 hrs temporal resolution. The satellite wind data is obtained from the National Environmental Satellite Data and Information Service (NESDIS).

Table 3.4 Biases and RMSE of 2 m temperature (T), 2 m moisture (Q), and 10 m wind speed (WSPD) for 0-48 hr model forecasts over U.S. SGP at 3-km grid spacing

Coupling coefficient (C_{zil}) case	**Bias**			**RMSE**		
	2 m T (K)	*2 m Q (10^{-3}×kg kg^{-1})*	*WSPD (m s^{-1})*	*2 m T (K)*	*2 m Q (10^{-3}×kg kg^{-1})*	*WSPD (m s^{-1})*
CS0.01	-3.27	0.41	1.49	4.09	2.13	3.49
CS0.05	-3.16	0.30	1.63	4.01	2.08	3.47
CS0.1	-3.01	0.22	1.40	3.90	2.05	3.48
CS0.3	-2.67	-0.02	1.43	3.69	2.03	3.47
CS0.5	-2.47	-0.18	1.35	3.62	2.05	3.35
CS0.8	-2.36	-0.37	1.29	3.65	2.12	3.20
CSvar	-3.04	0.20	1.53	3.93	2.09	3.38

Table 3.4 shows the mean bias and RMSE of 2 m temperature and moisture, and 10 m wind speed for the 0-48 hr model forecasts. All model runs show cold biases, with CS0.01 and CSvar show the largest cold biases in the surface layer. This is a result of strong surface coupling strength causing more *H* being lost from the surface leading to a cooler surface. The bias and RMSE of 2 m temperature increase as the coupling strength became stronger, and the 2 m moisture of CS0.01, CS0.05, and CS0.1 show wet biases. The coupling coefficients in CS0.3, CS0.5, and CS0.8 lead to dry biases and the smallest bias of the 2 m moisture occurs in CS0.3. The impact of the surface coupling strength on the 10 m winds is relatively small.

(c) Planetary Boundary Layer: Temperature, Humidity and Wind speed profile

The area-averaged statistical analyses are conducted using soundings and the impacts of C_{zil} on PBL are evaluated. The vertical profile is analyzed from 1000 to 700 hPa since majority of the impact is within the boundary layer. Fig. 3.7a shows that all the experiments have cold biases in the vertical and CS0.8 has the smallest temperature bias below 900 hPa but the largest bias above it. Thus, weak coupling strength leads to stronger vertical temperature gradients. CS0.01 and CSvar show similar temperature biases and good agreement with specific humidity profiles (Fig. 3.7b) up to the 850 hPa level. The influence of the surface coupling strength on the vertical profiles of temperature and humidity is notable in the different experiments, and the impacts are the highest in the surface layer on specific humidity. The wind speed vertical profile in Fig. 3.7c indicates that the largest difference, 0.5 m s^{-1}, occurs at the 925 hPa level, and once again the surface coupling strength appears to have insignificant impacts on the wind speed.

Table 3.5 Area-averaged accumulated precipitation (mm) over U.S. SGP at 3-km grid spacing

Coupling coefficient (C_{zil}) case	**Rainfall (mm)**
CS0.01	22.21
CS0.05	22.16
CS0.1	22.17
CS0.3	21.29
CS0.5	20.21
CS0.8	18.86
CSvar	21.59
STAGE-IV	22.93

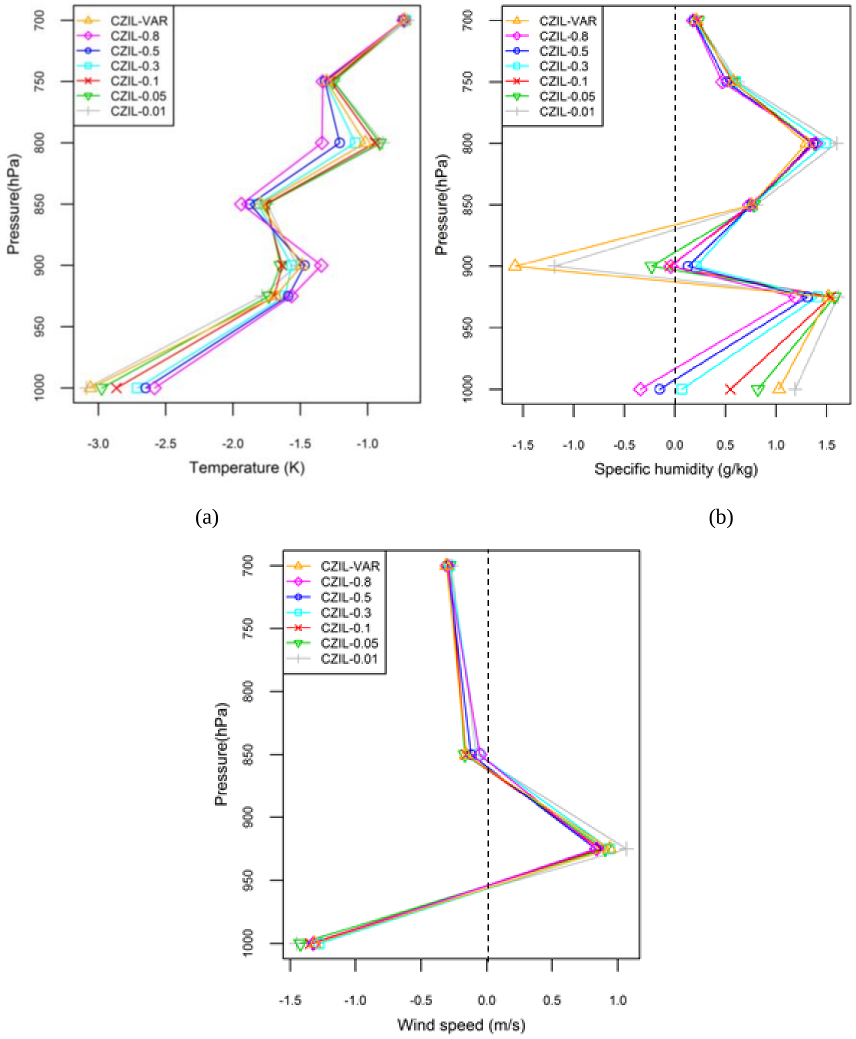

(a)

(b)

(c)

Fig. 3.7 Vertical profiles of area-averaged bias over the U.S. SGP 3-km grid spacing domain at 1800 UTC 12 June 2002 (a) temperature (K), (b) specific humidity (10^{-3} × kg kg^{-1}), and (c) wind speed (m s^{-1}).

(d) Precipitation

The area-averaged accumulated precipitation for the 48 hrs forecasts initiated at 1200 UTC 12 June 2002 is summarized in Table 3.5. The strongest coupling strength of CS0.01 leads to the largest amount of area-averaged accumulated precipitation. CS0.01 also shows close agreement of accumulated area-averaged precipitation to the observation, and the amount of rainfall for CSvar and CS0.3 are similar to each other. Since heavier rainfall is obtained by increasing the coupling strength through decreased values of C_{zil}, it is possible that the model's ability to correctly simulate rainfall can be tuned through surface coupling coefficient, particularly in areas where there is a known bias with convection triggering and rainfall under prediction. The weak coupling tends to produce weak convective system with less precipitation whereas the strong coupling results in more water vapor into the atmosphere and ultimately more precipitation. Interestingly, the coupling strength does not appear to affect the timing of the peak rains, and only alters the amount of the precipitation. These results need to be examined with a larger ensemble of CP experiments, but are consistent to those reported in Trier et al. (2011) for the U.S. SGP.

To further explore the impact of C_{zil} on precipitation, 3 hr (0000 UTC - 0300 UTC 13 June 2002) accumulated precipitation (Fig. 3.8) was analyzed. The experiments with constant C_{zil} values have similar precipitation patterns in the U.S. SGP domain. Results again highlight that the constant surface coupling strength does not affect the general location but only the magnitude of the simulated precipitation. However, the dynamic C_{zil} improves both the pattern and location of the simulated precipitation in our experiments. For instance, results show that the 3 hr accumulated precipitation of $C_{zil\text{-}var}$ has a better spatial agreement to the STAGE-IV observed precipitation than those of the constant values in the northern part of Texas. Therefore, the dynamic C_{zil} shows promising potential for improving the simulation of warm rain quantitative forecast over the U.S. SGP.

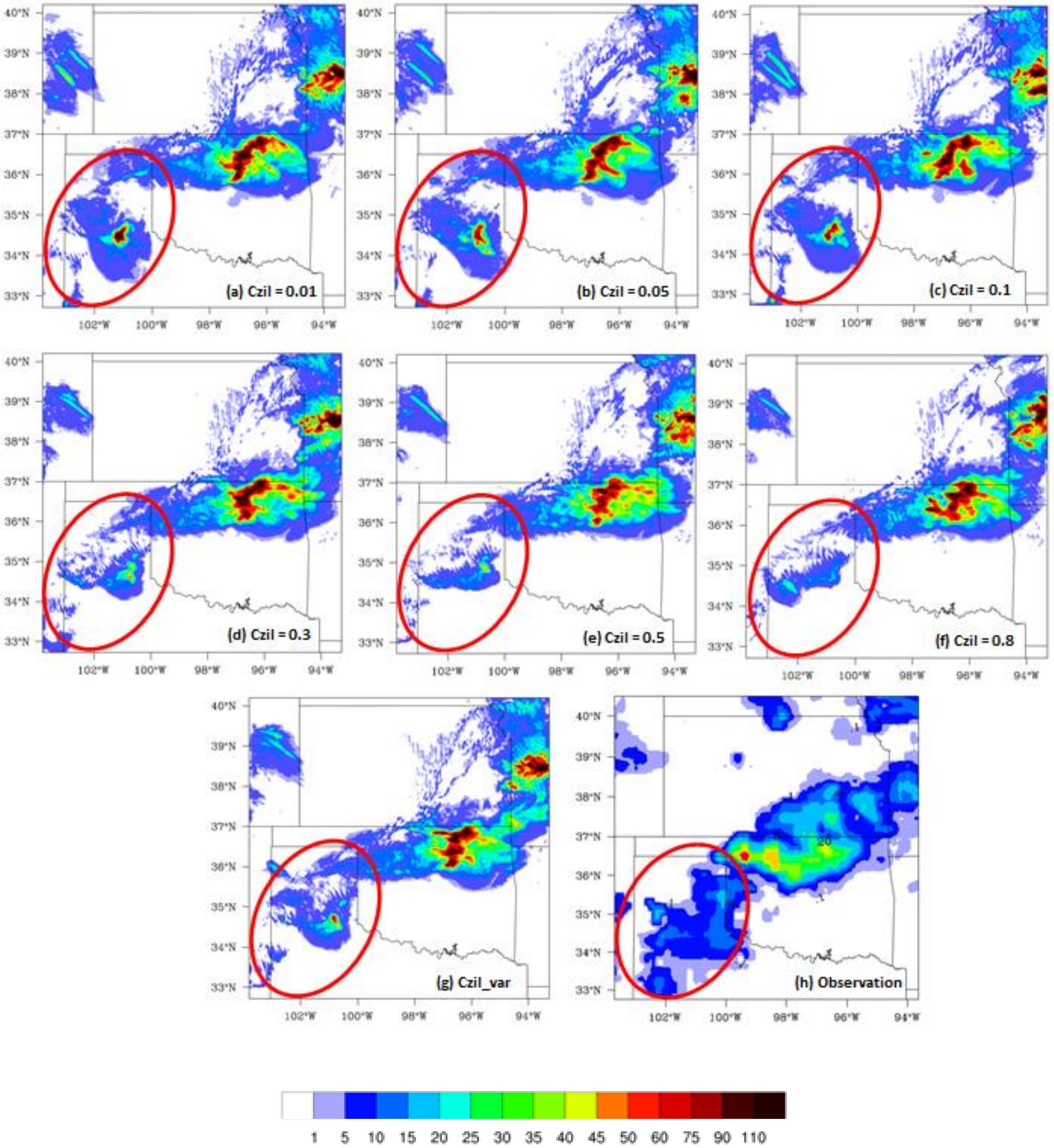

Fig. 3.8 Comparisons of the 3 hrs accumulated precipitation (0000 – 0300 UTC) on 13 June 2002 over the U.S. SGP 3-km grid spacing domain between the model forecasts with (a) C_{zil} = 0.01, (b) C_{zil} = 0.05, (c) C_{zil} = 0.1, (d) C_{zil} = 0.3, (e) C_{zil} = 0.5, (f) C_{zil} = 0.8, (g) dynamic $C_{zil\text{-}var}$, and (h) the STAGE-IV observed precipitation.

3.4.2.2 Europe

(a) Analysis of surface flux, 2 m temperature, and friction velocity

The surface flux observations used for the European domain correspond to Black Forest, Germany (48.54°N, 8.397°E) and are centered in the 3 km grid spacing model domain (Fig. 3.1b). The study region is characterized by significant amounts of orographic rainfall in summer. The flux analysis shows that CE0.1 and CEvar have similar *LE* (Fig. 3.9a), but the simulated *LE* with the weak coupling strength of CE0.8 leads to about 22 $\mathrm{Wm^{-2}}$ reduction than that with the strong coupling strength of CE0.05. The mean of the 24 hrs observed *LE* is 50.77 $\mathrm{W\ m^{-2}}$, and CE0.3 (52.50 $\mathrm{W\ m^{-2}}$ for *LE*) is found to be close to the observation. The mean of *LE* for the dynamic C_{zil} experiment (58.66 $\mathrm{W\ m^{-2}}$) shows better agreement with the observation than that for CE0.8 (38.26 $\mathrm{W\ m^{-2}}$), but the dynamic C_{zil} experiments do not improve the simulated *LE*. Majority of the model simulations overestimated *H* before evening (1800 UTC, 7 pm local time). During the night time after 1800 UTC, model forecasts of *LE* have good agreement with the observations, and *H* for CE0.3, CE0.5, and CE0.8 agree well with observations. The overestimation of *LE* from the model leads to more moisture in the surface layer and decreases the 2 m temperature. As a result, the 2 m temperature is underestimated by 2-5 K in all C_{zil} experiments (Fig. 3.9c). The 10 m wind speed again indicates that surface coupling strength has little impact on the surface wind speed.

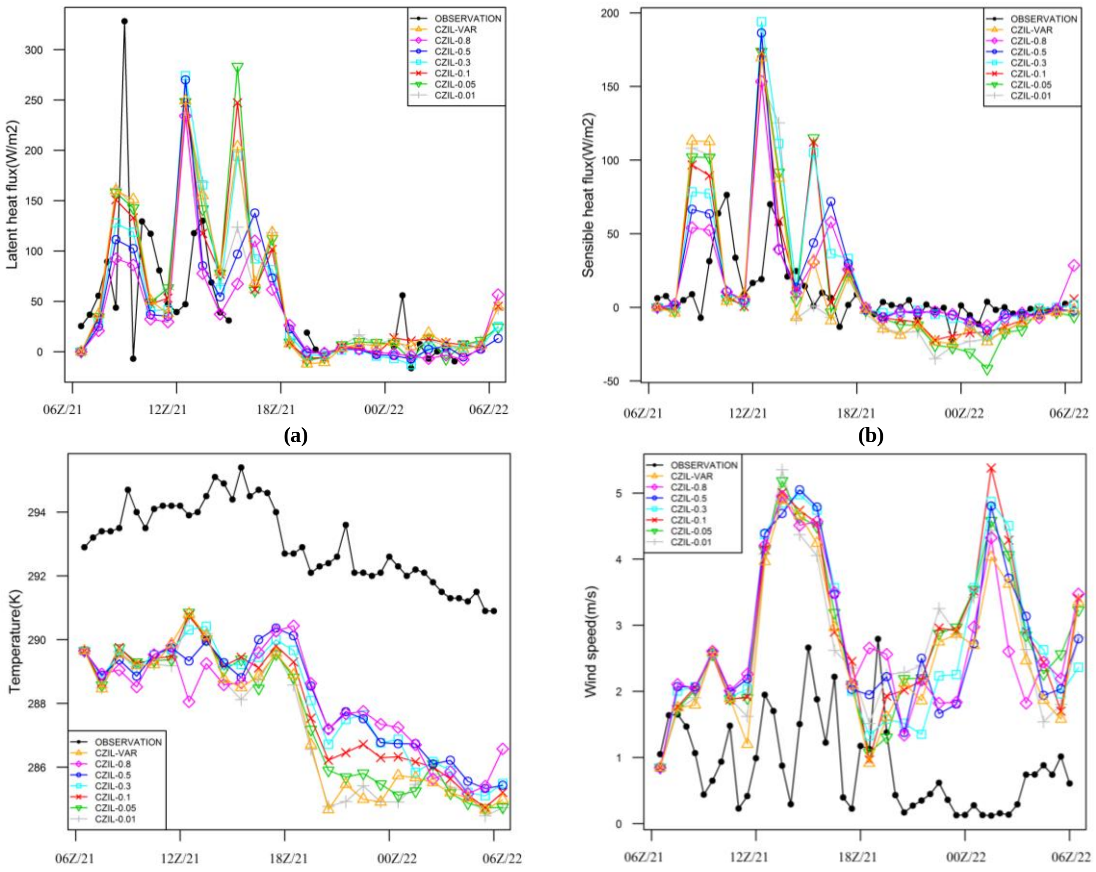

(a) (b)

(c) (d)

Fig. 3.9 Comparisons between the 0-24 hr CE experiments initialized at 0600 UTC 21 July 2007 and the observation of (a) latent heat flux (W m^{-2}), (b) sensible heat flux (W m^{-2}), (c) surface temperature (K), and (d) wind speed (m s^{-1}), at Black Forest, Germany (48.54°N, 8.397°E).

(b) Analysis of 2 m temperature and specific humidity, 10 m wind speed, and precipitation

The area-averaged analysis is conducted based on data from nearly 200 stations in the 3-km grid spacing domain. In Fig. 3.10a, the 2 m specific humidity bias suggests that during 1200 - 0000 UTC the surface coupling strength of CE0.01, CE0.05, CE0.1, and the dynamic coupling strength of CEvar lead to more moisture, while the moderate and the weak surface coupling strength coefficients of CE0.5 and CE0.8 produce drier boundary layer. The model simulated moisture is improved for CE0.3. Fig. 3.10b shows that there is about a 1-4 K 2 m temperature cold biases in all the experiments. Reductions in the temperature bias are noted for the moderate and the weak coupling strength of CE0.5 and CE0.8. CE0.1 which is the default coupling coefficient in current WRF model shows similar 2 m temperature and moisture biases to CEvar, but both of them fail to improve surface temperature and moisture. The 10 m wind speed was also analyzed and the biases of the different coupling strength increased before 1800 UTC when a heavy rainfall occurred and then the biases decreased in the evening. The similarity of patterns in Fig. 3.10c corresponds well to our previously stated conclusion for other regions that the surface coupling appears to have insignificant impact on surface wind speeds. The higher winds contribute to the low temperature bias through increased mechanical mixing.

The Equitable Threat Score (ETS) of 3 hrs accumulated precipitation over the 9 km grid spacing domain in Europe are assessed to analyze the coupling strength influence. The Experimental Real-Time TRMM Multi-Satellite Precipitation Analysis (TMPA) data are used for comparisons. As seen in Fig. 3.10d, the runs show limited skill, but the impacts of the coupling strength is still evident. A more reasonable precipitation simulation is found with the weak coupling strength coefficient of CE0.8. Results indicate that the dynamic C_{zil}, and weak coupling strength may be helpful to improve summer convection simulations over Europe.

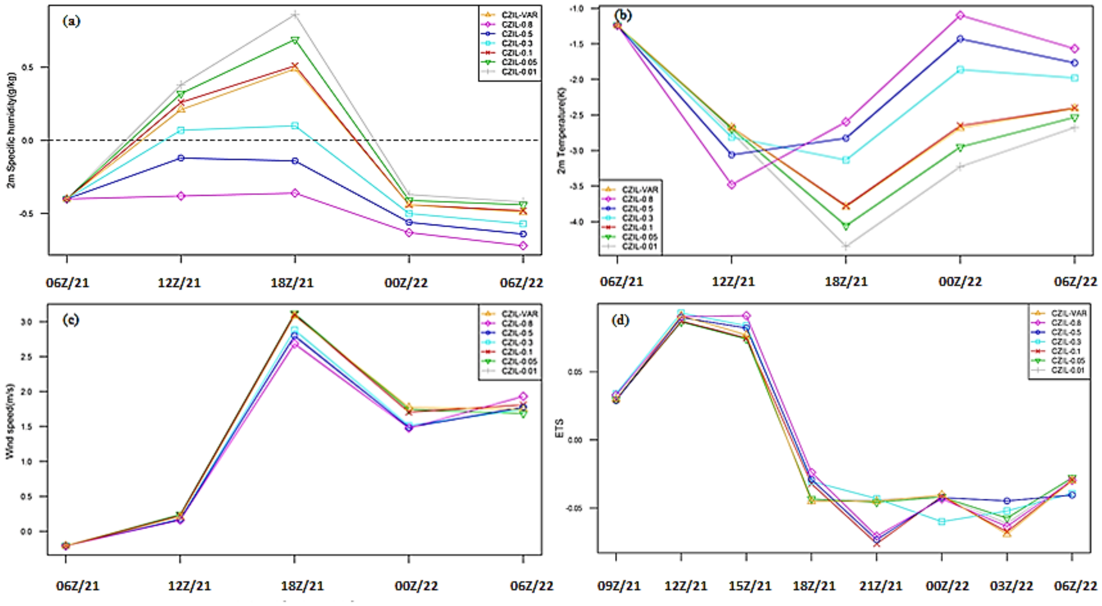

Fig. 3.10 0-24 hr model forecast, initialized at 0600 UTC 21 July 2007, area-averaged bias over Europe 3-km grid spacing domain of (a) 2 m specific humidity (10^{-3} × kg kg^{-1}), (b) 2 m temperature (K), (c) 10 m wind speed (m s^{-1}), and (d) ETS of 3 hrs accumulated precipitation from 0600 UTC 21 July to 0600 UTC 22 July 2007 over the European 9-km grid spacing domain.

3.4.2.3 North India

(a) Reflectivity

A series of X-band Doppler weather radars (DWRs) are operated by India Meteorological Department (IMD) in weather mode for detection of localized weather phenomenon (Routray et al. 2010). The reflectivity product from the New Delhi DWR is used for model comparisons. Fig. 3.11 presents the radar reflectivity field from all the experiments and the observation corresponding to 1200 UTC 12 May 2012. CI0.5 and CI0.8 show wider regions of stratiform precipitation (25-40 dBZ) which are closer to the observation. Strong coupling strength leads to lighter rain and smaller areas of precipitation, but the dynamic C_{zil} modestly improved the precipitation intensity and

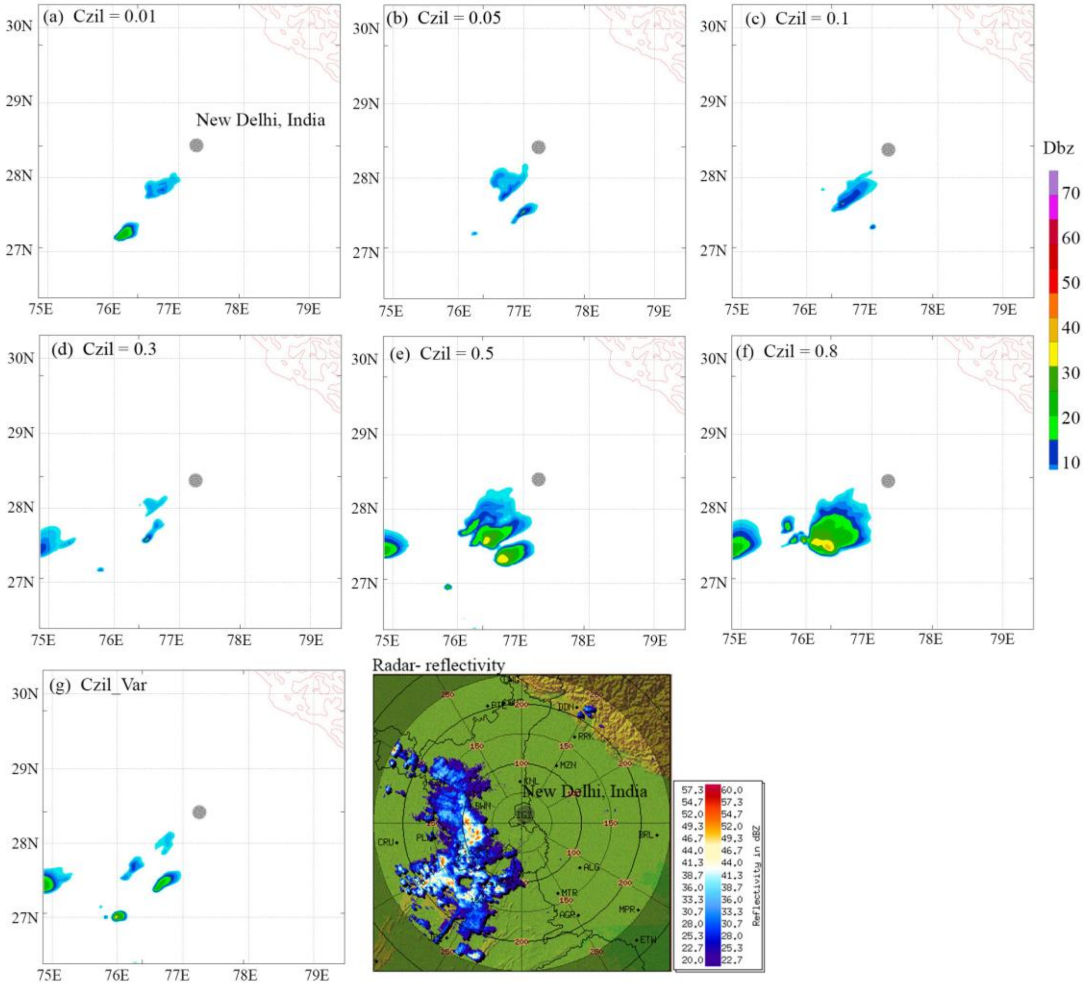

Fig. 3.11 Comparisons of reflectivity at 1200 UTC 12 May 2012 over India 3-km grid spacing domain between model forecasts with (a) C_{zil}=0.01, (b) C_{zil}=0.05, (c) C_{zil}=0.1, (d) C_{zil}=0.3, (e) C_{zil}=0.5, (f) C_{zil}=0.8, (g) dynamic $C_{zil\text{-}var}$, and (h) the observation.

distribution. The estimated reflectivity fields are converted to surface rainfall intensity using the Z-R relationship (Marshall et al. 1947) and the results are shown in Fig. 3.12. While all model runs underestimate the accumulated precipitation, the coupling strength over north India can be considered reasonable with C_{zil} = 0.5, and 0.8. Note that the precipitation amount is also influenced by large scale processes and not from local coupling mechanism alone. During May over north India, most of the land is cultivated and the dry parched surface produces thermals into the atmosphere. These thermals when interacting with larger moisture source often lead to regional precipitation events. The model appears to capture these feedbacks as the weak coupling is dominant over cultivated but parched land surface.

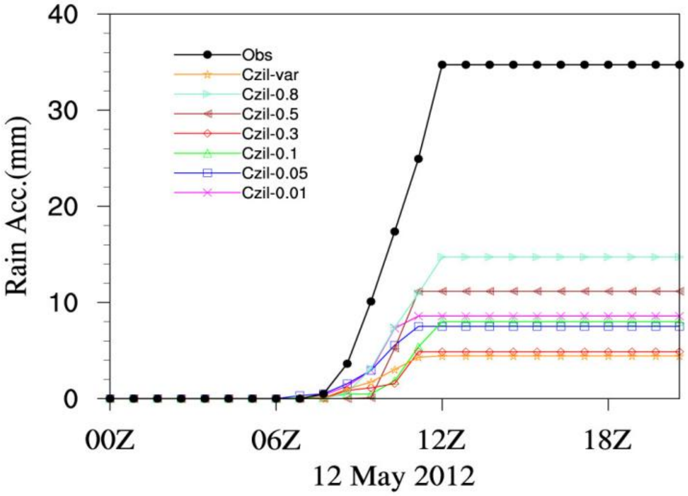

Fig. 3.12 Comparison of accumulated precipitation initiated at 0000 UTC 12 May 2012 over India 3-km grid spacing domain between model forecasts and the observation.

(b) Statistical analysis

The 0-24 hr area-averaged 2 m temperature and moisture, and 925 mb wind speed biases are shown in Fig. 3.13 and the mean values of the bias are presented in Table 3.6. All the runs show cold biases but a better response in simulating 2 m temperature is achieved with the weak coupling strength of CI0.8. CIvar and CI0.5 show similar feedbacks on temperature, while the strong coupling strength of CI0.01 produces the largest temperature bias. All the coupling runs show dry biases, and a slightly better response occurs with the strong coupling coefficient of CI0.01. Since the strong coupling strength leads to relatively more moisture than the other runs, as a feedback the *LE* of the strong coupling run is higher. As the surface coupling strength is linked to the evolution of moisture in the model (Trier et al. 2011), the weak coupling strength produces drier environment for the PBL, resulting in reduced moisture (Fig. 3.14b). The wind speeds at 925 hPa of all experiments show similar biases before 1200 UTC, but large differences are noted between 1200 UTC 11 May and 0000 UTC 13 May 2012 and CIvar has the least bias. The vertical profiles of the area-averaged bias from the surface to 700 hPa levels in the PBL are shown in Fig. 3.14. Significant impacts of the coupling strength are found below 925 hPa, where all the simulations show lower temperature, less moisture, and larger wind speed biases. The wind speed profile shows mixed results, whereas the CIvar indicates an improved response.

TRMM data are used to assess the ETS of 3 hrs accumulated precipitation over the 9 km grid spacing India domain (Fig. 3.13d). All model runs show similar precipitation results though the weak coupling strength leads to higher ETS scores and a better precipitation forecast. The observation and model based histograms of 147 stations (grid) based WRF 2 m temperature and 2 m specific humidity are generated in Figs. 3.15 and 3.16. The histogram of CI0.8 shows similar distribution as compared to the range of 305-310 K in the 2 m temperature observation histogram. All of the other coupling strengths produce lower frequencies of 305-310 K range but higher frequencies are observed within the range of 300-305 K. The histograms correspond well with the results of area-averaged biases, emphasizing that the weak coupling strength has the best results for simulating the 2 m temperature. On the contrary, the 2 m specific humidity histogram of CI0.8 has the largest difference compared to observations indicating that the weak coupling strength is not able to capture the 2 m specific humidity over the northern Indian region. So, "what is an optimum coupling strength for the Indian monsoon region?" is still an open question. Our results do indicate that the constant value used in the default Noah/WRF model is not the optimal value.

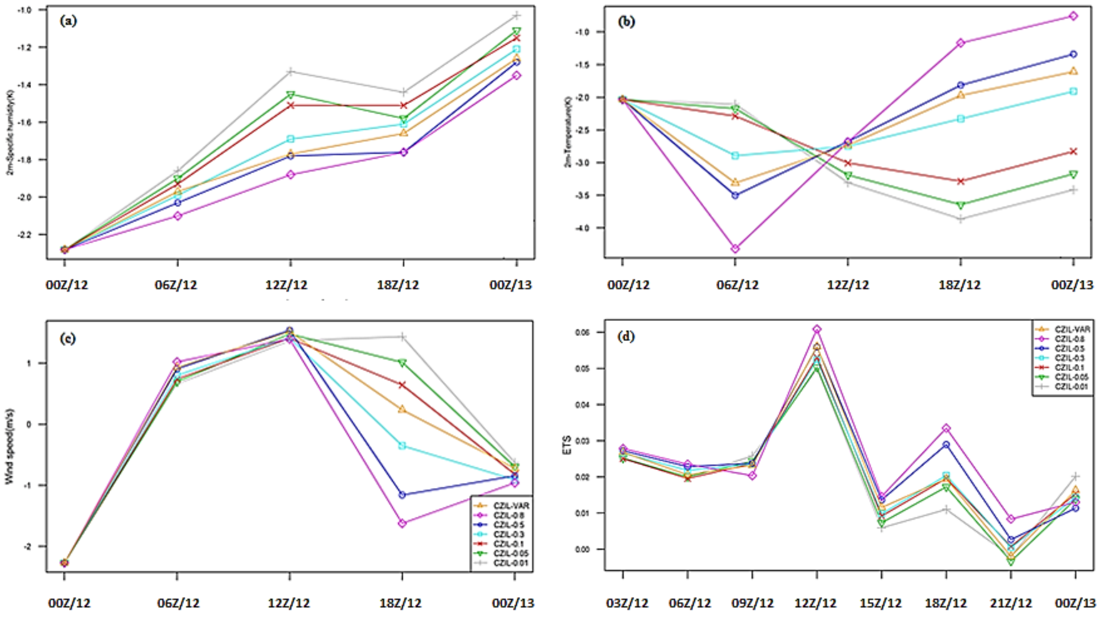

Fig. 3.13 0-24 hr model forecast initialized at 0000 UTC 12 May 2012, area-averaged bias over the Indian 3-km grid spacing domain of (a) 2 m specific humidity (10^{-3} × kg kg^{-1}), (b) 2 m temperature (K), (c) 10 m wind speed (m s^{-1}), and (d) ETS of 3 hrs accumulated precipitation from 0000 UTC 12 July to 0000 UTC 13 May 2012 over the Indian 9-km grid spacing domain.

Table 3.6 Biases of 2 m temperature (T), 2 m moisture (Q), and surface wind speed (WSPD) for 0-24 hr model forecasts over India domain at 3-km grid spacing

Coupling coefficient (C_{zil}) case	**2 m T (K)**	**2 m Q (10^{-3}×kg kg^{-1})**	**WSPD (m s^{-1})**
CI0.01	-2.95	-1.59	0.11
CI0.05	-2.84	-1.66	0.04
CI0.1	-2.69	-1.68	-0.06
CI0.3	-2.38	-1.76	-0.26
CI0.5	-2.27	-1.83	-0.37
CI0.8	-2.19	-1.87	-0.49
CIvar	-2.33	-1.79	-0.06

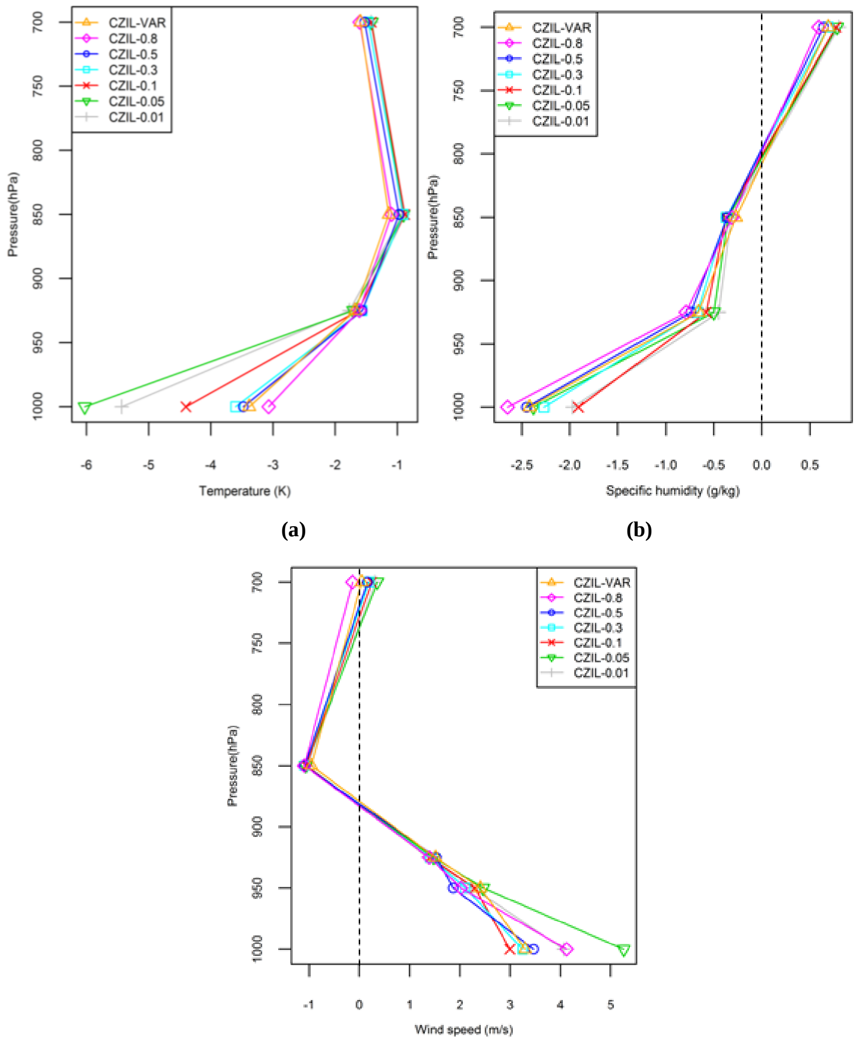

(a) (b)

(c)

Fig. 3.14 Vertical profiles of area-averaged bias over the Indian 3-km grid spacing domain at 1200 UTC 12 May 2012 for (a) temperature (K), (b) specific humidity (10^{-3} × kg kg^{-1}), and (c) wind speed (m s^{-1}).

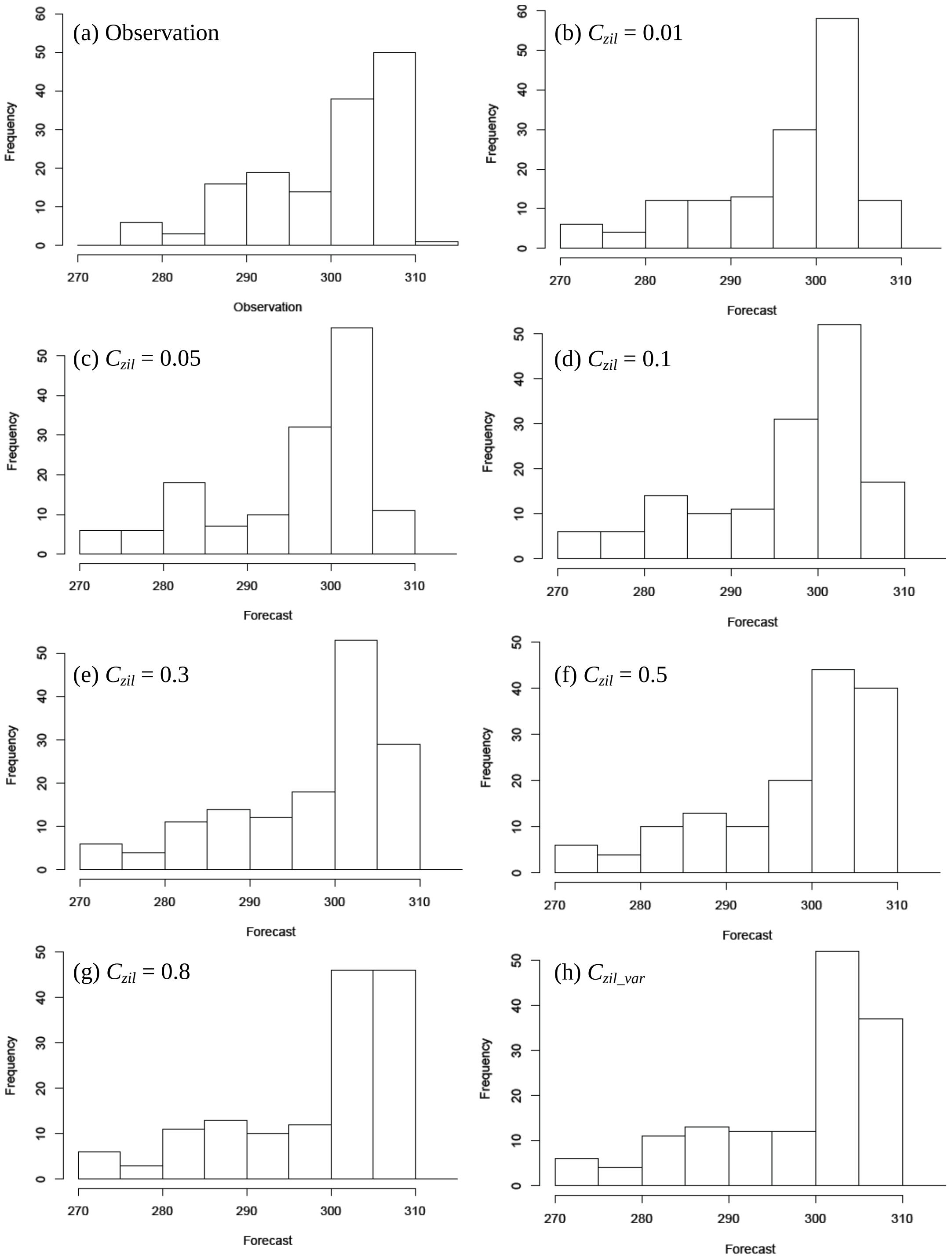

Fig. 3.15 147 points histograms of the observation and the WRF model forecasts for 2 m temperature (K): (a) Observation, (b) C_{zil} = 0.01, (c) C_{zil} = 0.05, (d) C_{zil} = 0.1, (e) C_{zil} = 0.3, (f) C_{zil} = 0.5, (g) C_{zil} = 0.8, and (h) dynamic $C_{zil\text{-}var}$.

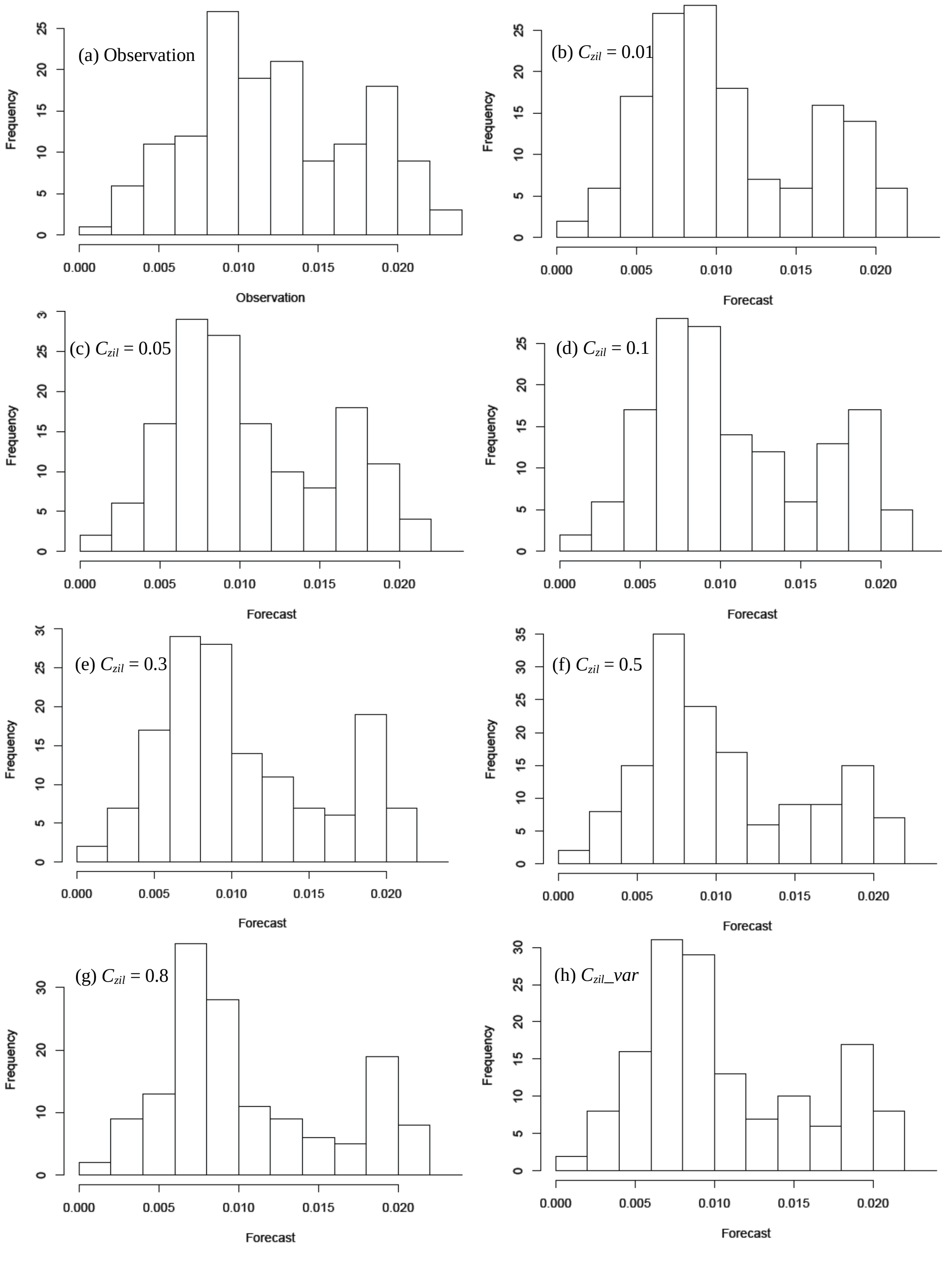

Fig. 3.16 147 points histograms of the observation and the WRF model forecasts for 2 m specific humidity (kg kg^{-1}): (a) Observation, (b) C_{zil} = 0.01, (c) C_{zil} = 0.05, (d) C_{zil} = 0.1, (e) C_{zil} = 0.3, (f) C_{zil} = 0.5, (g) C_{zil} = 0.8, and (h) dynamic $C_{zil-var}$.

3.4.2.4 West Africa

(a) Surface flux analysis

The impact of different coupling strengths on surface heat fluxes over the West African domain is shown in Figs. 3.17 a and b. CAvar results in a better estimation of *LE* but overestimates *H*. The *H* for CA0.3 has a good agreement with the observation, but the bias increases with stronger coupling when the coupling coefficient is decreased from 0.3 to 0.01. Since the *LE* of CA0.3 also matches well to the observations, the coupling strength of CA0.3 could be able to modify the surface fluxes over West Africa. The surface air temperature is affected by *H* and is expected to be sensitive to surface coupling strength. The runs with strong coupling strength show good agreement between the 2 m temperature and observations (Fig. 3.17c), but CAvar results in about 1-3 K lower temperature before 0300 UTC and higher temperatures after that. The constant coupling coefficients have little impacts on the 10 m wind speed, but the impact of C_{zil} on friction velocity is significant over West Africa. Since the smaller C_{zil} leads to larger roughness length for heat which means rougher surface for heat and moisture, the surface turbulence is stronger and results in larger friction velocity. Although the temporal patterns of the friction velocity are similar among the different coupling runs, the strong coupling strength and the dynamic C_{zil} lead to relatively poor simulations of the friction velocity (Fig. 3.17d).

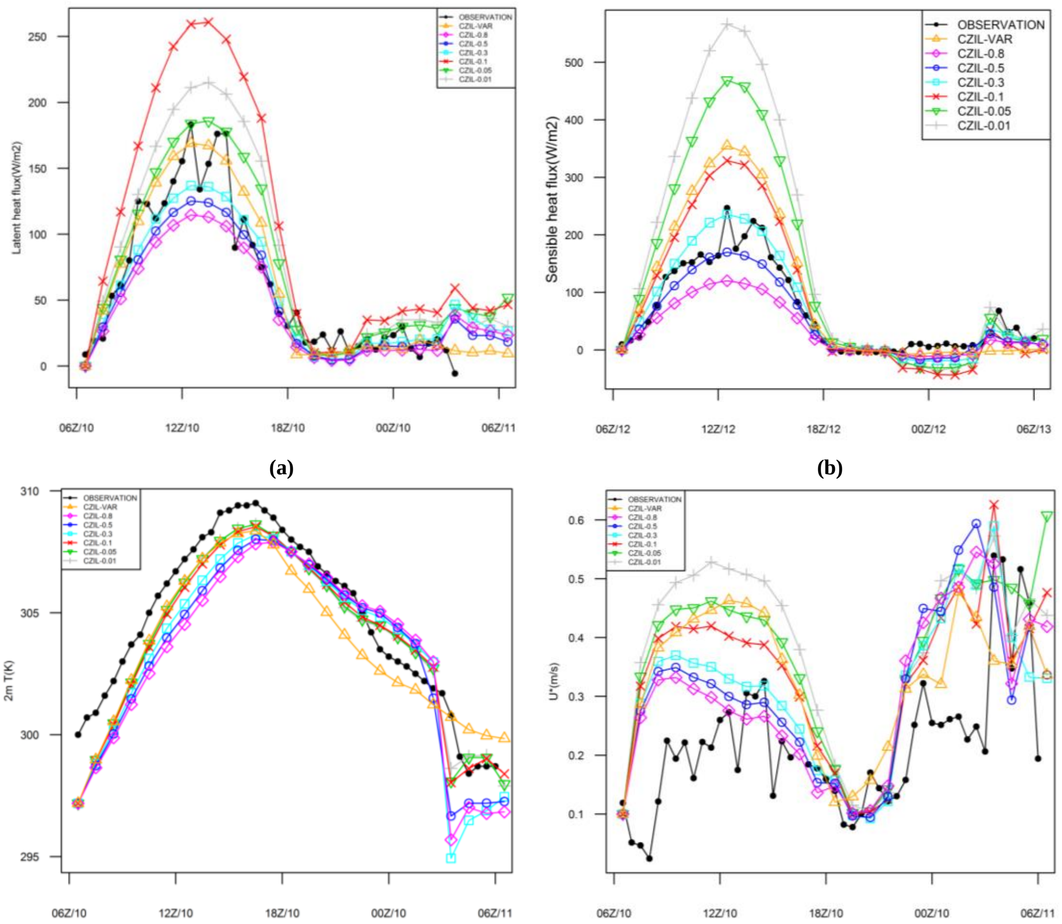

(a)

(b)

(c)

(d)

Fig. 3.17 Comparisons between the 0-24 hr CA experiments and the observation of (a) latent heat flux (W m^{-2}), (b) sensible heat flux (W m^{-2}), (c) 2 m temperature (K), and (d) friction velocity (m s^{-1}), initialized at 0600 UTC 10 August 2006 for Niamey (13.478°N, 2.174°E), Niger, Africa.

(b) Statistical analysis

As seen in Fig. 3.18a, the area-averaged bias of the 2 m moisture decreases in the morning, and CA0.1 and CAvar show generally similar and small biases. The 2 m temperature of all simulations show cold biases; and CA0.1 and CAvar also have similar surface temperature biases. This agreement is noted not just in the surface fields but also in the vertical profiles of temperature and moisture (Figs. 3.18 c and d). All runs show wet and cold biases in the vertical profiles, though the weak coupling strength of CA0.8

results in the best performance. The impacts of the coupling strength are more significant at the surface. All the model runs have generally similar humidity biases around 925 hPa, but the different responses caused by the surface coupling strength show up again around 900 hPa. The wind speed forecast is improved by strong coupling strength in the surface layer, but the weak surface coupling strength run shows a smaller bias between the levels of 925 hPa and 850 hPa (Fig. 3.18e). The impact noted on wind speed for this case is not entirely apparent and is likely a result of the larger domain considered in this experiment.

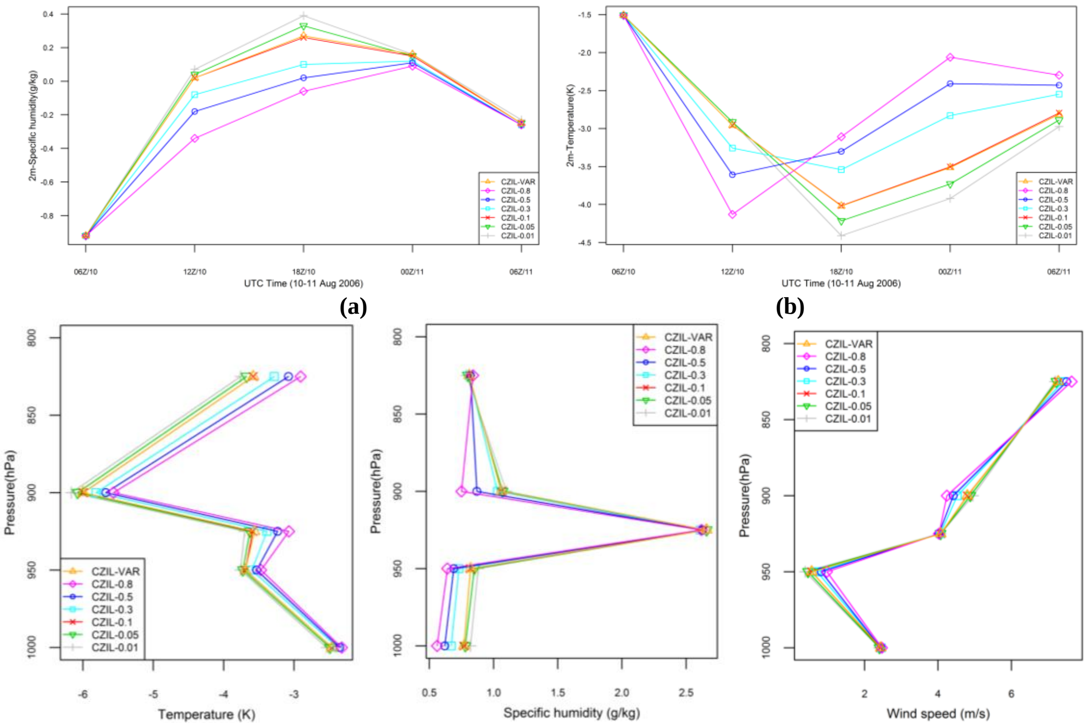

(a) (b)

(c) (d) (e)

Fig. 3.18 0-24 hr model forecast, initialized at 0600 UTC 10 August 2006, area-averaged bias over the West African 3-km grid spacing domain of (a) 2 m specific humidity (10^{-3} × kg kg^{-1}), (b) 2 m temperature (K); Vertical profiles of domain averaged bias over a 3-km grid spacing domain for (c) temperature (K), (d) specific humidity (10^{-3} × kg kg^{-1}), and (e) wind speed (m s^{-1}) at 1200 UTC 10 August 2006.

(c) Precipitation

The 3 hrs accumulated precipitation over the West African region is simulated by all C_{zil} experiments and again the TRMM-based precipitation estimates are used for comparisons.

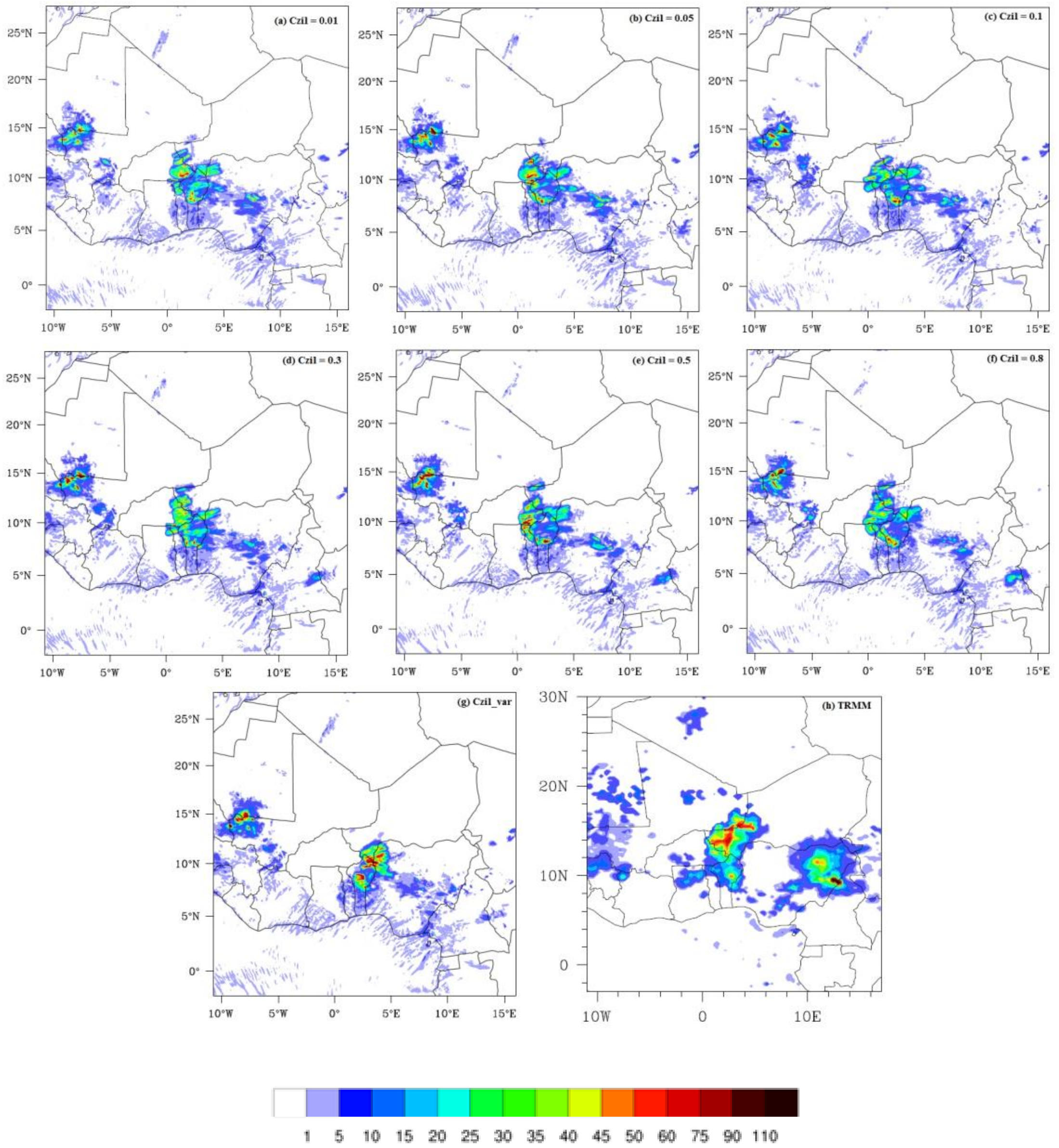

Fig. 3.19 Comparisons of the 3 hrs accumulated precipitation (0300 – 0600 UTC) on 11 August 2006 over west Africa 3-km grid spacing domain between model forecasts with (a) C_{zil}=0.01, (b) C_{zil}=0.05, (c) C_{zil}=0.1, (d) C_{zil}=0.3, (e) C_{zil}=0.5, (f) C_{zil}=0.8, (g) dynamic $C_{zil\text{-}var}$, and (h) the TRMM-based precipitation.

Again the results show consistency in that the surface coupling strength affects precipitation intensity and not the location. The dynamic C_{zil} experiment (Fig. 3.19g) successfully simulates one of the heavy rainfall systems identified in the TRMM-based precipitation estimates, but was missed in other experiments (Fig. 3.19h).

3.5 Conclusions and discussions

In this study, the impact of land-atmosphere coupling was assessed using an offline Noah LSM and the coupled Noah/WRF model for select summer time mesoscale convection and heavy rainfall cases over the U.S. SGP, Europe, northern India, and West Africa regions. The potential benefit of using the dynamic formulation for representing the land atmosphere coupling was studied over the four different coupling "hotspot" regions. The area-averaged statistical analysis of 2 m temperature and moisture and 10 m wind speeds were conducted and the impacts of surface coupling strength on precipitation were evaluated. The C_{zil} is found to have good potential to modulate the model results and particularly improve the simulation of the convective systems. The dynamic coupling strength helps improve the precipitation forecasts in terms of intensity but not necessarily its location.

The impacts of the coupling effect on the convection vary across different land-cover types and over different regions. Over the different regions, the model biases response varies with the changes in coupling strength. Significant impacts from surface coupling strength are found between the surface layer and the 925 hPa level. In summer, over the U.S. SGP the strong coupling leads to cold and wet boundary layer, resulting in strong convective system and heavier rainfall, whereas the coupling over northern India is relatively weak and produces lighter rain and smaller areas of precipitation due to the cultivated parched land surface. However, because of the unavailability of observed surface fluxes in India, the coupling impacts on surface energy and surface variables need further analysis when additional data become available. The model performance with different C_{zil} values may vary with different PBL schemes or CPs. Thus, additional ensemble experiments are needed in future studies.

Surface heat fluxes show the largest impact in terms of the coupling strengths assigned over different regions. Results indicate that the constant surface coupling coefficient adopted in the current coupled Noah/WRF model has deficiency in producing correct surface fluxes. Over the U.S. SGP, H is better simulated by the weak coupling coefficient (C_{zil} = 0.8), while LE from runs with the strong coupling coefficients (C_{zil} = 0.01 and 0.05) and the dynamic $C_{zil\text{-}var}$ match the observations better. In addition, the strong coupling strength overestimates the surface temperature and is able to modify the surface and atmospheric characteristics. The surface heat fluxes are overestimated during the daytime in all the model runs over the European domain. The runs with C_{zil} = 0.5 and the dynamic $C_{zil\text{-}var}$ have a similar LE evolution, and the coupling strength C_{zil} = 0.3 leads to an improvement of LE. Over West Africa, the current WRF model leads to coupling effects that are too strong and could be improved by decreasing the coupling coefficient to 0.3 in the land model. The dynamic C_{zil_var} is able to improve the simulations of the surface fluxes over West Africa.

The model over predicts the sensible heat flux in the convective PBL with all coupling strengths and this may be due to errors in the different boundary layer formulations within the model (Hacker and Angevine 2013) and not just a coupling coefficient based problem. The weak coupling strength also potentially acts to buffer or reduce the biases. A strong vertical moisture gradient is a sign of the weak coupling effects. Excess moisture is reduced by the weak coupling strength which produces a drier environment for the PBL due to the linkage between the surface coupling strength and the evolution of moisture in the model. Over prediction of the 10 m wind speed produces too large momentum fluxes over the four regions, and the momentum fluxes are generally insensitive to the coupling strength (except in the case of West Africa region).

One important and consistent result that emerged from analysis over the different regions is that the precipitation locations are not affected by the coupling strength in all the experiments, but the coupling strength does have impacts on the magnitude of the precipitation and changes the local spatial and temporal patterns of the rainfall. Our investigation also reveals that improvements made to the existing surface and atmosphere coupling strength by adopting the dynamic coupling coefficient are helpful in improving precipitation predictions.

There is high uncertainty in land-atmosphere coupling findings and the results from this and prior studies need to be considered with caution. Zones identified as coupling hotspots in climate studies, and the associated coupling strength would likely change depending on the model roughness/coupling coefficient assigned. Thus the "actual" coupling itself is perhaps a model artifact-albeit a useful one to study different processes including improving predictability. As a result, the zone of “high” or “low” coupling strength should be considered in the context of the model and parameterizations used. More efforts need to be directed toward adopting the dynamic C_{zil} rather than a constant value that is currently used in the Noah/WRF like models. Model results are consistently though modestly improved and encouraging when a dynamic C_{zil} is used. Therefore, the dynamic C_{zil} formulation is recommended for use in future studies but with a caution for use over complex terrains. Evaluating the impact of coupling coefficient in a coupled model is highlighted as the results may be different than in the offline mode. Our results indicate that identifying the correct coupling is a challenge as it can improve one variable and deteriorate another. The coupling coefficient has significant control on the model performance particularly the quantitative precipitation forecasts and is thus an important feature for studying hydrometeorological extremes such as droughts and heavy rain events.

CHAPTER 4. IMPROVING HIGH-RESOLUTION WEATHER FORECASTS USING THE WEATHER RESEARCH AND FORECASTING (WRF) MODEL WITH AN UPDATED KAIN-FRITSCH SCHEME[3]

4.1 Introduction

Numerical weather prediction (NWP) forecast models have been greatly improved, motivated by the role of providing accurate forecasts about severe weather events to mitigate the loss of life and property. Furthermore, credibility of climate change simulations at urban-scales can be increased by first improving the accuracy of high-resolution model simulations at weather prediction timescales (Chen et al. 2011). In particular, moist processes play an important role in properly simulating weather, air pollution, climate and the hydrological cycle. Clouds and precipitation formed in these processes are important forecast products, thus accurate prediction of precipitation is one of the most beneficial areas of NWP improvement. For this reason, key processes occurring within clouds, including microphysical and dynamical processes, need to be well understood and modeled.

Cloud microphysics schemes have been used in NWP models, but those microphysical processes may not be accurately represented due to the lack of supporting measurements for many processes occurring at finer spatial and temporal scales. For example, the

---

[3] Zheng, Y., K. Alapaty, J. A. Herwehe, A. D. Del Genio, D. Niyogi, 2015: Improving high-resolution weather forecasts using the Weather Research and Forecasting (WRF) model with an updated Kain-Fritsch scheme. *Mon. Wea. Rev.*, doi: 10.1175/MWR-D-15-0005.1 (In press).

formulation described in Kain et al. (2008) has been found to be appropriate for WRF Single Moment 6-class (WSM6) microphysics (Hong et al. 2004) and has been successfully used in some numerical studies (e.g., Done et al. 2004; Deng and Stauffer 2006; Wulfmeyer et al. 2006; Case et al. 2008; Niyogi et al. 2011). However, according to Clark et al. (2012), many such studies are not able to accurately clarify unique precipitation particle and other physical parameters in different microphysical processes using regional models such as the WRF model (Skamarock and Klemp 2008). This problem revealed that many characteristics of the model results were quite sensitive to the choice of microphysics scheme (Weisman et al. 2008; Dawson et al. 2010; Bryan and Morrison 2012). Clark et al. (2012) also found that no single microphysics scheme could surpass the others in performance during the 2010 National Oceanic and Atmospheric Administration's (NOAA's) Hazardous Weather Testbed (HWT) Spring Forecasting Experiment. There is also much debate on whether more complex microphysics schemes provide value for precipitation forecasts (e.g., Luo et al. 2010; Seifert and Stevens 2010; van Lier-Walqui et al. 2012; Van Weverberg et al. 2013). Based on the microphysics scheme sensitivity study of Blossey et al. (2007), microphysics was found to have little impact on decreasing a model's apparently excessive precipitation efficiency. Additionally, Cintineo et al. (2014) pointed out that large uncertainties remain in how various microphysics schemes represent subgrid-scale microphysical processes. Thus, as grid spacing decreases, cloud microphysics schemes have limitations in representing moist convection (Arakawa and Jung 2011; Gustafson Jr. et al. 2013; Molinari and Dudek 1992).

One reason for the partial failure of cloud microphysics schemes can be attributed to the fact that grid-scale dynamics is separated from cloud physics. Additionally, there will be clouds that are unresolved by high spatial resolutions (e.g., ~1 to 10 km grid spacings) and their effects need to be accounted for to improve predictability (e.g., Molinari and Dudek, 1992; Seaman et al. 1998). Thus, from these studies it can be inferred that, at high spatial resolutions, usage of a cloud microphysics scheme alone (without an active parameterized convection scheme) may not be sufficient to represent moist convection and precipitation for warmer periods in weather forecasts.

The dynamic cloud processes that describe cloud formation and growth can impact the timing, location, and intensity of precipitation. In many NWP models, the fractional cloudiness can influence atmospheric radiation budgets as well as the dynamics and thermodynamics, but in the past, subgrid-scale cumulus cloudiness and the associated radiative impacts have been largely neglected outside of global climate models. Alapaty et al. (2012) and Herwehe et al. (2014) emphasized and documented the importance of incorporating such subgrid-scale cloud-radiation interactions using the Kain-Fritsch (KF) CPS (Kain 2004) and the Rapid Radiation Transfer Model, Global (RRTMG) schemes (Iacono et al. 2008). In order to represent subgrid-scale clouds at higher resolutions, it will be shown that there is a need to relax some of the assumptions used in CPs (e.g., the KF scheme). We address some of these issues that cause CPSs to degrade progressively as resolution is increased, in particular for high-resolution modeling (for grid spacings on the order of 1-10 km).

One of the many key parameters in CPSs is the convective adjustment timescale, a characteristic time scale with which convective available potential energy (CAPE) is reduced at an exponential rate by convection. This parameter is set as a constant value in many regional and global models with the exception of a very few models (e.g., the European Centre for Medium-Range Weather Forecasts model, Bechtold et al. 2008). Literature indicated that there is some uncertainty in the specification of this parameter. For example, Mishra and Srinivasan (2010) improved the simulation of the seasonal mean precipitation significantly by increasing the adjustment time scale value from 1 hour to 8 hours, while Done et al. (2006) found that varying the adjustment timescale from minutes to one day resulted in changing all CP-generated subgrid-scale rainfall to only grid-scale precipitation. In addition, the magnitude of convective heating and drying rates has been found to correlate with local CAPE more strongly at finer scales when grid spacing is on the order of 1-10 km (Kain 2004). Another key cloud process is the interaction between convection and its environment through entrainment and detrainment. These processes are quite complex and are of vital importance in regional and global models (e.g., Tokioka et al. 1988; Kain and Fritsch 1990; Kang et al. 2009). In many global models (e.g., Neale et al. 2010), the entrainment rate is specified and is a parameter often adjusted to improve results; however, there are very few regional and global models in which the entrainment rate is empirically estimated (e.g., Kain 2004; Chikira and Sugiyama 2010; Del Genio et al. 2012). But for high-resolution simulations, assumptions made in the entrainment formulation of the KF scheme need to be reconsidered. The convective momentum transport by cumulus convection is not included in many regional models, but for high-resolution modeling the importance of including such subgrid-scale transport on grid-scale vertical motions deserves attention since it could help reduce model spin up time.

Based on the above considerations, a few updates that were explored using the KF convection scheme are: inclusion of subgrid-scale cloud radiation interactions, a dynamic adjustment timescale, impact of subgrid-scale cloud updraft mass fluxes on grid-scale vertical velocity, and an entrainment methodology based on the lifting condensation level (LCL). These changes introduce scale dependency for some of these key parameters in the KF scheme with an expectation that they will improve weather forecasts at 9- and 3-km grid spacings.

Since forecasts are sensitive to the initial conditions and small changes in the initial conditions can lead to big changes farther out in time (Rabier et al. 1996; Stensrud et al. 2000), an accurate specification of the initial model state (i.e., the analysis of the atmospheric state) can make a significant improvement in high-resolution NWP model forecasts (Ehrendorfer 1997; Simmons and Hollingsworth 2002). In this study, we also explore impacts of initial conditions on short-term high-resolution forecasts, as well as the sensitivity to different initial conditions of a high-resolution NWP model that includes an updated parameterized cloud dynamics. For that reason, we have made an attempt to study the impacts of introducing scale-aware convective parameterized cloud dynamics for high-resolution forecasts using two different initial analyses.

To improve the prediction of precipitation distribution and variability, this study introduces several changes to the KF CPS in the WRF model and evaluates their impacts on high-resolution short-term forecasts. Since high-resolution models can have varying degrees of sensitivities to physics, dynamics, and initial conditions, the objectives of this study are limited to understanding of the impacts of using (1) initial conditions obtained from two different analysis fields, and (2) a scale-dependent UKF scheme on high-resolution precipitation forecasts using WRF version 3.4.1 (Skamarock and Klemp 2008). This paper is organized as follows: Section 2 presents methods for updating the KF scheme; Section 3 describes the design of the numerical simulations; Section 4 evaluates the WRF model performance; and summary and conclusions are provided in Section 5.

4.2 Methodology

For the purpose of improving high-resolution precipitation forecasts, we developed an updated KF scheme based on the study of subgrid-scale cloud-radiation interactions by Alapaty et al. (2012) by introducing grid resolution dependency and modifying the adjustment timescale and entrainment processes which influence surface precipitation. To help mitigate model spin up issues in short-range weather forecasts and associated precipitation, we also considered the impacts of subgrid-scale cloud updraft mass fluxes on grid-scale vertical velocity.

Multisensor Precipitation Estimates (MPE, also known as Stage IV Next-Generation Radar) hourly rainfall products and the satellite infrared cloud observations were used for validation of the model forecasts. MPE Stage IV is a national precipitation analysis obtained from consideration of Next-Generation Radar data and precipitation gauges (Lin and Mitchell 2005). MPE data at 4-km spatial resolution were obtained at hourly intervals and interpolated for a 3 km grid spacing in our study. The high spatial resolution of MPE data makes it possible to evaluate high-resolution NWP model precipitation forecasts.

4.2.1 The KF CPS

The KF CPS (Kain and Fritsch 1990, 1993; Kain 2004) has been used successfully over the years, incorporated in the Pennsylvania State University–National Center for Atmospheric Research Mesoscale Model (Wang and Seaman 1997), the National Centers for Environmental Prediction (NCEP) Eta Model (Black 1994), the WRF model (Skamarock and Klemp 2008), and the new Model for Prediction Across Scales (MPAS) (Skamarock et al. 2012). The KF scheme is a mass flux parameterization and uses the Lagrangian parcel method, and it can be generally grouped into three parts: 1) the convective trigger function, 2) the mass flux formulation, and 3) the closure assumptions. The early version of the KF scheme (Kain and Fritsch 1990, 1993) utilized a simple cloud model with moist updrafts and downdrafts, and has been modified for use by NWP models. Several components of that KF scheme have been changed (Kain, 2004) to include an updraft formulation (i.e., imposing a minimum entrainment rate, specified cloud radius to vary as a function of subcloud-layer convergence, allowing a minimum cloud depth to vary as a function of cloud-base temperature, and allowing shallow convection), a downdraft formulation (i.e., introducing a new downdraft algorithm), and a closure assumption (i.e., calculating CAPE based on the path of an entraining parcel). In this study, we have used that latest version of the KF scheme (i.e., Kain, 2004) to introduce several new science updates which are described in the following section.

4.2.2 A brief description of subgrid-scale cloud-radiation interactions

In most NWP models, subgrid-scale CPs do not consider cumulus cloud feedbacks to radiation due to a lack of knowledge on how to estimate fractional cloudiness as a function of parameterized clouds, resulting in biases in both regional weather and climate simulations (Herwehe et al. 2014). Alapaty et al. (2012) introduced a subgrid-scale cumulus cloudiness formulation to the KF CPS (Kain 2004) and the RRTMG models (Iacono et al. 2008). The inclusion of subgrid-scale cloud-radiation interactions created more realistic longwave and shortwave radiation variability, leading to the improvement of several meteorological parameters at both the weather and climate timescales. Here, we extend the study of subgrid-scale cloud-radiation interactions by relaxing some of the assumptions used in the KF scheme and hypothesize that our UKF scheme will reduce excessive precipitation in weather forecasts for short-term high-resolution modeling studies.

4.2.3 A dynamic formulation for the adjustment timescale

The adjustment timescale (τ) is the time over which CAPE is reduced to stabilize the atmosphere, originally introduced by Frisch and Chappell (1980). In the default configuration of many NWP models, a constant value of τ is specified as a global constant. The KF scheme uses a technique that was proposed by Fritsch and Chappell (1980) for the estimation of τ based on the mean tropospheric horizontal wind speed and grid resolution. However, as noted by Stensrud (2007), this formulation may approach its limitation either for high resolution grids or for environments with strong winds, such as hurricane simulations. Because of this limitation, τ was found to be one of the parameters that caused wet biases in simulated precipitation amounts at 12-km grid spacing (Bullock et al. 2015). As we move from coarser (~15 km) to high resolution (~1 km) grids, one would expect the impacts of parameterized convection to gradually become less significant. However, many CPSs cannot work properly at these finer scales because the tendencies produced by parameterized convection dominate over resolved convection (Arakawa and Jung 2011; Molinari and Dudek 1992). To make CPSs (such as KF) seamless across these spatial scales, τ should increase with increased grid resolution such that atmospheric stability restoration is gradually taken over by the resolved convective processes. However, it does not occur with the existing τ methodology used in the KF scheme as demonstrated by Bullock et al. (2015). To that effect, a formulation for τ is developed by using cloud macrophysical parameters following the notion used by Bechtold et al. (2008).

Considering the fact that many KF parameters are tied to grid spacing of around 25 km (Kain 2004), we derive a new grid resolution-dependent dynamic formulation of the adjustment timescale based on Bechtold et al. (2008):

$$\tau = \frac{Depth\ Scale}{Velocity\ Scale} F_n(Dx) \tag{4.1}$$

$$\tau = \frac{H}{W}\beta \tag{4.2}$$

$$\beta = \left[1 + ln\left(\frac{25}{Dx}\right)\right] \tag{4.3}$$

where H is cloud depth (m), and W is cloud averaged vertical velocity (m s^{-1}). Dx is the horizontal grid-spacing (km), and β is a scaling parameter dependent on the model's horizontal grid spacing Dx (km), analogous to but different from that of Bechtold et al. (2008).

For a spectrum of grid resolutions, the adjustment timescale τ from Eq. 4.1 without the scaling parameter β would be of the same order. Thus, as argued earlier, the scaling parameter helps the scheme represent a smooth transition from parameterized cloud physics to resolved grid-scale cloud physics. For a 25 km grid, the scaling parameter β will become 1.0, while for a 1 km grid it would be about four times larger. Proposed spatial variation of the scaling parameter closely follows the logarithmic-bimodal distribution of cloud fraction dependency on horizontal grid resolution derived from a cloud resolving modeling study (Arakawa and Wu 2013). In our study, as resolution increases, τ increases and thus reduces the number of parameterized updrafts, which conforms to the main theme of Arakawa and Wu (2013) that subgrid-scale cloud fraction should cover only a small portion of a grid cell. Since the cloud depth (H) is readily available from the KF, cloud averaged vertical velocity scale (W) is the only unknown in the Eq. 4.2 and it is estimated as follows.

We extend the shallow convection study of Grant and Lock (2004) that used large eddy simulations (LES) and observations of the Barbados Oceanographic and Meteorological Experiment (BOMEX; Holland and Rasmusson 1973) to relate cloud depth-averaged vertical velocity W to the product of KF cloud base updraft mass flux and entrained CAPE as:

$$W = (\delta m_b A_e)^{1/3} \tag{4.4}$$

where δ is a constant and set to unity so that Eq. 4.4 is consistent with that of Grant and Lock, m_b is the cloud-base updraft mass flux per unit density (m s^{-1}), and A_e is diluted/entrained CAPE (m^2 s^{-2}).

Since Eq. 4.4 was originally developed for shallow convective clouds, in order to extend it for deep convective clouds, we have introduced the constant, δ. It is interesting to note that Grant and Lock (2004) did not note that Eq. 4.4 is related to the cloud work function originally proposed by Arakawa and Schubert (1974) for a spectrum of convective clouds. Thus, Eq. 4.4 also works for deep convective clouds since it is essentially the cube-root of a simplified form of the cloud work function. The cloud work function is defined as the buoyancy flux contribution to the rate of change of convective kinetic energy per unit cloud base mass flux, which then can be related to the product of vertically averaged cloud mass flux and entrained CAPE (A_e). Thus, δ becomes the ratio of vertically averaged cloud mass flux and cloud base mass flux, resulting in Eq. 4.4. From the study of Lawrence and Rasch (2005) that used the Zhang and McFarlane (1995) scheme, we find that vertically averaged mass flux is very close to the cloud base mass flux and thus δ can vary from about 0.9 to 1.1 for deep convection. However, in this study, we set δ to unity for the deep moist convection.

Our new dynamic formulation for the adjustment timescale can then be written as

$$\tau = \frac{H}{(\delta m_b A_e)^{1/3}}\,\beta = \frac{H}{(\delta m_b A_e)^{1/3}}\left[1 + ln\left(\frac{25}{Dx}\right)\right] \qquad (4.5)$$

Thus, the adjustment timescale in Eq. 4.5 increases as resolution increases, resulting in longer time allowed for CAPE consumption by parameterized cloud physics and, hence, stabilization of the atmosphere by the KF scheme, facilitating a gradual transition of the stability restoration by the KF scheme to the grid-scale cloud physics.

4.2.4 Enhancement of grid-scale vertical velocity using subgrid-scale updraft mass fluxes

Many studies (e.g., Han and Pan 2011; Richter and Rasch 2008; Mallard et al. 2013) cite the need for inclusion of convective momentum transport into the KF scheme for proper simulation of hurricanes. But, for high-resolution convective precipitation forecasts, it is not clear whether subgrid-scale updraft mass flux plays an important role on grid-scale momentum, mass, and energy transport. To address an aspect of this issue, we considered impacts of subgrid-scale updraft mass fluxes on grid-scale vertical velocity using a simple linear methodology. One potential benefit is that it can help reduce model spin up time over convectively active regions by increasing the grid-scale vertical velocity. The proposed simple linear mixing methodology for enhancing grid-scale vertical velocity is expressed as

$$W_{up} = \frac{M_{up}}{\rho} = \frac{M/Dx^2}{\rho} \qquad (4.6)$$

$$W_n = W_g + W_{up} \qquad (4.7)$$

where W_{up} is the effective vertical velocity of subgrid-scale updraft (m s^{-1}), M_{up} is the subgrid-scale updraft mass flux (kg m^{-2} s^{-1}), ρ is the convective plume density (kg m^{-3}), M is the updraft mass rate (kg s^{-1}), W_n is the reformulated grid-scale vertical velocity (m s^{-1}), and W_g is the grid-scale vertical velocity (m s^{-1}).

4.2.5 Entrainment methodology based on LCL

From Kain (2004) the equation of the minimum entrainment rate for convective plumes is given by

$$\Delta M_e = M_b \frac{C}{R} \Delta P \tag{4.8}$$

where ΔM_e is the mixing rate (kg s^{-1}), M_b is the updraft mass rate at cloud base (kg s^{-1}), $C=0.03$ is a constant (m Pa^{-1}) which controls the overall magnitude of the entrainment rate for convective plumes, R is the radius of cloud base and dependent on the magnitude of vertical velocity at the lifting condensation level (LCL) (m), and ΔP is the pressure depth of a model layer (Pa).

The magnitude of the constant C used in the Eq. 4.8 is the same as that of the non-dimensional Tokioka parameter, α = 0.03, (Tokioka et al. 1988) used in global climate studies (e.g., Kang et al. 2009; Kim et al. 2011; Lin et al. 2013) for entrainment rate estimation. These global studies showed that the hyperactivity of a subgrid-scale convection scheme can be largely modulated by tuning the Tokioka parameter, which allows grid-scale processes to perform the needed moisture conditioning of the large-scale atmosphere. These studies also showed that the subgrid-scale precipitation decreases as the Tokioka parameter increases, resulting in an increase of grid-scale precipitation for improved climate simulations. Dependence of the entrainment on horizontal grid resolution for radiatively driven shallow (stratocumulus) clouds was studied by Stevens and Bretherton (1999) using a large-eddy simulation model. Their study found that when the horizontal spacing is coarsened, the entrainment rate decreased without any noticeable changes in the overall structure of the subcloud layer and cloud layer. The role of entrainment for continental deep convective clouds was extensively studied by Del Genio and Wu (2010). One of their findings was that at finer spatial resolutions, their inferred entrainment rate was greater because turbulence was more resolved. They also used the WRF model at different grid resolutions and found the inferred entrainment rate at 125 m grid spacing to be stronger than that inferred at 600 m grid spacing. Entrainment in deep convective clouds was also studied by Romps and Kuang (2010) using a LES model. It was shown that the purity of convection decreases with finer grids (ranging from 3200 to 100 m spacings), suggesting increased entrainment with finer grid spacing. Finally, in a recent cloud resolving modeling study, Bryan and Morrison (2012) concluded that changes in the simulated squall line intensity differences between two model grid resolutions (1 and 0.25 km) were primarily attributed to the increased entrainment. Thus, all these studies clearly highlighted the dependency of entrainment on the horizontal grid resolution (i.e., entrainment increases as grid resolution increases). de Rooy et al. (2013) provides a detailed review of entrainment in cumulus convection and highlights the study of Houghton and Cramer (1951) that entrainment needs to be partitioned into two parts: (1) entrainment due to large-scale processes; and (2) entrainment due to turbulence at cloud edges. Since the first type of entrainment is being represented by the Eq. 4.8, we have included the second type of entrainment through the usage of Tokioka parameter. Thus, we considered all of these findings when reformulating the entrainment rate (Eq. 4.8) in the KF scheme to make it more adaptable to high-resolution model forecasts and to work seamlessly across spatial scales. We introduce this feature via a dynamic Tokioka parameter that increases as model resolution increases. Thus, the resolution dependent Tokioka parameter helps to represent grid spacing effects on convective cloud-entrainment interactions similar to that documented in the literature. Hence, consistent with the above global climate and large-eddy simulation studies, we have introduced a scale dependency for the Tokioka parameter by multiplying it with the β shown in Eq. 4.3, and also replaced R by Z_{LCL} (m) – subcloud layer depth – which is the height of the LCL above the ground. The main advantage of using Z_{LCL} instead of R is that at higher resolutions, R generally approaches the upper limit of 2 km used in the KF scheme, thus, it is not consistent with the assumption that subgrid-scale cloud fraction covers only a small area of a grid cell (e.g., Arakawa and Wu, 2013). In such situations, the diameter of the KF cloud will become 4 km and thus, at the 3 km grid spacing used in this study, usage of R is inappropriate as the assumed subgrid cloud diameter exceeds the grid size.

Then, the new minimum entrainment equation can be written as:

$$\Delta M_e = M_b \frac{\alpha\beta}{Z_{LCL}} \Delta P \qquad (4.9)$$

Thus, Eq. 4.9 attempts to include both the types of entrainment consistent with the descriptions of de Rooy et al. (2013).

4.3 Design of Simulations

The WRF model (Skamarock and Klemp 2008) is commonly used for a wide range of meteorological studies across scales ranging from meters to thousands of kilometers and timescales from days to decades. An increasing number of researchers are employing it to study regional weather (e.g., Chen et al. 2011) and historic and future climate (e.g., Otte et al. 2012). However, recent regional climate research noted that WRF often produced excessive precipitation within highly energetic convective systems (Done et al. 2004; Hong et al. 2010; Alapaty et al. 2012; Herwehe et al. 2014). We hypothesize that including the effects of parameterized scale-aware cloud dynamics into a high-resolution WRF simulation will reduce the excessive rainfall biases by properly representing convective timescale, grid-scale vertical velocity, and entrainment effects.

The WRF model version 3.4.1 was used to conduct all weather forecast simulations over the U.S. SGP due to its importance as a land-atmosphere coupling “hotspot” (Koster et al. 2004; Zheng et al. 2014) and the availability of various observations. The main land-cover types include grassland, cropland, savannas, and a mixture of crop and natural vegetation. To understand the effects of using parameterized cloud dynamics for high-resolution forecasts, we tested three WRF model configurations with two-way interacting nests for the SGP. In our model simulations we used two choices [the Goddard microphysics scheme and the WRF double-moment 6-class scheme (WDM6)] for grid-scale cloud processes for both grid spacings (9 and 3 km). However, for subgrid-scale cloud representation, we used three approaches: (1) disabled subgrid-scale convection, allowing only explicit convection; (2) the latest KF scheme (Kain, 2004); and (3) our

UKF scheme. Details on the cloud formulations used in this study are described in the Table 4.1, showing a total of 36 numerical experiments. We have assigned a unique experiment name for each set of numerical simulation and these are referred to as EXP (explicit convection only), BASE [with the Kain (2004) KF], and UKF (with the update KF). For example, for each simulation period, EXP case has two numerical simulations, as identified under Experiment Number in the Table 4.1, referring to two types of initial conditions. To study impacts due to the choice of microphysics representation with the UKF scheme and its effects on regional weather simulations, we performed another set of six numerical experiments. These experiments were designed to compare the performance of the Goddard microphysics scheme with the WDM6. Note that no nudging or data assimilation was used in any of the simulations.

One degree 6-hourly NCEP Global Final Analysis (FNL) data derived from the Global Forecast System (GFS) and 0.5 degree 6-hourly Climate Forecast System Reanalysis (CFSR) data were used separately to develop lateral boundary and initial conditions for the large-scale atmospheric fields, soil parameters (i.e., soil moisture and temperature), and sea surface temperature (SST). The WRF model was configured with two-way interactive nested domains using horizontal grid spacing of 9 km (290 × 280 grid points; Domain 1 in Fig. 4.1a) and 3 km (307 × 274 grid points; Domain 2 in Fig. 4.1a). Locations of observational sites in Domain 2 are shown in Fig. 4.1b. In the vertical, the model was configured with 28 eta levels with a model top at 50 hPa. Prominent physics options in the WRF model configuration included the RRTMG radiation models (Iacono et al. 2008), the Goddard microphysics scheme (Tao et al. 1989), the Mellor-Yamada-

Janjic (MYJ) planetary boundary layer (PBL) scheme (Janjic 2002), and the Noah land-surface model (Chen and Dudhia 2001). We focus our evaluation on assessing the updated model's ability to forecast the location and intensity of surface precipitation, surface longwave and shortwave radiation, and surface temperature fields.

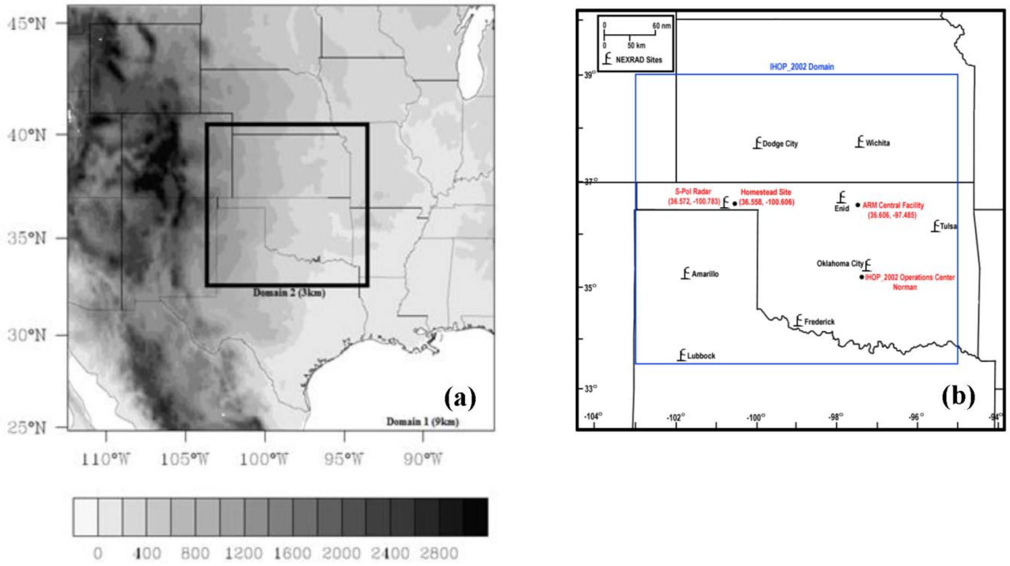

Fig. 4.1 (a) Topography map of the nested model domain over the U.S. SGP, and (b) the IHOP_2002 domain and fixed deployment locations (https://www.eol.ucar.edu/field_projects/ihop2002).

Table 4.1 Summary of the numerical experiments

Simulation period	Experiment No.	Experiment name	Initial conditions	Microphysics scheme	9-km grid spacing	3-km grid spacing
0000 UTC 4 June – 0000 UTC 6 June 2002	1	EXP	GFS	Goddard microphysics scheme	KF scheme	No cumulus parameterization
	2		CFSR			
	3	BASE	GFS		KF scheme	KF scheme
	4		CFSR			
	5	UKF	GFS		UKF scheme	UKF scheme
	6		CFSR			
0000 UTC 16 June – 0000 UTC 18 June 2002	7	EXP	GFS	Goddard microphysics scheme	KF scheme	No cumulus parameterization
	8		CFSR			
	9	BASE	GFS		KF scheme	KF scheme
	10		CFSR			
	11	UKF	GFS		UKF scheme	UKF scheme
	12		CFSR			
0000 UTC 5 July – 0000 UTC 7 July 2010	13	EXP	GFS	Goddard microphysics scheme	KF scheme	No cumulus parameterization
	14		CFSR			
	15	BASE	GFS		KF scheme	KF scheme
	16		CFSR			
	17	UKF	GFS		UKF scheme	UKF scheme
	18		CFSR			
0000 UTC 28 July – 0000 UTC 30 July 2010	19	EXP	GFS	Goddard microphysics scheme	KF scheme	No cumulus parameterization
	20		CFSR			
	21	BASE	GFS		KF scheme	KF scheme
	22		CFSR			
	23	UKF	GFS		UKF scheme	UKF scheme
	24		CFSR			
	25	DYNTAU	GFS		KF scheme with only dynamic τ update	
	26		CFSR			
	27	WUP	GFS		KF scheme with only updraft mass flux update	
	28		CFSR			
	29	ENT	GFS		KF scheme with only entrainment update	
	30		CFSR			
0600 UTC 14 June – 0600 UTC 16 June 2002	31	EXP	GFS	WDM6 scheme	KF scheme	No cumulus parameterization
	32		CFSR			
	33	BASE	GFS		KF scheme	KF scheme
	34		CFSR			
	35	UKF	GFS		UKF scheme	UKF scheme
	36		CFSR			

4.4 Results and Discussions

The primary goal of this study is to investigate the suitability of the UKF scheme for high-resolution simulations representing and forecasting surface precipitation. Another goal is to study the impacts of two types of initial conditions obtained from different analyses on high-resolution model simulations. For this purpose, WRF simulations using the 1.0 degree 6-hourly FNL datasets derived from GFS (denoted as GFS) to specify the initial states as well as boundary conditions are compared to those which used the 0.5 degree 6-hourly CFSR data (denoted as CFSR) as initial and boundary conditions. Four different regional precipitation patterns and time periods were selected for this experiment. An additional microphysics scheme sensitivity study (using the Goddard and WDM6 microphysics schemes) was designed to explore whether various microphysics schemes accompanied with the UKF scheme are able to produce appropriate precipitation forecasts for these high-resolution simulations.

4.4.1 Simulation period 0000 UTC 4 June – 0000 UTC 6 June 2002: Experiments 1-6:

Representative examples of observed and simulated 12-hour accumulated precipitation at 9-km grid spacing and 6-hour accumulated precipitation at 3-km grid spacing starting at 0000 UTC 5 June 2002 are shown in Figs. 4.2 and 4.3. It is apparent that the model forecasts with GFS contain precipitation at appropriate general locations and with a similar spatial structure when compared to the Stage IV observed precipitation (Figs. 4.2g and 4.3g). However, the precipitation forecasts over the central to eastern regions of the domains using CFSR as initial and boundary conditions [Fig. 4.2 (d-f) and Fig. 4.3 (d-f)] are shifted to the north, while in Figs. 4.2 (d-f) the precipitation patterns over central

Mexico and Gulf of Mexico (based on observed cloud cover) seem to be reasonably simulated. Such precipitation location offset indicates that the reanalysis systems may be impacted by interactions between the observational data and the assimilation system and can create unrealistic precipitation distributions shortly after the model is initialized. It also indicates that some forecasts are more sensitive to initialization than to convective parameterization or physics. The 6-hour accumulated precipitation from the 3-km grid spacing UKF GFS forecast (Fig. 4.3c) depicts a broad area of heavy precipitation over the western parts of the domain similar to that seen in the observations (Fig. 4.3g). It is also noted that the high-resolution UKF model simulations show improvement in the precipitation distribution. For instance, in Figs. 4.2 and 4.3 the heavy precipitation which occurred along the border of Oklahoma and Texas is shifted to the north and east in the BASE run (Figs. 4.2b and 4.3b), but is well simulated by the UKF run (Figs. 4.2c and 4.3c). In addition, around Lake Michigan the 12-hour accumulated precipitation from the 9-km grid spacing forecast from UKF (Fig. 4.2c) has less coverage than that in the other two model runs using EXP and BASE (Figs. 4.2 a and b), again making UKF's precipitation coverage more similar to the observations. Note that the MPE observations are only limited to land areas and thus no observational data exists over the ocean. Thus, large precipitation over the ocean [lower right corner in the Figs. 4.2 (a-f)] simulated by the model cannot be verified.

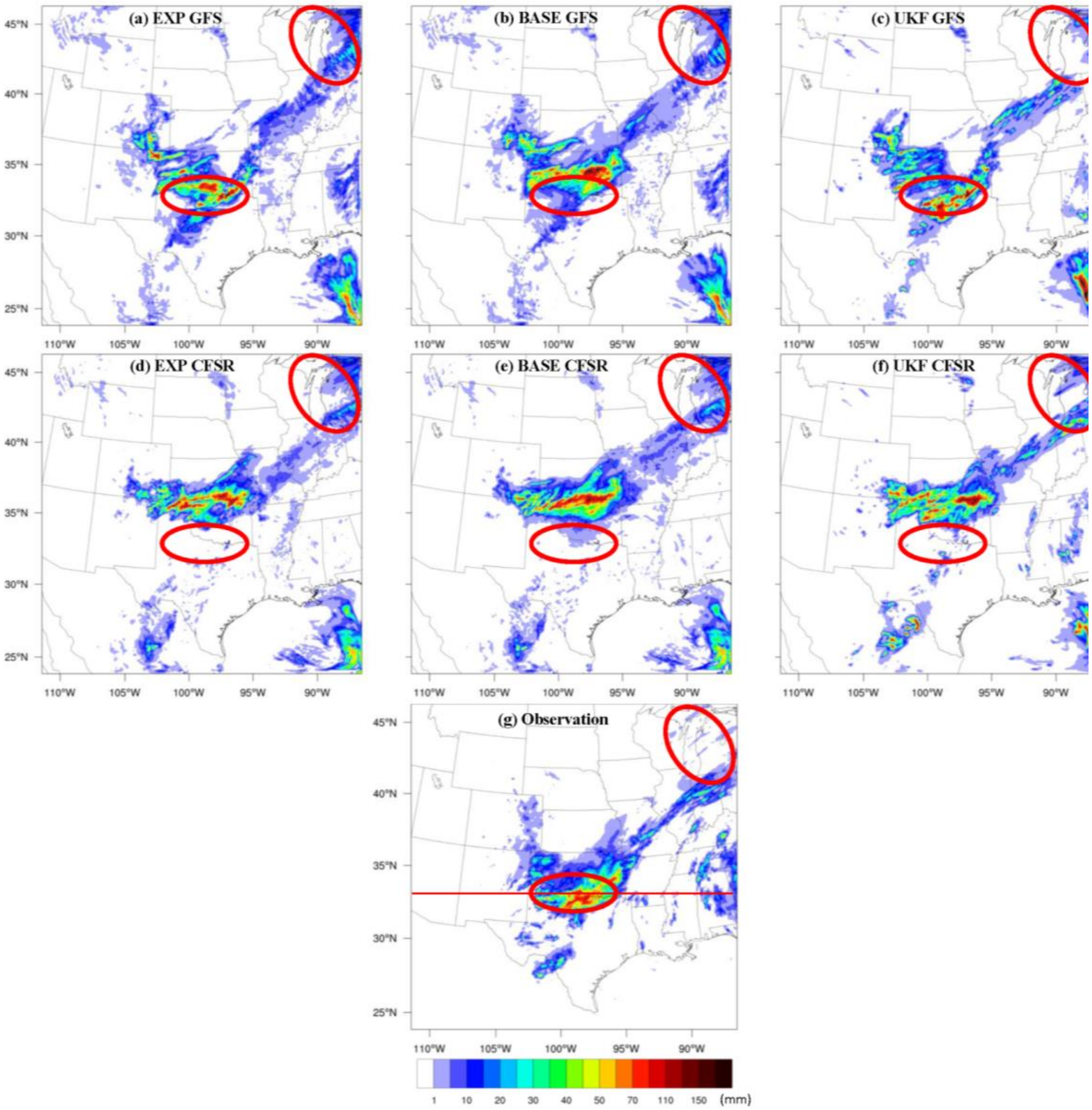

Fig. 4.2 Comparative example of simulated 12-hour (0000 UTC – 1200 UTC 5 June 2002) accumulated precipitation (mm) over a 9-km grid spacing domain with GFS (top), CFSR (middle) for EXP (a, d), BASE (b, e), and UKF (c, f), and (g) Stage IV observed precipitation.

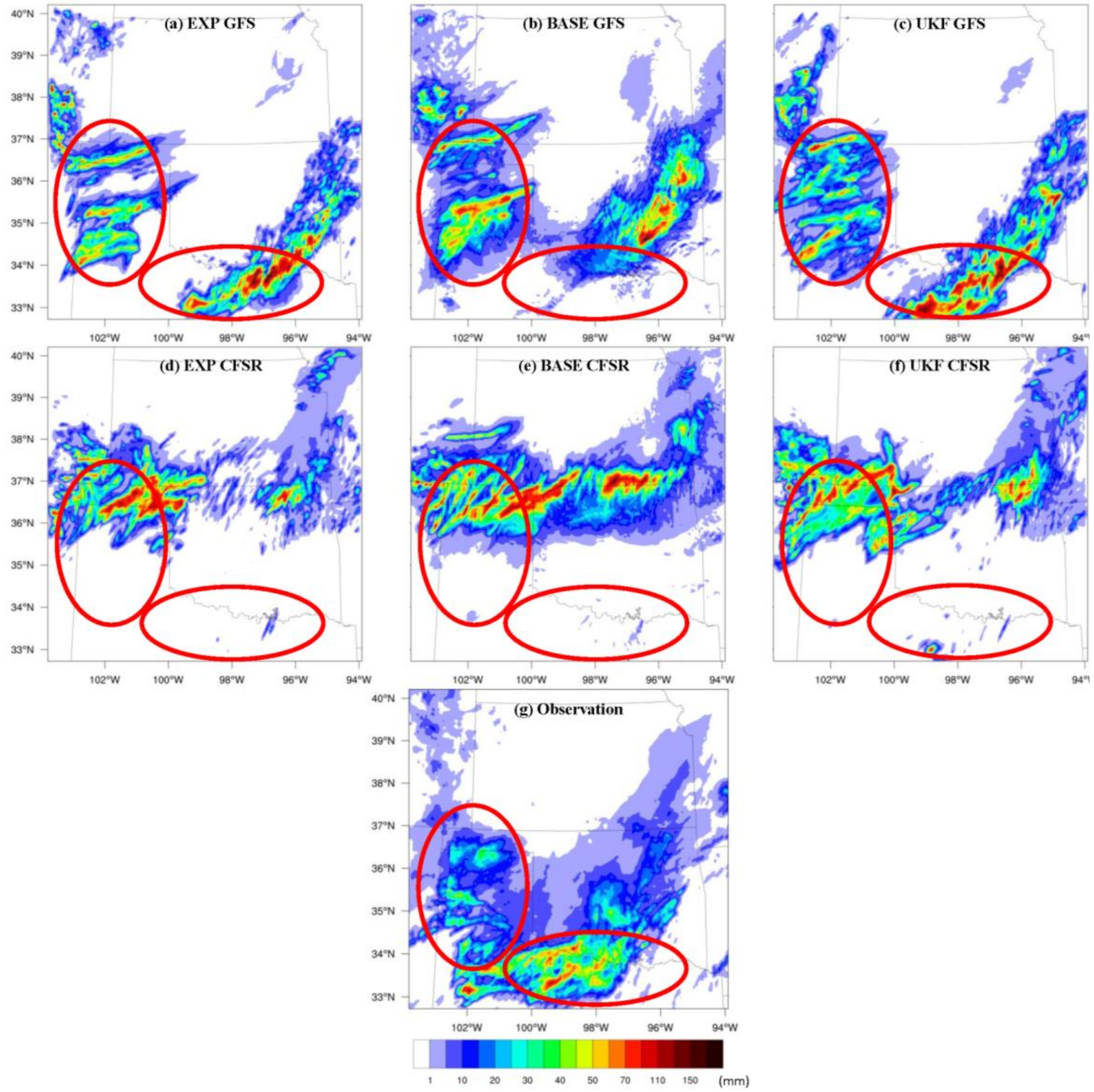

Fig. 4.3 Comparative example of simulated 6-hour (0000 UTC – 0600 UTC 5 June 2002) accumulated precipitation (mm) over a 3-km grid spacing domain with GFS (top), CFSR (middle) for EXP (a, d), BASE (b, e), and UKF (c, f), and (g) Stage IV observed precipitation.

For cloudy skies, outgoing longwave radiation (OLR) is reduced as opposed to clear skies and thus intercomparison of modeled OLR (W m^{-2}) can point out differences in simulations of cloud placement and depth. The OLR at 1800 UTC (1pm CDT) 5 June 2002 for WRF simulations with GFS for the 9- and 3-km grid spacing domains

(Experiments 1, 3, and 5 in Table 4.1) are shown in Fig. 4.4. The time shown is for the 42nd forecast hour of the 48-hour simulations when convection is active. Satellite cloud coverage images available from the NOAA's Aviation Digital Data Services [http://aviationweather.gov/adds/] are used for comparison to the EXP, BASE, and UKF runs. The OLR over the 9-km grid spacing domain [Figs. 4.4(a-d)] indicates that the southwest to northeast orientation of a band of low OLR for the UKF is more comparable to the satellite observation and contains more detailed information due to the subgrid-scale effects that are included here but not present in the BASE and EXP runs. It also shows less OLR for the UKF due to subgrid clouds (i.e., Michigan, Alabama, Mississippi, and Texas) and more OLR under less cloudy regions (i.e., Indiana, Ohio, and Kentucky) compared with those for EXP and BASE. In addition, as one of the key components of the surface energy budget, the representation of downward shortwave radiation (DSR) is also used for the comparison. Fig. 4.5 shows DSR for 1800 UTC (1pm CDT) 5 June 2002 along with satellite cloud coverage showing widespread cloudiness throughout Texas, Oklahoma, Missouri, Tennessee, Kentucky, Indiana, and Illinois. The DSR for the 9-km grid spacing over Tennessee, Kentucky, Mississippi and Alabama in EXP and BASE indicates clear sky conditions (Figs. 4.5 b and c). However, in UKF, the DSR indicates more cloud coverage (Fig. 4.5d) similar to that seen in the observations (Fig. 4.5a). Further, the DSR for the 3-km grid spacing simulations [Figs. 4.5 (f-h)] indicate that the cloud coverage for UKF is larger and in better agreement with the observations (Fig. 4.5e). This result is primarily because of the UKF scheme where the radiative effects of subgrid-scale clouds can be realistically represented even in grid spacing smaller than 4 km. Thus, the UKF configuration improves the cloud cover simulation, producing more realistic simulated radiation which could contribute to a better precipitation forecast.

Improved representation of cloudiness also affects the temporal variations of surface radiation in UKF for high-resolution model forecasts. For example, the measured 48-hour variations of downward longwave and shortwave fluxes and the corresponding simulations at New Salem (37.31°N, 98.94°W), KS (IHOP_2002 site 7) at 3-km grid spacing (Figs. 4.6 a and b) indicate that UKF modulates the radiative impacts in the model, particularly during the second day of the forecast. Both the EXP and BASE show large biases in shortwave fluxes with more than 600 W m^{-2} overestimations in the second day. The UKF simulation decreases the downward shortwave flux while increasing the downward longwave flux with the help of improved representation of cloudiness (Figs. 4.6 a and b), leading to an overall improvement in the temporal variability of the surface fluxes. The increased cloudiness from UKF also reduces the surface temperature (Fig. 4.6c) by about 5°C. The UKF also shows a better simulation than the others in terms of variability, especially for the last 6 hours of the run. However, the impact on the 2-m specific humidity (Fig. 4.6d) is not significantly different among runs because it depends on several land surface parameters such as soil moisture.

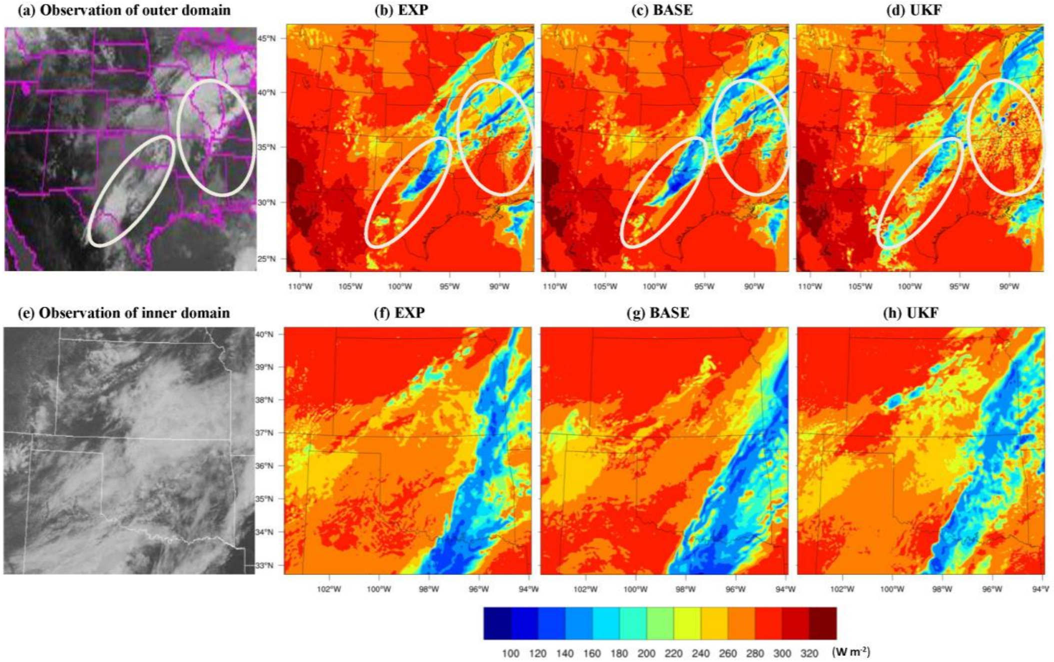

Fig. 4.4 Outgoing longwave radiation (W m^{-2}) with GFS at 1800 UTC (1 pm CDT) 5 June 2002 over a 9-km grid spacing domain (top) and 3-km grid spacing domain (bottom) for EXP (b, f), BASE (c, g), and UKF (d, h).

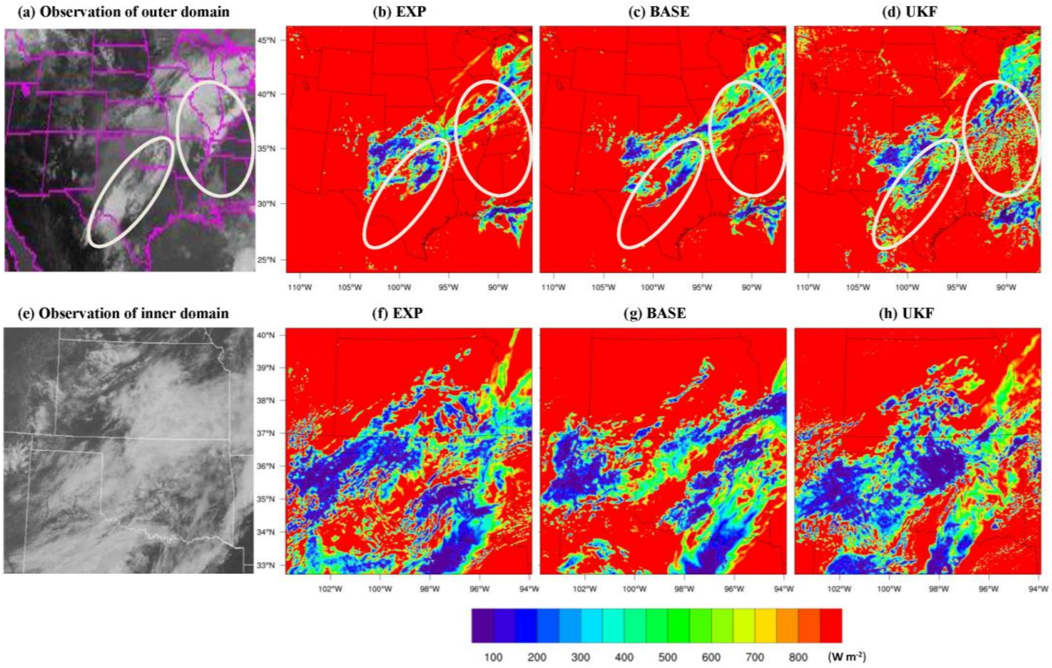

Fig. 4.5 Surface shortwave radiation (W m^{-2}) with GFS at 1800 UTC (1 pm CDT) 5 June 2002 over a 9-km grid spacing domain (top) and 3-km grid spacing domain (bottom) for EXP (b, f), BASE (c, g), and UKF (d, h).

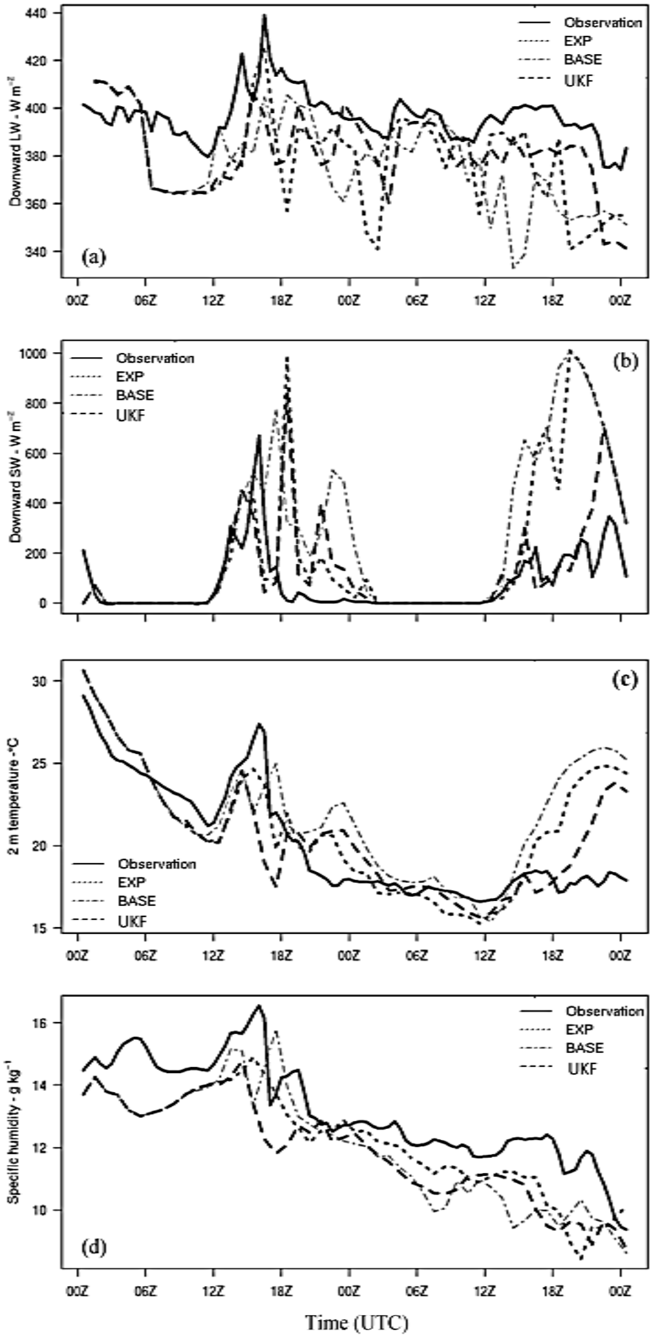

Fig. 4.6 48-hour variation (0000 UTC 4 June – 0000 UTC 6 June 2002) of (a) downward longwave flux at ground surface (W m^{-2}), (b) downward shortwave flux at ground surface (W m^{-2}), (c) temperature at 2 m (°C), and (d) specific humidity at 2 m (g kg^{-1}), at New Salem (37.31°N, 98.94°W), KS, from IHOP_2002 site 7 measurements (solid line) and corresponding simulations in EXP (dotted line), BASE (dot-dash line), and UKF (dash line) with GFS at 3-km grid spacing.

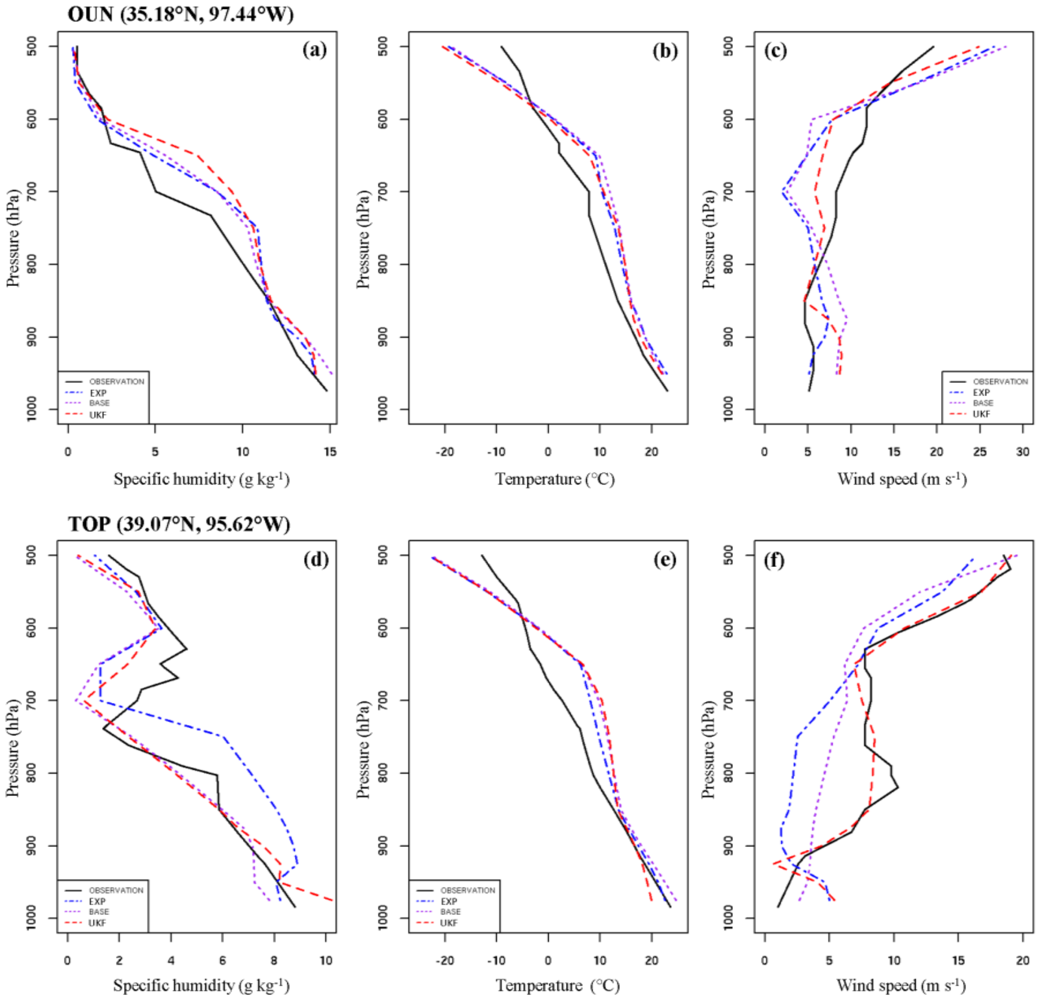

Fig. 4.7 Sounding profile at 0000 UTC 6 July 2002 of specific humidity (g kg^{-1}) (a, d), potential temperature (K) (b, e), and wind speed (m s^{-1}) (c, f), valid at Norman, OK (OUN, 35.18°N, 97.44°W) (top) and Topeka, KS (TOP, 39.07°N, 95.62°W) (bottom).

To study the functionality of the new science updates used in the KF scheme on the entire model atmosphere, we present sounding profiles (Fig. 4.7) at 0000 UTC 6 July 2002 for specific humidity, potential temperature, and wind speed at Norman, OK (OUN, 35.18°N, 97.44°W) and Topeka, KS (TOP, 39.07°N, 95.62°W) simulated at 3-km grid spacing and compared with respective observations available from the University of Wyoming (http://weather.uwyo.edu/upperair/sounding.html). For both observation sites, there is no clear indication of which simulation is outperforming the others, indicating that the UKF has only minor differences with the other simulations for this observational time. However, tropospheric wind speeds and surface specific humidity simulated by the UKF seem to be closer to the observations. A detailed comparison of lower tropospheric profiles is presented in the following section.

4.4.2 Simulation period 0000 UTC 28 July – 0000 UTC 30 July 2010: Experiments 19-24:

To extend this case study, a second set of 48-hour simulations was initialized at 0000 UTC 28 July 2010 (Experiments 19-24). Comparative examples of simulated 6-hour accumulated precipitation on the second day over 9- and 3-km grid spacings are shown in Figs. 4.8 and 4.9. It is noted that the initial conditions still play an important role in the model simulation, but the precipitation forecast with CFSR has no spatial shift in this case, relative to observations. The general rainfall locations of UKF with GFS and CFSR are similar and close to the observations. The KF scheme in the EXP and the BASE runs with 9-km grid spacing again result in heavier amounts of rainfall (Figs. 4.8 a-b and d-e), while UKF reduces the excessive precipitation and leads to a much better simulation. In the 3-km grid spacing precipitation forecast (Fig. 4.9), excessive precipitation occurs with the BASE run, but better forecasts are evident in EXP and UKF. Since the high-resolution MPE (Stage IV) hourly rainfall products have some biases (e.g., Wang et al. 2008; Westcott et al. 2008; Westcott 2009), the visible satellite cloud observation is

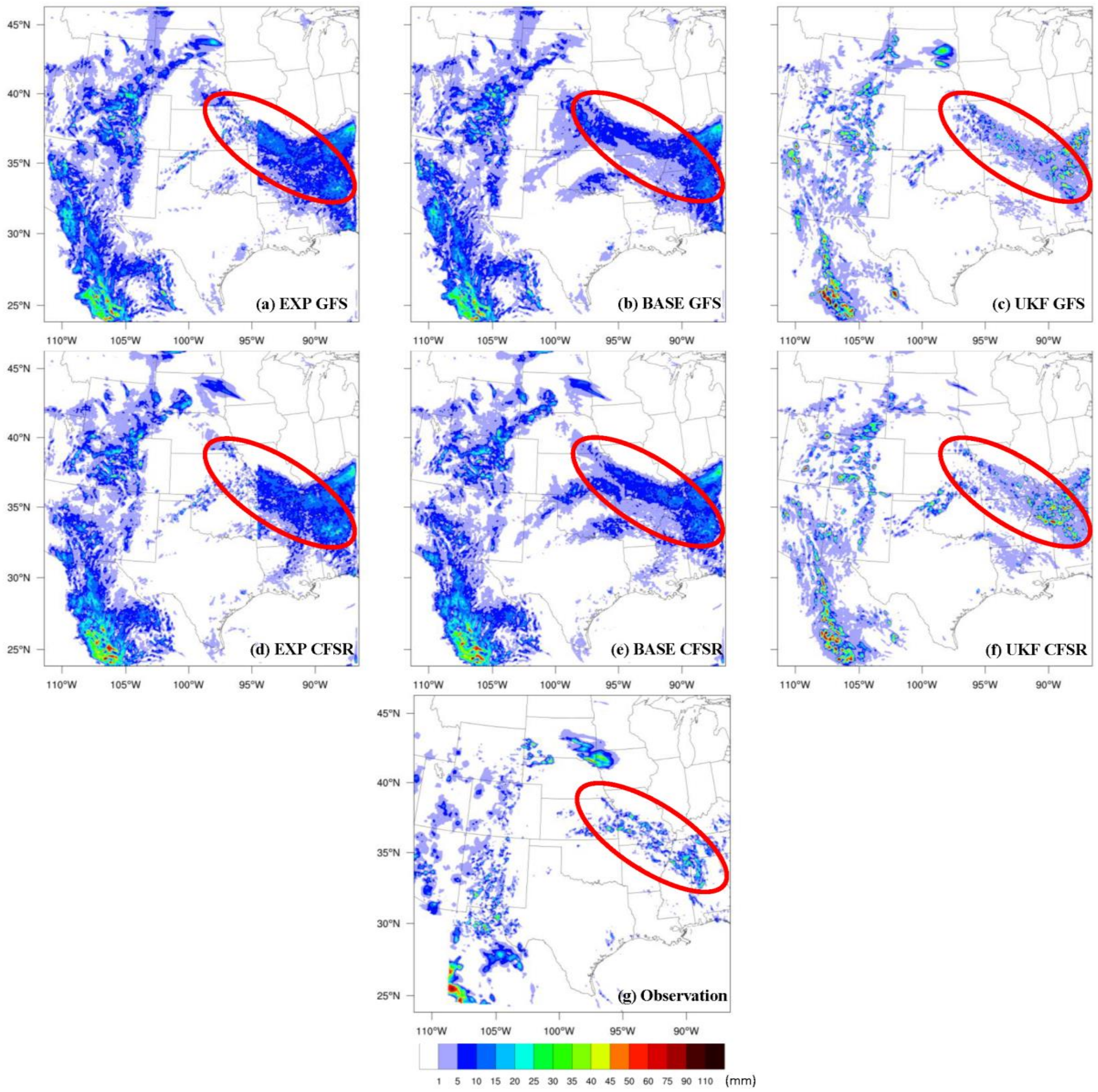

Fig. 4.8 Comparative example of simulated 6-hour (1800 UTC 29 July – 0000 UTC 30 July 2010) accumulated precipitation (mm) over a 9-km grid spacing domain with GFS (top), CFSR (middle) for EXP (a, d), BASE (b, e), and UKF (c, f), and (g) Stage IV observed precipitation.

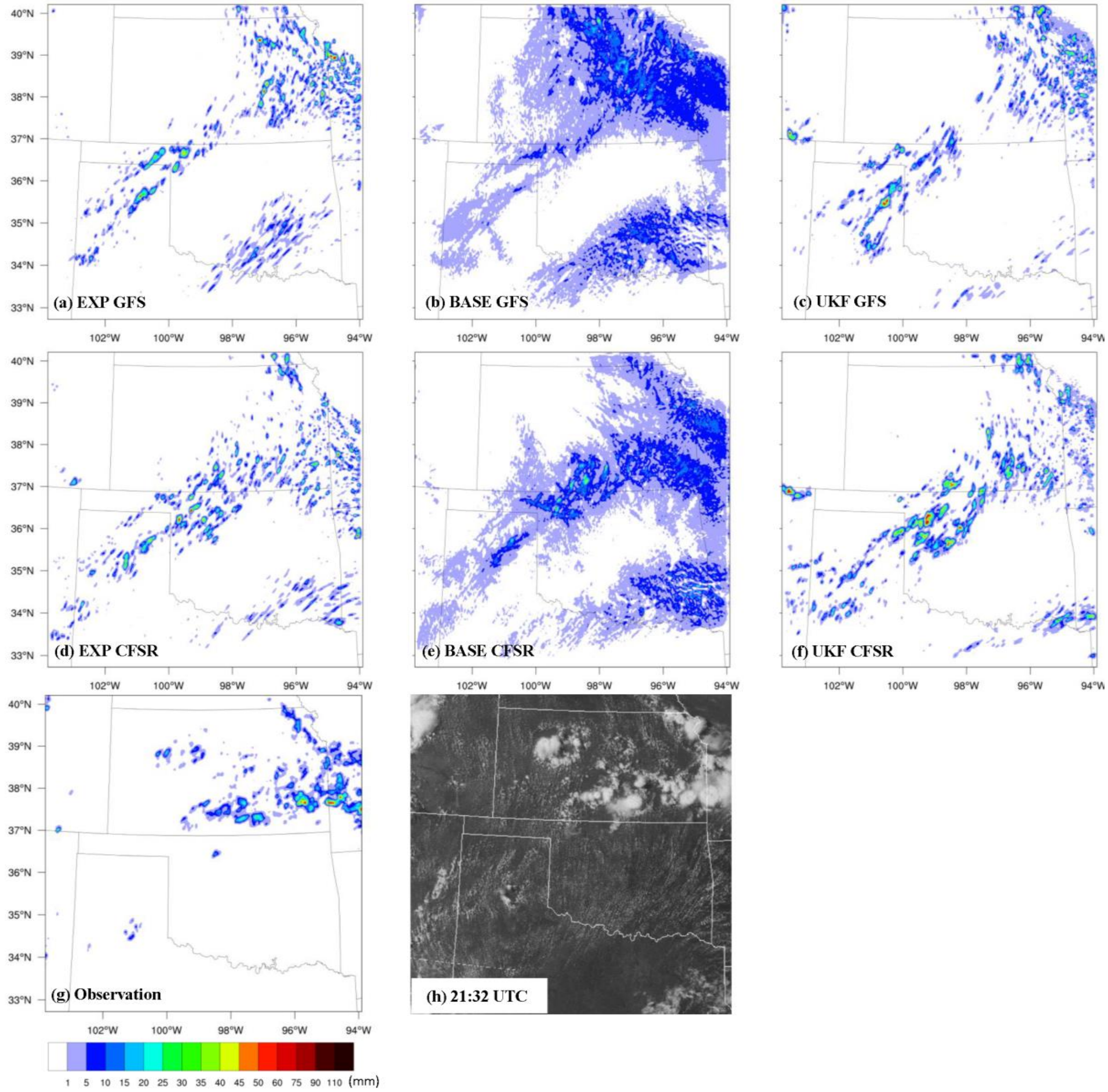

Fig. 4.9 Comparative example of simulated 6-hour (1800 UTC 29 July – 0000 UTC 30 July 2010) accumulated precipitation (mm) over a 3-km grid spacing domain with GFS (top), CFSR (middle) for EXP (a, d), BASE (b, e), and UKF (c, f), and (g) Stage IV observed precipitation and (h) visible satellite image valid at 2132 UTC 29 July 2010. The satellite image is obtained from http://aviationweather.gov/adds/ managed by NOAA's Aviation Digital Data Services.

included in the analysis to provide additional information. For the 9- and 3-km grid spacing runs, the observed 6-hour accumulated precipitation does not exceed 1 mm in most of the northern Texas panhandle, however, cloudiness (which is taken as a key input parameter in our research) can be seen in Texas in the visible satellite image (Fig. 4.9h).

The observed cloudiness indicates that the precipitation fields simulated in the high resolution grid by EXP and UKF in Figs. 4.9 (a, c, d, and f) are comparable to each other. Furthermore, it is demonstrated that the explicit treatment of convection (no cumulus parameterization) with a 3-km grid spacing at times can adequately predict convective systems and precipitation, consistent with the results of Done et al. (2004). For this case study, the UKF results successfully demonstrate that it does not decrease the accuracy of precipitation forecasts, relative to the EXP (explicit treatment of convection). However, Done et al. (2004) also pointed out that for some cases, explicit precipitation treatments suffered with an increasing propagated bias in the forecasts which may be mitigated using UKF treatment.

Three rain rate thresholds (5, 15, and 25 mm h^{-1}) were used to separate out light, medium, and heavy precipitation for the experiments. Within the thresholds, precipitation, which was accumulated over time, was area-averaged over the 3-km grid spacing domain. Fig. 4.10 shows the 48-hour (0000 UTC 28 July – 0000 UTC 30 July 2010) period area-averaged accumulated precipitation for simulations in EXP, BASE, and UKF, reflecting dynamic changes in modeling of convective events, and for forecasts with GFS and CFSR, reflecting the change in initial and boundary conditions. As expected, results show that the area-averaged precipitation rates from the high-resolution simulation with UKF are closer to the corresponding Stage IV observations in precipitation intensity and the timing of convection initiation for both GFS and CFSR. It can be seen that improvements of the area-averaged precipitation are made by UKF with GFS for the very light rain rates (0-5 mm h^{-1}), the moderate rain rates (15-25 mm h^{-1}), and the heavier rain rates (greater than 25 mm h^{-1}), while the BASE run performs poorest for all the rates. The difference in the light rain rates (5-15 mm h^{-1}) with GFS between EXP and UKF is very small. The area-averaged rainfall simulated using CFSR is found to be heavier compared to the GFS results. In addition, the 48-hour averaged root mean square error (RMSE) for the 3-km domain is shown in Table 4.2. In general, the 48-hour averaged RMSE of the area-averaged precipitation is greatly decreased by UKF for all rainfall rates. It indicates that UKF outperforms the other two simulations at every threshold, regardless of the dataset used for initial and boundary conditions. The differences in the area-averaged RMSE between GFS and CFSR for EXP are small (less than or equal to 0.10 mm h^{-1} at every threshold) for all but greater than 25 mm h^{-1} cases, while the differences for BASE are obviously larger (~ 0.16 to 0.33 mm h^{-1}). Although a negligibly small difference is seen for UKF for the very light rain rate, the differences in RMSE between GFS and CFSR for the other rates are larger. In the heavier rainfall threshold, differences in the 48-hour averaged RMSE are significant for all the experiments (i.e., 0.29 mm h^{-1} for EXP, 0.26 mm h^{-1} for BASE, and 0.25 mm h^{-1} for UKF). These differences reflect the influence of model initial conditions on the convection scheme's contribution to the precipitation forecast, suggesting that changes in the model initial conditions can have a direct effect on the simulation of precipitation through the CP used in NWP models.

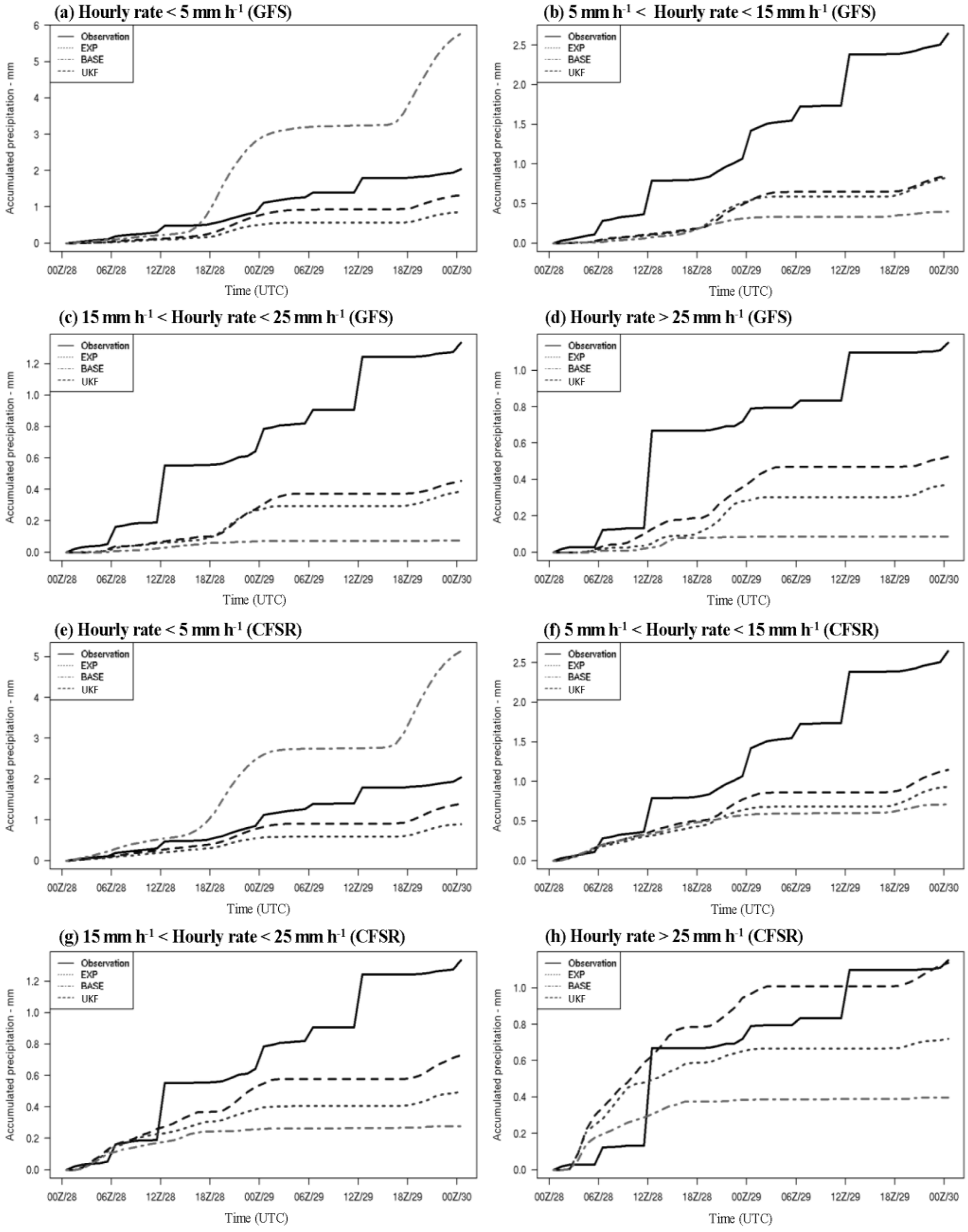

Fig. 4.10 48-hour (0000 UTC 28 July – 0000 UTC 30 July 2010) area-averaged over 3-km grid spacing precipitation (mm) from Stage IV observations (solid line) and corresponding simulations of EXP (dotted line), BASE (dot-dash line), and UKF (dashed line) with GFS (a-d) and CFSR (e-h).

Table 4.2 48-hour averaged root mean square error (RMSE) of area-averaged precipitation over a 3-km grid spacing domain

RMSE	GFS				CFSR			
	0-5 mm h^{-1}	5-15 mm h^{-1}	15-25 mm h^{-1}	greater than 25 mm h^{-1}	0-5 mm h^{-1}	5-15 mm h^{-1}	15-25 mm h^{-1}	greater than 25 mm h^{-1}
EXP	0.74	1.09	0.60	0.55	0.70	1.00	0.50	0.26
BASE	1.68	1.29	0.77	0.71	1.35	1.07	0.61	0.45
UKF	0.47	1.06	0.55	0.43	0.45	0.87	0.37	0.18

Fig. 4.11 shows the vertical profile of virtual potential temperature for two grid cells for the 9- and 3-km grid spacings at 0000 UTC 29 July 2010. Note that all three simulations miss the shallow surface inversion at Topeka, KS (TOP, 39.07°N, 95.62°W) (Figs. 4.11 c and d) and EXP and UKF underestimate the surface temperature (Figs. 4.11 a and b). It is difficult to pick out whether EXP or UKF performed better at Amarillo, TX (AMA, 35.23°N, -101.7°W) since EXP looks slightly better in the lower levels and UKF performs best in the upper portion of the profile (Figs. 4. 11 a and b). Also note that the virtual potential temperatures for UKF are almost constant with height in the PBL and close to the observations from the International H2O Project (IHOP), indicating that the MYJ scheme used in the WRF simulations with the UKF scheme is capable of simulating improved well-mixed boundary layers.

4.4.3 Simulation period 0000 UTC 5 July – 0000 UTC 7 July 2010: Experiments 13-18:

A distinct widespread northeast to southwest rainfall was observed in Oklahoma during the local afternoon hours of 6 July 2010 (Figs. 4.12 and 4.13). Estimated 6-hour (1800 UTC 5 July – 0000 UTC 7 July 2010) accumulated precipitation for the EXP, BASE, and UKF simulations and the Stage IV observed precipitation are compared and shown in

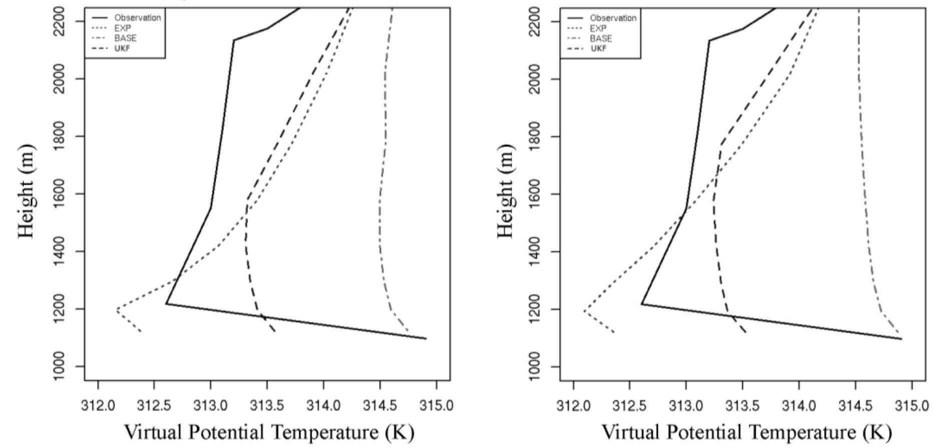
(a) 0000 UTC 29 July, 2010 at dx = 9 km, Amarillo (TX,USA) (b) 0000 UTC 29 July, 2010 at dx = 3 km, Amarillo (TX,USA)

(c) 0000 UTC 29 July, 2010 at dx = 9 km, Topeka (KS,USA) (d) 0000 UTC 29 July, 2010 at dx = 3 km, Topeka (KS,USA)

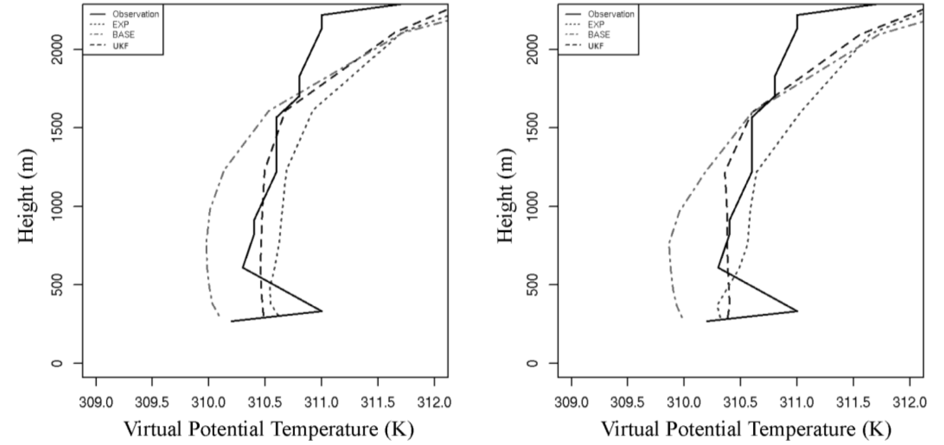

Fig. 4.11 Vertical profile of virtual potential temperature (K) at 0000 UTC 29 July 2010 at 9-km grid spacing domain (a,c) and 3-km grid spacing domain (b,d) valid at Amarillo, TX (AMA, 35.23°N, -101.7°W) (top) and Topeka, KS (TOP, 39.07°N, 95.62°W) (bottom).

Figs. 4.12 and 4.13. In Fig. 4.12, the UKF scheme successfully reduced excessive rainfall produced by the BASE scheme. More interestingly, over the parent domain of EXP, scale separation issues with two-way nesting can be seen in the precipitation field as the convection scheme differs across the nest boundary (Figs. 4.12 a and d). This boundary issue is alleviated by using the same convection scheme (as in BASE or UKF) in the inner domain [Figs. 4.12 (b-c) and 4.12 (e-f)].

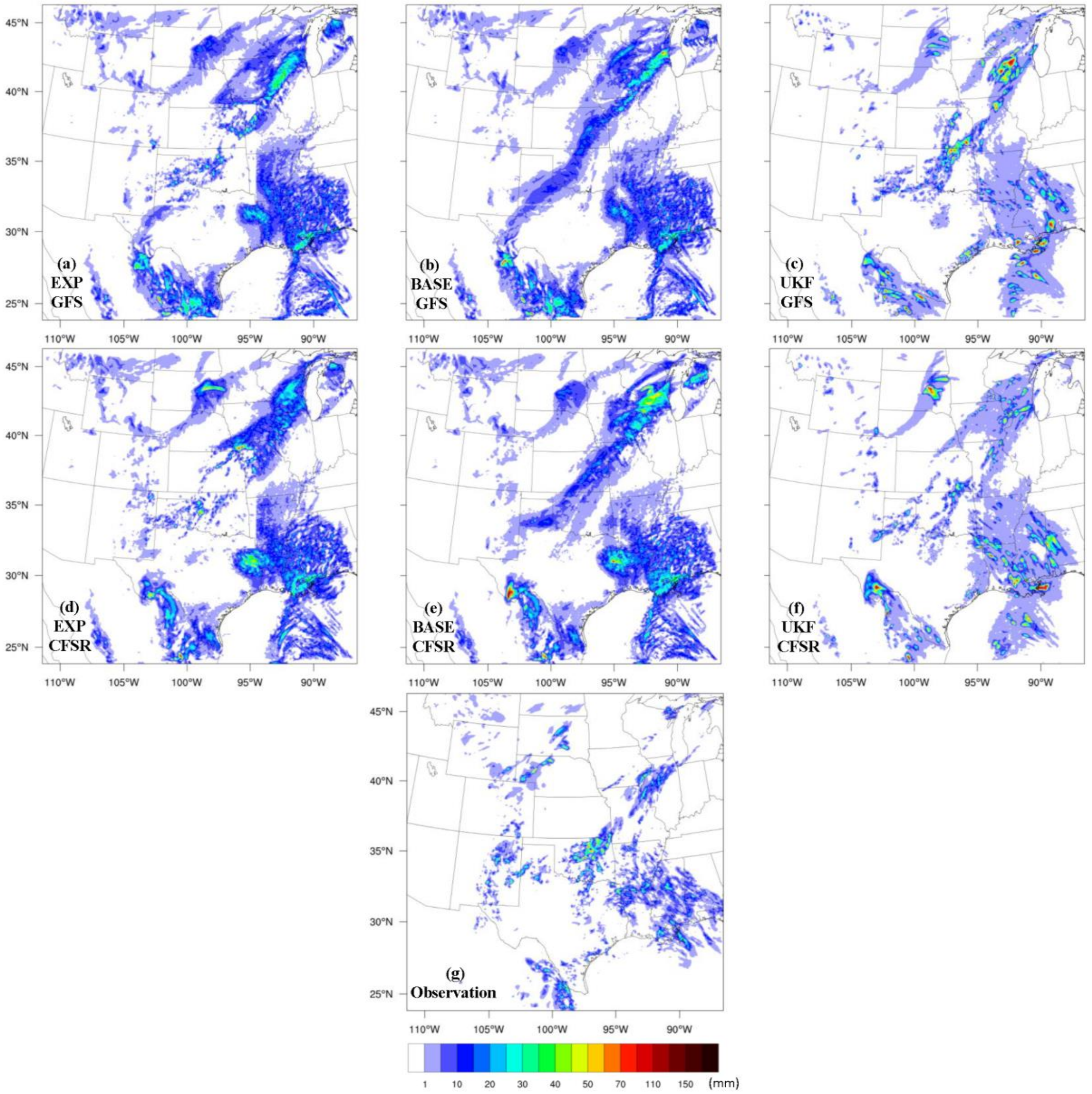

Fig. 4.12 Comparative example of simulated 6-hour (1800 UTC 6 July – 0000 UTC 7 July 2010) accumulated precipitation (mm) over a 9-km grid spacing domain with GFS (top), CFSR (middle) for EXP (a, d), BASE (b, e), and UKF (c, f), and (g) Stage IV observed precipitation.

In the 3-km grid spacing simulations (Fig. 4.13), EXP forecasts more precipitation in northeast Kansas, while producing less precipitation than observed in Oklahoma. The improvement of using better initial conditions on high-resolution rainfall predictions can be seen in EXP and UKF, and at 3-km grid spacing, the precipitation simulated by UKF

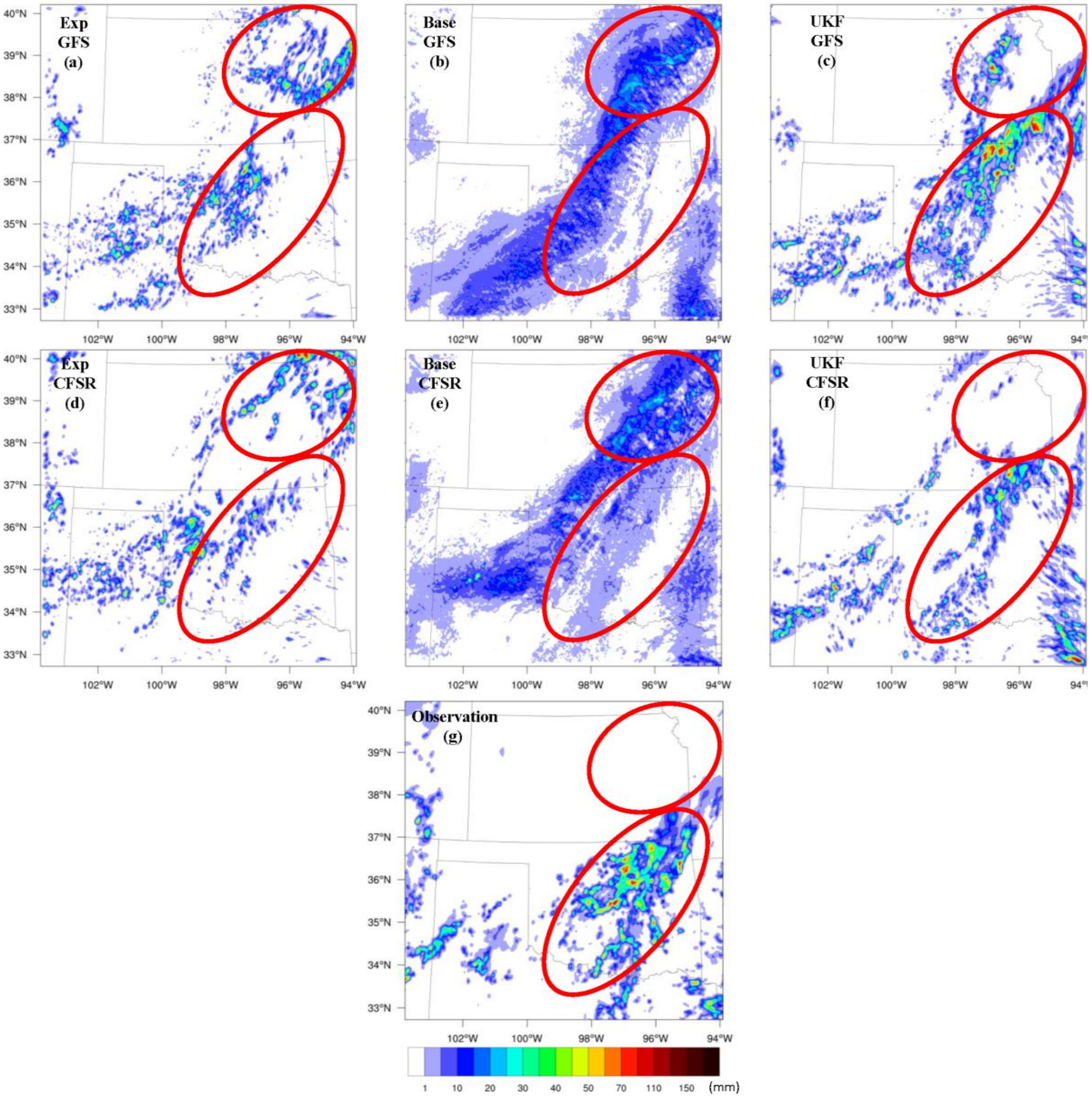

Fig. 4.13 Comparative example of simulated 6-hour (1800 UTC 6 July – 0000 UTC 7 July 2010) accumulated precipitation (mm) over a 3-km grid spacing domain with GFS (top), CFSR (middle) for EXP (a, d), BASE (b, e), and UKF (c, f), and (g) Stage IV observed precipitation.

with GFS is similar to the Stage IV observation. However, the BASE run simulates more rainfall than observed and there are no obvious improvements when changing initial conditions. Since the UKF is able to improve the high-resolution precipitation forecast by introducing subgrid-scale effects, an instantaneous east-west oriented transect of the subgrid-scale rain rate simulated at 9- and 3-km grid spacings is taken across Oklahoma and northern Texas at 2000 UTC 5 July 2010 (Fig. 4.14). It is found that the simulated convective rain rate for the finer resolution model (i.e., 3-km grid spacing) is generally less than that for the coarser resolution model (i.e., 9-km grid spacing) and confirms that subgrid-scale precipitation decreases when the model resolution increases.

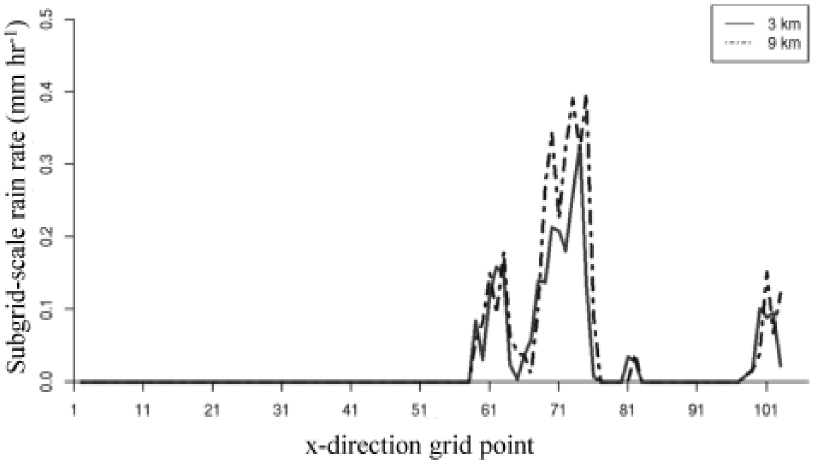

Fig. 4.14 The subgrid-scale rain rate (mm hr^{-1}) simulated at 9- and 3-km grid spacings from the UKF scheme with GFS at 2000 UTC 5 July.

4.4.4 Sensitivity to microphysics schemes: Experiments 7-12 and 31-36:

Sensitivity analysis is useful for diagnosing the impacts of interactions of convective treatment and microphysics on regional forecasts of rainfall. A 48-hour period starting at 0600 UTC 14 June 2002 during IHOP_2002 is examined due to significant convective activity and a large regional event that occurred over the most of the Oklahoma and larger regions of Kansas and north Texas (Wilson and Roberts 2006). Sensitivity experiments (Experiments 7-12 and 31-36 in Table 4.1) were conducted by varying model convective and microphysics schemes. Six-hour accumulated precipitation

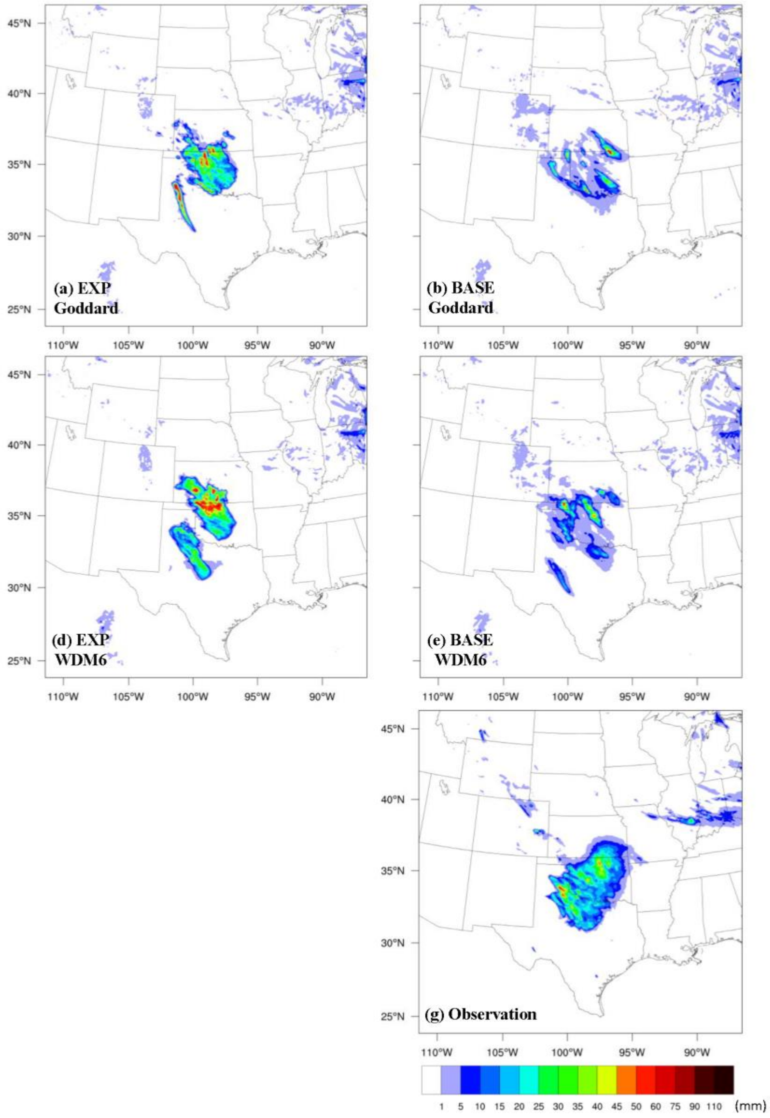

Fig. 4.15 Comparative example of simulated 6-hour (0000 UTC – 0600 UTC 16 June 2002) accumulated precipitation (mm) over a 9-km grid spacing domain with the CFSR and Goddard microphysics scheme (top), WRF Double-Moment 6-class scheme (middle) for the EXP (a, d), BASE (b, e), and UKF (c, f), and (g) Stage IV observed precipitation.

forecasts from all the experiments are compared to Stage IV precipitation analyses. Fig. 4.15 provides an example of 9-km grid spacing forecasts of 6-hour accumulated precipitation with the two microphysical parameterizations and three convective treatments. Since the outer domain is large compared to the inner domain, it mitigates

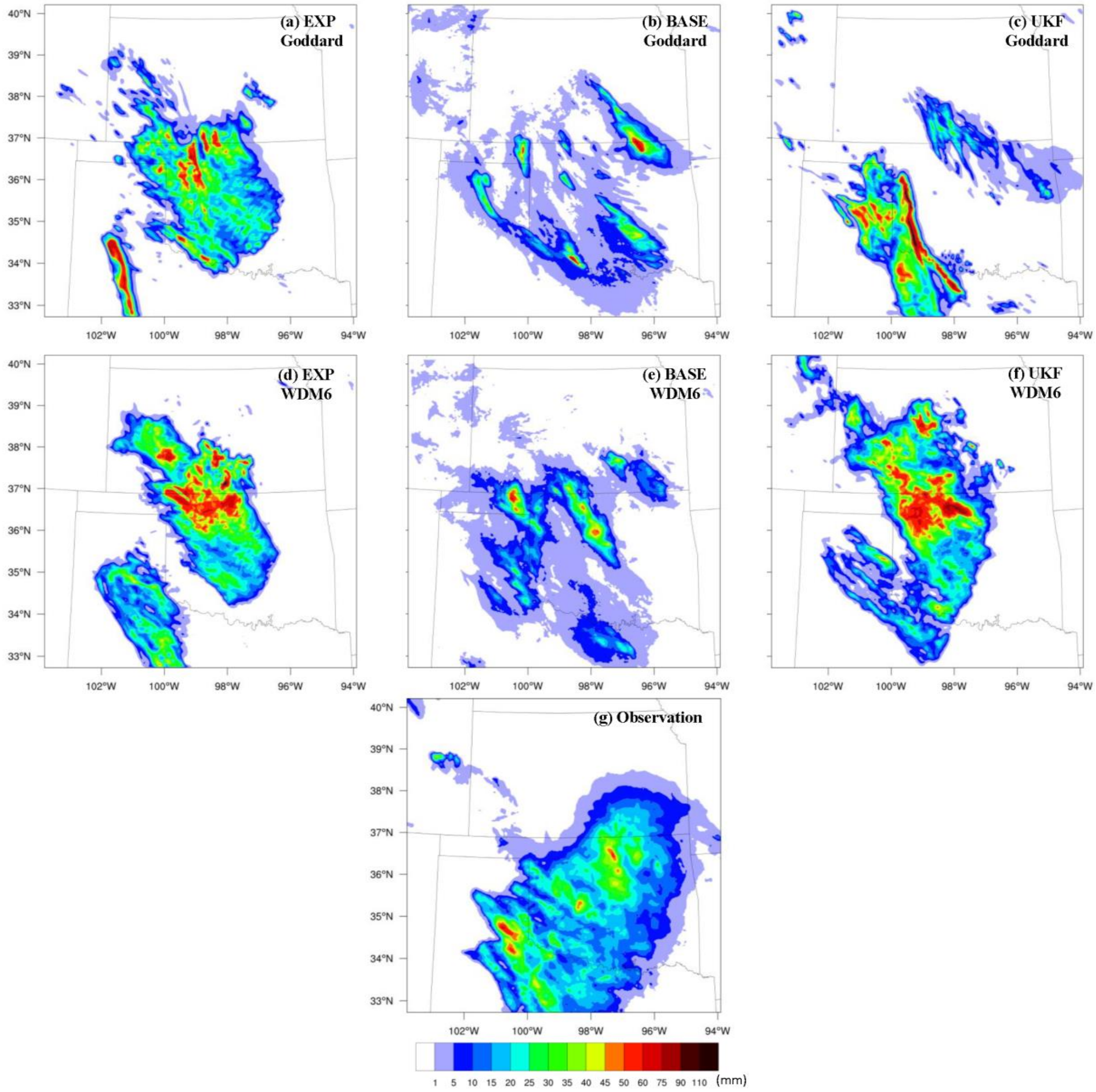

Fig. 4.16 Comparative example of simulated 6-hour (0000 UTC – 0600 UTC 16 June 2002) accumulated precipitation (mm) over a 3-km grid spacing domain with the CFSR and Goddard microphysics scheme (top), WRF Double-Moment 6-class scheme (middle) for EXP (a, d), BASE (b, e), and UKF (c, f), and (g) Stage IV observed precipitation.

the lateral boundary condition impacts on the inner domain. Fig. 4.15 shows that the distributions of simulated precipitation vary significantly with different combinations of convective and microphysics schemes. Fig. 4.16 shows an example of the sensitivity of precipitation to microphysical parameterization at 3-km grid spacing. The WDM6 scheme produces a large swath of precipitation with high values in the center. The Goddard scheme with UKF is not able to provide a large area of precipitation, although the orientation of the precipitation distribution is similar to observed rainfall. These results demonstrate that the impact of using the UKF scheme will vary from case to case and improvements may not be consistent with differing microphysics schemes. Therefore, for the cases where good initial conditions are not present, the microphysics scheme and the UKF scheme have limitations on improving the precipitation forecast.

4.4.5 Sensitivity to each science update: Experiments 25-30:

We recall that the three updates which include properly representing timescale (DYNTAU), grid-scale vertical velocity (WUP), and entrainment effect (ENT), have been employed to modify the original KF scheme, and as a result, the UKF scheme has substantially reduced the excessive precipitation biases for NWP high-resolution forecasts. To find out which update is dominating the precipitation differences, six additional simulations (Experiments 25-30 in Table 4.1) using each update separately initialized by GFS and CFSR were conducted for simulation period 0000 UTC 28 July – 0000 UTC 30 July 2010. Fig. 4.17 shows 48-hour (0000 UTC 28 July – 0000 UTC 30 July 2010) 3-km grid spacing area-averaged accumulated precipitation (mm) from Stage IV observations (black solid) and corresponding simulations in DYNTAU, WUP, ENT, UKF, and BASE using GFS (Fig. 4.17a) reanalysis data.

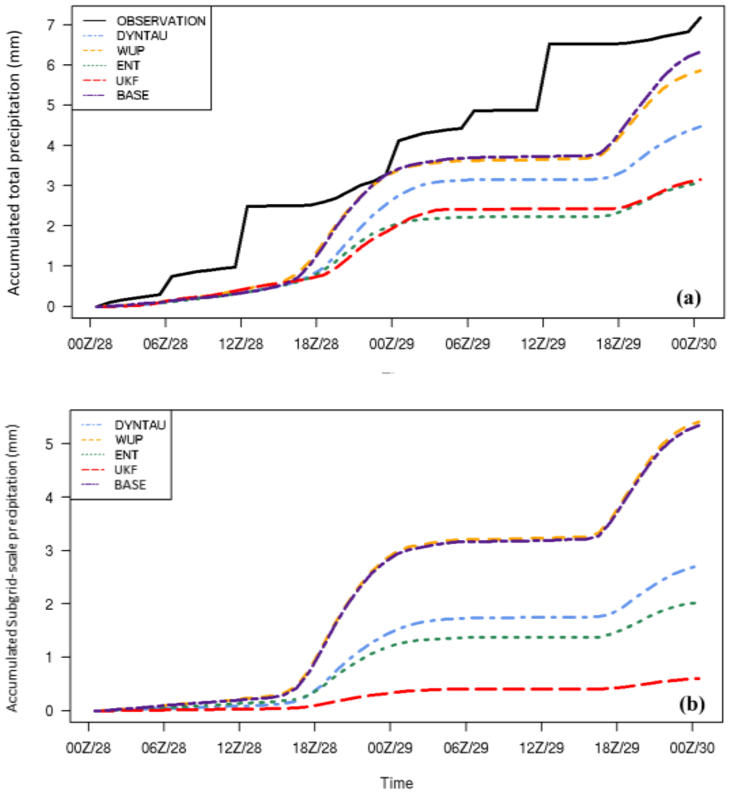

Fig. 4.17 48-hour (0000 UTC 28 July – 0000 UTC 30 July 2010) area-averaged over 3-km grid spacing (a) accumulated total precipitation (mm) with GFS and (b) accumulated subgrid-scale precipitation (mm) with GFS: Stage IV observations (black solid) and corresponding simulations of DYNTAU (blue dot-dash), WUP (orange dashed), ENT (green dotted), UKF (red long-dashed), and BASE (purple double dash).

Since BASE produced more precipitation over wide areas as compared to the observation at 3-km grid spacing (Fig. 4.9), the simple area-averaged precipitation for BASE compensates its low precipitation intensity with an overprediction of areal rainfall coverage, resulting in better agreement of the area-averaged accumulated total precipitation with the observation. WUP slightly reduces the area-averaged total precipitation compared to BASE, indicating that the update with subgrid-scale updraft mass flux impacts on grid-scale vertical velocity helps to slightly increase saturation levels of the environment, thereby leading to a minor increase in subgrid-scale precipitation. DYNTAU is found to contribute more to decreasing the simulated rainfall amount. One modeling fact of many CPSs is that as model resolution increases, impacts from a standard subgrid-scale parameterization become more significant. However, with the adjustment timescale (τ) update, the value of τ increases and results in longer time to remove CAPE for atmospheric stabilization, resulting in the simulated precipitation by DYNTAU being reduced, a desired feature. In the update of the entrainment effects, the introduced scale-dependent Tokioka parameter, as well as the LCL-based methodology, in the high-resolution simulation helps to achieve the proper representation of convective clouds through increased entrainment. As a result, the hyperactivity of the subgrid-scale convection scheme is alleviated, leading to a decrease of subgrid-scale precipitation. Consistently, ENT reduces the precipitation from BASE, and it shows the minimum area-averaged precipitation among all of the simulations with a separated update. To summarize, the three different updates contribute differently to the precipitation changes and show non-linear impacts. We also found similar results using the CFSR reanalysis data (not shown). To further assess the relative contribution of each of the updates on precipitation components, i.e., subgrid-scale versus grid-scale, Fig. 4.17b shows 48-hour accumulated subgrid-scale precipitation obtained from using each of the updates. In the literature, a few studies (e.g., Wang et al. 2009; Snively and Gallus 2014; Van Weverberg et al. 2013) use the term "cloud-permitting" scale (quasi-convective resolution) for grid spacings which are smaller than 4 km. These studies demonstrate that grid-scale microphysics schemes are adequate to produce reasonable precipitation in model forecasts/simulations at cloud-permitting scales, implying that the subgrid-scale convective component is either weak or absent. As shown by comparisons of Figs. 4.17 a and b, the total precipitation in the UKF simulation is dominated by grid-scale precipitation, with the amount of subgrid rainfall below 1 mm for the entire forecast. To further examine relative intensity of precipitation with each of the updates, in Fig. 4.18 we present the accumulated value of 48-hour (0000 UTC 28 July – 0000 UTC 30 July 2010) 3-km grid spacing area-averaged precipitation (mm) from Stage IV and corresponding simulations in DYNTAU, WUP, ENT, UKF, and BASE with GFS for certain thresholds of hourly rates. For the rate less than 5 mm h^{-1}, UKF slightly under predicts while ENT is on average closest to the observations. Simulations with the other updates overpredict the observed rate. Results indicate that too much drizzle has been simulated by BASE and modifying the grid-scale vertical velocity alone cannot significantly improve the precipitation forecast. DYNTAU and ENT contribute to reduce the drizzle, and UKF, which includes all three updates, shows good improvement for the forecast of drizzle. But, for the rest of the hourly rates, UKF outperforms the other simulations. However, UKF still tends to underpredict precipitation values at rates greater than 5 mm h^{-1}. Fig. 4.19 shows the accumulated 48-hour (0000 UTC 28 July – 0000 UTC 30 July 2010) area-averaged subgrid-scale precipitation (mm) for 3-km grid spacing from simulations in DYNTAU, WUP, ENT, UKF, and BASE with GFS when the hourly rates are in the same thresholds as shown in Fig. 4.18. It can be seen that UKF primarily contributes to the precipitation forecast when rate is less than 5 mm h^{-1}, but negligibly improves the simulation when the rate is greater than 5 mm h^{-1} and less than 15 mm h^{-1}, and has zero contribution with higher hourly rain rates.

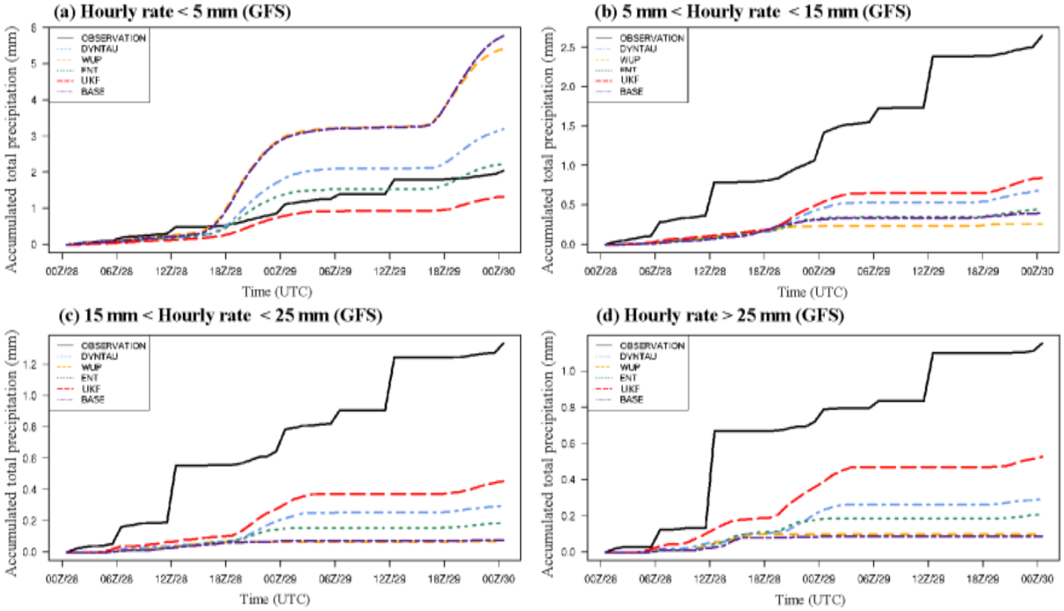

Fig. 4.18 48-hour (0000 UTC 28 July – 0000 UTC 30 July 2010) area-averaged over 3-km grid spacing total precipitation (mm) from Stage IV observations (black solid) and corresponding simulations of DYNTAU (blue dot-dash), WUP (orange dashed), ENT (green dotted), UKF (red long-dashed), and BASE (purple double dash) with GFS.

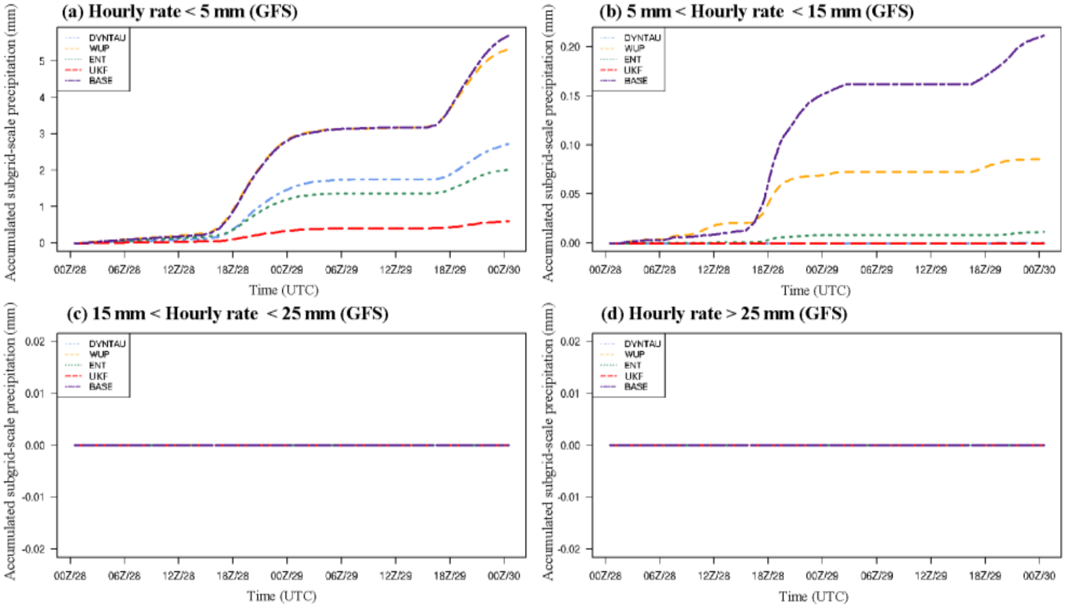

Fig. 4.19 48-hour (0000 UTC 28 – 0000 UTC 30 July 2010) area-averaged over 3-km grid spacing subgrid-scale precipitation (mm) from simulations of DYNTAU (blue dot-dash), WUP (orange dashed), ENT (green dotted), UKF (red long-dashed), and BASE (purple double dash) with GFS.

4.5 Summary and conclusions

The impacts of introducing parameterized cloud dynamics on high-resolution WRF model forecasts were examined at 9- and 3-km grid spacing, simulating regional precipitation over U.S. SGP with several cases of 48-hour forecasts. An updated KF scheme, including subgrid-scale cloud-radiation interactions (Alapaty et al. 2012; Herwehe et al. 2014), a dynamic adjustment timescale, a simple linear method using cloud updraft mass fluxes impacting grid-scale vertical velocity, and a LCL-based methodology for parameterizing entrainment, was developed for high-resolution simulations and implemented in the WRF model (version 3.4.1). The aforementioned parameters were adapted to be scale dependent, as shown in Equations 2, 5, and 9. Four cases of regional precipitation were selected and thirty-six 48-hour WRF experiments that were made with three different treatments of convection (no cumulus convection representation, original KF, and UKF) were initialized separately with two different initial conditions: the 1.0 degree 6-hourly GFS-FNL dataset and 0.5 degree 6-hourly CFSR data. To determine the precipitation forecast sensitivity to microphysics and emphasize the importance of initial conditions, six model runs [which included three different treatments of convection and two different microphysics schemes (Goddard microphysics scheme and WDM6)], were initialized with CFSR. Overall, the UKF scheme is found to generally improve the high-resolution simulation of longwave and shortwave radiation associated with cloud patterns, and produce precipitation patterns and intensity that are closer to the observations.

Experiments using GFS and CFSR for initialization were conducted to assess how the initial condition dataset impacts forecasts. These studies show that the general distribution and intensity of precipitation forecasts are significantly influenced by initial conditions obtained from different analysis fields. The area-averaged precipitation simulated using CFSR is found to be heavier compared to the GFS results. Simulations using the UKF scheme outperform the other simulations at light, medium, and heavy precipitation rates, regardless of the dataset used for initial conditions. The larger differences in the area-averaged RMSE between the two initial conditions are found with the original KF scheme, but for heavy precipitation rates (greater than 25 mm h^{-1}), significant differences due to changes in initial conditions are noted in all of the convective treatments (Table 4.2). Sensitivity analysis demonstrates that the precipitation forecasts are more sensitive to the type of initialization than to grid-scale microphysics or convective treatments in our case studies. Therefore, a good initial condition dataset is necessary for a good NWP model forecast, consistent with that documented in the literature (Rabier et al. 1996; Stensrud et al. 2000).

In this study we find that grid resolution-dependent parameterized convective physics in the KF scheme results in improvement of high-resolution forecasts. Thus, the UKF scheme in the WRF model at high-resolution scales produces more accurate surface radiation values and results in the improvement of simulated cloudiness. The UKF scheme not only reduces excessive rainfall amounts, but also improves both the location and intensity of precipitation in high-resolution (3 and 9 km) forecasts. Regional climate simulations that are being performed by our group do indicate that each of the science updates presented in this paper results in a large reduction in monthly precipitation biases, which will be reported in a follow up paper.

CHAPTER 5. IMPACT OF LAND-ATMOSPHERE-CONVECTION INTERACTIONS ON REGIONAL PRECIPITATION INTENSITY AND VARIATION IN WRF[4]

5.1 Introduction

Accurate and site-specific forecasts of short-term precipitation are of key importance for predicting extreme weather events such as excessive rainfall and flash flood. A variety of mesoscale processes are involved in affecting the regional convection and precipitation, ranging from land processes, boundary layer processes, and convective cloud processes.

The land surface heterogeneity can influence the exchanges of radiative, moisture, heat, and momentum fluxes with the atmosphere, and can lead to critical impacts on the development of convective and rainfall events (Hadfield et al. 1992; Avissar et al. 1998; Niyogi et al. 2006; LeMone et al. 2008). Many land-surface parametrization schemes have been developed, in particular, to represent the water and energy budgets at the land surface, water storage in the ground, and evapotranspiration to the atmosphere (Niyogi et al. 1999; Pitman 2003; Dirmeyer et al. 2006). Thus, an essential role of the land-surface parameterization is to provide accurate inputs to boundary layer and convective processes to properly represent hydrology cycling.

---

[4] Zheng, Y., K. Alapaty, D. Niyogi, 2015: Impact of land-atmosphere-convection interactions on regional precipitation intensity and variation in WRF (In submission).

However, several parameters employed in the land-surface parametrization schemes are very uncertain, leading to too much evaporation and precipitation (Pitman 1994; Henderson-Sellers et al. 1995, 1996; Niyogi et al. 1999; Pitman et al. 1999; Betts 2007; Abramowitz 2008; Fischer et al. 2010; Niu et al. 2011; Han et al. 2014). For example, the surface latent heat fluxes do not solely depend on the land surface processes but also on the land-atmosphere coupling, affecting regional convection and precipitation (Pielke 2001; Findell and Eltahir 2003; Koster et al. 2004, 2006; Santanello et al. 2011; Trier et al. 2011; Taylor et al. 2012).

Areas with strong coupling between soil moisture and summer rainfall are generally identified as “hot spots” (Koster et al. 2004), where wetter-than-usual soil moisture may lead to higher-than-usual evapotranspiration, and result in stronger potential impact on convection and increased precipitation. The strength of the coupling between land and atmosphere varies from place to place and from time to time. For example, Zheng et al. (2015a) have pointed out that the adoption of a dynamic coupling coefficient helped improving simulation of surface fluxes and the resulting atmospheric state, and in turn improved the intensity of the simulated precipitation. Therefore, the improvements in land-atmosphere coupling will help reduce uncertainties in land-atmosphere feedbacks.

The role of a convective parameterization in a numerical model is often thought as primary contributor to the simulated precipitation locations and amounts. However, these convection schemes that are capable of generating different patterns of precipitation and driving mesoscale circulations need to be well understood and improved. Particularly, at the intermediate-scales (i.e., for horizontal grid spacings between ~1 and ~10 km) many CPS do not work properly. When an explicit convection scheme has been employed in most of these high resolution studies, many times precipitation forecasts were found to be unsatisfactory. Based on the considerations of unresolved clouds and their effects in simulating moist convection and precipitation for warmer periods, some of the assumptions used in the convective parameterizations have been relaxed to make a CPS suitable for high resolution grids (Alapaty et al. 2012; Herwehe et al. 2014; Bullock et al. 2015; Zheng et al. 2015b). Thus, a CPS can be seamlessly adaptable to the intermediate-scales and work properly for high-resolution model forecasts.

Therefore, based on our previous studies (Zheng et al. 2015a and b), we study the impacts of different representations of land surface processes, land-atmosphere coupling strength, and a convective parameterization scheme on short-term regional precipitation forecasts. We also explore to what extent the improvements in land-atmosphere-convection interactions in the Weather Research and Forecasting (WRF) model benefit the short-term regional precipitation intensity and variation. This paper is organized as follows: Section 2 presents methods including the three aspects of improvements and the design of numerical simulations; Section 3 evaluates the model results; and discussions are in Section 4.

5.2 Methodology

Eight different representations of the three processes (land surface processes representation, coupling strength, and subgrid-scale convection processes) are used in this study. The Noah LSM has prognostic land states, including surface skin temperature, soil moisture and soil temperature at four soil layers (0.1, 0.3, 0.6, and 1.0 m thickness), canopy water content, snowpack water equivalent content and depth. The soil moisture prognostic calculation in the Noah LSM is based on Richard's equation:

$$\frac{\partial \theta}{\partial t} = \frac{\partial}{\partial z}\left(D\frac{\partial \theta}{\partial z}\right) + \frac{\partial K}{\partial z} + F_{\theta} \qquad (5.1)$$

where θ is the soil water content, z is the elevation, t is time, F_{θ} represents the sources (i.e., rainfall) and sinks (i.e., evaporation) of soil moisture, K is the hydraulic conductivity, and D is the soil water diffusivity. Both D and K are functions of soil texture.

The soil temperature prognostic equation is:

$$C(\theta)\frac{\partial T}{\partial t} = \frac{\partial}{\partial z}\left(K_t(\theta)\frac{\partial T}{\partial z}\right) \qquad (5.2)$$

where C and K_t are functions of soil texture and soil moisture. The surface energy balance and water balance in the Noah LSM are:

$$R_{net} = H + LE + G + SPGH \qquad (5.3)$$

$$\Delta S = P - R - E \qquad (5.4)$$

where R_{net} is the net radiation, H is the sensible heat flux, LE is the latent heat flux, G is the ground heat flux, and $SPGH$ the snow phase-change heat flux. Additionally, ΔS is the change in soil moisture content, P is the precipitation, R is the runoff, and E is the evaporation.

Within the Noah LSM, the surface coupling strength controls the ratio of the roughness lengths for momentum and heat which more effectively impact surface fluxes. It has been demonstrated that the coupling strength coefficient which is dynamically linked as a function of canopy height can help improve regional precipitation intensities, compared to using the default constant coefficient (Chen and Zhang 2009; Zheng et al. 2015a). The dynamical coupling strength is represented as:

$$C_{zil} = 10^{(-0.4h)} \tag{5.5}$$

where C_{zil} is the surface coupling strength, and h is the canopy height (meter).

For the convective parameterization, one of the crucial improvements in the UKF CPS is its scale dependency with the scaling parameter β, which makes the scheme a smooth transition from parameterized cloud physics to resolved grid-scale cloud physics:

$$\beta = \left[1 + \ln\left(\frac{25}{Dx}\right)\right] \tag{5.6}$$

where Dx (km) is the model's horizontal grid spacing. Additionally, the UKF CPS includes the subgrid-scale cloud-radiation interactions, a dynamic adjustment timescale, impacts of cloud updraft mass fluxes on grid-scale vertical velocity, and lifting condensation level (LCL) l-based entrainment methodology. The primary formulations in the UKF CPS are:

$$\tau = \frac{H}{(\delta m_b A_e)^{1/3}}\,\beta \tag{5.7}$$

$$W_n = W_g + W_{up} = W_g + \frac{M/Dx^2}{\rho} \tag{5.8}$$

$$\Delta M_e = M_b \frac{\alpha\beta}{Z_{LCL}} \Delta P \tag{5.9}$$

where τ is the adjustment timescale, H is cloud depth (m), δ is a constant and set to unity, m_b is the cloud-base updraft mass flux per unit density (m s^{-1}), and A_e is diluted/entrained convective available potential energy (CAPE; $m^2\ s^{-2}$); W_n is the reformulated grid-scale vertical velocity ($m\ s^{-1}$), W_g is the grid-scale vertical velocity ($m\ s^{-1}$), W_{up} is the effective vertical velocity of subgrid-scale updraft ($m\ s^{-1}$), ρ is the convective plume density ($kg\ m^{-3}$), and M is the updraft mass rate ($kg\ s^{-1}$); ΔM_e is the mixing rate ($kg\ s^{-1}$), M_b is the updraft mass rate at cloud base ($kg\ s^{-1}$), $\alpha=0.03$ is a constant ($m\ Pa^{-1}$) which controls the overall magnitude of the entrainment rate for convective plumes, Z_{LCL} is the height of the LCL above the ground (m), and ΔP is the pressure depth of a model layer (Pa).

5.3 Numerical simulations design

The WRF model (WRF 3.4.1; Skamarock et al. 2008) is configured with 2 two-way nests of 9 km (290 × 280 grid points) and 3 km (307 × 274 grid points) horizontal grid spacing, and 28 eta vertical levels with a model top at 50 hPa over the U.S. SGP domain (Fig. 5.1). The research domain was selected due to its importance as one of the land-atmosphere coupling hotspot regions and the availability of various observations. One degree 6-hourly NCEP Global Final Analysis (FNL) data derived from the Global Forecast System (GFS) was used as initial conditions for the atmospheric fields, soil states, and sea surface temperature. The major physics options in the WRF model included the RRTMG radiation models (Iacono et al. 2008), the Goddard microphysics scheme (Tao et al. 1989), and the Mellor-Yamada-Janjic (MYJ) planetary boundary layer (PBL) scheme (Janjic 2002).

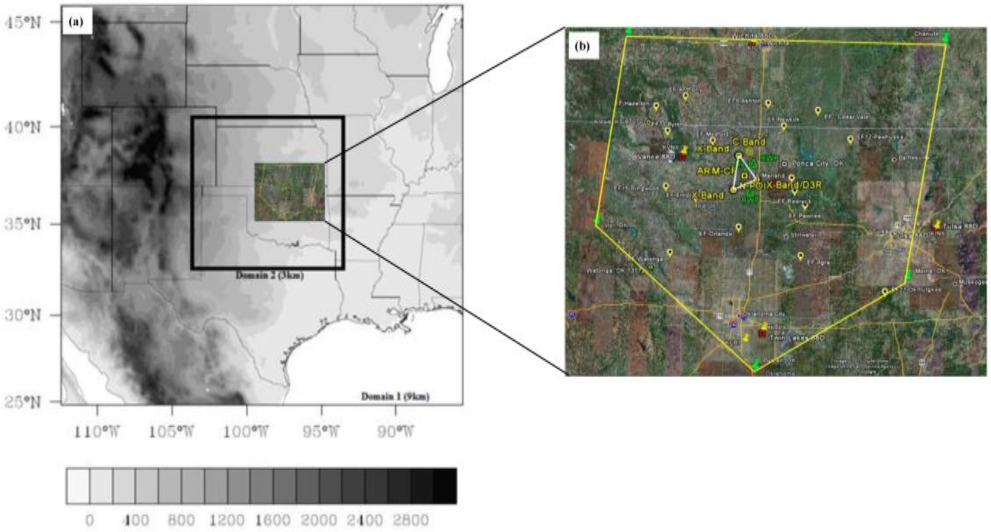

Fig. 5.1 (a) WRF nested domain with topography height (meters), and (b) map of the MC3E study domain.

A convection case [from 0000 UTC on 19 May (i.e., 1800 CST on 7 July) to 0000 UTC on 21 May (i.e., 1800 CST on 8 July), 2011] of squall line with extended trailing stratiform observed during a major joint field campaign [the Midlatitude Continental Convective Clouds Experiment, also known as MC3E (Jensen et al. 2010) was selected to examine the enhanced coupled WRF model's ability to simulate the variation and intensity of rainfall. A total of eight WRF configurations were tested with two LSM models (slab model and Noah LSM), with/without dynamic land-atmosphere coupling strength, and two treatments for the CPS [the latest KF scheme (Kain 2004), and the UKF scheme (Zheng et al. 2015b). The summary of the experiments is shown in Table 5.1. Observations from the MC3E at the Atmospheric Radiation Measurement (ARM) SGP facilities, and the high spatial resolution Multisensor Precipitation Estimates (MPE, also known as Stage IV Next-Generation Radar) hourly rainfall products (Lin and Mitchell 2005), were used for model comparisons.

Table 5.1 Summary of the numerical experiments

Experiment	Land surface model	Land-atmosphere coupling strength	Convective parameterization scheme
S_KF	Slab	0.1	KF
S_V_KF	Slab	Varying	KF
S_UKF	Slab	0.1	UKF
S_V_UKF	Slab	Varying	UKF
N_KF	Noah	0.1	KF
N_V_KF	Noah	Varying	KF
N_UKF	Noah	0.1	UKF
N_V_UKF	Noah	Varying	UKF

* S: slab model, N: Noah LSM, V: dynamical C_{zil}, KF: the latest KF scheme, UKF, the updated KF scheme.

5.4 Results

5.4.1 Precipitation

The operational WRF model 6-hour total precipitation forecasts valid from 1200 to 1800 UTC on 20 May 2011 are shown in Figs. 5.2 (for the outer domain with 9 km grid spacing) and 5.3 (for the inner domain with 3 km grid spacing). For the 9 km grid spacing forecasting, an observed area of heavy rainfall is clearly evident across the central domain and in a northeast orientation (Fig. 5.2i). Forecasts (retrospective) with the slab model produce a smaller area of heavy rain, and the precipitation is located further to the southeast [as seen in the red circle in Figs. 5.2 (a-d)]. Forecasts with the Noah LSM and KF show less intense precipitation in the red circle area (Figs. 5.2 e and f) but the spatial patterns, though displaced, are closer to observations. It can be seen that the dynamical coupling strength only slightly improves the precipitation intensity (Fig. 5.2f). The heavier rainfall simulated in the Noah/WRF UKF runs (i.e., N_UKF and N_V_UKF runs) is further to the north across Oklahoma, which is closer to the observation (Figs. 5.2 g and h) but with an underprediction of light precipitation in the northern regions in the highlighted area. For the 3 km grid spacing (for the inner domain), the slab/WRF runs cannot well simulate the precipitation (Figs. 5.3 a and b), even with the help of the dynamical coupling strength and the UKF scheme (Figs. 5.3 c and d). In these forecasts, heavy precipitation is predicted in wrong locations. Thus, the LSM has a more dominate role in rainfall forecasting and the simple LSM may produce incorrect precipitation patterns and intensities due to obvious limitations in the slab land surface parameterization. The Noah/WRF KF runs (i.e., N_KF and N_V_KF runs) show a widespread area of precipitation distribution with much of the rainfall predicted to receive between 1 and 25 mm, and these runs miss the observed heavier rainfall across the eastern part of Oklahoma (Figs. 5.3 e and f). The UKF scheme significantly improves the precipitation forecast for the 3 km grid spacing Noah/WRF simulation (Fig. 5.3g), and the dynamical coupling strength helps yield a positive impact on the high-resolution simulated precipitation intensity (Fig. 5.3h). Thus, the high-resolution WRF model coupled to the Noah LSM, the dynamical coupling strength, and the UKF CPS, can lead to more accurate forecasting for precipitation amounts and locations.

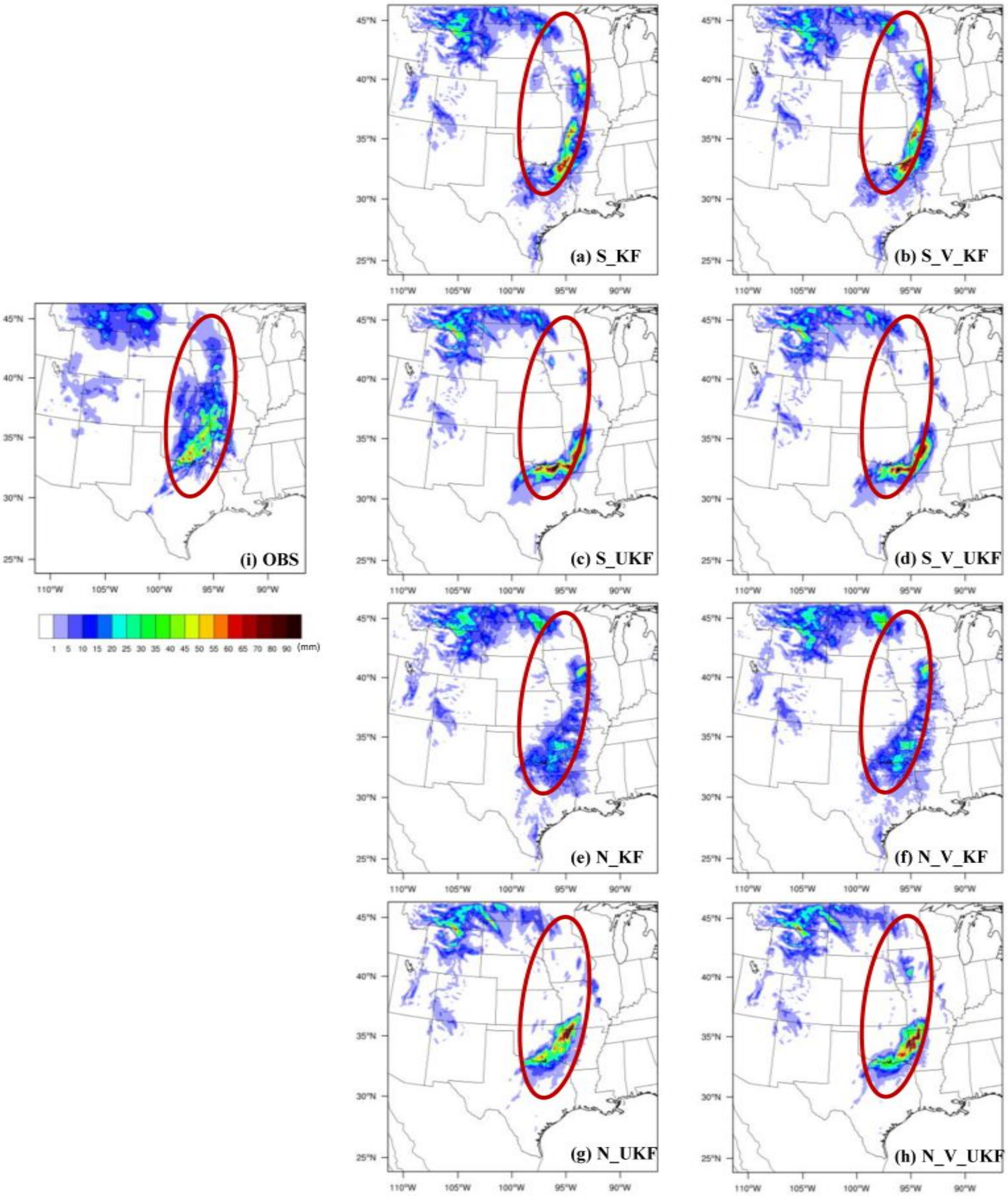

Fig. 5.2 6-hour accumulated precipitation (1200 UTC – 1800 UTC on 20 May 2011) over the outer domain with 9 km grid spacing compared with the Stage IV observation.

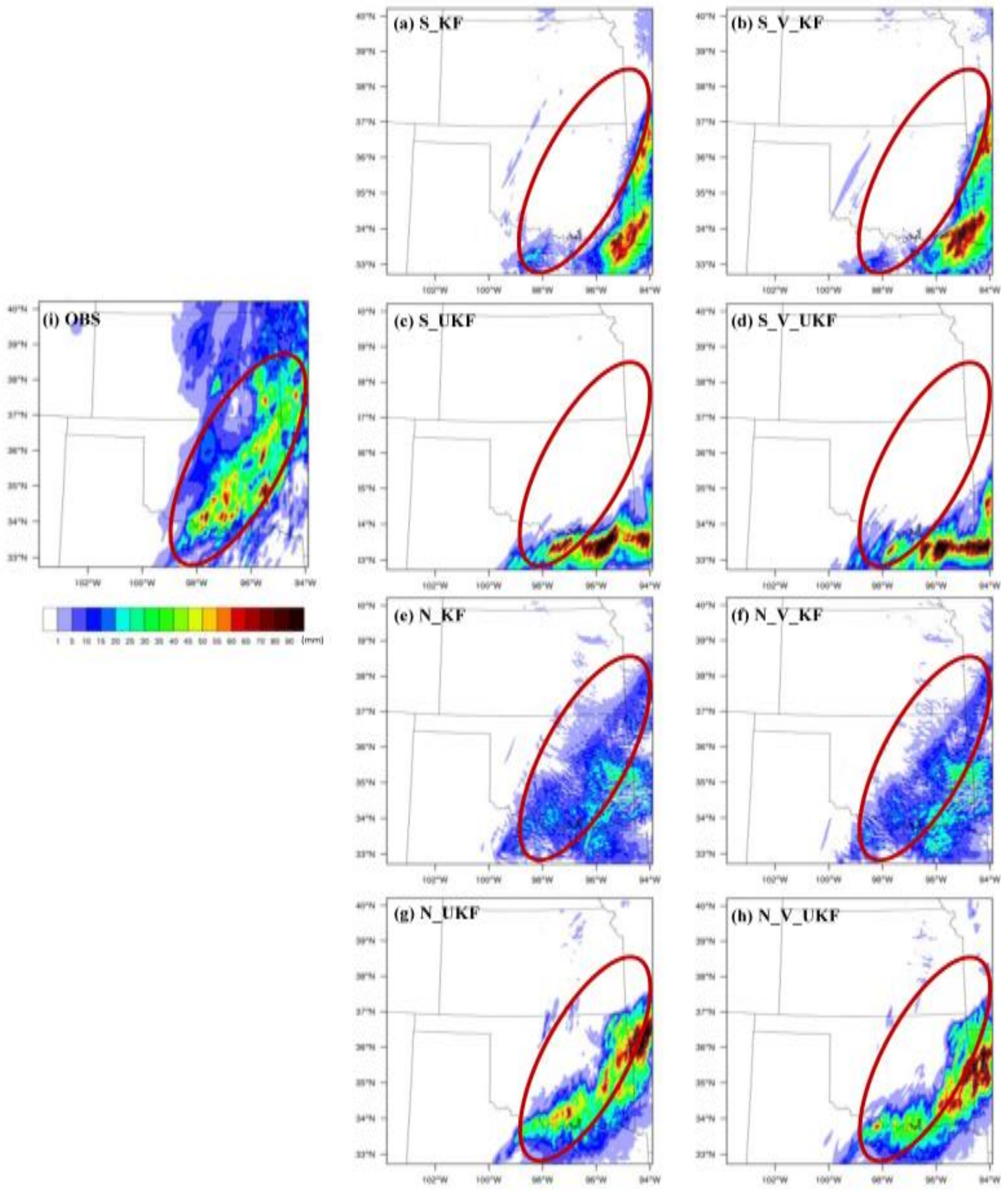

Fig. 5.3 6-hour accumulated precipitation (1200 UTC – 1800 UTC on 20 May 2011) over the inner domain with 3 km grid spacing compared with the Stage IV observation.

Three rain rate thresholds (5, 15, and 25 mm h^{-1}) were used to separate out the light, medium, and heavy precipitation for the model runs, and the 48-hour (0000 UTC 19 – 0000 UTC 21 May 2011) time series of area-averaged precipitation over the 3 km grid spacing domain from Stage IV observations and corresponding simulations are shown in Fig. 5.4. Consistent with the results from Zheng et al. (2015b), the UKF CPS has significantly improved precipitation intensity forecasts (i.e., increasing about 33% accuracy for the light rain, 44% accuracy for the medium rain, and 50% accuracy for the heavy rain), and the timing of convection initiation for all the rain rate thresholds. Additionally, the area-averaged precipitation for the N_V_UKF run (the red lines in Fig. 5.4) and the S_V_UKF run (the blue lines) are closer to the observations compared to the results from the N_UKF run (the cyan lines) and the S_UKF run (the orange lines). This indicates that the WRF model coupled with the dynamical coupling strength and UKF CPS can well forecast the convective events. It is also noted that the impact of the dynamical coupling strength on area-averaged precipitation becomes more significant in the second simulation day, particularly for the medium rain rate (Fig. 5.4 b and c). Thus, a spin up time of at least 24 hours is preferred for high-resolution model simulations. The experiment with Noah LSM again outperforms that with the simple slab model at every threshold, emphasizing the crucial role of land processes in land-atmosphere-convection interactions.

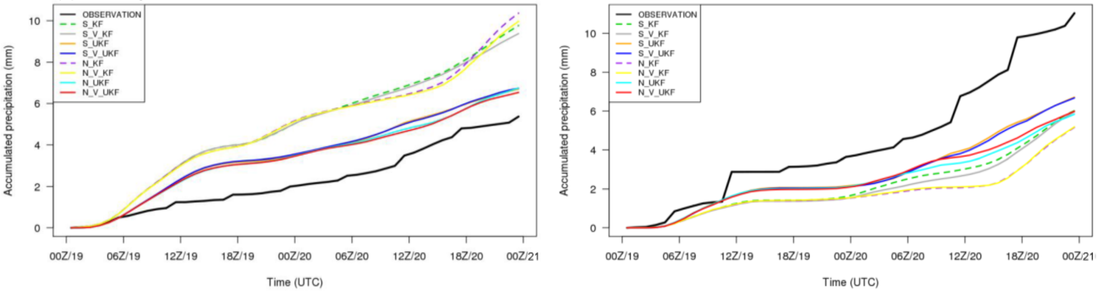
(a) Hourly rate < = 5 mm h^{-1}

(b) 5 mm h^{-1} < Hourly rate < = 15 mm h^{-1}

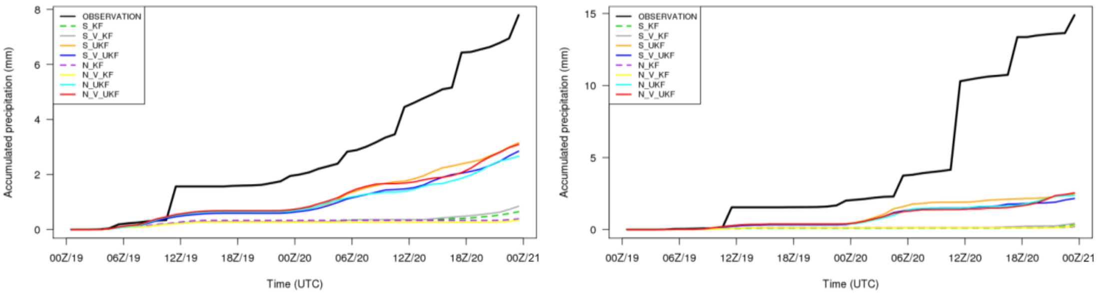
(c) 15 mm h^{-1} < Hourly rate < = 25 mm h^{-1}

(d) Hourly rate > 25 mm h^{-1}

Fig. 5.4 48-hour (0000 UTC 19 – 0000 UTC 21 May 2011) time series of area-averaged precipitation (mm) from Stage IV observations (solid black line) and simulations with different rain rate thresholds.

5.4.2 Soundings

A squall line was observed at midnight on 20 May (0600 UTC) confirming that the convective storm occurred in a rather stable environment. Soundings over two different sites were examined [Dodge City, KS (DDC; 37.46° N, -99.58° W) and Amarillo, TX (AMA; 35.13° N, -101.43° W)] at 1200 UTC 20 May (6 hours after convection initiation), to study the coupled mesoscale models' performance (Fig. 5.5). The soundings observations are available from the University of Wyoming (http://weather.uwyo.edu/upperair/sounding.html). In the lower boundary layer the soundings for N_V_UKF are much warmer, while the potential temperatures for S_V_UKF are closer to the observations. All runs show moister and stronger wind soundings above the 925 hPa pressure level in the PBL. The specific humidity profile for N_V_UKF is closer to observations over the DDC site, but S_V_UKF shows a better simulated specific humidity profile over the AMA site. There is no clear indication that the dynamical coupling strength could lead to better soundings and convection simulation when coupled with the UKF CPS, however, the comparison between the 3 km grid spacing runs with UKF and KF CPS clearly indicates that the UKF scheme outperforms the KF scheme in simulating the vertical moisture and wind speed profiles.

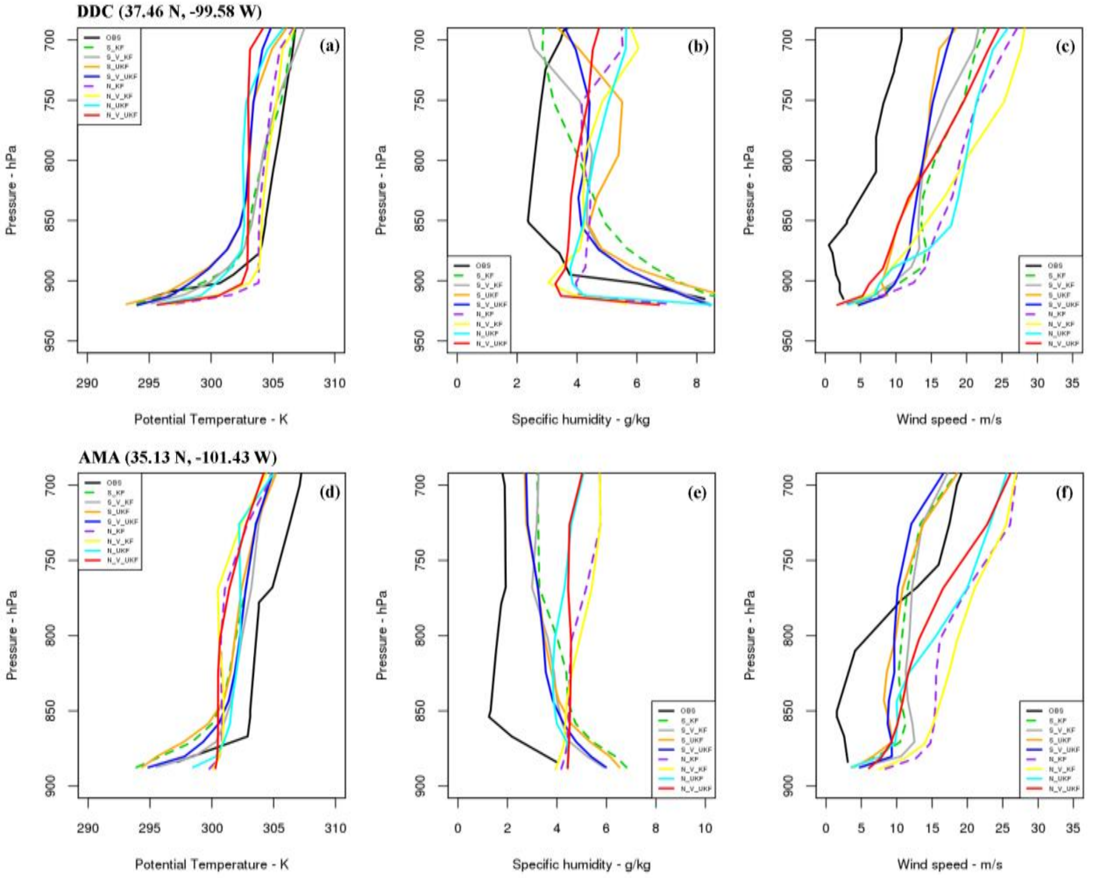

Fig. 5.5 Vertical profiles of model-simulated potential temperature (a, d), specific humidity (b, e), and wind speed (c, f) at the sites of Dodge City, KS (DDC; 37.46°N, -99.58°W) and Amarillo, TX (AMA; 35.13°N, -101.43°W) at 1200 UTC on 20 May 2011 compared with observations.

5.4.3 Vertical velocity

Large-scale vertical velocity is a key component of dynamic fields that is critical to convection simulations. In the WRF model, the large-scale vertical velocity is determined internally during the simulation. Fig. 5.6 shows a time-series of the large-scale vertical velocity from all experiments at Dodge City, KS (DDC; 37.46°N, -99.58°W) over the period from 0000 UTC 20 May to 0000 UTC 21 May 2011. The impacts of using different combinations of LSM, coupling strength, and CPS, have also been reflected in the vertical velocity field, resulting in different patterns of updrafts and downdrafts. A strong core structure of downdraft between 600 hPa and 800 hPa was observed in the morning for the S_V_KF run (Fig. 5.6b), as well as an updraft core below 700 hPa in the afternoon for the N_V_UKF run (Fig. 5.6h). Stronger updrafts and downdrafts in the troposphere have been noted associated with the UKF scheme. Thus, the variations of vertical velocity distribution with height and time are different for different experiments. These differences in the simulated vertical velocity could lead to significant differences in the simulation of convective clouds. These results also demonstrate that the UKF scheme could provide more detailed fluctuations of the vertical velocity.

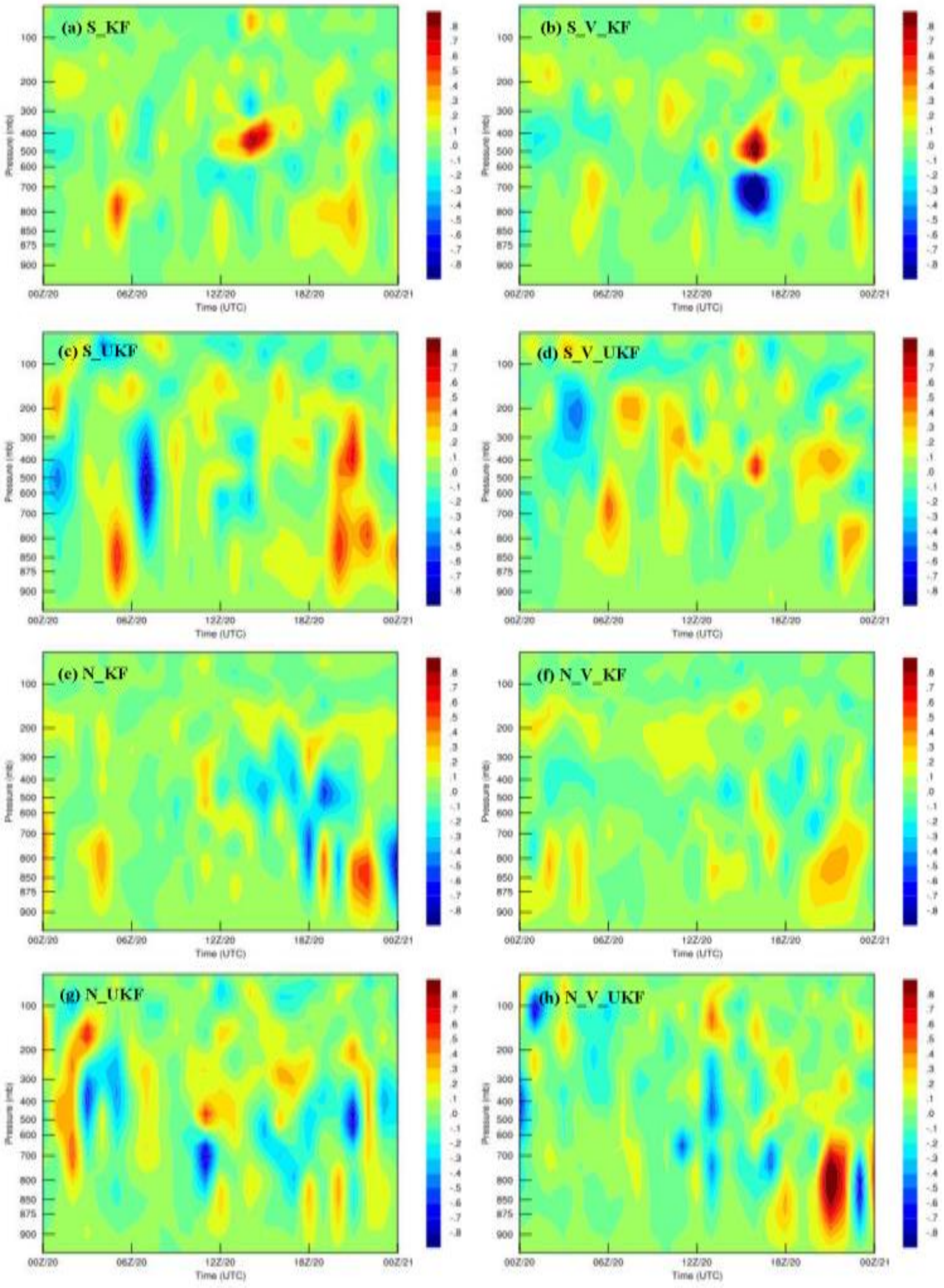

Fig. 5.6 Simulated large-scale vertical velocity (m s^{-1}) at Dodge City, KS (DDC; 37.46°N, -99.58°W).

5.4.4 Horizontal wind speeds and mixing ratio

Given the assumption that differences in land-surface parameterizations and land-atmosphere coupling strength are the primary roles in leading to the differences in wind and moisture fields, Fig. 5.7 shows the instantaneous high horizontal wind vectors and mixing ratio at the middle of the PBL height (~ 1 km) at 1200 UTC 20 May 2011 from different experiments. The differences in the wind field and moisture field lead to changes in the distribution and intensity of moisture convergence. The coupling strength and the convection scheme have a greater impact on the wind field density and wind direction. The change in wind direction reflects the changes in dynamics during the convective simulation. The water vapor mixing ratio is much higher in the southeastern part of the domain, and these patterns are also notable in the 6-hour precipitation over the inner domain in Fig. 5.3. Thus, the moisture field has a close positive relationship to the precipitation, indicating that the correct simulation of the water vapor mixing ratio in the PBL is crucial in precipitation forecasting. The different representations of soil moisture in the two LSMs (i.e., the slab model has constant soil moisture while the Noah model has time-varying soil moisture) can lead to the different patterns of water vapor mixing ratio, and it is concluded that the primary reason for the unrealistic precipitation simulated by slab/WRF (Figs. 5.2 and 5.3) is due to the constant value of the soil moisture availability in the bucket slab model. The dynamical coupling strength coefficient has a more significant impact on the moisture field and wind vector field when the UKF is employed for the WRF simulations. Therefore, the WRF model coupled with the more detailed LSM, the dynamical coupling strength coefficient, and the

UKF together, is able to reproduce a more reasonable precipitation forecast, particularly with the help of the improved simulation of water vapor mixing ratio in the PBL.

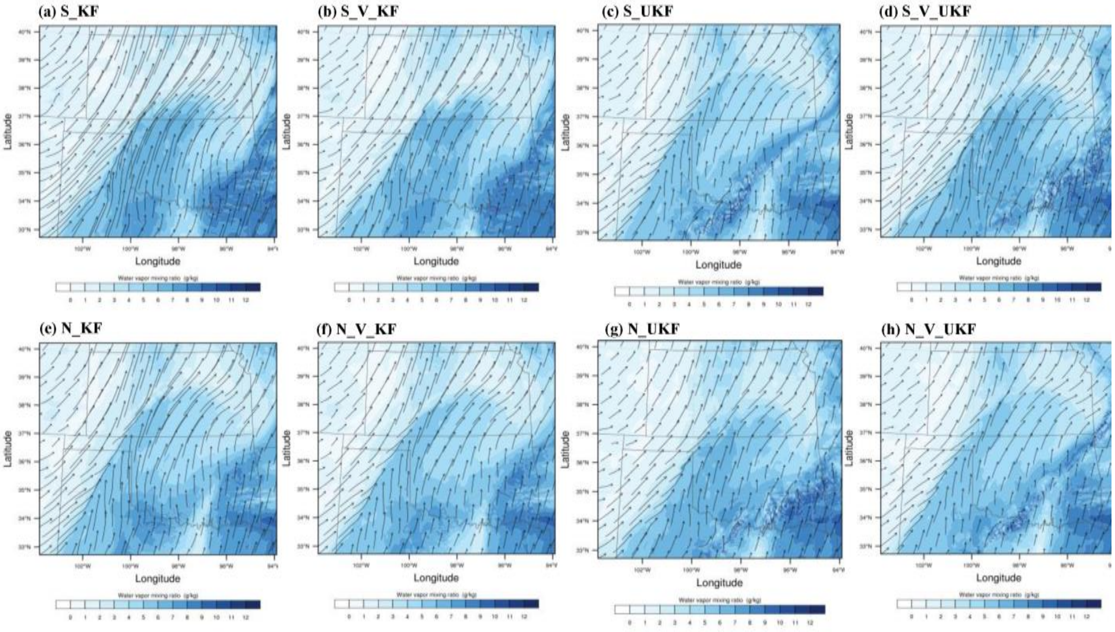
(a) S_KF (b) S_V_KF (c) S_UKF (d) S_V_UKF

(e) N_KF (f) N_V_KF (g) N_UKF (h) N_V_UKF

Fig. 5.7 Simulated horizontal wind fields (wind vectors) and hydrometeor mixing ratio (white-blue shaded) at 1 km height at 12:00 UTC on 20 May 2011 over the inner domain with 3 km grid spacing.

5.4.5 Surface fluxes

The impact of the land-atmosphere-convection interactions on the important near-surface variables was also assessed (Fig. 5.8). The simulations using 3 km grid spacing were compared to minute observations of 2 m temperature and 2 m relative humidity data, and half-hourly observations of surface sensible heat flux and latent heat flux data. All these data are from the ARM measurements located over the MC3E study domain. The near-surface variables are more sensitive to the parameterizations during the daytime. For 2 m temperature, all WRF model runs show a warm bias in the morning after 1500 UTC 20 May. The 2 m temperature for the S_KF run shows a curve very similar to observations during the nighttime (before 0900 UTC 20 May), while the results from other simulations are also in a reasonable range and close to observations (Fig. 5.8a). For 2 m relative humidity, the WRF model runs show a wet bias in the nighttime but strong dry biases during the daytime (Fig. 5.8b). The N_V_UKF increases instead of reducing the dry bias for the daytime simulation. It is found that the choice of LSM plays a crucial role in these bias magnitude differences, and the WRF model coupled with the three-aspect improvements is not able to significantly reduce the bias primarily due to soil moisture impacts in the model. However, it is not evident that the WRF model coupled with the simple slab model could lead to accurate regional convection and rainfall. Additionally, it was determined that the cause is internal to the WRF model itself. The surface sensible and latent heat fluxes indicate that the WRF configuration with a dynamical coupling strength coefficient could greatly help reduce surface flux bias (Figs. 5.8 c and d), leading to improved heat and moisture transfer simulations in the PBL. Therefore, the effect of the dynamical coupling strength is substantial in the convection and precipitation forecasts.

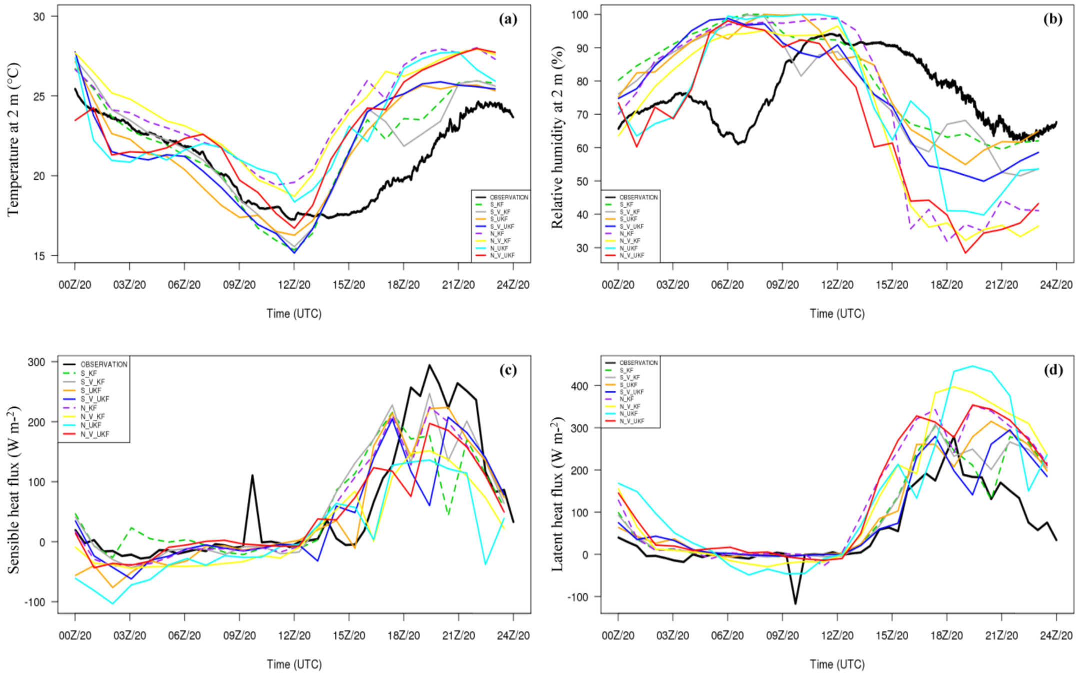

Fig. 5.8 24-hour (0000 UTC 20 May – 0000 UTC 21 May 2011) time series of (a) temperature at 2 m (°C), (b) relative humidity at 2 m (%) at ARM site E11 (36.88°N, -98.29°W), and (c) surface sensible flux (W m^{-2}) and (d) surface latent heat flux (W m^{-2}) at ARM site E4 (37.95°N, -98.33°W) over the 3 km grid spacing domain compared with observations (solid black line).

5.4.6 CAPE/CIN

Fig. 5.9 shows the time series of the CAPE and convection inhibition (CIN) calculated from observed soundings at Dodge City, KS (DDC; 37.46°N, -99.58°W), and the Skew-T at 0000 UTC 20 May 2011. CAPE is calculated as the vertical sum of the buoyancy which raises an air parcel along a reversible moist adiabatic from the level of free convection (LFC) to the equilibrium level (EL) (Moncrieff and Miller 1976). CIN is the negative value of CAPE below LFC, and can be thought of as a measure of the work that an air parcel must do to reach the LFC where it will finally become positively buoyant. The magnitude of CAPE is strongly dependent on the environmental soundings profile. Since the elevated convective storms occurred with a strong squall line that was observed on 20 May 2011, and the convection had near saturated soundings in the unstable PBL, large CAPE with strong diurnal variation had been diagnosed by Xie et al. (2014). As seen in Fig. 5.9a and b, both CAPE and CIN are sensitive to the influence of LSM, coupling strength, and CPS. The simulated magnitude peaks of CAPE occurred around midnight (from 0400 UTC to 0500 UTC 20 May). The large magnitudes of CAPE for the Noah/WRF simulations are earlier and larger than those for the slab/WRF simulations. The simulations with the UKF scheme significantly reduced the CAPE value, possibly leading to a decrease in the simulated precipitation rate under such unstable and saturated conditions. However, to investigate if convection could be well captured (or improved) by the mesoscale WRF model coupled with the improved scheme/parameterizations, a longer simulation period or another case for deep convection should be conducted. Most CIN values are distributed in the range from -400 to 0 J kg^{-1}. The small absolute values of CIN for the slab/WRF simulations suggest the higher precipitation rates that are seen in Figs. 5.2 (a-d) and 5.3 (a-d). Therefore, the changes in the LSM, surface coupling strength, and CPS in the WRF model can greatly affect the simulations of CAPE and CIN, resulting in changes in the precipitation forecasts. It is concluded that the simulation of the convective precipitation development processes in the high-resolution mesoscale model could be improved via the improved CAPE and CIN.

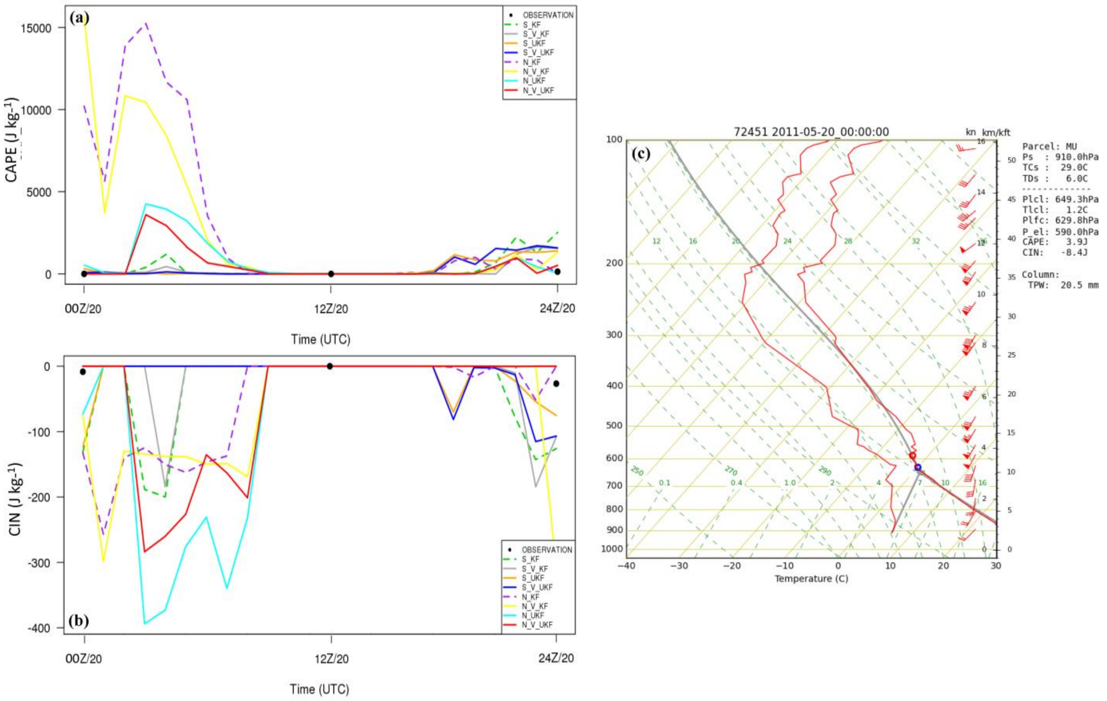

Fig. 5.9 24-hour (0000 UTC 20 May – 0000 UTC 21 May 2011) time series of (a) CAPE (J kg^{-1}), (b) CIN (J kg^{-1}) at Dodge City, KS (DDC; 37.46°N, -99.58°W), and (c) the skew-T plot at 0000 UTC 20 May 2011.

5.5 Discussion

The impact of including the effects of LSM, land-atmosphere coupling strength, and CPS on the fields of precipitation, surface scalars, and convection were examined for 48-hour weather simulations over the U.S. SGP domain. From the experiments conducted with an observed squall line during the summertime, it was found that including a more detailed land surface parameterization, a dynamical surface coupling strength coefficient, and the UKF scheme together, improves the mesoscale simulations of several meteorological and convection parameters in the high-resolution WRF model. The land-atmosphere-convection feedbacks therefore can be well represented. Generally, the LSM plays a dominate role in the short-term convection and rainfall forecasts, the dynamical coupling strength helps improve precipitation intensity, and the UKF scheme helps create more realistic moist convective process parameters and precipitation variability. By studying the parameterized schemes in the land-atmosphere-convection interactions, the close relationship between the land surface, PBL processes, and convective activities is examined. This research will directly benefit the regional climate and hydrological modeling communities by providing more accurate prediction of high-resolution regional convection and rainfall. This research will also help improve the understanding and parameterization of moist processes in regional meteorological models, particularly over the regions that have close feedback between soil moisture and precipitation.

CHAPTER 6. CONCLUSIONS

The interactions between land-surface variability and cloud dynamics and their impacts on regional convection and rainfall have been studied based on the synthesis of numerical modeling analyses and field observations. A number of numerical experiments were conducted over a variety of land-atmosphere coupling hotspot regions across the globe. Model simulations of regional convection and rainfall were improved by studying the impacts of the heterogeneous land surface, the land-atmosphere surface coupling strength, and improving the KF CPS for regional short-term weather forecasts.

Land-surface heterogeneity in LULC plays a key role in influencing the simulation of surface fluxes and PBL dynamics. Land heat and water storages and their relationship with fluxes can be changed to some extent by land-surface heterogeneity. Nonlinear impacts are found in simulated surface temperature, moisture, and wind speeds along with heterogeneity length scale changes. Spatial variations of the surface heat flux are found to decrease nonlinearly as the length scale of land-surface heterogeneity increases (becoming more homogeneous). The different land-surface parameterizations represent the impact of land-surface heterogeneity in different manners and show a variety of modeling biases. The simple slab soil model is found to be more sensitive to land-surface heterogeneity impacts, whereas the more detailed land-surface parameterizations (e.g., Noah LSM and HRLDAS) are less sensitive to heterogeneity length scale changes. Larger biases have been noted in the coupled slab/WRF runs. Results also indicate that in wet conditions, the surface heat fluxes over land which contains higher evaporation and stronger coupling strength (e.g., grassland, forest, and wet cropland) are greatly impacted by land-surface parameterizations. The Noah LSM performs better over different types of LULC. Vertical fluxes of heat and moisture in the PBL are affected by surface energy partitioning and the turbulent parameterization for mass and energy transfer between the heterogeneous land surface and the PBL within the coupled LSM/WRF models are explored to show the substantial impacts. The impact of land-surface parameterizations on turbulent energy spectra is found to be more significant at lower frequencies in the spectra where larger eddies dominate. The slab/WRF overpredicts the energy spectra of surface temperature and moisture and underestimates the energy cascade. The response of turbulent spectra to the length scales of land-surface heterogeneity indicate that the energy spectra respond nonlinearly to heterogeneous length scale changes and the simulated vertical velocity is less sensitive to land-surface parameterizations at finer-scale heterogeneous land surfaces. Additionally, the WRF model coupled with a more detailed land-surface parameterization can more accurately simulate turbulent spectra over a heterogeneous land surface. An important finding from the spectral analysis is that the atmospheric circulation, which is roughly four times the spatial heterogeneity length scale, can be adequately resolved in the coupled mesoscale WRF model. This result shows that the land-surface heterogeneity effect would be a function of the degree of the heterogeneity spatial scales represented in the LSM.

Vertical fluxes of heat and moisture in the PBL are affected by the impact of land-surface heterogeneity and LSMs on surface energy partitioning, influencing simulations of mesoscale atmospheric circulations and regional convective weather processes. Results show that vertical profiles of turbulent flux and TKE can also be used to represent impacts of the land-surface parameterization and land-surface heterogeneity. Results indicate that HRLDAS/WRF well simulates the vertical turbulent moisture flux and total TKE in the PBL, and is able to capture the stronger gradients of the moisture flux at the surface and entrainment zone. Thus, the more detailed land-surface representation can not only improve the mean fields of surface flux simulations but also turbulent processes, leading to improved simulations of land-atmosphere interactions over heterogeneous land surfaces. Therefore, a positive impact of the improved land-surface parameterization over a fine-scale heterogeneous land surface has been identified via the simulated turbulent processes and mesoscale simulations.

The coupling between the atmosphere and the land surface plays an important role in regional convection and precipitation. The potential benefit of examining the land atmosphere coupling over four different coupling “hotspot” regions indicates that the land surface coupling strength coefficient C_{zil} has the potential to modulate mesoscale model results and improve the simulation of convective systems. Additionally, the dynamic formulation for representing land atmosphere coupling helps improve precipitation forecasts in terms of intensity but not necessarily in its location.

Impacts of the coupling effect on regional convection vary across different land-cover types and over different areas. Surface heat fluxes have the largest impact in terms of the coupling strength assigned over the different regions. Results indicate that the constant surface coupling coefficient used in the current coupled Noah/WRF model is deficient in producing correct surface fluxes. Model biases respond differently along with changes in surface coupling strength. The current WRF model in use over West Africa leads to coupling effects that are too strong and could be improved by using the coupling coefficient of 0.3 or the dynamic C_{zil}. It is also noted that in summer over the U.S. SGP, strong coupling leads to a cold and wet boundary layer resulting in a strong convective system and heavier rainfall, but due to the cultivated parched land surface over northern India, the coupling is found to be relatively weak, leading to lighter rain and smaller areas of precipitation.

Thus the high uncertainty in land-atmosphere coupling findings indicates that the coupling strength for the "hotspot" regions needs to be carefully considered and the zone of "high" or "low" coupling strength should be evaluated in the context of the model and parameterizations used. Since the modestly improved and encouraging model results are associated with using a dynamic C_{zil}, more efforts need to be directed toward adopting the dynamic coupling coefficient rather than the constant value currently used in the Noah/WRF models. It is a challenge to identify the correct coupling for land-atmosphere interactions as it can improve one variable and deteriorate another. In addition, the coupling coefficient has significant control on model performance particularly the quantitative precipitation forecasts and is therefore an important feature in the study of hydrometeorological extremes such as droughts and heavy rain events. The results highlight that evaluating and improving land-atmosphere coupling could potentially improve model performance across the globe.

Moist processes, especially the representation of clouds and their microphysical processes, are of vital importance in forecasting convection and precipitation. However at high spatial resolutions, the use of cloud microphysics alone may not be sufficient to represent moist convection and precipitation for warmer periods in weather forecasts (Clark et al. 2012). To reduce precipitation bias and errors occurring at high resolution scales due to uncertainties in the initial meteorological conditions and/or in grid-scale cloud microphysics schemes, in this research dissertation the scale-aware parameterized cloud dynamics for high-resolution forecasts were introduced to the KF CPS in the WRF model. The UKF scheme includes subgrid-scale cloud-radiation interactions (Alapaty et al. 2012; Herwehe et al. 2014), a dynamic adjustment timescale, cloud updraft mass fluxes impacting grid-scale vertical velocity, and an LCL-based methodology to parameterize entrainment. The UKF scheme is found to generally improve high-resolution simulation of longwave and shortwave radiation associated with cloud patterns, and produce precipitation patterns and intensity that are closer to the observations.

Results from experiments using two different initial conditions (GFS and CFSR) indicate that the general distribution and intensity of precipitation forecasts are significantly influenced by initial conditions obtained from different analysis fields. The simulated area-averaged precipitation initiated by CFSR is found to be heavier than forecasts using

GFS. The larger differences in the area-averaged RMSE between the two initial conditions are found in the original KF scheme, but significant differences are noted in all of the convective treatments for very heavy precipitation rates (greater than 25 mm h^{-1}). From the sensitivity analysis, results indicate that precipitation forecasts are more sensitive to initialization than to grid-scale microphysics or convective treatments, thus a good initial condition dataset is necessary for NWP model forecasts.

The UKF scheme in the WRF model at high-resolution scales is found to produce more accurate surface radiation values and results in the improvement of simulated cloudiness. Three different updates to the KF scheme which include properly representing timescale, grid-scale vertical velocity, and the entrainment effect are found to contribute differently to the precipitation changes and show nonlinear impacts. Results show that the UKF primarily contributes to precipitation forecasts when the rain rate is less than 5 mm h^{-1}, negligibly improving the simulation when the rate is greater than 5 mm h^{-1} and less than 15 mm h^{-1}, and has no contribution with higher hourly rain rates. Additionally, results show that the UKF scheme not only reduces excessive rainfall amounts, but improves both the location and intensity of precipitation in high-resolution forecasts.

A series of retrospective 48-hour experiments were conducted to explore how the land-atmosphere-convection interactions affect the WRF model based on the above results. The impacts of using different combinations of (i) LSM, (ii) land-atmosphere surface coupling strength, and (iii) UKF CPS on short-term moist processes in the WRF model were assessed accordingly. Results show that the LSM has a more dominate role in simulating surface and near-surface temperature, boundary layer water vapor mixing ratio, and regional rainfall. The simple LSM could produce an inappropriate water vapor mixing ratio and latent heat flux due to its simple parameterizations, resulting in incorrect precipitation intensity and variability. The dynamic coupling strength coefficient could significantly reduce surface flux uncertainties and positively impact precipitation intensity emphasizing its substantial role in convection and precipitation forecasting. The UKF improves the high-resolution precipitation intensity forecast by about 43%. The precipitation simulation for the WRF model coupled with the dynamical coupling strength and the UKF CPS has good agreement with observations indicating that the representation of moist processes could be improved by improving the interactions between land-atmosphere coupling and convective parameterization. Particularly, for the 3 km grid spacing simulation, the UKF scheme can lead to better simulated sounding profiles compared to the KF scheme. Results also show that the UKF scheme could provide more detailed fluctuation of vertical velocity which needs to be considered critically in the simulation of convective clouds. Thus, the interactions between the land surface, PBL processes, and convective activities have been assessed by examining the parameterized schemes in LSM, land-atmosphere coupling strength, and CPS. The land-atmosphere-convection interactions could be well represented by employing a more detailed land surface parameterization, a dynamical surface coupling strength coefficient, and the UKF scheme, together.

However, there are some important aspects of the research limitation that should be aware. For example, the data limitation over certain regions needs further analysis when additional data become available, and the current study addresses diurnal convection and precipitation situations in summertime only. Additional ensemble experiments related to different sets of parameterization schemes are needed for further sensitivity analysis, and additional sets of simulations with different ranges of relative soil moisture saturation are needed to gain further insights into the longer-term behavior of the land-atmosphere-convection system. Thus, further insights to the sensitivity of model parameters and precipitation predictability would lead to a better understanding of land-atmosphere feedback and moist process mechanism. Additionally, some open questions such as, "At what spatial scale would the land surface heterogeneity trigger mesoscale circulations that can affect the moist convection in climate models and may result in changes or missing in large-scale circulations? How would the land-atmosphere coupling strength be influenced due to the climate change and what would be the resulting impacts on cloud formation and moist convection? For the climate system and climate sensitivity, to what extent (e.g., initial condition, model resolution, and parameterization) to improve the global/regional climate models for a better understanding and more appropriate representation of clouds and moist convection, rather than obtaining more expensive models?" would be of great interest to explore.

Overall, through the study of the impacts of land surface heterogeneity on turbulent flow and mesoscale simulations, the land-atmosphere coupling strength over certain regions across the globe with strong feedbacks between soil moisture and precipitation, and the dynamical scale-awareness UKF convection scheme, this research dissertation has examined the nature and magnitude of land surface, land-atmosphere coupling, convection, and the interactions and feedbacks affecting and controlling regional moist processes. Three substantial results were identified that help to explain the numerical modeling for convection and land surface interactions: 1) Atmospheric feedbacks that are roughly four times of the land heterogeneity spatial scale can be adequately resolved in the coupled mesoscale model; 2) Evaluating and using a dynamic land-atmosphere coupling strength could potentially improve convective model performance over areas where there is a known bias with convection triggering and rainfall; and 3) A grid resolution-dependent parameterized convective physics in the convection scheme reduces fine scale precipitation biases and could work properly at grey scales. These results offer a strategy to obtain information related to land surface, appropriate land-atmosphere coupling strength, and grey scale convective parameterization, and also have significantly improved the accuracy of the WRF model at high-resolutions for short-term convective weather forecasting.

This research is essential for regional climate and hydrological modeling communities. The understanding and improvements developed in this dissertation may also lead to methodologies to implement new processes in land surface schemes, find sensitivities in moist convection, and diagnose uncertainties and errors in mesoscale and large-scale circulations. The scientific strategies in this research dissertation could greatly enhance high-resolution mesoscale model performance and benefit moist process representation for both regional and global meteorological models. This improved understanding of regional convection and rainfall could essentially contribute to severe weather exploration, tropical cyclone post-landfall risk estimation, and other convection-related phenomenon.

REFERENCES

REFERENCES

Abramowitz, G., R. Leuning, M. Clark, and A. Pitman, 2008: Evaluating the performance of land surface models, *J. Clim.*, **21(21)**, 5468-5481, doi: 10.1175/2008JCLI2378.1.

Alapaty, K., S. Raman, and D. Niyogi, 1997: Uncertainty in the specification of surface characteristics: A study of prediction errors in the Boundary Layer. *Bound-Lay. Meteorol.,* **82**: 475-502, doi: 10.1023/A:1017166907476.

Alapaty, K., J. A. Herwehe, T. L. Otte, C. G. Nolte, O. R. Bullock, M. S. Mallard, J. S. Kain, and J. Dudhia, 2012: Introducing subgrid-scale cloud feedbacks to radiation for regional meteorological and climate modeling, *Geophys. Res. Lett.,* **39**, L24809, doi: 10.1029/2012GL054031.

Alfieri, J. G., and P. D. Blanken, 2012: How representative is a point? The spatial variability of surface energy fluxes across short distances in a sand-sagebrush ecosystem. *J. Arid. Environ.,* **48**: 42-49, doi: 10.1016/j.jaridenv.2012.04.010.

Alfieri, J. G., D. Niyogi, H. Zhang, M. A. LeMone, and F. Chen, 2009: Quantifying the spatial variability of surface fluxes using data from the 2002 International H2O Project. *Bound-Lay. Meteorol.,* **133**: 323-341, doi: 10.1007/s10546-009-9406-2.

Arakawa, A., and W. H. Schubert, 1974: Interaction of a cumulus cloud ensemble with the large-scale environment, Part I. *J. Atmos. Sci*., **31**, 674–701.

Arakawa, A., and J.-H. Jung, 2011: Multiscale modeling of the moist-convective atmosphere — A review. *Atmos. Res.*, **102**, 263-285.

Arakawa, A., and C.-M. Wu, 2013: A Unified Representation of Deep Moist Convection in Numerical Modeling of the Atmosphere. Part I. *J. Atmos. Sci*., **70**, 1977–1992.

Avissar R., and R. A. Pielke, 1989: A parameterization of heterogeneous land surfaces for atmospheric numerical models and its impact on regional meteorology. *Mon. Wea. Rev.*, **117**, 2113-2136, doi: 10.1175/1520-0493(1989)117<2113:APOHLS>2.0.CO;2.

Avissar, R., and F. Chen, 1993: Development and analysis of prognostic equations for mesoscale kinetic energy and mesoscale (subgrid scale) fluxes for large-scale atmospheric models. *J. Atmos. Sci.*, **50**: 3751-3774, doi: 10.1175/1520-0469(1993)050<3751:DAAOPE>2.0.CO;2.

Avissar, R., and Y. Liu, 1996: Three-dimensional numerical study of shallow convective clouds and precipitation induced by land surface forcing. *J. Geophys. Res.*, **101**(D3): 7499-7518, doi: 10.1029/95JD03031.

Avissar, R., E. W. Eloranta, K. Gürer, and G. J. Tripoli, 1998: An evaluation of the large-eddy simulation option of the regional atmospheric modeling system in simulating a convective boundary layer: A FIFE Case Study. *J. Atmos. Sci.*, **55**, 1109-1130.

Avissar, R., and T. Schmidt, 1998: An evaluation of the scale at which ground-surface heat flux patchiness affects the convective boundary layer using large-eddy simulations. *J. Atmos. Sci.*, **55**: 2666-2689, doi: 10.1175/1520-0469(1998)055<2666:AEOTSA>2.0.CO;2.

Baidya Roy, S., and R. Avissar, 2000: Scales of response of the convective boundary layer to surface heterogeneity. *Geophys. Res. Lett.*, **27**: 533-536, doi: 10.1029/1999GL010971.

Baldi M., G. A. Dalu, R. A. Pielke, and F. Meneguzzo, 2005: Analytical evaluation of mesoscale fluxes and pressure field. Environ. *Fluid Mech.*, **5**, 1-2, doi: 10.1007/s10652-005-8089-6, 3-33.

Bechtold, P., M. Köhler, T. Jung, F. Doblas-Reyes, M. Leutbecher, M. J. Rodwell, F. Vitart, and G. Balsamo, 2008: Advances in simulating atmospheric variability with the ECMWF model: From synoptic to decadal time-scales. *Q.J.R. Meteorol. Soc.*, **134**, 1337–1351, doi: 10.1002/qj.289.

Betts, A. K., 2007: Coupling of water vapor convergence, clouds, precipitation, and land-surface processes. *J. Geophys. Res.: Atmos.*, **112** (D10), doi: 10.1029/2006JD008191.

Black, T. L., 1994: The New NMC Mesoscale Eta Model: Description and Forecast Examples. *Wea. Forecasting,* **9**, 265–278, doi: 10.1175/1520-0434(1994)009<0265:TNNMEM>2.0.CO;2.

Blackadar, A. K., 1979: High resolution models of the planetary boundary layer. *Adv. Environ. Sci. Eng.*, Vol. 1, No. 1, J. Pfafflin and E. Ziegler, Eds., Gordon and Breach, 50-85.

Blanken, P. D., 1998: Turbulent flux measurements above and below the overstory of a boreal aspen forest. *Bound-Lay. Meteorol.,* **89**: 109-140, doi: 10.1023/A:1001557022310.

Blossey, P. N., C. S. Bretherton, J. Cetrone, and M. Kharoutdinov, 2007: Cloud-Resolving model simulations of KWAJEX: Model sensitivities and comparisons with satellite and radar observations. *J. Atmos. Sci.*, **64**, 1488–1508, doi: 10.1175/JAS3982.1.

Brunsell, N. A., D. B. Mechem, and M. C. Anderson, 2011: Surface heterogeneity impacts on boundary layer dynamics via energy balance partitioning. *Atmos. Chem. Phys.*, **11**: 3403-3416, doi:10.5194/acp-11-3403-2011.

Bryan, G. H., and H. Morrison, 2012: Sensitivity of a simulated squall line to horizontal resolution and parameterization of microphysics. *Mon. Wea. Rev.*, **140**, 202–225.

Bukovsky, M. S., and D. J. Karoly, 2009: Precipitation simulations using WRF as a nested regional climate model. *J. Appl. Meteor. Climatol.*, **48.10**, 2152-2159, doi: 10.1175/2009JAMC2186.1.

Bullock, O. R. Jr., K. Alapaty, G. A. Herwehe, T. L. Spero, and C. G. Nolte, 2015: A dynamically computed convective time scale for the Kain-Fritsch convective parameterization scheme. *Mon. Wea. Rev.*, **143**, 2105–2120, doi: 10.1175/MWR-D-14-00251.1.

Cai, X., Z.-L. Yang, Y. Xia, M. Huang, H. Wei, L.R. Leung, and M.B. Ek, 2014: Assessment of simulated water balance from Noah, Noah-MP, CLM, and VIC over CONUS using the NLDAS test bed. *J. Geophys. Res. Atmos.*, **119** (24): 13751–13770, doi: 10.1002/2014JD022113.

Case, J. L., W. L. Crosson, S. V. Kumar, W. M. Lapenta, and C. D. Peters-Lidard, 2008: Impacts of high-resolution land surface initialization on regional sensible weather forecasts from the WRF Model. *J. Hydrometeor*, **9**, 1249–1266, doi: 10.1175/2008JHM990.1.

Case, J. L., S. V. Kumar, J. Srikishen, and G. J. Jedlovec, 2011: Improving numerical weather predictions of summertime precipitation over the southeastern United States through a high-resolution initialization of the surface state. *Wea. Forecasting.*, **26**: 785–807, doi: 10.1175/2011WAF2222455.1.

Charusombat, U., D. Niyogi, S. Garrigues, A. Olioso, O. Marloie, M. Barlage, F. Chen, M. Ek, X. Wang, and Z. Wu, 2012: Noah-GEM and Land Data Assimilation System (LDAS) based downscaling of Global Reanalysis surface fields: Evaluations using observations from a CarboEurope agricultural site, COMPAG. *Comput. Electron. Agr.*, **86**, 55-74, doi: 10.1016/j.compag.2011.12.001.

Chen, F., and R. Avissar, 1994: Impact of land-surface moisture variability on local shallow convective cumulus and precipitation in large-scale models. *J. Appl. Meteor.*, **33**: 1382-1401, doi: 10.1175/1520-0450(1994)033<1382:IOLSMV>2.0.CO;2.

Chen, F., Z. Janjic, and K. Mitchell, 1997: Impact of atmospheric surface-layer parameterizations in the new land-surface scheme of the NCEP mesoscale Eta model. *Bound.-Layer. Meteor.*, **85.3**, 391-421, doi: 10.1023/A:1000531001463.

Chen, F., and J. Dudhia, 2001: Coupling an advanced land surface hydrology model with the Penn State–NCAR MM5 modeling system. Part I: Model implementation and sensitivity. *Mon. Wea. Rev.*, **129**, 569–585.

Chen, F., K. W. Manning, M. A. LeMone, S. B. Trier, J. G. Alfieri, R. Roberts, M. Tewari, and Coauthors, 2007: Description and evaluation of the characteristics of the NCAR High-Resolution Land Data Assimilation System. *J. Appl. Meteor. Climatol.*, **46.6**, 694-713, doi: 10.1175/JAM2463.1.

Chen, F., and Y. Zhang, 2009: On the coupling strength between the land surface and the atmosphere: From viewpoint of surface exchange coefficients. *Geophys. Res. Lett.* **36.10**, L10404, doi: 10.1029/2009GL037980.

Chen, F., and Coauthors, 2011: The integrated WRF/urban modelling system: development, evaluation, and applications to urban environmental problems. *Int. J. Climatol.*, **31**, 273–288, doi: 10.1002/joc.2158.

Cheng, Y., V. M. Canuto, and A. M. Howard, 2002: An improved model for the turbulent PBL. *J. Atmos. Sci.*, **59**: 1550-1565.

Chikira, M., and M. Sugiyama, 2010: A cumulus parameterization with state-dependent entrainment rate. Part I: Description and sensitivity to temperature and humidity profiles. *J. Atmos. Sci.*, **67**, 2171–2193.

Ching, J., R. Rotunno, M. LeMone, A. Martilli, B. Kosovic, P. A. Jimenez, and J. Dudhia, 2014: Convectively induced secondary circulations in fine-grid mesoscale numerical weather prediction models. *Mon. Wea. Rev.*, **142**, 3284–3302, doi: 10.1175/MWR-D-13-00318.1.

Cintineo, R., J. A. Otkin, M. Xue, and F. Kong, 2014: Evaluating the performance of planetary boundary layer and cloud microphysical parameterization schemes in convection-permitting ensemble forecasts using synthetic GOES-13 satellite observations. *Mon. Wea. Rev.*, **142**, 163–182, doi: 10.1175/MWR-D-13-00143.1.

Clark, A. J., and Coauthors, 2012: An overview of the 2010 Hazardous Weather Testbed Experimental Forecast Program Spring Experiment. *Bull. Amer. Meteor. Soc.*, **93**, 55–74, doi: 10.1175/BAMS-D-11-00040.1.

Dawson, D. T., M. Xue, J. A. Milbrandt, and M. K. Yau, 2010: Comparison of evaporation and cold pool development between single-moment and multimoment bulk microphysics schemes in idealized simulations of tornadic thunderstorms. *Mon. Wea. Rev.*, **138**, 1152–1171, doi: 10.1175/2009MWR2956.1.

Deardorff, J. W., and G.E. Willis, 1982: Investigation of the frozen-turbulence hypothesis for temperature spectra in a convectively mixed layer. *Phy. Fluids*, **25**, 21-28.

Del Genio, A. D., and J. Wu, 2010: The role of entrainment in the diurnal cycle of continental convection. *J. Climate*, **23**, 2722-2738.

Del Genio, A. D., Y. Chen, D. Kim, and M.-S. Yao, 2012: The MJO transition from shallow to deep convection in CloudSat/CALIPSO data and GISS GCM simulations. *J. Climate*, **25**, 3755-3770, doi:10.1175/JCLI-D-11-00384.1.

de Rooy, W. C., P. Bechtold, K. Frohlich, C. Hoehnegger, H.Jonker, D. Mironov, A.P. Siebesma, J. Teixeira, and J. Yano, 2013: Entraiment and detrainment in cumulus convection: An overview. *Q. J. R. Meteorol. Soc.*, **129**, 1-19.

Deng, A., and D. R. Stauffer, 2006: On improving 4-km mesoscale model simulations. *J. Appl. Meteor. Climatol.*, **45**, 361–381, doi: 10.1175/JAM2341.1.

Dirmeyer, P. A., 2000: Using a global soil wetness dataset to improve seasonal climate simulation. *J. Climate.*, **13,** 2900–2922.

Dirmeyer, P. A., R. D. Koster, and Z. Guo, 2006: Do global models properly represent the feedback between land and atmosphere?. *J. Hydrometeorol.*, **7.6,** 1177-1198, doi: 10.1175/JHM532.1.

Dirmeyer, P. A., X. Gao, M. Zhao, Z. Guo, T. Oki, and H. Naota, 2006: GSWP-2: Multimodel analysis and implications for our perception of the land surface. *Bull. Amer. Meteor. Soc.*, **87**: 1381-1397, doi: 10.1175/BAMS-87-10-1381.

Done, J. M., G. C. Craig, S. L. Gray, P. A. Clark, and M. E. B. Gray, 2006: Mesoscale simulations of organized convection: Importance of convective equilibrium. *Q. J. R. Meteorol. Soc.*, **132**, 737–756, doi: 10.1256/qj.04.84.

Dudhia, J., 1989: Numerical study of convection observed during the winter monsoon experiment using a mesoscale two-dimensional model. *J. Atmos. Sci.*, **46.20**, 3077-3107, doi: 10.1175/1520-0469(1989)046<3077:NSOCOD>2.0.CO;2.

Eastman, J. L., R. A. Pielke, and D. J. McDonald, 1998: Calibration of soil moisture for large eddy simulations over the FIFE area. *J. Atmos. Sci.*, **55**, 1131-1140.

Ehrendorfer, M., 1997: Predicting the uncertainty of numerical weather forecasts: a review. *Meteor. Z.*, **6**, 147-183.

Ek, M. B., K. E. Mitchell, Y. Lin, E. Rogers, P. Grunmann, V. Koren, G. Gayno, and J. D. Tarpley, 2003: Implementation of Noah land surface model advances in the National Centers for Environmental Prediction operational mesoscale Eta model. *J. Geophys. Res.*, **108.D22**, 8851, doi: 10.1029/2002JD003296.

Eltahir, E. A. B., 1998: A soil moisture-rainfall feedback mechanism: 1. Theory and observations. *Water. Resour. Res.*, **34(4)**: 765-776, doi: 10.1029/97WR03499.

Findell K. L, and E. A. B. Eltahir, 2003: Atmospheric controls on soil moisture-boundary layer interactions: Part I: Framework development. *J. Hydrometeorol.,* **4**: 552–569, doi: 10.1029/2001JD001515.

Findell, K. L., P. Gentine, B. R. Lintner, and C. Kerr, 2011: Probability of afternoon precipitation in eastern United States and Mexico enhanced by high evaporation. *Nat. Geosci.*, **4**: 434-439, doi: 10.1038/ngeo1174.

Fritsch, J. M., and C. F. Chappell, 1980: Numerical prediction of convectively driven mesoscale pressure systems. Part I: Convective parameterization. *J. Atmos. Sci*., **37**, 1722-1733.

Fischer, E. M., S. I. Seneviratne, D. Lüthi, and C. Schär, 2007: Contribution of land-atmosphere coupling to recent European summer heat waves. *Geophys. Res. Lett.*, **34.6**, L06707, doi: 10.1029/2006GL029068.

Flaounas, E., S. Bastin, and S. Janicot, 2011: Regional climate modelling of the 2006 West African monsoon: sensitivity to convection and planetary boundary layer parameterisation using WRF. *Climate Dyn.,* **36.5-6**, 1083-1105, doi: 10.1007/s00382-010-0785-3.

Grant, A. L. M. and A. P. Lock, 2004: The turbulent kinetic energy budget for shallow cumulus convection. *Q. J. R. Meteorol. Soc.,* **130**, 401–422, doi: 10.1256/qj.03.50.

Gustafson Jr., W. I., P.-L. Ma, H. Xiao, B. Singh, P. J. Rasch, and J. D. Fast, 2013, The Separate Physics and Dynamics Experiment (SPADE) framework for determining resolution awareness: A case study of microphysics, *J. Geophys. Res. Atmos.*, **118**, 9258–9276, doi: 10.1002/jgrd.50711.

Gutmann, E. D., and E. E. Small, 2007: A comparison of land surface model soil hydraulic properties estimated by inverse modeling and pedotransfer functions. *Water Resour. Res.*, **43.5**, W05418, doi: 10.1029/2006WR005135.

Hacker, J. P., and W. M. Angevine, 2013: Ensemble data assimilation to characterize surface-layer errors in numerical weather prediction models. *Mon. Wea. Rev.*, **141.6**, 1804-1821, doi: 10.1175/MWR-D-12-00280.1.

Hadfield, M. G., W. R. Cotton, and R. A. Pielke, 1992: Large-eddy simulations of thermally forced circulations in the convective boundary layer. Part II: The effect of changes in wavelength and wind speed. *Bound.-Layer Meteor.*, **58**, 307-328.

Han, J., and H.-L. Pan, 2011: Revision of convection and vertical diffusion schemes in the NCEP Global Forecast System. *Wea. Forecasting*, **26**, 520–533, doi: 10.1175/WAF-D-10-05038.1.

Han, X., H.-J. Hendricks Franssen, C. Montzka, and H. Vereecken, 2014: Soil moisture and soil properties estimation in the Community Land Model with synthetic brightness temperature observations. *Water Resour. Res.*, **50**, 6081–6105, doi: 10.1002/2013WR014586.

Henderson-Sellers, A., A. J. Pitman, P. K. Love, P. Irannejad, and T. H. Chen, 1995: The Project for Intercomparison of Land Surface Parameterization Schemes (PILPS): Phases 2 and 3. *Bull. Amer. Meteor. Soc.*, **76**: 489-503, doi: 10.1175/1520-0477(1995)076<0489:TPFIOL>2.0.CO;2

Henderson-Sellers, A., K. McGuffie, and A. J. Pitman, 1996: The Project for Intercomparison of Land-surface Parametrization Schemes (PILPS): 1992 to 1995. *Clim. Dyn.*, **12(12)**: 849-859, doi: 10.1007/s003820050147.

Herwehe, J. A., K. Alapaty, T. L. Spero, and C. G. Nolte, 2014: Increasing the credibility of regional climate simulations by introducing subgrid-scale cloud – radiation interactions. *J. Geophys. Res.*, ***119***, 5317-5330, doi: 10.1002/2014JD021504.

Hirsch, A. L., A. J. Pitman, and J. Kala, 2014: The role of land cover change in modulating the soil moisture-temperature land-atmosphere coupling strength over Australia. *Geophys. Res. Lett.*, **41,** doi: 10.1002/2014GL061179.

Holland, J. Z., and E. M. Rasmusson, 1973: Measurement of atmospheric mass, energy, and momentum budgets over a 500-kilometer square of tropical ocean. *Mon. Wea. Rev.*, **101**, 44–55.

Holt, T. R., D. Niyogi, F. Chen, K. Manning, M. A. LeMone, and A. Qureshi, 2006: Effect of Land-Atmosphere Interactions on the IHOP 24-25 May 2002 Convection Case. *Mon. Wea. Rev.*, **134.1**, 113-133, doi: 10.1175/MWR3057.1.

Hong, S.-Y., and H. L. Pan, 1996: Nonlocal boundary layer vertical diffusion in a medium-range forecast model. *Mon. Wea. Rev.*, **124**: 2322–2339, doi: 10.1175/1520-0493(1996)124<2322:NBLVDI>2.0.CO;2.

Hong, S.-Y., J. Dudhia, and S.-H. Chen, 2004: A revised approach to ice microphysical processes for the bulk parameterization of clouds and precipitation. *Mon. Wea. Rev.*, **132**, 103–120, doi: 10.1175/1520-0493(2004)132<0103:ARATIM>2.0.CO;2.

Hong, S.-Y., K.-S. Sunny Lim, Y.-H. Lee, J.-C. Ha, H.-W. Kim, S.-J. Ham, and J. Dudhia, 2010: Evaluation of the WRF double-moment 6-class microphysics scheme for precipitating convection. *Adv. Meteor.*, 2010, 707253, doi:10.1155/2010/707253.

Houghton, H., and H. Cramer, 1951: A theory of entrainment in convective currents. *J. Meteorol.*, **8**, 95-102.

Houze, R. A. Jr, 2012: Orographic effects on precipitating clouds. *Rev. Geophys.,* **50**, RG1001, doi: 10.1029/2011RG000365.

Huang, H. Y., and S. A. Margulis, 2009: On the impact of surface heterogeneity on a realistic convective boundary layer. *Water. Resour. Res.,* **45**: W04425, doi: 10.1029/2008WR007175.

Iacono, M. J., J. S. Delamere, E. J. Mlawer, M. W. Shepard, S. A. Clough, and W. D. Collins, 2008: Radiative forcing by long-lived greenhouse gases: Calculations with the AER radiative transfer models. *J. Geophys. Res.,* **113**, D13103, doi: 10.1029/2008JD009944.

Janjic, Z. I., 1994: The step-mountain eta coordinate model: Further developments of the convection, viscous sublayer, and turbulence closure schemes. *Mon. Wea. Rev.*, **122.5**, 927-945, doi: 10.1175/1520-0493(1994)122<0927:TSMECM>2.0.CO;2.

Janjic, Z. I., 2000: Comments on “Development and evaluation of a convection scheme for use in climate models”. *J. Atmos. Sci.*, **57.21**, 3686, doi: 10.1175/1520-0469(2000)057<3686:CODAEO>2.0.CO;2.

Janjic, Z. I., 2001: Nonsingular implementation of the Mellor-Yamada level 2.5 scheme in the NCEP Meso model. NOAA/NWS/NCEP Office Note 437, 61 pp.

Janjic, Z. I., 2002: Nonsingular Implementation of the Mellor-Yamada Level 2.5 Scheme in the NCEP Meso model. *NCEP Office Note* No. 437, 61pp.

Jensen, M. P., et al., 2010: Midlatitude Continental Convective Clouds Experiment (MC3E), DOE/SC-ARM/10-0004.

Kain, J. S., and J. M. Fritsch, 1990: A one-dimensional entraining/detraining plume model and its application in convective parameterization. *J. Atmos. Sci.,* **47**, 2784–2802, doi: 10.1175/1520-0469(1990)047<2784:AODEPM>2.0.CO;2.

Kain, J. S., and J. M. Fritsch, 1993: Convective parameterization for mesoscale models: The Kain–Fritsch scheme. *The Representation of Cumulus Convection in Numerical Models, Meteor. Monogr.,* No. 24, *Amer. Meteor. Soc.,* 165–170.

Kain, J. S., 2004: The Kain–Fritsch convective parameterization: An Update. *J. Appl. Meteor.,* **43**, 170–181, doi: 10.1175/1520-0450(2004)043<0170:TKCPAU>2.0.CO;2.

Kain, J. S., and Coauthors, 2008: Some practical considerations regarding horizontal resolution in the first generation of operational convection-allowing NWP. *Wea. Forecasting,* **23**, 931–952, doi: 10.1175/WAF2007106.1.

Kang, S. L., K. J. Davis, and M. A. LeMone, 2007: Observations of the ABL structures over a heterogeneous land surface during IHOP_2002. *J. Hydrometeor.,* **8.2**, 221-244, doi: 10.1175/JHM567.1.

Kang, S. M., D. M. W. Frierson, and I. M. Held, 2009: The tropical response to extratropical thermal forcing in an idealized GCM: the importance of radiative feedbacks and convective parameterization. *J. Atmos. Sci.,* **66**, 2812–2827, doi: 10.1175/2009JAS2924.1.

Kim, D., A. H. Sobel, E. D. Maloney, D. M. W. Frierson, and I.-S. Kang, 2011: A Systematic Relationship between Intraseasonal Variability and Mean State Bias in AGCM Simulations. *J. Climate*, **24**, 5506–5520, doi: 10.1175/2011JCLI4177.1.

Koster, R. D., M. J. Suarez, R. W. Higgins, and H. M. Van den Dool, 2003: Observational evidence that soil moisture variations affect precipitation. *Geophys. Res. Lett.*, **30.5**, 1241, doi: 10.1029/2002GL016571.

Koster, R. D., and Coauthors, 2004: Regions of strong coupling between soil moisture and precipitation, *Science,* **305**: 1138-1140, doi: 10.1126/science.1100217.

Koster, R. D., Y. C. Sud, Z. Guo, P. A. Dirmeyer, G. Bonan, K. W. Oleson, E. Chan, and Coauthors, 2006: GLACE: the global land-atmosphere coupling experiment. Part I: overview. *J. Hydrometeorol.*, **7.4**, 590-610, doi: 10.1175/JHM510.1.

Lawrence, M. G., and P. J. Rasch, 2005: Tracer transport in deep convective updrafts: Plume ensemble versus bulk formulations. *J. Atmos. Sci*., 62, 2880–2894.

LeMone, M. A., F. Chen, J. G. Alfieri, M. Tewari, B. Geerts, Q. Miao, R. L. Grossman, and R. L. Coulter, 2007: Influence of land cover and soil moisture on the horizontal distribution of sensible and latent heat fluxes in southeast Kansas during IHOP_2002 and CASES-97, *J. Hydrometeorol.,* **8**: 68-87, doi: 10.1175/JHM554.1.

LeMone, M. A., M. Tewari, F. Chen, J. G. Alfieri, and D. Niyogi, 2008: Evaluation of the Noah land surface model using data from a fair-weather IHOP_2002 day with heterogeneous surface fluxes. *Mon. Wea. Rev.*, **136.12**, 4915-4941, doi: 10.1175/2008MWR2354.1.

LeMone, M. A., F. Chen, M. Tewari, J. Dudhia, B. Geerts, Q. Miao, R. Coulter, and R. Grossman, 2010: Simulating the IHOP_2002 fair-weather CBL with the WRF-ARW-Noah modeling system. Part I: Surface fluxes and CBL structure and evolution along the eastern track. *Mon. Wea. Rev.,* **138.3,** 722-744, doi: 10.1175/2009MWR3003.1.

LeMone, M. A., M. Tewari, F. Chen, and J. Dudhia, 2013: Objectively determined fair-weather CBL depths in the ARW-WRF model and their comparison to CASES-97 observations. *Mon. Wea. Rev.*, **141**: 30-54, doi: 10.1175/MWR-D-12-00106.1.

LeMone M. A., M. Tewari, F. Chen, and J. Dudhia, 2014: Objectively determined fair-weather NBL features in ARW-WRF and their comparison to CASES-97 Observations. *Mon. Wea. Rev.*, **142**: 2709–2732, doi: 10.1175/MWR-D-13-00358.1.

Lin, Y., and K. E. Mitchell, 2005: The NCEP Stage II/IV hourly precipitation analyses: Development and applications. Preprints, *19th Conf. on Hydrology, San Diego, CA, Amer. Meteor. Soc.*, 1.2.

Lin, Y., M. Zhao, Y. Ming, J.-C. Golaz, L. J. Donner, S. A. Klein, V. Ramaswamy, and S. Xie, 2013: Precipitation partitioning, tropical clouds, and intraseasonal variability in GFDL AM2. *J. Climate*, **26**, 5453–5466, doi: 10.1175/JCLI-D-12-00442.1.

Lorenz, R., and A. J. Pitman, 2014: Effect of land-atmosphere coupling strength on impacts from Amazonian deforestation. *Geophys. Res. Lett.*, **41**, doi: 10.1002/2014GL061017.

Luo, Y., Y. Wang, H. Wang, Y. Zheng, and H. Morrison, 2010: Modeling convective-stratiform precipitation processes on a Mei-Yu front with the Weather Research and Forecasting model: Comparison with observations and sensitivity to cloud microphysics parameterizations. *J. Geophys. Res.*, **115**, D18117, doi: 10.1029/2010JD013873.

Mallard, M. S., G. M. Lackmann, A. Aiyyer, and K. Hill, 2013: Atlantic hurricanes and climate change. Part I: Experimental design and isolation of thermodynamic effects. *J. Climate*, **26**, 4876–4893.

Marshall, J. S., R. Langille, and W. Palmer, 1947: Measurement of rainfall by radar. *J. Meteor.*, **4**, 186-192, doi: 1520-0469(1947)004<0186:MORBR>2.0.CO;2.

Mishra, S. K., and J. Srinivasan, 2010: Sensitivity of the simulated precipitation to changes in convective relaxation time scale. *Ann. Geophys.*, **28**, 1827–1846, doi: 10.5194/angeo-28-1827-2010.

Molinari, J., and M. Dudek, 1992: Parameterization of convective precipitation in mesoscale numerical models: A critical review. *Mon. Wea. Rev.*, **120**, 326–344.

Moncrieff, M. W., and M. J. Miller, 1976: The dynamics and simulation of tropical cumulonimbus and squall lines. *Q.J.R. Meteorol. Soc.*, **102**: 373-394, doi: 10.1002/qj.49710243208.

Moncrieff, M. W., 2004: Analytic representation of the large-scale organization of tropical convection. *J. Atmos. Sci.*, **61.13**, 1521-1538, doi: 10.1175/1520-0469(2004)061<1521:AROTLO>2.0.CO;2.

Mlawer, E. J., S. J. Taubman, P. D. Brown, M. J. Iacono, and S. A. Cough, 1997: Radiative transfer for inhomogeneous atmosphere: RRTM, a validated correlated-k model for the longwave. *J. Geophys. Res.*, **102.D14,** 16663-16682, doi: 10.1029/97JD00237.

Neale, R. B., and Coauthors, 2010: Description of the NCAR Community Atmospheric Model (CAM5.0), *NCAR Tech. Note* NCAR/TN-486+STR, 268 pp.

Niyogi, D., S. Raman, and K. Alapaty, 1999: Uncertainty in specification of surface characteristics, Part ii: Hierarchy of interaction explicit statistical analysis. *Bound.-Lay. Meteorol.*, **91.3**, 341-366, doi: 10.1023/A:1002023724201.

Niyogi, D., T. Holt, S. Zhong, P. C. Pyle, and J. Basara, 2006: Urban and land surface effects on the 30 July 2003 mesoscale convective system event observed in the southern Great Plains. *J. Geophys. Res.*, **111**, D19107, doi: 10.1029/2005JD006746.

Niyogi, D., R. Mahmood, and J. O. Adegoke, 2009a: Land-use/land-cover change and its impacts on weather and climate. *Bound-Lay. Meteorol.*, **133**: 297-298, doi: 10.1007/s10546-009-9437-8.

Niyogi, D., K. Alapaty, S. Raman, and F. Chen, 2009b: Development and evaluation of a coupled photosynthesis-based gas exchange evapotranspiration model (GEM) for mesoscale weather forecasting applications. *J. Appl. Meteorol. Climatol.*, **48**: 349-368, doi:10.1175/2008JAMC1662.1.

Niyogi, D., P. Pyle, M. Lei, S. P. Arya, C. M. Kishtawal, M. Shepherd, F. Chen, and B. Wolfe, 2011: Urban modification of thunderstorms: An observational storm climatology and model case study for the Indianapolis urban region. *J. Appl. Meteor. Climatol.*, **50**, 1129–1144, doi: 10.1175/2010JAMC1836.1.

Niu, G. Y., and Coauthors, 2011: The community Noah land surface model with multiparameterization options (Noah-MP): 1. Model description and evaluation with local-scale measurements. *J. Geophys. Res.*, **116**: D12109, doi: 10.1029/2010JD015139.

Otte, T. L., C. G. Nolte, M. J. Otte, and J. H. Bowden, 2012: Does nudging squelch the extremes in regional climate modeling?. *J. Climate*, **25**, 7046–7066, doi: 10.1175/JCLI-D-12-00048.1.

Pielke, R. A., and M. Uliasz, 1993: Influence of landscape variability on atmospheric dispersion. *J. Air Waste Mgt.*, **43**, 989-994.

Pielke, R. A., 2001: Influence of the spatial distribution of vegetation and soils on the prediction of cumulus convective rainfall. *Rev. Geophys.*, **39.2**, 151-177, doi: 10.1029/1999RG000072.

Pielke, R. A., A. Pitman, D. Niyogi, R. Mahmood, C. McAlpine, F. Hossain, K. K. Goldewijk, U. Nair, R. Betts, S. Fall, M. Reichstei, P. Kabat, and N. de Noblet, 2011: Land use/land cover changes and climate: modeling analysis and observational evidence. *WIREs. Clim. Change.*, **2.6**, 828-850, doi: 10.1002/wcc.144.

Pitman, A. J., 1994: Assessing the sensitivity of a land-surface scheme to the parameter values using a single column model. *J. Clim.*, **7(12)**, 1856-1869, doi: 10.1175/1520-0442(1994)007<1856:ATSOAL>2.0.CO;2.

Pitman, A. J. et al., 1999: Key results and implications from phase 1 (c) of the project for intercomparison of land-surface parametrization schemes. *Clim. Dyn.*, **15(9)**, 673-684, doi: 10.1007/s003820050309.

Pitman, A. J., 2003: The evolution of, and revolution in, land surface schemes designed for climate models. *Int. J. Climatol.*, **23**: 479-510, doi: 10.1002/joc.893.

Rabier, F., E. Klinker, P. Courtier, and A. Hollingsworth, 1996: Sensitivity of forecast errors to initial conditions. *Q.J.R. Meteorol. Soc.*, **122**, 121–150, doi: 10.1002/qj.49712252906.

Redelsperger, J. L., C. D. Thorncroft, A. Diedhiou, T. Lebel, D. J. Parker, and J. Polcher, 2006: African Monsoon Multidisciplinary Analysis: An international research project and field campaign. *Bull. Amer. Meteor. Soc.,* **87.12**, 1739-1746, doi: 10.1175/BAMS-87-12-1739.

Reen, B. P., D. R. Stauffer, and K. J. Davis, 2014: Land-surface heterogeneity effects in the planetary boundary layer. *Bound-Lay. Meteorol.,* **150.1**: 1-31, doi: s10546-013-9860-8.

Richter, J. H., and P. J. Rasch, 2008: Effects of convective momentum transport on the atmospheric circulation in the community atmosphere model, Version 3. *J. Climate*, **21**, 1487–1499, doi: 10.1175/2007JCLI1789.1.

Romps, D. M., and Z. Kuang, 2010: Do undiluted convective plumes exist in the upper tropical troposphere? *J. Atmos. Sci*., **67**, 468-484.

Routray, A., U. C. Mohanty, S. R. H. Rizvi, D. Niyogi, K. K. Osuri, and D. Pradhan, 2010: Impact of Doppler weather radar data on numerical forecast of Indian monsoon depressions. *Q. J. R. Meteorol. Soc.*, **136**, 1836–1850, doi: 10.1002/qj.678.

Ruiz-Barradas, A., and S. Nigam, 2005: Warm season rainfall variability over the US Great Plains in observations, NCEP and ERA-40 reanalyses, and NCAR and NASA atmospheric model simulations. *J. Climate.*, **18.11**, 1808-1830, doi: 10.1175/JCLI3343.1.

Santanello, J. A., C. D. Peters-Lidard, and S. V. Kumar, 2011: Diagnosing the Sensitivity of Local Land–Atmosphere Coupling via the Soil Moisture–Boundary Layer Interaction. *J. Hydrometeor*, **12**, 766–786, doi: 10.1175/JHM-D-10-05014.1.

Santanello Jr., J. A., C. D. Peters-Lidard, A. Kennedy, and S. V. Kumar, 2013a: Diagnosing the nature of land-atmosphere coupling: A case study of dry/wet extremes in the U.S. Southern Great Plains. *J. Hydrometeor*, **14**: 3–24, doi: 10.1175/JHM-D-12-023.1.

Santanello Jr., J. A., S. V. Kumar, C. D. Peters-Lidard, K. Harrison, and S. Zhou, 2013b: Impact of land model calibration on coupled land–atmosphere prediction. *J. Hydrometeor*, **14**, 1373–1400, doi: 10.1175/JHM-D-12-0127.1.

Schmid, H. P., 1994: Source areas for scalars and scalar fluxes. *Bound-Lay. Meteorol.*, **67(3)**: 293-318, doi: 10.1007/BF00713146.

Schmid, H. P., 2002: Footprint modeling for vegetation atmosphere exchange studies: a review and perspective. *Agr. Forest. Meteorol.*, **113**:159-183, doi: 10.1016/S0168-1923(02)00107-7.

Seaman, N. L., S. A. Michelson, P. C. Shafran, and D. R. Stauffer, 1998: Forecast of a severe squall line development in MM5 using explicit moist physics at 4-km resolution. *12th Conf. on Numerical Weather Prediction*, Phoenix, AZ, *Amer. Meteor. Soc.*, J1–J4.

Seifert, A., and B. Stevens, 2010: Microphysical Scaling Relations in a Kinematic Model of Isolated Shallow Cumulus Clouds. *J. Atmos. Sci.*, **67**, 1575–1590, doi: 10.1175/2009JAS3319.1.

Seneviratne, S. I., D. Lüthi, M. Litschi, and C. Schär, 2006: Land-atmosphere coupling and climate change in Europe. *Nature*, **443**, 205-209, doi: 10.1038/nature05095.

Seneviratne, S. I., T. Corti, E. L. Davin, M. Hirschi, E. B. Jaeger, I. Lehner, B. Orlowsky, and A. J. Teuling, 2010: Investigating soil moisture–climate interactions in a changing climate: A review. *Earth Sci. Rev.*, **99**, 125–161.

Simmons, A. J., and A. Hollingsworth, 2002: Some aspects of the improvement in skill of numerical weather prediction. *Q. J. R. Meteor. Soc.*, **128,** 647–677.

Skamarock, W. C., 2004: Evaluating mesoscale NWP models using kinetic energy spectra. *Mon. Weather. Rev.*, **132 (12)**: 3019-3032, doi:10.1175/MWR2830.1.

Skamarock, W. C., and D. Dempsey, 2005: High resolution winter season NWP: Preliminary evaluation of the WRF-ARW and WRF-NMM models in the DWFE forecast experiment. Preprints, 17th Conf. on Numerical Weather Prediction, Washington, DC, Amer. Meteor. Soc., 16A.3.

Skamarock, W. C., J. B. Klemp, J. Dudhia, D.O. Gill, D. Barker, M. G. Duda, X. Huang, and W. Wang, 2008: A description of the Advanced Research WRF version 3. NCAR/TN–4751 STR, 113 pp.

Skamarock, W. C., and J. B. Klemp, 2008: A time-split nonhydrostatic atmospheric model for weather research and forecasting applications. *J. Comput. Phys.*, **227**, 3465-3485.

Skamarock, W. C., J. B. Klemp, M. G. Duda, L. D. Fowler, S.-H. Park, and T. D. Ringler, 2012: A Multiscale Nonhydrostatic Atmospheric Model Using Centroidal Voronoi Tesselations and C-Grid Staggering. *Mon. Wea. Rev.*, **140**, 3090–3105.

Snively, D. V., and W. A. Gallus Jr., 2014: Prediction of Convective Morphology in Near-Cloud-Permitting WRF Model Simulations. *Wea. Forecasting*, **29**, 130–149, doi: 10.1175/WAF-D-13-00047.1

Stensrud, D. J., J. Bao, and T. T. Warner, 2000: Using initial condition and model physics perturbations in short-range ensemble simulations of mesoscale convective systems. *Mon. Wea. Rev.*, **128**, 2077–2107.

Stensrud, D. J., 2007: Parameterization Schemes: Keys to Understanding Numerical Weather Prediction Models. *Cambridge publication*, 462 pp.

Steven, D. E., and C. S. Bretherton, 1999: Effects of resolution on the simulation of stratocumulus entrainment. *Q. J. R. Meteorol. Soc*., **125**, 425-439.

Stokes, G. M., and S. E. Schwartz, 1994: The Atmospheric Radiation Measurement (ARM) program: Programmatic background and design of the cloud and radiation test bed. *Bull. Amer. Meteor. Soc.*, **75**: 1201–1221, doi: 10.1175/1520-0477(1994)075<1201:TARMPP>2.0.CO;2.

Stull, R. B., 1988: An Introduction to Boundary Layer Meteorology. *Kluwer Academic Publishers*, 666pp.

Tao, W. K., J. Simpson, and M. McCumber, 1989: An ice-water saturation adjustment. *Mon. Wea. Rev.,* **117**, 231-235, doi: 10.1175/1520-0493(1989)117<0231:AIWSA>2.0.CO;2.

Taylor, C. M., R. A. M. De Jeu, F. Guichard, P. P. Harris, and W. A. Dorigo, 2012: Afternoon rain more likely over drier soils, *Nature*, **489**, 423-426, doi: 10.1038/nature11377.

Tokioka, T., K. Yamazaki, A. Kotoh, and T. Ose, 1988: The equatorial 30-60 day oscillation and the Arakawa–Schubert penetrative cumulus parameterization. *J. Meteor. Soc. Japan*, **66**, 883–900.

Trier, S. B., F. Chen, and K. W. Manning, 2004: A study of convection initiation in a mesoscale model using high-resolution land surface initial conditions. *Mon. Wea. Rev.*, **132.12**, 2954-2976, doi: 10.1175/MWR2839.1.

Trier, S. B., F. Chen, K. W. Manning, M. A. LeMone, and C. A. Davis, 2008: Sensitivity of the PBL and precipitation in 12-Day simulations of warm-season convection using different land surface models and soil wetness conditions. *Mon. Wea. Rev.*, **136**, 2321–2343. doi: 10.1175/2007MWR2289.1

Trier, S. B., M. A. LeMone, F. Chen, and K. W. Manning, 2011: Effects of surface heat and moisture exchange on ARW-WRF warm-season precipitation forecasts over the central United States. *Wea. Forecasting.*, **26.1**, 3-25, doi: 10.1175/2010WAF2222426.1.

van Lier-Walqui, M., T. Vukicevic, and D. J. Posselt, 2012: Quantification of Cloud Microphysical Parameterization Uncertainty Using Radar Reflectivity. *Mon. Wea. Rev.*, **140**, 3442–3466, doi: 10.1175/MWR-D-11-00216.1.

Van Weverberg, K., and Coauthors, 2013: The Role of Cloud Microphysics Parameterization in the Simulation of Mesoscale Convective System Clouds and Precipitation in the Tropical Western Pacific. *J. Atmos. Sci.,* **70**, 1104–1128, doi: 10.1175/JAS-D-12-0104.1.

Venkata Ratnam, J., and E. A. Cox, 2006: Simulation of monsoon depressions using MM5: sensitivity to cumulus parameterization schemes. *Meteorol. Atmos. Phys.*, **93.1-2**, 53-78, doi: 10.1007/s00703-005-0160-9.

Wang, J., R. L. Bras, and E. A. B. Eltahir, 1996: A stochastic linear theory of mesoscale circulation induced by the thermal heterogeneity of the land surface. *J. Atmos. Sci.*, **53**: 3349-3366, doi: 10.1175/1520-0469(1996)053<3349:ASLTOM>2.0.CO;2.

Wang, X., H. Xie, H. Sharif, and J. Zeitler, 2008: Validating NEXRAD MPE and stage III precipitation products for uniform rainfall on the Upper Guadalupe River Basin of the Texas Hill Country. *J. Hydrol.*, **348**, 73–86, doi: 10.1016/j.jhydrol.2007.09.057.

Wang, Y., C. N. Long, L. R. Leung, J. Dudhia, S. A. McFarlane, J. H. Mather, S. J. Ghan, and X. Liu, 2009: Evaluating regional cloud-permitting simulations of the WRF model for the Tropical Warm Pool International Cloud Experiment (TWP-ICE, Darwin 2006). *J. Geophys. Res.* **114**, 1-21, DOI: 10.1029/2009JD012729.

Wang, W., and N. L. Seaman, 1997: A comparison of convective parameterization schemes in a mesoscale model. *Mon. Wea. Rev.,* 125:252-278.

Weaver, C. P., 2004a: Coupling between large-scale atmospheric processes and mesoscale land-atmosphere interactions in the U.S. Southern Great Plains during summer. Part I: Case studies. *J. Hydrometeorol.*, **5**: 1223-1246, doi: 10.1175/JHM-396.1.

Weaver, C. P., 2004b: Coupling between large-scale atmospheric processes and mesoscale land-atmosphere interactions in the U.S. Southern Great Plains during summer. Part II: Mean Impacts of the Mesoscale. *J. Hydrometeorol.*, **5**: 1247-1258, doi: 10.1175/JHM-397.1.

Weaver, C. P., S. Baidya Roy, and R. Avissar, 2002: Sensitivity of simulated mesoscale atmospheric circulations resulting from landscape heterogeneity to aspects of model configuration. *J. Geophys. Res.*, 107(0), doi: 10.1029/2001JD000376.

Weckwerth, T. M., and D. B. Parsons, 2006: A Review of Convection Initiation and Motivation for IHOP_2002. *Mon. Wea. Rev.*, **134**, 5-22, doi: 10.1175/MWR3067.1.

Wei, H. L., Y. L. Xia, K. E. Mitchell, and M. B. Ek, 2013: Improvement of the Noah land surface model for warm season processes: Evaluation of water and energy flux simulation, *Hydrol. Processes*, 27(2), 297–303.

Weisman, M. L., C. Davis, W. Wang, K. W. Manning, and J. B. Klemp, 2008: Experiences with 0–36-h explicit convective forecasts with the WRF-ARW model. *Wea. Forecasting*, **23**, 407–437, doi: 10.1175/2007WAF2007005.1.

Westcott, N. E., H. V. Knapp, and S. D. Hilberg, 2008: Comparison of gage and multi-sensor precipitation estimates over a range of spatial and temporal scales in the Midwestern United States. *J. Hydrol.*, **351**, 1–12, doi: 10.1016/j.jhydrol.2007.10.057.

Westcott, N. E., 2009: Differences in multi-sensor and rain-gauge precipitation amounts. *Water Mgt.*, **162**, 73–81, doi: 10.1680/wama.2009.162.2.73.

Willis, G. E., and J. W. Deardorff, 1976: On the use of Taylor's translation hypothesis for diffusion in the mixed layer. *Q. J. R. Meteorol. Soc.*, **102(434)**: 817-822, doi: 10.1002/qj.49710243411.

Wilson, J. W., and R. D. Roberts, 2006: Summary of convective storm initiation and evolution during IHOP: Observational and modeling perspective. *Mon. Wea. Rev.*, **134**, 23–47.

Wulfmeyer, V., and Coauthors, 2006: Four-Dimensional variational assimilation of water vapor differential absorption lidar data: The first case study within IHOP_2002. *Mon. Wea. Rev.*, **134**, 209–230, doi: 10.1175/MWR3070.1.

Wulfmeyer, V, A. Behrendt, H. Bauer, C. Kottmeier, U. Corsmeier, A. Blyth, G. Craig, and Coauthors, 2008: The convective and orographically induced precipitation study: a research and development project of the world weather research program for improving quantitative precipitation forecasting in low-mountain regions. *Bull. Amer. Meteor. Soc.*, **89.10**, 1477-1486, doi: 10.1175/2008BAMS2367.1.

Xie, S., Y. Zhang, S. E. Giangrande, M. P. Jensen, R. McCoy, and M. Zhang, 2014: Interactions between cumulus convection and its environment as revealed by the MC3E sounding array. *J. Geophys. Res. Atmos.*, **119**, 11,784-11,808, doi: 10.1002/2014JD022011.

Xue ,Y., H.-M. H. Juang, W.-P. Li, S. Prince, R. DeFries, Y. Jiao, and R. Vasic, 2004: Role of land surface processes in monsoon development: East Asia and West Africa. *J. Geophys. Res.*, **109**, D03105, doi: 10.1029/2003JD003556.

Yates, D. N., F. Chen, and H. Nagai, 2003: Land surface heterogeneity in the Cooperative Atmosphere Surface Exchange Study (CASES-97). Part II: Analysis of spatial heterogeneity and its scaling. *J. Hydrometeorol.*, **4**: 219-234, doi: 10.1175/1525-7541(2003)4%3C219:LSHITC%3E2.0.CO;2.

Zilitinkevich, S. S., 1995: Non-local turbulent transport: Pollution dispersion aspects of coherent structure of convective flows. *Air Pollution III,* **1**, 53-60, doi: 10.2495/AIR950071.

Zhang, G. J., and N. A. McFarlane, 1995: Sensitivity of climate simulations to the parameterization of cumulus convection in the Canadian Climate Center general circulation model. *Atmos.–Ocean*, **33**, 407–446.

Zhang, J., W. C. Wang, and L. R. Leung, 2008: Contribution of land-atmosphere coupling to summer climate variability over the contiguous United States. *J. Geophys. Res.*, **113**, D22109, doi: 10.1029/2008JD010136.

Zhang, N., Q. L. Williams, and H. Liu, 2010: Effects of land-surface heterogeneity on numerical simulations of mesoscale atmospheric boundary layer processes. *Theor. Appl. Climatol.,* **102**: 307-317, doi: 10.1007/s00704-010-0268-9.

Zheng, Y., A. Kumar, and D. Niyogi, 2015a: Impacts of land-atmosphere coupling on regional rainfall and convection. *Climate Dyn.,* **44**, 2383–2409, doi: 10.1007/s00382-014-2442-8.

Zheng, Y., K. Alapaty, J. A. Herwehe, A. D. Del Genio, and D. Niyogi, 2015b: Improving high-resolution weather forecasts using the Weather Research and Forecasting (WRF) model with an updated Kain-Fritsch scheme. *Mon. Wea. Rev., in press*, doi: 10.1175/MWR-D-15-0005.1.

Zhong, S., and J. C. Doran, 1995: A modeling study of the effects of inhomogeneous surface fluxes on boundary-layer properties. *J. Atmos. Sci.,* **52**, 3129–3142, doi: 10.1175/1520-0469(1995)052<3129:AMSOTE>2.0.CO;2.

Zhou, B., J. S. Simon, and F. K. Chow, 2014: The convective boundary layer in the Terra Incognita. *J. Atmos. Sci.*, **71**, 2545–2563, doi: 10.1175/JAS-D-13-0356.1.

APPENDIX

Appendix: Acronyms

ADP – Automated Data Processing

AGCM – Atmospheric General Circulation Model

AMMA – African Monsoon Multidisciplinary Analysis

AMF – ARM Mobile Facility

ARM – Atmospheric Radiation Measurement

BASE – Original KF Scheme

BOMEX – Barbados Oceanographic and Meteorological Experiment

CAPE – Convective Available Potential Energy

CFSR – Climate Forecast System Reanalysis

COPS – Convective and Orographically-induced Precipitation Study

CP – Convective Parameterization

CPS – Convective Parametrization Scheme

Czil – Zilitinkevich Coefficient C

DWR – Doppler Weather Radar

EC – Eddy Covariance

EL – Equilibrium Level

ETS – Equitable Threat Score

EXP – Explicit Treatment of Convection

FFT – Fast Fourier Transform

FNL – NCEP Global Final Analysis

GFS – Global Forecast System

GLACE – Global Land-Atmosphere Coupling Experiment

GOES – Geostationary Operational Environmental Satellites

HRLDAS – High Resolution Land Data Assimilation System

HWT – Hazardous Weather Testbed

IHOP_2002 – International H_2O Project 2002

IMD – India Meteorological Department

KF – Kain-Fritsch

LCL – Lifting Condensation Level

LES – Large Eddy Simulations

LFC – Level of Free Convection

LSM – Land Surface Model

LULC – Land Use and Land Cove

MPAS – Model for Prediction across Scales

MPE – Multisensor Precipitation Estimates

MYJ – Mellor-Yamada-Janjic

NCEP – National Centers for Environmental Prediction

NESDIS – National Environmental Satellite Data and Information Service

NOAA – National Oceanic and Atmospheric Administration

NWP – Numerical Weather Prediction

PBL – Planetary Boundary Layer

RMSE – Root Mean Square Error

RRTM – Rapid Radiative Transfer Model

RRTMG – Rapid Radiation Transfer Model, Global

SGP – Southern Great Plains

SST – Sea Surface Temperature

TKE – Turbulent Kinetic Energy

TMPA – TRMM Multi-satellite Precipitation Analysis

TRMM – Tropical Rainfall Measuring Mission

UKF – Updated KF Scheme

USGS – United States Geological Survey

WDM6 – WRF double-moment 6-class scheme

WSM6 – WRF Single Moment 6-class

WPS – WRF Preprocessing System

WRF-ARW – Advanced Research Weather Research and Forecasting

VITA

VITA

YUE ZHENG

Department of Earth, Atmospheric, and Planetary Sciences and Indiana State Climate Office
LILY 2-420, 915 W. State Street, Purdue University, West Lafayette, IN 47907

EDUCATION

Purdue University **West Lafayette, IN**

Ph.D., Atmospheric Sciences 2011-present

Dissertation: Impacts of Land-Atmosphere Interactions on Regional Rainfall and Convection

Expected graduation 2015

University of Kansas **Lawrence, KS**

Ph.D. student, transferred to Purdue University 2009-2011

Beijing Normal University **Beijing, China**

M.S., Cartography and Geography Information System 2006-2009

Thesis: Modeling Microwave Emission from Vegetated Surface Based on L-system Simulation

Beijing Forestry University **Beijing, China**

B.S., Resources Environment and the Management of Urban and Rural Planning 2002-2006

Thesis: Analysis of the impacts of Spatial Heterogeneity on Urban Heat Island effects

RESEARCH EXPERIENCE

Purdue University **West Lafayette, IN**

Indiana State Climate Office and Land Surface Lab

Graduate Researcher; Advisor: Dr. Dev Niyogi 2011-present

- Explored impact of interactions between land-surface and cloud on mesoscale convection and precipitation
- Examined the role of fine-scale surface heterogeneity on boundary layer dynamics
- Assessed the impact of land-atmosphere coupling strength on mesoscale convection and rainfall

US Environmental Protection Agency Research Triangle Park, NC

Student Researcher; Mentor: Dr. Kiran Alapaty Summer 2013

- Improved the prediction accuracy of high-resolution (1~10 km) short-term precipitation by incorporating scale-aware cloud dynamics in WRF model

University of Kansas Lawrence, KS

Graduate Researcher; Advisor: Dr. Nathanial Brunsell 2009-2011

- Scaling surface observations with Eddy Covariance and examined the role of land cover variability on boundary layer dynamics
- Water survey in Canon City, Colorado

Beijing Normal University Beijing, China

State Key Laboratory of Remote Sensing Science

Graduate Research Assistant; Advisor: Lixin Zhang 2006-2009

- Improved simulation of microwave radiation for vegetated surface based on radiometer field experiments, models, and computer graphics
- Participation in and support for Watershed Allied Telemetry Experimental Research remote sensing field campaign

ADDITIONAL ACADEMIC EXPERIENCE

Purdue University (Teaching Assistant) **West Lafayette, IN**

EAPS 221 Survey of Atmospheric Science Spring 2014

EAPS 591 Climate Time Series Analysis Fall 2013

Tecumseh Jr. High School **Lafayette, IN**

Co-Teach Science Fall 2012

- Worked with teachers to integrate research and new approaches into local middle school classrooms
- Taught lessons as the primary teacher

Beijing Normal University (Teaching Assistant) **Beijing, China**

Microwave Remote Sensing Fall 2007, 2008

- Taught undergraduates radiometer field experiment

PUBLICATIONS

Zheng, Y., A. Kumar, D. Niyogi (2015) Impacts of land-atmosphere coupling on regional rainfall and convection. *Climate Dynamics* 44: 2383-2409, doi: s00382-014-2442-8.

Zheng, Y., K. Alapaty, J. A. Herwehe, A. D. Del Genio, D. Niyogi (2015) Improving high-resolution weather forecasts using the Weather Research and Forecasting (WRF) model with an updated Kain-Fritsch scheme. *Monthly Weather Review*, doi: 10.1175/MWR-D-15-0005.1.

Zheng, Y., N. A. Brunsell, J. G. Alfieri, D. Niyogi (2015) Impacts of land surface coupling on Boundary Layer simulation over heterogeneous landscapes. *Earth Interactions*, *Land Use Land Cover Change Special Issue*. (Under revisions)

Zheng, Y., K. Alapaty, D. Niyogi (2015) Impact of land-atmosphere-convection interactions on regional precipitation intensity and variation in WRF. (In submission)

Han, T., **Y. Zheng**, G. Gong (2015) Energy and exergy analysis of building thermal load in different climate zones in China. *Energy and Buildings*. (In press)

A. Chevuturi, A. P. Dimri, S. Das, **Y. Zheng**, A. Kumar, D. Niyogi (2015) Numerical simulation of an intense precipitation event over Rudraprayag in the Central Himalayas during 13-14 September 2012. *Earth Interactions*. (In submission)

Zheng, Y., L. Zhang (2009) Study of the Effects of Vegetation on Microwave Radiation of Frozen Soil in Cold Regions. *Journal of Glaciology and Geocryology* 31(2): 214-219.

Zheng, Y., G. Sun (2008) The Animation of Tree Development Based on Timed L-system. *The 16th International Conference on Geoinformatics and Joint Conference on GIS and Built Environment.*

Zheng, Y., L. Zhang, G. Sun (2008) Understanding the Vegetation Effects at Frozen Environment by Theory and Field Experiment. *IEEE International Geoscience & Remote Sensing Symposium.*

CONFERENCE PRESENTATIONS

Y. Zheng, K. Alapaty, J. A. Herwehe, A. Del Genio, D. Niyogi, Improving High-Resolution Weather Forecasts using the Weather Research and Forecasting (WRF) Model with an Improved Kain-Fritsch Scheme, 27th Conference on Weather Analysis and Forecasting (WAF), Chicago, IL, 19 Jun. - 3 Jul. 2015

K. Alapaty, J. Herwehe, R. Bullock, **Y. Zheng**, A. Sims, M. Mallard, L. Fowler, Testing of multi-scale Kain-Fritsch scheme using regional and global Models, the 16th Annual WRF Users Workshop, Boulder, CO, Jun. 15-19, 201

Y. Zheng, K. Alapaty, D. Niyogi, A. Kumar, Improving high-resolution weather forecasts using the Weather Research and Forecasting (WRF) model with updated Kain-Fritsch scheme, AGU Fall Meeting, San Francisco, CA, Dec. 8-12, 2013

K. Alapaty, R. Bullock, **Y. Zheng**, J. Herwehe, D. Niyogi, J. Kain, Precipitation biases in high-resolution regional weather and climate simulations: What are the causes?, UC Davis, CA, Sep. 10-12, 2013

Y. Zheng, N. A. Brunsell, D. Niyogi, Explore the Impacts of Soil Moisture/Temperature Variation on ABL from a Turbulent Mechanism Perspective, 20th Symposium on Boundary Layer Turbulence, Boston, MA, Jul. 9-13, 2012

SKILLS

WRF and related pre/post-processing (WPS, ARW-post, UPP)

Linux and high performance computing environment

C and FORTRAN

Data analysis and visualization packages (NCL and GrADS)

Statistical analysis and software (R, Matlab, and MET)

Geographic Information Systems and related software (ArcGIS and MapInfo)

Remote Sensing and related software (ENVI and ERDAS)

GRANTS AND AWARDS

Incentive Grant, Purdue University	2013
Community Service Learning Grant	2012
Graduate Academic Excellence Award, Beijing Normal University	2008-2009
Second Prize, the 2nd Symposium of Geography Graduate Academia, Beijing	2006
Outstanding Student Award four years in a row, Beijing Forestry University	2002-2006

PUBLICATIONS

PUBLICATIONS

Zheng, Y., A. Kumar, D. Niyogi (2015) Impacts of land-atmosphere coupling on regional rainfall and convection. *Climate Dynamics* **44**: 2383-2409, doi: s00382-014-2442-8.

Zheng, Y., K. Alapaty, J. A. Herwehe, A. D. Del Genio, D. Niyogi (2015) Improving high-resolution weather forecasts using the Weather Research and Forecasting (WRF) model with an updated Kain-Fritsch scheme. *Monthly Weather Review*, doi: 10.1175/MWR-D-15-0005.1.

Zheng, Y., N. A. Brunsell, J. G. Alfieri, D. Niyogi (2015) Impacts of land surface coupling on Boundary Layer simulation over heterogeneous landscapes. *Earth Interactions, Land Use Land Cover Change Special Issue.* (Under revisions)

Zheng, Y., K. Alapaty, D. Niyogi (2015) Impact of land-atmosphere-convection interactions on regional precipitation intensity and variation in WRF. (In submission)